



UNIVERSITAT<sub>DE</sub>  
BARCELONA

**A biogeochemical study  
of an abandoned Pb-Zn mine in the Aran Valley, Spain;  
applications of natural attenuation of heavy metals  
via secondary hydrozincite precipitation**

Max Greene Giannetta



Aquesta tesi doctoral està subjecta a la llicència **Reconeixement 4.0. Espanya de Creative Commons.**

Esta tesis doctoral está sujeta a la licencia **Reconocimiento 4.0. España de Creative Commons.**

This doctoral thesis is licensed under the **Creative Commons Attribution 4.0. Spain License.**

# A biogeochemical study of an abandoned Pb-Zn mine in the Aran Valley, Spain; applications of natural attenuation of heavy metals via secondary hydrozincite precipitation



Max Greene Giannetta

PhD Thesis

2022









Dedicated to  
my mom and dad,  
Laura and Russ,  
and my brother, Leo.



UNIVERSITAT DE  
BARCELONA



UNIVERSITAT DE BARCELONA

FACULTAT DE CIÈNCIES DE LA TERRA

**A biogeochemical study of an abandoned Pb-Zn  
mine in the Aran Valley, Spain; applications of  
natural attenuation of heavy metals via secondary  
hydrozincite precipitation**

MAX GREENE GIANNETTA

2022





UNIVERSITAT DE BARCELONA

FACULTAT DE CIÈNCIES DE LA TERRA

PROGRAMA DE DOCTORAT DE CIÈNCIES DE LA TERRA

**A biogeochemical study of an abandoned Pb-Zn mine in the Aran Valley, Spain; applications of natural attenuation of heavy metals via secondary hydrozincite precipitation**

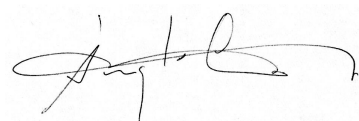
Memòria presentada per Max Greene Giannetta per optar al títol de doctor per la Universitat de Barcelona



Director  
Dr. Jordi Cama i Robert



Director  
Dr. Josep M. Soler



Tutor  
Dr. M. Àngels Canals Sabaté



Doctorand  
Max Greene Giannetta





This PhD study was financed by projects CGL2017-82331-R (Spanish Ministry of Economy and Competitiveness) CEX2018-000794-S (Spanish Ministry of Science and Innovation) and 2017SGR (Catalan Government).





# TABLE OF CONTENTS

ACKNOWLEDGEMENTS.....	15
ABSTRACT/RESUM.....	17
LIST OF FIGURES.....	21
LIST OF TABLES.....	27
<b>CHAPTER 1 – GENERAL INTRODUCTION</b>	
1.1 The Aran Valley.....	29
1.2 Environmental Impact of Mining Activities.....	32
1.3 Motivation and Objectives.....	33
1.4 Thesis Outline.....	35
<b>CHAPTER 2 – CHARACTERIZATION OF THE VICTORIA MINE</b>	
2.1 Introduction to the Victoria Mine.....	37
2.2 Methods	
2.2.1 <i>Field Sampling</i> .....	41
2.2.2 <i>Discharge and Solute Mass Fluxes</i> .....	48
2.2.3 <i>Water Chemistry Analysis</i> .....	49
2.2.4 <i>Hydrozincite Characterization</i>	
2.2.4.1 <i>XRD Analyses</i> .....	50
2.2.4.2 <i>Electron Microprobe Analyses</i> .....	51
2.2.4.3 <i>Total acid digestion</i> .....	51
2.2.5 <i>Hydrozincite Solubility Experiment</i> .....	52
2.3 Results	
2.3.1 <i>Aqueous Chemistry Results</i> .....	54
2.3.2 <i>Discharge and Solute Flux Results</i> .....	58
2.3.3 <i>X-ray Diffraction Results</i> .....	60
2.3.4 <i>Electron Microprobe and SEM Results</i> .....	63
2.3.5 <i>Total Digestion Results</i> .....	69
2.3.6 <i>Solubility Experiment Results</i> .....	71
2.3.7 <i>Equilibrium Constant for Hydrozincite</i> .....	72
2.3.8 <i>Mineral Solubility along the Flow Path</i> .....	74

<b>2.4 Discussion</b>	
<b>2.4.1 Apparent Hydrozincite Solubility</b> .....	76
<b>2.4.2 Composition of the Mine Water</b> .....	78
<b>2.4.3 Composition of Hydrozincite</b> .....	80
<b>2.4.4 Metal Mobility</b> .....	82
<b>2.4.5 Comparison to Literature</b> .....	84
<b>2.4.6 Mechanisms Controlling Hydrozincite Composition</b> .....	86
<b>2.4.7 Hydrozincite and Smithsonite</b> .....	88
<b>2.5 Conclusions and Outlook</b> .....	90

## CHAPTER 3 – MODELING OF THE VICTORIA MINE SYSTEM

<b>3.1 Introduction</b> .....	93
<b>3.2 Objectives and Model Overview</b> .....	93
<b>3.3 Description of the RTM Code</b> .....	97
<b>3.4 Model Setup and Parameterization</b> .....	99
<b>3.4.1 Host Rock Reference Models</b>	
3.4.1.1 Flow Path Length.....	99
3.4.1.2 Mineral Distribution and Reactions.....	100
3.4.1.3 Water Flow Velocity.....	104
3.4.1.4 Initial and Input Water Composition.....	105
3.4.1.5 Construction of the Host Rock Models.....	106
<b>3.4.2 Gallery Reference Model</b> .....	108
<b>3.4.3 Case 1: Flow Velocity</b> .....	109
<b>3.4.4 Case 2: Hydrozincite Solubility</b> .....	110
<b>3.4.5 Case 3: Dispersivity</b> .....	111
<b>3.4.6 Case4: Homogeneous Host Rock</b> .....	111
<b>3.4.7 Solute Mass Flux and Discharge</b> .....	112
<b>3.5 Simulation Results and Discussion</b>	
<b>3.5.1 Host Rock Reference Model Results</b> .....	113
<b>3.5.2 Gallery Reference Model Results</b> .....	116
<b>3.5.3 Case 1: Flow Velocity</b>	
3.5.3.1 Host Hock Model Sensitivity.....	120
3.5.3.2 Gallery Model Sensitivity.....	125

3.5.4 <i>Case 2: Hydrozincite Solubility</i> .....	128
3.5.5 <i>Case 3: Dispersivity</i> .....	131
3.5.6 <i>Case 4: Homogeneous Host Rock</i> .....	132
3.5.7 <i>Solute Mass Flux and Discharge</i> .....	136
3.6 <b>Summary and Conclusions</b> .....	138
<b>CHAPTER 4 – MICROBIOLOGY OF THE VICTORIA MINE</b>	
4.1 <b>Introduction</b> .....	143
4.2 <b>Objectives</b> .....	145
4.3 <b>Methods</b>	
4.3.1 <i>Bioreactor Experiments</i> .....	146
4.3.2 <i>Sampling and DNA Extraction</i> .....	147
4.3.3 <i>MiSeq-Sequencing and Bioinformatics</i> .....	148
4.4 <b>Results</b>	
4.4.1 <i>Bioreactor Experiment Results</i> .....	150
4.4.2 <i>Sequencing and Bioinformatics Results</i> .....	152
4.5 <b>Discussion</b>	
4.5.1 <i>Comparison to Literature</i> .....	160
4.5.2 <i>Extent of Microbial Activity</i> .....	161
4.5.3 <i>Diversity and Microbial Strategy</i> .....	161
4.6 <b>Conclusions</b> .....	163
<b>CHAPTER 5 – GENERAL DISCUSSION AND CONCLUSIONS</b> .....	165
<b>SUPPLEMENTARY INFORMATION</b> .....	171
<b>REFERENCES</b> .....	177





## ACKNOWLEDGMENTS

Completing a doctoral dissertation is not an individual effort. Over these last three and a half years several individuals supported me and I would be remiss if they went unnoticed.

*On the academic side of things:*

I would like to express my gratitude to my committee (Dr. Ignasi Queralt, Dr. Cristina Domènech, and Dr. Eva Marguí) for their contribution to making this achievement possible. And, special thanks to my UB tutor Dr. M. Àngels Canals Sabaté.

To my doctoral advisors Dr. Jordi Cama and Dr. Josep Soler. I am grateful for your help in guiding me through my project in a uniquely challenging time in history. Thank you both for your time and efforts dedicated to meetings, help with my sampling campaigns in the Aran Valley, attention to detail, and useful suggestions for both the project and the final writing of my thesis. It was not a simple or easy process and I thank you both for all that you've done.

To Dr. Robert Benaiges. Thank you for inviting me to the Aran Valley in the summer 2019. That trip gave me the spark of inspiration that eventually led to the development and completion of my doctoral study. Also, I appreciate your help with my microbiological endeavors during my time here.

A special thanks to Jordi Bellès for all of your help around the lab and department. I always look forward to a sharing a meal or a drink with you. Cheers!

To Joan Gutiérrez Leon. Thank you for the countless scientific discussions in the office. Those chats helped me progress and you provided a great source of ideas and helped me crystalize my own.

A special thanks to Jordi Gavaldà for leading me and my team safely into the Victoria Mine. Your support and expertise has been a crucial component of my project.

And to all those in IDAEA who were around for drinks, chats, lunches, and various celebrations, thank you all! Your part in all of this does not go unforgotten.

*One the family and social side of things:*

Mom and Dad, thank you both for the countless hours of conversations and your sound advice. It wasn't easy moving to a new country and doing a PhD, but your support made the experience much more manageable and enjoyable. I love you both. I suppose the best thanks I can give to you is to say, I'm almost done!

Leo, my bro, thank you for lending an ear when I needed to vent a bit and for your fresh perspective on things. Your advice is always appreciated and I am extremely grateful to have you in my life. Lots of love.

A very special thanks to all of my friends here in Barcelona, who showed me what it means to integrate into a new culture and have fun with it. You all gave me climbing adventures, great trips around Europe, heated volleyball matches, and some of the best nights I can remember.

And last but not least, I would like to extend my sincere thanks to all of my friends, both here in Barcelona and back in the USA (and those in other countries). You all know who you are and I can only hope all of you know that I am eternally grateful for your friendship.

That will do it for now. Onward!

## ABSTRACT

The Aran Valley in Catalonia (Spain) was the site of large-scale Zn, Pb, Cu, Fe, and Ag mining from the late 19<sup>th</sup> century until approximately 1950. Although mining activities ceased over 70 years ago, some of the abandoned mining relics (e.g. tunnels, processing facilities, and tailings dumps) exhibit elevated concentrations of metals (e.g. Zn, Cd and Ni) in the associated water systems, thus posing a health risk to the associated ecosystem. In this study, the largest underground mine in the Aran Valley (the Victoria Mine) was chosen as a field site to showcase the processes affecting metal mobility in the environment. The mine is composed of 15 km of tunnel galleries, many of which are flooded today, and is situated beneath a steep mountain slope. Moreover, the lowermost gallery exhibits a continuous output of water, whose composition reflects a flow path through system.

Three sampling campaigns to the mine (October 2019, July 2020, and June 2021) provide a spatiotemporal dataset showing the evolution of solute concentrations through the system along a flow path. Rainwater from the upper catchment flows into the host rock above the mine where it dissolves ore materials (primarily Zn (sphalerite) and Fe (pyrite) sulfides with Ni and Cd impurities) causing elevated Zn, Ni, and Cd concentrations where these waters enter the mine. From there, the precipitation of hydrozincite ( $Zn_5(CO_3)_2(OH)_6$ ) along the tunnel gallery acts as a metal polishing mechanism resulting in significantly diminished metal concentrations (e.g. Zn from 155 to 10 ppm, Ni from 377 to 32 ppb, and Cd from 105 to 22 ppb). Hydrozincite has been shown to be product of biomineralization in other sites. However, by way of DNA sequencing of local bacterial communities, bioreactor experiments, morphological comparisons biomineralized samples and geochemical modeling, it is confirmed that the mineral forms abiotically at the Victoria Mine.

Characterization of the solid samples taken from the mine reveals several different morphologies, Zn zonations in hydrozincite (i.e. purity changes), and small amounts of smithsonite ( $ZnCO_3$ ) and calcite ( $CaCO_3$ ). In general, all solids show layering, which is a result of intermittent precipitation of distinct solid products. These precipitation patterns are likely a result of changing solute concentrations and precipitation rates. The cause of these changes is hypothesized to be rain events, which change the water residence time in both the host rock and in the gallery, thereby altering the water composition.

Solubility experiments and speciation calculations done using the CrunchFlow code demonstrate that hydrozincite here does not have a constant  $K_{eq}$  value, but rather a range of values ( $30.0 < \log[K_{eq}] < 37.68$  at 7°C). This behavior is presumed to be a result of precursor effects, such that amorphous solids with higher solubilities may form before the structured hydrozincite. Notably, all analyzed solids from the collected mine samples show significant amounts of amorphous material (i.e. broad XRD peaks).

A CrunchFlow reactive transport model constructed to capture the processes occurring along the flow path through the catchment (i.e. rainwater infiltration and flow through the host rock → mixing of different gallery source (drip) waters → flow of water through the gallery), successfully reproduces the measured concentrations. Further, the model predicts the formation of hydrozincite, calcite, and smithsonite while maintaining their relative proportions consistent with that observed in the samples. Sensitivity analyses of the most relevant parameter values (e.g. hydrozincite solubility, flow velocity, dispersivity and mineral reactivities) is performed as a way to capture the range of behaviors expected to occur, and thereby predict future changes to metal mobility. The model confirms that changes to flow velocity, which would translate to changes in volumetric discharge through the system caused by rain events, could be the cause of mineral layering and metal zonation in hydrozincite. The model also confirms that the natural metal attenuation process is expected to occur through a wide range of system perturbations. Thus, the abandoned mine poses little risk to the neighboring ecosystem.

## RESUM

A Catalunya, la Vall d'Aran va ser el lloc d'explotació a gran escala de Zn, Pb, Cu, Fe i Ag des de finals del segle XIX fins aproximadament l'any 1950. Tot i que les activitats mineres van cessar fa més de 70 anys, els sistemes d'aigua associats a les relíquies d'algunes de les mines abandonades (per exemple, galeries, instal·lacions de processament i abocadors de residus) presenten concentracions elevades de metalls, la qual cosa suposa un risc per a la salut dels ecosistemes associats.

En aquest treball, s'ha escollit la mina Victòria (la mina subterrània de zinc més gran de la Vall d'Aran) com a àrea d'estudi per mostrar els processos que afecten la mobilitat dels metalls en el seu entorn. La mina està situada a sota d'un vessant escarpat de la muntanya i està formada per 15 km de galeries, moltes inundades actualment. A la galeria més baixa hi ha una sortida d'aigua contínua, la composició de la qual reflecteix el camí del flux a través de la mina i de la roca mare.

S'han realitzat tres campanyes de mostreig a la mina (octubre 2019, juliol 2020 i juny 2021). Les dades espacio-temporal obtingudes mostren l'evolució de les concentracions dels soluts a través del sistema seguint el camí del flux. L'aigua de pluja que s'infiltra per la part superior (zona de captació) dissol els minerals sulfurs que formen la roca mare (principalment sulfurs de Zn (esfalerita) i de Fe (pirita) amb impureses de Ni i Cd), augmentant així les concentracions de Zn, Ni i Cd de l'aigua que circula per la mina. En aquestes condicions s'afavoreix la precipitació d'hidrozincita ( $Zn_5(CO_3)_2(OH)_6$ ) al llarg de la galeria. Aquest mecanisme comporta una disminució significativa de les concentracions dels metalls en els fluxos d'aigua. Per exemple, la concentració de Zn disminueix de 155 a 10 ppm, la de Ni de 377 a 32 ppb, i la de Cd de 105 a 22 ppb.

S'ha demostrat que en altres llocs la hidrozincita és un producte biomineral. Tanmateix, a partir de la seqüenciació d'ADN de les comunitats microbianes de la galeria, dels resultats experimentals biòtics, de les comparacions morfològiques amb mostres conegudes com a producte de la biomineralització i de la modelització geoquímica, es confirma que en la mina Victoria la formació del mineral és abiòtica.

La caracterització de les mostres sòlides recollides a la mina evidencia morfologies diferents, zonacions de Zn en la hidrozincita (és a dir, canvis de puresa) i l'existència de petites quantitats de smithsonita ( $ZnCO_3$ ) i de calcita ( $CaCO_3$ ). En general, tots els sòlids presenten unes bandes com a conseqüència de la precipitació intermitent de diferents productes sòlids.



Aquests patrons de precipitació deuen resultar de canvis en les concentracions de soluts i de les velocitats de precipitació. Com a hipòtesi, es planteja que la causa d'aquests canvis són diferents esdeveniments de pluja que modifiquen el temps de residència de l'aigua tant a la roca mare com a la galeria, produint una alteració de la composició de l'aigua.

Els resultats dels experiments de solubilitat i els càlculs d'especiació fets amb el codi CrunchFlow demostren que el producte de solubilitat de la hidrozincita no té un valor constant, sinó un rang de valors ( $30,0 < \log[K_{eq}] < 37,7$  a  $7\text{ °C}$ ). Se suposa que aquest comportament és degut a la formació de precursors amorfs amb solubilitats més elevades prèvia a la formació de la hidrozincita estructurada. De fet, els pics amplis en els difractograms de DRX de totes les mostres sòlides recollides a la mina evidencien quantitats significatives de material amorf.

Fent servir el codi CrunchFlow, s'ha elaborat un model de transport reactiu que captura els processos que ocorren al llarg del recorregut del flux a través de la captació: infiltració d'aigua de pluja i flux a través de la roca mare → barreja de diferents orígens d'aigua (goteig) de la galeria → flux d'aigua a través de la galeria. El model reproduïx satisfactòriament les concentracions mesurades i alhora prediu la formació d'hidrozincita, calcita i smithsonita mantenint les proporcions relatives observades a les mostres. S'ha realitzat una anàlisi de sensibilitat variant els valors dels paràmetres geoquímics i hidrodinàmics més rellevants (la solubilitat de la hidrozincita, la velocitat del flux, la dispersivitat i les reactivitats minerals) per avaluar el comportament de la mobilitat dels metalls i possible canvis futurs. El model confirma que els canvis en la velocitat del flux, és a dir, els canvis en la descàrrega volumètrica a través del sistema causats per esdeveniments de pluja, serien la causa de les bandes de minerals i de la zonació metàl·lica en la hidrozincita. El model també confirma que l'atenuació natural dels metalls és un procés factible en un ampli rang de pertorbacions del sistema. Per tant, la mina abandonada estudiada suposa poc risc per a l'ecosistema associat.

## LIST OF FIGURES

- Figure 1.1** (top) A Google Earth image showing the location of the Aran Valley. (bottom) A map of the Aran Valley showing the age of geological formations. The box marked "1" represents the location of the Bossost-Arres mining district, and the box marked "2" represents the location of the Liat-Horcalh mining district. The geologic map was modified from Santamaria *et al.* (2008).....**30**
- Figure 2.1** Sketch of a cross section of the Victoria Mine. Each tunnel gallery was labeled either by a distinct name or by its corresponding altitude in meters. For example, the entrance to the second lowest gallery, known as the 1330 Gallery, resides at an altitude of 1,330 meters. Figure modified from Santamaria *et al.* (2008).....**37**
- Figure 2.2.** A cropping of a 1:50,000 geologic map of the Victoria Mine catchment in the Bossost-Arres mining district (Geologic Institute of Catalonia, map # 39). The approximate location of the Victoria Mine is represented by the black star and catchment boundaries are marked with a blue dotted line.....**38**
- Figure 2.3.** Drawing of an aerial view of the various tunnels, levels, and installations of the Victoria Mine. The green, purple, and light blue colors correspond the Artiga/Miracle ore vein, Northeast ore vein, and Principal ore vein, respectively. However, the colored lines themselves are manmade tunnels (e.g. the 1330 gallery corresponds to the Northwest Vein). The blue and red diamonds represent the entrance and the end of the sample path (310 m) within the 1330 Gallery, respectively, while the black dotted line shows the sample path. The magenta diamond represents the approximate location of the outlet of the Sinçay Gallery where the mine effluent was sampled. Figure modified from Santamaria *et al.* (2008).....**39**
- Figure 2.4.** Google Earth image of the Victoria Mine catchment system and locations of outdoor sampling intervals. Sampling locations correspond to Table 2.1 and Figure 2.5, however sample locations 5-10 are omitted. The red line represents the catchment boundaries and the red oval with the "X" is the approximate location of the Victoria Mine. Artiga Creek was never sampled because it was dry during all three sampling campaigns. Blue arrows represent water and the corresponding flow direction.....**42**
- Figure 2.5.** A schematic (not to scale) of the Victoria Mine catchment system and sampling locations in this study. Each sample location is represented by a black circle with a number corresponding to Table 2.1. Each light brown trapezoid corresponds to an altitude labeled on the left-hand side. The "9 m salt dilution transect" refers to the nine-meter mixing length of the salt dilution procedure done to calculate volumetric discharge of the effluent. The "vertical shaft" between Gallery 1330 and the Sinçay Gallery is assumed to connect the two galleries. The "host rock infiltration" represents where surface waters from the upper catchment flow and react in with the surrounding host rock and unexploited ore material (e.g. sphalerite) before dripping/flowing into the mine. Water and the corresponding flow direction are denoted by blue arrows.....**43**
- Figure 2.6.** Photos taken from inside and outside of the Victoria Mine during the 2019 campaign. From A to I represents walking "upstream" with respect to the flow of water (i.e. moving deeper into the gallery). (A) Melics Creek nine meters downstream from where the mine effluent merges (sample-3). Microbial DNA was sampled here in 2019. (B) Jordi Cama measuring pH at the entrance of the Sinçay Gallery/mine effluent (sample-4). (C) The entrance of the 1330 Gallery. (D) 65 m from the gallery entrance and the first occurrence of flowing water and actively precipitating hydrozincite. Microbial DNA was sampled here in 2019. (E) ≈100 meters from the gallery entrance. Water is flowing on the floor and hydrozincite is present. (F) Drip water at 140 m from the entrance (sample-6). (G) 160 m from the entrance where a shaft is flooded (sample-7). (H) ≈170 m from the gallery entrance where the "floating skin" morphology of hydrozincite can be observed. The white mineralization is floating on top of the water. This is ubiquitous throughout the gallery. (I) 190 m from the entrance and the first occurrence of a reddish precipitate (sample-8).....**45**

**Figure 2.7.** Photos from inside the 1330 Gallery in the Victoria Mine in 2019. (A) Approximately 210 m from the entrance of the gallery showing a  $\approx 50$  m flooded section of the tunnel. (B) Hydrozincite displaying a blue coloration at  $\approx 260$  m from the entrance. Images C - F correspond to 280 m from the gallery entrance (sample-9) where water is flowing and dripping rapidly from several locations in the ceiling and walls. (C) Flow structures on the walls and ceilings at 280 m. Most of the flow comes from the left side of the image. (D) Flow structures and terraces formed by hydrozincite. To the left (not seen) there is a vertical shaft where most of the water is flowing. (E) A close-up image of the flow structures seen on the wall in image D. (F) Stalactites forming on the ceiling. A close-up image of the same stalactites seen in image C. (G) 310 m from the entrance (sample-10 a.k.a. red goo) showing the red seep coming from the wall and accumulating on the floor. Microbial DNA was sampled here in 2019. (H) Approximately 350 m from the gallery entrance showing the hydrozincite nodules.....**46**

**Figure 2.8.** Photographs of four observed morphologies of hydrozincite found in the Victoria Mine. Morphologies are as follows: (1) nodular, (2) smooth layered, (3) floating skin, and (4) botryoidal. In this image, the distance between two horizontal or vertical dots represents 0.5 cm.....**50**

**Figure 2.9.** (left) A photo taken of the batch dissolution experiment at 3.7°C inside of a walk-in cooler. The air pump can be seen hanging in the top left section of the image. The white angular mineral suspended in the liquid is a sample of the floating skin hydrozincite (Figure 2.8(3)). (right) A schematic of the batch experiment showing the constant bubbling ("air flow") and stirring, while the pH meter was fixed in position for in-situ measurements. The sample port was maintained closed while sampling was not occurring, and there was an outlet hole for air to escape so as not to build pressure within the vessel.....**52**

**Figure 2.10.** *In-situ* measurements of alkalinity, temperature, conductivity, and pH from 2019-2021. Flow moves from right to left. The blue-shaded regions denote locations outside of the mine while the non-shaded regions denote locations inside the mine. Numbers on the x-axis correspond to sampling locations as described in Table 2.1 and Figure 2.5. Conductivity was not measured in the gallery in 2019. See table S1 for uncertainty.....**56**

**Figure 2.11.** Major ion concentrations at sampling locations (mM). Analytical uncertainty is  $\pm 4\%$ . Here, flow moves from right to left. The highest measured concentrations are placed in the top row, and the lowest concentrations at the bottom. The blue-shaded regions denote locations outside of the mine while the non-shaded regions denote locations inside the mine. Numbers on the x-axis correspond to sampling locations as described in Table 2.1 and Figure 2.5. The "X 2003" in the legend above refers to the Zn measurements done by Marques et al. (2003).....**56**

**Figure 2.12.** Minor ion concentrations at sampling locations given in  $\mu\text{M}$ . Water flows from right to left. The blue-shaded regions denote locations outside of the mine while the non-shaded regions denote locations inside the mine. Numbers on the x-axis correspond to sampling locations as described in Table 2.1 and Figure 2.5. The "X 2003" in the legend above refers to the Ni, Fe, and Cd measurements done by Marques et al. (2003). Analytical uncertainty is  $\pm 4\%$  for these values.....**57**

**Figure 2.13.** Salt calibration curve and breakthrough curves from field conductivity measurements during the three sampling campaigns. The linear regression (Eq. 2.1) can be viewed in the NaCl Calibration plot along with an  $R^2$  value, which is equal to 1.....**58**

**Figure 2.14.** Three plots showing the relationship between volumetric discharge and elemental mass flux. Discharge was normalized to the highest value measured; 40.4 L/min in 2021. Each plot shows a dotted line that represents a linear best fit for the data. The slope ( $m$ ) and  $R^2$  from each regression was recorded in the table on the right. (A) Calcium and sulfate showing the two highest mass fluxes. (B) Zn, Na, Si, K, and Mg showing similar intermediate mass fluxes. (C) Cd, Sr, Li, and Ni showing the lowest mass fluxes.....**59**

**Figure 2.15.** Qualitative X-ray powder diffraction analysis results (black line) overlaid over ideal crystal peaks (red lines) for six hydrozincite samples. These six samples are composed of pure hydrozincite; however, the peaks are relatively wide, suggesting that they are not completely crystalline or contain impurities. The floating skin sample shows a small amount brianyoungite ( $Zn_3[CO_3,SO_4][OH]_4$ )..... **61**

**Figure 2.16.** Qualitative X-ray powder diffraction analysis results (black line) overlaid over ideal crystal peaks (colored lines) for two sphalerite ore samples taken from the Victoria Mine. The samples are composed mainly of sphalerite, however, there are several other mineral phases present. In Sphalerite Ore 1, there are small amounts of quartz, illite, clinocllore, and calcite. Sphalerite Ore 2 contains small amounts of quartz, calcite, pyrrhotite, clinocllore, annite, and possibly grunerite..... **62**

**Figure 2.17.** Backscattered electron images of four hydrozincite morphologies; Nodule (A-B), Smooth Layered (C), Floating Skin (D-I), and Botryoidal (J-L). Scale bars are shown at the bottom of each image. Each red dot represents the location of electron microprobe analysis. In general, white zones are richer in Zn than grey zones..... **63**

**Figure 2.18A.** Results from elemental scans of Cd, Ca, Mg, Fe, and Zn in the nodule morphology sample. The bottom right image is the backscattered electron image of the location where the scan was completed. The elemental "level" refers to a relative variation in concentration for a given scan, not an absolute concentration..... **64**

**Figure 2.18B.** Results from elemental scans of Cd, Ca, Mg, Fe, and Zn in the smooth layered morphology sample. The bottom right image is the backscattered electron image of the location where the scan was completed. The elemental "level" refers to a relative variation in concentration for a given scan, not an absolute concentration..... **65**

**Figure 2.18C.** Results from elemental scans of Cd, Ca, Mg, Fe, and Zn in the floating skin morphology sample. The bottom right image is the backscattered electron image of the location where the scan was completed. The elemental "level" refers to a relative variation in concentration for a given scan, not an absolute concentration..... **65**

**Figure 2.18D.** Results from elemental scans of Cd, Ca, Mg, Fe, and Zn in the botryoidal morphology sample. The bottom right image is the backscattered electron image of the location where the scan was completed. The elemental "level" refers to a relative variation in concentration for a given scan, not an absolute concentration..... **66**

**Figure 2.19.** Results from electron microprobe point analysis of a transect of two samples. The left column is showing the analysis of the nodule morphology sample, and the right column corresponds to a botryoidal sample. The numbers on the SEM image correspond to the x-axis for each sample..... **68**

**Figure 2.20.** Concentration and pH results through time from the hydrozincite dissolution experiments. The black points represent the 20.0°C experiment and the blue points represent the 3.7°C experiment. Nickel was only measured during the 3.7°C experiment. It should be noted that the same 3.0 g piece of hydrozincite (floating skin morphology) was used for each temperature condition. The warmer 20.0°C condition was the first experiment, and later the colder 3.7°C condition was done. Analytical uncertainty is ±6% for concentration values..... **72**

**Figure 2.21.** Resulting SI values and ionic strength (mol/L) from speciation calculations in CrunchFlow. Each calculation input has been adjusted to its corresponding measured water composition from the 2020 and 2021 sampling campaigns. Sample locations correspond to Table 2.1. The blue shaded regions represent samples locations outside of the mine, while non-shaded regions represent samples taken from inside the mine. Uncertainty here is ±6% based on the analytical techniques..... **74**

**Figure 2.22.** (top) Calculated SI values of hydrozincite based on 2021 water measurements plotted with respect to sampling locations (x-axis). Each line represents the SI for a given  $\log[K_{eq}]$ . The red circle denotes the location (sample-10) where a new  $\log[K_{eq}]$  was calculated to be 37.68 and corresponds to the red markers/lines. The black circle denotes the location (sample-5) where a new  $\log[K_{eq}]$  was calculated to be 35.53 and corresponds to the black markers/lines. These new  $\log[K_{eq}]$  values are calculated based on the assumption that the water at each sampling location is at equilibrium with respect to hydrozincite (SI = 0). (bottom) The SI of hydrozincite based on the 2020 water measurements implementing the new  $\log[K_{eq}]$  values based on the 2021 measurements. Uncertainty is  $\pm 6\%$  for these values due to measurement uncertainty.....78

**Figure 2.23.** Secondary electron images of  $ZnCO_3$  needle structures by Sharma et al. (2018). These needles are similar to those exhibited in the floating skin and botryoidal samples. Especially those found on the terminating mineral boundaries (Figure 2.17(H and I)).....89

**Figure 3.1.** Conceptual diagram of the host rock and gallery models. The water composition at the end of the calcite zone (31.5 m) from the 1D high reactivity model (HRM) and the 1D low reactivity model (LRM) are used to inform the gallery model. Those two waters are allowed to mix inside of the mixing cell (U) before flowing down the 250-m domain. The flux proportion of LRM/HRM = 10. Numbers represent sampling intervals defined in Table 2.1 and the blue arrows denote flow direction.....94

**Figure 3.2.** Sketch of the 2D grid implemented in CrunchFlow to simulate the mixing of the resulting HRM and LRM compositions and subsequent flow down the gallery. Each box is 0.5 m x 0.5 m. The numbers (e.g. 1,2) represent x,y indexes in the 2D mesh. Arrows represent directional Darcy fluxes ( $V$ ), and the size is proportional to the flux. Black circles represent no-flow boundaries. The grey "Inert" cells are composed of non-active minerals and a porosity of 0.001 to ensure no transverse flow.....96

**Figure 3.3.** CrunchTop simulation results of the host rock reference case. Flow goes from left to right with an ALV of 1.5 m/day. The high reactivity model (HRM) and low reactivity model (LRM) are plotted as a function of distance at  $t = 60$  days, where the residence time of the system is 30 days. The vertical lines divide the three zones as described in the "Conc. Zinc" plot. The non-saturated sulfide zone exists from 0 to 25.5 m, the saturated calcite zone exists from 25.5 m to 31.5 m, and the gallery zone exists from 31.5 m to 41.5 m. This is the same for all host rock models. measured sample 9 and 10 water compositions are plotted at 35 m with black and blue squares, respectively. The sample 11 data are plotted at 0 m. The plots for calcite, hydrozincite, smithsonite, and  $CO_2$  degassing rates have been scaled on the x-axis to more clearly visualize the model behavior. These five rates remain at zero outside of the visible range.....113

**Figure 3.4.** CrunchTop simulation results for the gallery model reference case plotted as a function of distance at  $t = 5$  days. Flow goes from left to right at an ALV = 0.48 m/min. (right) Simulation results showing data plotted from three years of sampling. (left) The same simulation results scaled to more clearly show model behavior....117

**Figure 3.5.** CrunchTop simulation results for the gallery model reference case plotted as a function of distance at  $t = 5$  days. Flow goes from left to right with an ALV = 0.48 m/min resulting in a water residence time of 8.7 hours. The calculated SI values from the 2020 and 2021 water measurements are done using a  $\log(K_{eq}) = 37.68$  for hydrozincite and plotted on the solubility diagrams.....118

**Figure 3.6.** High reactivity model (HRM) simulation results for the high flux case and low flux case. Flow goes from left to right at 0.75 and 3.0 m/day for the low and high flux case, respectively. The HRM reference case is also plotted and corresponds to the HRM results (blue) in Figure 25. In the high flux case, results are plotted as function of distance at  $t = 30$  days, where the residence time for the model is 15 days. The low flux results are plotted as a function of distance a  $t = 120$  days, where the residence time for the model is 60 days. The sample 11 data are plotted at 0 meters and the sample 9 data is plotted at 35 m as black squares. The plots for calcite, hydrozincite, smithsonite, and  $CO_2$  degassing rates have been scaled on the x-axis to more clearly visualize the model behavior. These five rates remain at zero outside of the visible range, except for smithsonite, which is slightly above zero ( $\sim 5.0e-09$  mol/m<sup>3</sup>/sec).....120

**Figure 3.7.** Low reactivity model (LRM) simulation results for the high flux case and low flux case. Flow goes from left to right at 0.75 and 3.0 m/day for the low and high flux case, respectively. The LRM reference case is also plotted and corresponds to the LRM results (black) in Figure 25. In the high flux case, results are plotted as function of distance at  $t = 30$  days, where the residence time for the model is 15 days. The low flux results are plotted as a function of distance at  $t = 120$  days, where the residence time for the model is 60 days. The sample 11 data are plotted at 0 meters and the sample 10 data is plotted at 35 m as black squares. The plots for calcite, hydrozincite, smithsonite, and CO<sub>2</sub> degassing rates have been scaled on the x-axis to more clearly visualize the model behavior. These five rates remain at zero outside of the visible range, except for smithsonite, which is slightly above zero ( $\sim 5.0e-09$  mol/m<sup>3</sup>/sec) .....122

**Figure 3.8.** Results of the 2D gallery model informed by the low and high flux host rock cases. Results are plotted as function of distance at  $t = 5$  days. Flow goes from left to right. The ALV is 0.24, 0.48, and 0.96 m/min for the low, ref., and high flux cases, respectively. The data from all sampling campaigns are shown with black square markers.....125

**Figure 3.9.** Results of the variable  $K_{eq}$  of hydrozincite cases in the 2D gallery model plotted with distance at  $t = 5$  days. Flow goes from left to right at an ALV of 0.48 m/min. The SI of hydrozincite, calcite, and smithsonite calculated from 2020 and 2021 field measurements are plotted with black squares. The SI of hydrozincite for these data points is based on a  $\log(K_{eq}) = 37.68$ .....128

**Figure 3.10.** The results plotted as a function of distance at  $t = 5$  days of three 2D gallery model simulations where only the dispersivity values were changed. Flow goes from left to right with an ALV of 0.48 m/min. The "high disp." case refers to the dispersivity set to 25 m, or 10% of the domain length. The "ref. disp." case refers to a dispersivity set to 2.5 m, or 1% of the domain length. Finally, the "low disp." case refers to the dispersivity set to 0.25 m, or 0.1% of the domain length. Data from sampling campaigns is not plotted.....131

**Figure 3.11.** CrunchTope simulation results in the high reactivity host rock model (HRM) comparing the homogeneous host rock case and the layered host rock (reference) case. Results are plotted as a function of distance at  $t = 60$  days. Flow goes from left to right with an ALV of 1.5 m/day. The vertical black lines represent zones of saturated and non-saturated rather than mineralogic composition since this model is mineralogically homogeneous. The gallery zone was not changed in this simulation, such that it is still effectively a non-saturated zone where flowing water is in contact with the atmosphere. The plots for calcite, hydrozincite, smithsonite, and CO<sub>2</sub> degassing rates have been scaled on the x-axis to more clearly visualize the model behavior. These five rates remain at zero outside of the visible range, except for smithsonite, which is slightly above zero ( $\sim 5.0e-09$  mol/m<sup>3</sup>/sec) in the reference model. The ferrihydrite precipitation rate  $1.2e-06$  mol/m<sup>3</sup>/sec from 0 to 27 meters and then drops to zero.....132

**Figure 3.12.** CrunchTope simulation results from the low reactivity host rock model (LRM) comparing the homogeneous host rock case and the layered host rock (reference) case. Results are plotted as a function of distance at  $t = 60$  days. The vertical black lines represent zones of saturated and non-saturated rather than mineralogic composition. The gallery zone was not changed in this simulation, such that it is still effectively a non-saturated zone where flowing water is in contact with the atmosphere. The plots for calcite, hydrozincite, smithsonite, and CO<sub>2</sub> degassing rates have been scaled on the x-axis to more clearly visualize the model behavior. These five rates remain at zero outside of the visible range, except for smithsonite, which is slightly above zero ( $\sim 5.0e-09$  mol/m<sup>3</sup>/sec) in the reference model. The ferrihydrite precipitation rate is  $4.1e-07$  mol/m<sup>3</sup>/sec from 0 to 27 meters and then drops to zero. ....134

**Figure 3.13.** Flux discharge relationships plotted from measurements (red) and the model (blue) for zinc, bicarbonate, calcium, and sulfate. Concentrations at 250 m in the gallery model were used in these calculations. The measured values are reported in section 2.3.2.....137

**Figure 4.1.** Image of the agarose gel plate after electrophoresis. DNA fragment travel direction is top to bottom. Every column is a separate sample of the PCR products. The PCR products were died with a fluorescent dye such that UV light causes the DNA to be visible; shown as the lightly colored horizontal lines. The pre-cast wells are the rectangles immediately below the numbers, and voltage-driven DNA migration was induced from top to bottom, although the gel plate was perfectly horizontal at the time of the electrophoresis. The “lad.” column contains the standard sulfate reducing bacteria DNA. The white arrow denotes the expected location of the DNA fragment containing the microbial 16s rRNA sequence. Each number is a natural sample and the “\*” denotes the products of a second PCR on the same DNA sample. The “pp1” and “pp2” refer to samples that are not a part of this study, and “(-)” represents the negative control (i.e. Milli-Q water).....148

**Figure 4.2.** Solute concentrations through time of the four bioreactor experiments. In the legend, "Out" refers to the outdoor sample-3 location, and "In" refers to the indoor sample-9 location. "...Stim." denotes the reactors that were amended with yeast extract. Analytical uncertainty for these measurements is  $\pm 4\%$ .....151

**Figure 4.3A.** Krona Diagrams showing OTUs of the upper Melics Creek outdoor microbial community (sample-11). A total of 66,207 reads are plotted. (top) Phylogenic makeup of the community where % refers to the overall bacterial population abundance. (bottom) Breakdown of the classes of the Proteobacteria where % refers to the proportion of Proteobacteria present. Image taken at sample location (a small creek on the right).....154

**Figure 4.3B.** Krona Diagrams showing OTUs of the microbial community at the sample-10 location inside of the 1330 Gallery (310 m from the entrance). A total of 79,555 reads are plotted Phylogenic makeup of the community where % refers to the overall bacterial population abundance. (bottom) Breakdown of the classes of the Proteobacteria where % refers to the proportion of Proteobacteria present. Image of where the red goo sample was taken.....155

**Figure 4.3C.** Krona Diagrams showing OTUs of the microbial community at the sample-5 location inside of the 1330 Gallery (65 m from the entrance). Phylogenic makeup of the community where % refers to the overall bacterial population abundance. (bottom) Breakdown of the classes of the Proteobacteria where % refers to the proportion of Proteobacteria present. The image is from where the sample was taken.....156

**Figure 4.3D.** Krona Diagrams showing OTUs of the outdoor microbial community at confluence of Melics Creek and the mine effluent (sample-3). Phylogenic makeup of the community where % refers to the overall bacterial population abundance. (bottom) Breakdown of the classes of the Proteobacteria where % refers to the proportion of Proteobacteria present. The image is from where the sample was taken.....157

**Figure 4.4.** SEM images of natural hydrozincite biominerals from the Naracauli River site. Figure modified from De Giudici *et al.* (2009).....160

**Figure S1.** Rarefaction curves for each sample calculated using the Galaxy Ecology platform (Afgan *et al.*, 2018).....173

## LIST OF TABLES

<b>Table 2.1.</b> Description of sampling locations to be referred to throughout this document. Samples 1-4 and 11 correspond to outdoor locations. Samples 5-10 correspond to locations inside the Victoria Mine. The distance labeled refers to the distance from the entrance of the 1330 Gallery. Sample 11 is an average of both Melics and Carné creeks. In addition to geochemical sampling, microbial DNA was preserved in 2019 at Sample locations 3, 5, 10, and 11. Samples of the water dripping into the 1330 gallery were only taken in 2021.....	44
<b>Table 2.2A.</b> Daily elemental mass fluxes coming from the Victoria Mine at sample-3 location. Values are given in grams per day.....	59
<b>Table 2.2B.</b> Daily elemental mass fluxes coming from the Victoria Mine at sample-3 location. Values are given in moles per day y.....	59
<b>Table 2.3.</b> Total acid digestion results from four 0.2500 g hydrozincite samples. The left table values are given in ppm. The "Total (%)" is the sum of mass recovered from the digestion given in %. Since hydrozincite is 60% Zn and 40% CO <sub>3</sub> and OH, a 60% recovered mass return would be expected because CO <sub>3</sub> was lost as CO <sub>2(g)</sub> and OH is lost during this analysis. All elemental concentrations are listed in descending order based on the average determined from the four samples. The standard deviation ( $\sigma$ ) showing the variability between the four samples is listed in the right column. Analytical uncertainty is $\pm 4\%$ .....	70
<b>Table 2.4.</b> CrunchFlow input for solute concentrations (M), pH, and gas concentrations used to make speciation calculations for each experimental condition.....	73
<b>Table 3.1.</b> Equilibrium constants ( $\log K_{eq}$ ) at 7°C for all mineral reactions. Minerals with ** are fake minerals used to maintain a partial pressure of CO <sub>2</sub> and O <sub>2</sub> in non-saturated and gallery domains.....	100
<b>Table 3.2.</b> Parameters for the mineral reaction rate laws. AtmiteCO <sub>2</sub> and AtmiteO <sub>2</sub> are fake minerals used to maintain an atmosphere of CO <sub>2(g)</sub> and O <sub>2(g)</sub> in non-saturated and gallery domains.....	101
<b>Table 3.3.</b> Mineral volume fractions and bulk surface areas (m <sup>2</sup> /m <sup>3</sup> rock) used in all CrunchFlow simulations for the 1D host rock and 2D gallery models. The lower table corresponds only to the homogeneous host rock case, where the 2D gallery model is not considered.....	102
<b>Table 3.4.</b> Initial and amending water compositions used for all CrunchFlow simulations given in mol/L. These are the pH and total concentrations of the primary species assigned in the input file. The "Sample 10/11" columns reflect the composition of the measured values from the corresponding sampling points. The "HRM/LRM input" labels reflect the composition of the water at the end of the calcite zone (31.5 m) when the host rock model simulations are completed (e.g. 60 days for the reference case).....	105
<b>Table 3.5.</b> The equilibrium constants ( $\log K_{eq}$ ) at 7°C for the equilibria of 86 secondary species in solution. Reactions are written as the destruction of 1 mole of the species using the following the primary species: H <sup>+</sup> , Na <sup>+</sup> , K <sup>+</sup> , Mg <sup>++</sup> , Fe <sup>++</sup> , SO <sub>4</sub> <sup>2-</sup> , Ca <sup>++</sup> , Zn <sup>++</sup> , Cd <sup>++</sup> , Sr <sup>++</sup> , Ni <sup>++</sup> , SiO <sub>2(aq)</sub> , HCO <sub>3</sub> <sup>-</sup> , O <sub>2(aq)</sub> .....	106
<b>Table 3.6.</b> Solute mass flux (mol/day) leaving the gallery model for seven different simulations.....	136
<b>Table 4.1.</b> Results from bioinformatics on the four sequenced samples. The grey-shaded columns represent sampled locations inside of the 1330 Gallery where there is no sunlight. Phylum are listed in order of abundance with respect to the sample-11 community.....	153
<b>Table S1.</b> <i>In-situ</i> measurements & ion concentration results from three sampling campaigns. Values given in ppm and ppb.....	171
<b>Table S2.</b> <i>In-situ</i> measurements & ion concentration results from three sampling campaigns. Values given in mM and $\mu$ M.....	172
<b>Table S3.</b> Dissolved organic carbon (DOC) concentrations from 2020 sampling campaign. Samples were filtered through a 0.22 $\mu$ m membrane. Analytical error is 0.05 ppm.....	173



**Table S4.** Electron microprobe point analysis results given in ppm solid. CO<sub>2</sub> is calculated.....174

## CHAPTER 1 – GENERAL INTRODUCTION

### 1. Introduction

#### 1.1 The Aran Valley

The Aran Valley is located in the northwestern corner of Catalonia. The Valley has a total area of 620 km<sup>2</sup> and is home to approximately 10,000 permanent residents, although winter tourism can bring that number over 40,000 inhabitants. Of the ten municipalities Vielha, the capital, is the largest in the region and resides at an altitude of 980 meters above sea level.

The region is characterized by an Atlantic climate due to its proximity to France and high altitude. Therefore, it receives more precipitation (1375 mm annual rainfall) than the southern regions of the Pyrenees, which are more influenced by the drier Mediterranean climate (climate-data.org). In the Aran Valley, watersheds eventually flow North and terminate in the Atlantic Ocean via France. Consequentially, the valley serves as the headwaters for the Garonne river which is an important resource for both the local population and SW France (e.g. Toulouse and Bordeaux) where the river subsequently terminates via the Gironde Estuary.

The Pyrenees has a long mining history that begins perhaps before, and certainly during Roman times. The Aran Valley was no exception. Mainly Fe, Cu, Pb, Ag and Zn ore have been the materials of interest, and most reside as metal-sulfide stratiform deposits scattered throughout the high-mountain topography. Specifically, in the Aran Valley, industrial exploitation of these ore-bodies on a major industrial scale began towards the end of the 19<sup>th</sup> century and continued until the mid-20<sup>th</sup> century when most mining sites were abandoned indefinitely. During this time, primarily Pb and Zn were targeted, though Fe-ore was also exploited in lesser quantities (Santamaria *et al.*, 2008). The Pb-Zn exploitation took place in two mining districts known as Bossost-Arres and Liat-Horcalh. The Bossost-Arres district is located in the NW region of the Aran Valley, while the Liat-Horcalh district is located in the NE region (Figure 1.1). The Bossost-Arres district consisted of three principal mines known as the *Margalita*, *Solitaria*, and the largest *Victoria*. Additionally, the only Fe mine in the region, the *Bausen Mine*, was also located in this district. In the Liat-Horcalh district, the principal mines included *Estrella*, *Preciosa Pepita*, the *Mauricio-Reparadora*, *Plan de Tor*, *Urets-Montoliu*, *Horcalh* and the largest, *Liat*. The eleven mines in the valley were located in high-alpine environments, such that all but the Victoria Mine were closed during the winter months.

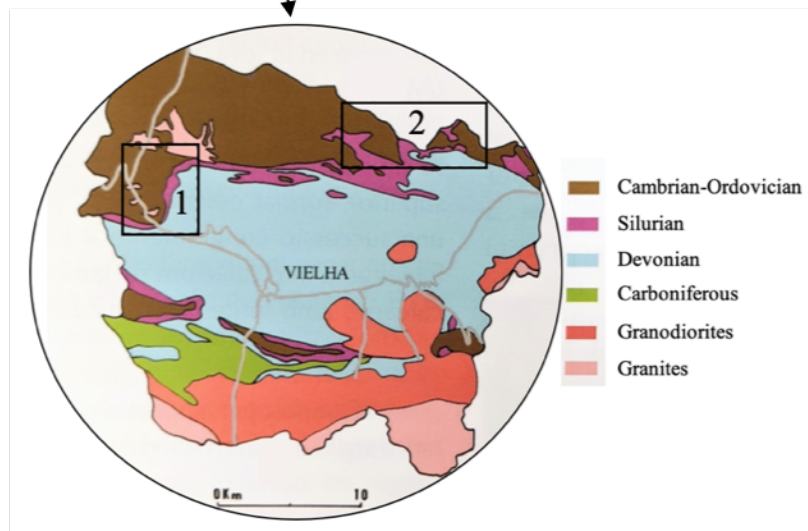


**Figure 1.1.** (top) A Google Earth image showing the location of the Aran Valley. (bottom) A map of the Aran Valley showing the age of geological formations. The box marked "1" represents the location of the Bossost-Arres mining district, and the box marked "2" represents the location of the Liat-Horcalh mining district. The geologic map was modified from Santamaria *et al.* (2008).

The winter marked a period of ‘seasonal isolation’ in which the Aran Valley was effectively inaccessible to Spain in winter as it was extremely difficult to traverse the 2000-meter snow-covered mountain pass that connected the two. Notably, it was not until 1948 when the original Vielha Tunnel was completed, which connected the Aran Valley to Catalonia and thereafter streamlined commerce. Today, a more modern and larger tunnel sits adjacent to the original, which was opened in 2007.

Due to both seasonal isolation and the general difficulty of access before completion of the Vielha Tunnel, much of the profits and business proceedings did not benefit Catalonia or Spain in the heyday of mining operations. Instead, the region was primarily exploited by foreign companies, namely French and Belgian, due to the ease of access from the French side of the Pyrenees.

From approximately 1900 to 1930, zinc ore was of principal interest in the Aran Valley as surveys concluded the existence of sphalerite (ZnS), also known as “Blende”, throughout the region. At the time, zinc was known to have a harmful effect on human health if consumed, however the ‘innovative’ material offered a wide range of future application (e.g. stainless steel), which eventually led to a global zinc boom. The year 1900 marked the arrival of the Belgian mining company known as *The Society of the Vielle Montang*, who monopolized the exploitation of the metal throughout a 30-year-period. From 1904 until 1930, several auxiliary companies were also created to meet international demand. These companies included *Société française des Mines du Val d’Aran*, *Société des Mines de Liat*, *Syndicat Minere*, *Société des mines de Zin du Margarita i Compagnie des Mines de Zinc de Bosost*, and *Societe Miniere de Victoria* (Santamaria *et al.*, 2008).

In 1930, however, the *Societe Miniere de Victoria* was nationalized by the Spanish government, which exploited the mine until the beginning of the Spanish Civil War in 1936, when all mining operations in the region came to a halt. The mining operations remained dormant well beyond the end of the civil war in 1939, and normal mining operations were not restored until the late 1940s. Beginning in 1950, public projects such as the construction of the Vielha tunnel and nearby hydroelectric facilities led to labor shortages in the area. Simultaneously, the price of Zn ore was becoming less economically viable for the mining companies. The combination of these factors led to the eventual abandonment of all mining operations in the Aran Valley in 1952.

Environmental policy at the time did not require reclamation of any kind for the abandoned tailings piles, processing facilities, and tunnel galleries. As a result, the abandoned relics were left exposed to natural weathering and erosion processes. Several surveys in the 1960's and 70's were done to determine if reopening the mines could be profitable, but restarting mining operations did not show economic potential. As a result, the abandoned mining sites and residues have stood relatively untouched for 70 years allowing the natural elements to deteriorate the relatively recently exposed earth materials (e.g. metal-sulfide ore).

## **1.2 Environmental Impact of Mining Activities**

Unfortunately, as is the case with countless abandoned mining sites, improper (or lack of) reclamation can lead to rapid dissolution of the exposed ore materials and other rocks that can release toxic metals into the neighboring environment. For example, sphalerite regularly incorporates significant amounts of cadmium (up to 5% wt.), and the zinc itself must not be overlooked (Schwartz, 2000). The US EPA submits that consumption of cadmium in concentrations above 5.0 ppb can be a human health risk. This implies that chronic exposure to cadmium even in trace amounts can cause several health problems including the enhanced weakening of bones (e.g. osteoporosis and osteomalacia), anemia, and kidney failure in extreme cases (Bernhoft, 2013).

One example of cadmium poisoning took place in Japan in the early 19<sup>th</sup> century. Mining operations targeting zinc ore released cadmium-rich waste into the neighboring rivers and streams as a byproduct of the purification process. That contaminated water was subsequently used for rice field irrigation, which led to mass cadmium poisoning, later termed “itai-itai disease”, where severe pain was felt in the spin and joints (Inaba *et al.*, 2005). Though significantly less toxic, chronic zinc exposure is also known to cause health problems such as bone marrow problems and neurologic effects (Agnew and Slesinger, 2021)

Since the primary target material in the Aran Valley was Zn-bearing sulfides (i.e. sphalerite), and most of these underground mines have been abandoned with little form of reclamation, there is a potential environmental risk that deserves to be considered and characterized. One study by Marguí *et al.* (2007) looked at the effects on vegetation caused by residual lead and zinc ore near a mineral treatment facility known as Pontaut in the Bossost-Arres mining district. They found that the leaves in the tree species (*Betula pendula*) was concentrating lead and zinc over 20 times background water concentrations. This study helped

to demonstrate the enhanced mobility of some heavy metals from untreated mining residues, and how they can be made bioavailable in the neighboring ecosystem.

As metals from mining residues become more bioavailable from normal weathering processes, adjacent soil microbial communities also experience elevated concentrations of heavy metals. A study by Beattie *et al.* (2018) sequenced the 16s rRNA genes to analyze operational taxonomic units (OTUs) of microbial communities in soils contaminated by mining operations in the Tri-State Mining District in the United States. They found that prolonged exposure to metals such as Pb, Cd, Zn and Mg caused both a change in microbial community composition and a decrease in overall bacterial species diversity when compared to less-contaminated soils in the study area. However, archaeal diversity was less affected than bacterial diversity. As a consequence of decreased bacterial diversity, the total health of the ecosystem can be negatively impacted as critical microbially-mediated elemental cycling and reactions become perturbed (Madsen *et al.*, 2011). A study by Leita *et al.* (1994) found that soils that were artificially enriched with Pb, Zn, or Ti had significantly less microbial biomass when compared to unenriched soils. Further, Smith *et al.* (2015) demonstrated that contamination events leave a signature on the microbial communities, such that DNA analysis of the exposed community is distinct from that of a non-exposed community, long after the contamination occurred. That is to say, the health of the ecosystem can suffer long after exposure to contaminants occurs.

### **1.3 Motivation and Objectives**

As mentioned previously, several abandoned mines exist in the Aran Valley that have yet to undergo significant reclamation. Since all of these mines bring about enhanced exposure of metal-sulfide materials to flowing water and oxygen, the transport and availability of potentially harmful dissolved metals has therefore been enhanced as well. These (relatively) recently exposed metal-rich rocks therefore pose a health risk to the surrounding environment, as demonstrated by Marguí *et al.* (2007) in the case of the *Betula pendula* tree species, and Beattie *et al.* (2018) in the case of the diversity of microbial communities. Additionally, the oxygen-rich rain water that infiltrates the open mining tunnels eventually flows out of the associated catchments, and into the Garonne River, which is later used as a water source for southwestern France.

The wet climate of the Aran Valley means that significant amounts of rain water (1375 mm annual rainfall) are able to infiltrate the mines, react with the residual metal-bearing ore materials that were once of economic interest, and transport these otherwise non-bioavailable elements into the adjacent ecosystem. The combination of these processes creates a potential for environmental impact that solicits further study.

The mission of this study is to quantify the chemical and biological processes that occur in the largest abandoned mine in the Aran Valley (The Victoria Mine), such that they can be later applied to other similar abandoned mines in the Pyrenees and beyond. More specifically, the goal is to examine metal mobility through the system and assess the potential health risk to the associated ecosystems. Annual sampling of the selected field site will serve to characterize the existing spatiotemporal geochemistry. Further, a reactive transport model parameterized using data from sampling campaigns can simulate host rock (i.e. ore material) dissolution and secondary mineral precipitation. Since secondary mineral precipitation can serve as a sink for heavy metals in natural systems (Wilkin, 2008), it is important that this process be characterized. This can serve to make useful predictions towards the extent of natural metal attenuation via mineral precipitation, which can help evaluate any environmental impact (or lack thereof). Additionally, batch experiments using the natural microbial populations from the field site were carried out to determine any microbial effects on the observed geochemistry.

In summary, the study of the Victoria Mine presents an opportunity to determine the ecological impact of abandoned Pb-Zn mines and to characterize the extent of any natural attenuation processes. A three-year observation of the abandoned mine can reveal the evolution of the geochemistry and assist in the parameterization of the associated reactive transport model (e.g. reaction rates, flow rates, and mineral stability). Ultimately, such a model could be applied to other abandoned mines alike to improve predictions towards metal mobility and environmental impact.

## 1.4 Thesis Outline

In Chapter 2, the waters and secondary minerals in the abandoned mine and the associated catchment are characterized. The spatiotemporal geochemistry of the water as it flows through the mine is quantified to help demonstrate if the system is at a steady state. The secondary mineral precipitates found in the mine are characterized using several analysis techniques (e.g. ion microprobe, XRD, acid digestion) to determine precipitation patterns and elemental composition and distribution. Through sampling and analysis techniques, it is concluded that high initial elevated metal concentrations in the mine (e.g. Zn and Cd) are attenuated along the flow path inside the gallery via hydrozincite precipitation, thereby reducing the environmental impact of the abandoned mine. A sample of hydrozincite was used in an experiment to determine the  $K_{eq}$  value because limited information is available in the literature. The experimentally determined value is used to make speciation calculations for all sampling locations and determine the saturation indices (SIs) of hydrozincite, calcite ( $\text{CaCO}_3$ ) and smithsonite ( $\text{ZnCO}_3$ ). Based on the calculated SI values, it was hypothesized that there is a variability in the apparent  $K_{eq}$  of hydrozincite (i.e. a range of  $K_{eq}$  values is determined), which would play a major role in metal mobility. These equilibrium values are subsequently implemented into the geochemical reactive transport model described in Chapter 3 to explore the hypothesized variability in hydrozincite solubility.

Chapter 3 consists of a modeling study of the Victoria Mine using the CrunchFlow geochemical modeling software package (Steeffel *et al.*, 2015). The modeling focuses on metal-sulfide mineral dissolution (namely sphalerite and pyrite) and subsequent metal polishing mechanisms (e.g. hydrozincite precipitation). This is accomplished by way of a two-phase model that is coupled via conservation of concentrations. The first phase of the model is constructed to simulate rainwater flow through the host rock above the mine where the dissolution of ore-bearing rocks occurs and subsequently increases the concentrations of metals in the water. This water eventually reaches the mining galleries where two inlets were discovered during field sampling campaigns. Specifically, the concentrations measured at two gallery inlets are reproduced by this model. The second phase of the model is constructed to simulate the surface water flow and secondary mineral precipitation along the gallery floor where several samples were taken, along distance, over the course of the three years. The initial water for the gallery model is composed of a flux-weighted mixture coming from the two inlets.



Concerning the host rock model, parameters such as mineral distribution, mineral reactivity and water flow velocity are unknown. Therefore, these parameters are examined across a range of reasonable values and scenarios to simulate possible outcomes. The gallery model (second phase) is used to reproduce the observed water concentration with distance and precipitates. Since flow velocity is unknown and the solubility of hydrozincite appears to vary, these parameter values are tested to produce results that capture the possible behavior in the mine. The model simulates the evolution of solute concentrations with distance and reproduces a theoretical solid that reflects those observed and characterized in Chapter 2. Notably, this is all done in an abiotic context. The model also suggests that the mine will continue to naturally attenuate dissolved metals given significant changes to the system.

Chapter 4 focuses on the microbiology at the site and its potential impact on metal mobility and the overall geochemistry of the system. Microbial DNA was sampled from several locations inside and outside of the mine and sequenced. The results of the sequencing give a taxonomic description (i.e. OTUs) of the bacterial communities at each sampling location. This is used to further determine the relative diversity of each community to make comparisons between indoor and outdoor locations.

Bioreactor experiments inoculated with natural sediments were performed to observed microbial community responses to dissolved carbon stimulation as this is a potential remediation pathway. SEM images of hydrozincite, found to be a product of biomineralization in other locations, was compared to the SEM images of the hydrozincite in the mine. The results were such that the hydrozincite at the Victoria Mine does not share morphological similarities to those exhibited biomineralized samples. The purpose of this chapter is to quantify any microbiological controls on geochemical cycling in the system. The conclusion is such that the processes occurring at the Victoria Mine are primarily abiotic.

Chapter 5 consists of a general discussion and conclusion concerning chapters 2, 3, and 4. This chapter discusses the overall research project as a whole, and includes a simplified conclusion that is based on the conclusions and discussions of the previous chapters.

## CHAPTER 2 – CHARACTERIZATION OF THE VICTORIA MINE

### 2.1 Introduction to the Victoria Mine

Active from 1907 to 1952, the Victoria Mine was the largest and most productive mine in the Aran Valley. During its most active days, approximately 200 miners would be working inside the 15 km of tunnels and 7.5 km of iron track used to remove ore material (Santamaria *et al.*, 2008). The mine is located in the Bossost-Arres mining district uphill from the town of Bossost (Figure 1.1). Its ten tunnel levels (Figure 2.1) occupy an altitude from 1,300 to 1,590 meters above sea level. The associated catchment has a total area of 3.2 km<sup>2</sup> and an elevation gain of 1,600 meters.

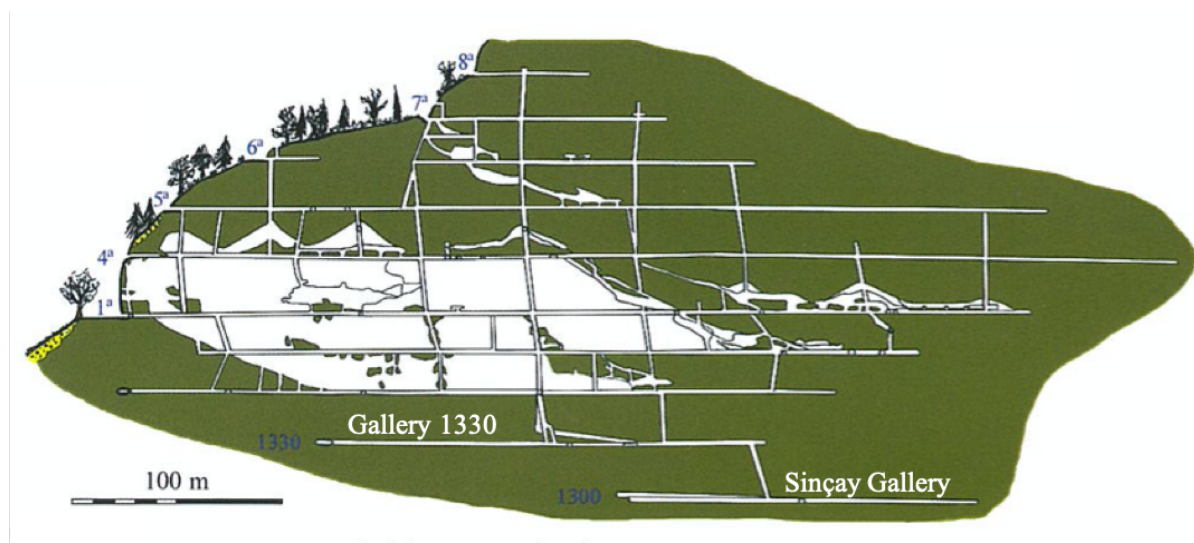


**Figure 2.1** Sketch of a cross section of the Victoria Mine from northwest (right) to southeast (left). Each tunnel gallery was labeled either by a distinct name or by its corresponding altitude in meters. For example, the entrance to second lowest gallery, known as the 1330 Gallery resides at an altitude of 1,330 meters. Figure modified from Santamaria *et al.* (2008).

The various operational levels are connected by ramps, wells, and shafts, which served as conduits to lower ore material down and out of the mine. Ore material was finally removed from the mine via the lowermost Sinçay Gallery, which was nearest to the cable-car station where the ore was lowered to the valley floor for further processing and purification. Today, these tunnels and vertical shafts serve as a conduit for water to flow freely through the mine, down the catchment, and into the Garonne River.

The exploited ore bodies consisted of stratiform metal-sulfide deposits emplaced in Ordovician shales, schists, and limestones (Cardellach and Álvarez-Pérez, 1979). The nature of these deposits imply that original metal-bearing rocks were fractured and folded, allowing hydrothermal fluids to more readily dissolve these metals. Subsequently, these metal-sulfur-rich hydrothermal fluids served to form the stratiform deposits. This metamorphism and

hydrothermal activity can be attributed to both the Hercynian (300 Ma) and Alpine (65 Ma) orogeny (García-Sansegundo, 1996). In the catchment, five distinct rock formations have been previously mapped (Figure 2.2). Above the elevation of the mine exists dark Devonian slates with some interbedded limestone (Dpf), Devonian red nodular limestone (Dcr), black Silurian-Devonian slates rich in pyrite with some interbedded limestone (SDpc), and an Ordovician limestone containing some quartzite, slate, and microconglomerate (Orpg). Below the elevation of the mine exists one rock unit of Cambrian-Ordovician interbedded sandstone and lutite (COrgl).

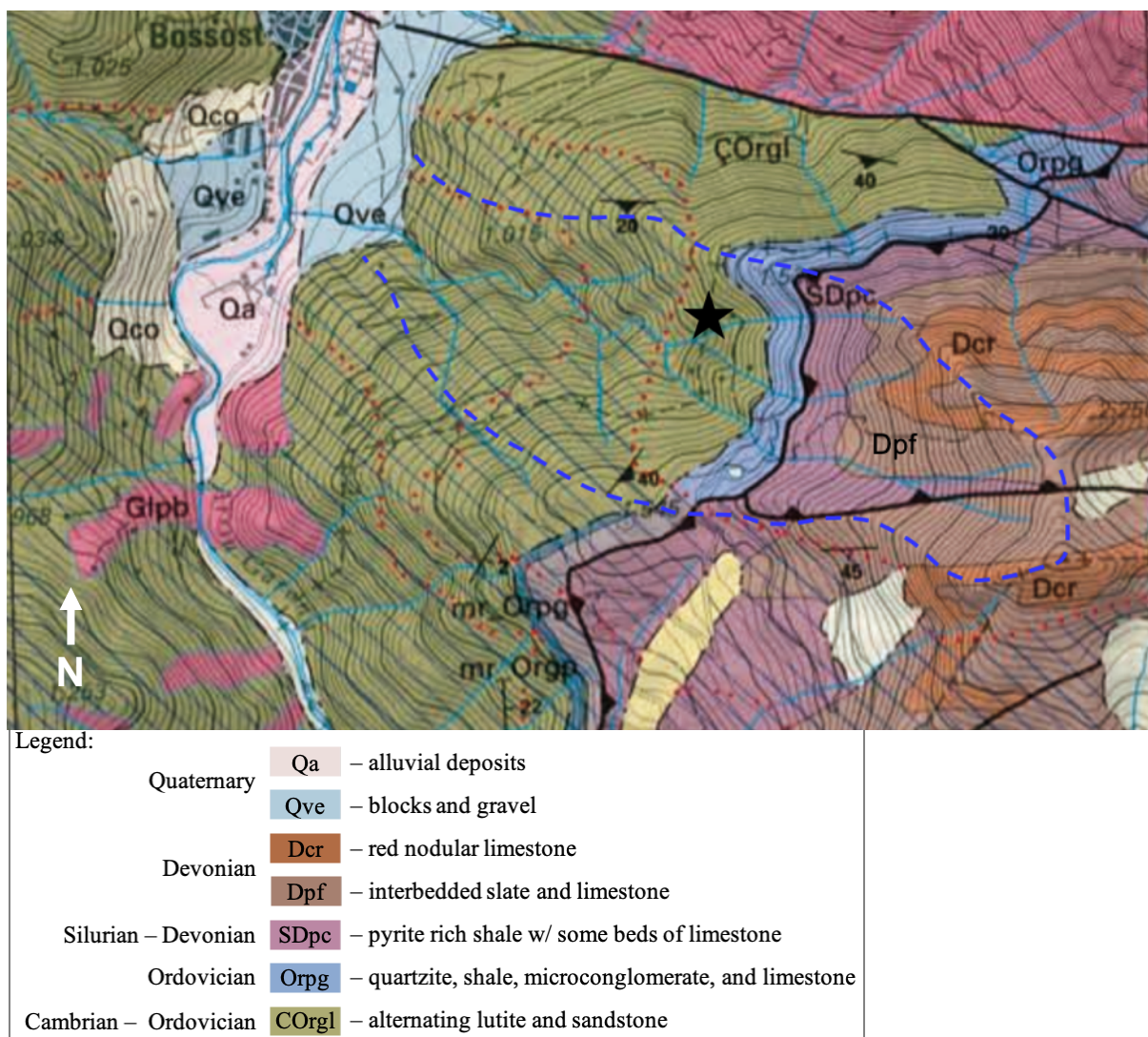


**Figure 2.2.** A cropping of a 1:50,000 geologic map of the Victoria Mine catchment in the Bossost-Arres mining district (Geologic Institute of Catalonia, map # 39). The approximate location of the Victoria Mine is represented by the black star and catchment boundaries are marked with a blue dotted line.

The low-grade regional metamorphism caused repeated mineralization and remobilization of the metal-sulfide materials, which resulted in massive metal-sulfide deposits within the Orla Series (COrgl, Figure 2.2) along veins and fractures. The result was such that four ore bodies were targeted in the Victoria Mine: (1) Artiga/Miracle Vein, (2) Northeast Vein, (3) Main Vein, and (4) Principal Vein (Figure 2.3). These ore bodies, oriented parallel to the main stratification (i.e. stratiform deposits), were composed of sphalerite, galena, chalcopyrite, pyrite, and pyrrhotite. However, sphalerite was the principal target material during exploitation at the Victoria Mine.

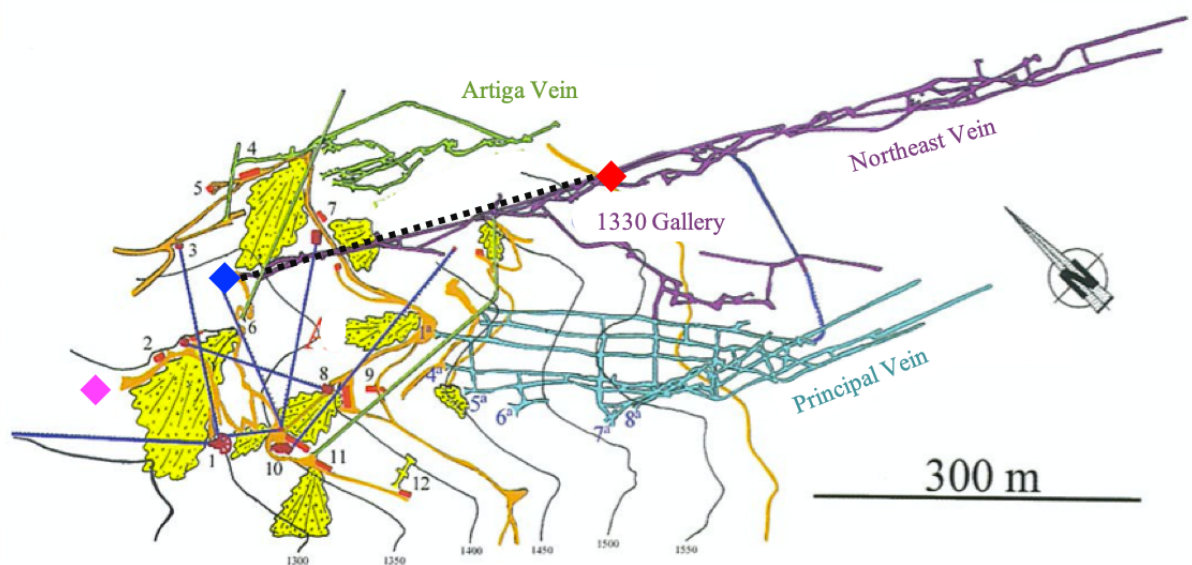


**Figure 2.3.** Drawing of an aerial view of the various tunnels, levels, and installations of the Victoria Mine. The green, purple, and light blue colors correspond the Artiga/Miracle ore vein, Northeast ore vein, and Principal ore vein, respectively. However, the colored lines themselves are manmade tunnels (e.g. the 1330 gallery corresponds to the Northwest Vein). The blue and red diamonds represent the entrance and the end of the sample path (310 m) within the 1330 Gallery, respectively, while the black dotted line shows the sample path. The magenta diamond represents the approximate location of the outlet of the Sinçay Gallery where the mine effluent was sampled. Figure modified from Santamaria *et al.* (2008).

A sample of the sphalerite ore from the mine was analyzed by Queralt (2006) using a novel energy dispersive X-ray fluorescence (EDXRF) method determining metal concentrations. Their results showed that Victoria Mine sphalerite on average can contain  $5,200 \pm 700$  ppm Cd,  $80,000 \pm 4,400$  ppm Fe, and  $1,000 \pm 300$  ppm Cu. This cadmium content is not unusual in sphalerite deposits. For instance, a comparison of 480 different sphalerite samples from across the world showed that Cd content in sphalerite can be as high as 50,000 ppm Cd by mass (Schwartz, 2000). Based on the same study conducted by Schwartz (2000), the Victoria Mine sphalerite would be considered typical in terms of its Cd content.

Due to the Cd-rich nature of the Victoria Mine sphalerite, an ecological risk could be created if this harmful metal were to become mobile via the dissolution of the sphalerite. Although mining activities ceased in 1952, there was no real reclamation effort of abandoned tunnel galleries and mining relics. Today these areas adjacent to the mine and processing facilities are characterized by elevated levels of Zn and Cd (Marguí *et al.*, 2004; Marguí *et al.*, 2007; Marques *et al.*, 2003). Many of these mining relics are still in contact with the natural waters of the region, which can serve as a source of toxic metals in the local ecosystem (Marguí *et al.*, 2007). Depending on the conditions experienced by these residues and exposed ore materials (e.g. dissolved oxygen (DO), pH, alkalinity, advective flow, rain events) the mobility and fate of metals such as Zn and Cd could be enhanced. Therefore, it is critical to quantify the availability of these metals, and further predict their mobility as it is controlled by the geochemical conditions and processes occurring at the site.

## **2.2 Methods**

### **2.2.1 Field Sampling**

Three individual sampling campaigns were conducted on the following dates; October 21-23 (2019), July 14-16 (2020), and June 7-9 (2021). The objective was to sample the water, solids (minerals and rocks), and soil/sediment microbiology along a perceived semi-continuous flow path. This was accomplished by sampling at twelve locations that represented three distinct geochemical conditions: above, within, and below the mine (Figures 2.4 and 2.5). It should be noted that the 2019 was an exploratory sampling campaign and did not include several of the sampling locations that were later determined to be important in 2020 and 2021. In general, the locations include the two creeks above the mine identified as source water for the system, six locations within the 1330 Gallery of the Victoria Mine, each designated by their distance from the entrance, three locations just outside of the Sinçay Gallery exit where the mine water combines with the natural catchment water, and the lowermost part of the Melics Creek before it leaves the catchment and joins the Garonne River (Figure 2.5). Throughout this study, the "Sample #" from Table 2.1 will be referred to for all schematics, images, and results. The " + drip" denotes sampling locations where water dripping/flowing from the ceilings and walls were collected in 2021.

Due to the size and relative geometric simplicity of the associated catchment, we assumed that much of the source water that infiltrates the mine comes from the upper section three creeks within the catchment; Melics Creek, Carné Creek, and Artiga Creek. However, Artiga Creek was dry during all three sampling campaigns. Given that the mine resides approximately 1000 meters below and 2 km in horizontal distance from the upper boundary of the catchment, and that the topography is extremely steep ( $44.8^\circ$  on average), it can be reasonably assumed that the infiltrating water is surface water from the upper catchment. Therefore, we assert that sampling the upper creeks provides reliable background concentrations for the water before it infiltrates the Victoria Mine. It should be noted that Sample-11 (Table 2.1) represents an average of Melics and Carné Creek.





**Figure 2.4.** Google Earth image of the Victoria Mine catchment system and locations of outdoor sampling intervals. Sampling locations correspond to Table 2.1 and Figure 2.5, however sample locations 5-10 are omitted. The red line represents the catchment boundaries and the red oval with the "X" is the approximate location of the Victoria Mine. Artiga Creek was never sampled because it was dry during all three sampling campaigns. Blue arrows represent water and the corresponding flow direction.

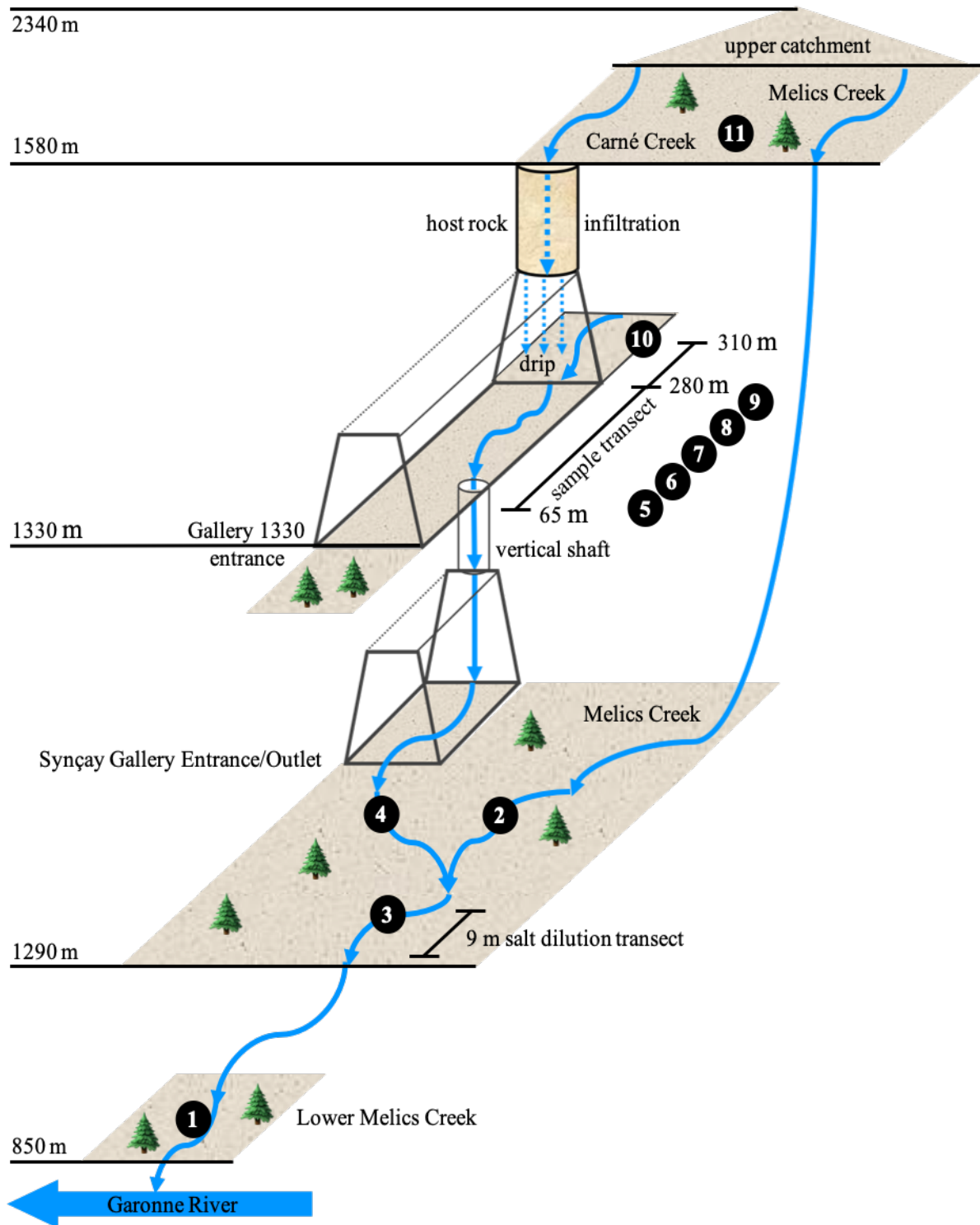


**Figure 2.5.** A schematic (not to scale) of the Victoria Mine catchment system and sampling locations in this study. Each sample location is represented by a black circle with a number corresponding to Table 2.1. Each light brown trapezoid corresponds to an altitude labeled on the left-hand side. The "9 m salt dilution transect" refers to the nine-meter mixing length of the salt dilution procedure done to calculate volumetric flux of the effluent. The "vertical shaft" between Gallery 1330 and the Synçay Gallery is assumed to connect the two galleries. The "host rock infiltration" represents where surface waters from the upper catchment flow and react in with the surrounding host rock and unexploited ore material (e.g. sphalerite) before dripping/flowing into the mine. Water and the corresponding flow direction are denoted by blue arrows.



<b>Sample #</b>	<b>Location Description</b>	<b>Additional Information</b>
1	lower Melics Creek	subsequently flows into Garonne River
2	Melics Creek adjacent to mine effluent	water running adjacent to the mine
3	combined Melics and mine effluent + DNA	mix of samples 2 and 4
4	Sinçay Gallery effluent	flux weighted average of mine system
5	65 meters + drip + DNA	first occurrence of hydrozincite
6	140 meters + drip	
7	162 meters	deep pool of blue water
8	190 meters + drip	first occurrence of red precipitate
9	280 meters + drip	constant flow and initial mine input
10	310 meters + DNA	dark red seepage and pooling (red goo)
11	Melics and Carné average + DNA	upper catchment/background water

**Table 2.1.** Description of sampling locations to be referred to throughout this document. Samples 1-4 and 11 correspond to outdoor locations. Samples 5-10 correspond to locations inside the Victoria Mine. The distance labeled refers to the distance from the entrance of the 1330 Gallery. Sample 11 is an average of both Melics and Carné creeks. In addition to geochemical sampling, microbial DNA was preserved in 2019 at Sample locations **3, 5, 10,** and **11**. Samples of the water dripping into the 1330 gallery were only taken in 2021.

Sampling within the Victoria Mine took place along a continuous 245-meter flow path beginning at 65 meters from the entrance of the 1330 Gallery and ending at a bifurcation of the gallery at 310 meters (Figures 2.6 and 2.7). The tunnel itself is approximately 1.5 meters wide by 2 meters tall (Figure 2.6(C) and 2.6(E)). There is a slight upward slope along the gallery, such that water flows from inside to outside of the mine. Sampling began at 65 meters - the first occurrence of flowing water. Additionally, this location corresponds to a vertical shaft that captures all of the water coming from further inside the mine. Via this shaft, the water is transported to the lowermost Sinçay Gallery. Once the water moves through the Sinçay Gallery, which was flooded during all sampling excursions, it subsequently leaves the mine through an entrance tunnel where it recombines with Melics Creek in a small grassy meadow. Melics Creek continues to flow down the catchment, and eventually discharges into the Garonne River next to the town of Bossost.

At approximately 280 m from the 1330 Gallery entrance there is a constant flow of water entering from the ceiling and walls. This location exhibits abundant precipitation of stalactites and other flow/drip structures, as well as centimeter to meter scale terraces formed by precipitates on the floor (Figure 2.7(D)). Notably, much of the water coming from the ceiling in this location fell down a shaft into the Sinçay gallery, although some of the water continued further down the 1330 Gallery. Since this water was flowing during all three sampling campaigns while other locations only exhibited flow during rain events (e.g. 2019 campaign), it is assumed that this is a perennial flow occurring all year round.



**Figure 2.6.** Photos taken from inside and outside of the Victoria Mine during the 2019 campaign. From A to I represents walking "upstream" with respect to the flow of water (i.e. moving deeper into the gallery). (A) Melics Creek nine meters downstream from where the mine effluent merges (sample-3). Microbial DNA was sampled here in 2019. (B) Jordi Cama measuring pH at the entrance of the Sinçay Gallery/mine effluent (sample-4). (C) The entrance of the 1330 Gallery. (D) 65 m from the gallery entrance and the first occurrence of flowing water and actively precipitating hydrozincite. Microbial DNA was sampled here in 2019. (E)  $\approx$ 100 meters from the gallery entrance. Water is flowing on the floor and hydrozincite is present. (F) Drip water at 140 m from the entrance (sample-6). (G) 160 m from the entrance where a shaft is flooded (sample-7). (H)  $\approx$ 170 m from the gallery entrance where the "floating skin" morphology of hydrozincite can be observed. The white mineralization is floating on top of the water. This is ubiquitous throughout the gallery. (I) 190 m from the entrance and the first occurrence of a reddish precipitate (sample-8).





**Figure 2.7.** Photos from inside the 1330 Gallery in the Victoria Mine in 2019. (A) Approximately 210 m from the entrance of the gallery showing a  $\approx 50$  m flooded section of the tunnel. (B) Hydrozincite displaying a blue coloration at  $\approx 260$  m from the entrance. Images C - F correspond to 280 m from the gallery entrance (sample-9) where water is flowing and dripping rapidly from several locations in the ceiling and walls. (C) Flow structures on the walls and ceilings at 280 m. Most of the flow comes from the left side of the image. (D) Flow structures and terraces formed by hydrozincite. To the left (not seen) there is a vertical shaft where most of the water is flowing. (E) A close-up image of the flow structures seen on the wall in image D. (F) Stalactites forming on the ceiling. A close-up image of the same stalactites seen in image C. (G) 310 m from the entrance (sample-10 a.k.a. red goo) showing the red seep coming from the wall and accumulating on the floor. Microbial DNA was sampled here in 2019. (H) Approximately 350 m from the gallery entrance showing the hydrozincite nodules.

Sampling intervals (i.e. sampling locations) were organized such that each location was downgradient from the subsequent location, so as not to contaminate the location with previous measurements and residues from our presence along the flow path. In other words, liquid samples were taken from low-altitude to high-altitude (i.e. downgradient to upgradient) along the flow path. For almost all sample intervals, conductivity, pH, alkalinity, and temperature was measured *in-situ*, and samples were taken for the measurement of ion concentrations. Additionally, during the 2020 campaign, samples were taken to measure for dissolved organic carbon (DOC).

The pH was measured using a WTW Multit 3510 IDS multimeter paired with a WTW SenTix 940 pH electrode. Prior to each day of measurement, a five-point calibration curve was generated using five different buffer solutions. Conductivity and temperature were measured using a WTW Cond 3110 conductivity meter paired with a WTW TetraCon 325 conductivity/temperature probe.

Each water sample was drawn into a new 10.0 mL BD syringe directly from the sample water source. The sample was then filtered through a 0.45  $\mu\text{m}$  membrane Frisette Q-Max RR Nylon Syringe filter into a Corning Costar microcentrifuge tube with snap cap (1.7 mL). Using a blue Eppendorf Research plus (10 – 1000  $\mu\text{L}$ ) pipette, 0.80 mL of the filtrate was then added into a pre-cleaned (soaked in Milli-Q water for 24 hours) Corning 15 mL centrifuge tube containing a pre-amended 9.2 mL of 2.0% trace-metal (i.e. dilution factor = 12.5). The samples were immediately placed in a cooler with ice, and later stored in a 3.7°C walk-in refrigerator after leaving the Aran Valley. Using the excess of the same filtered water, alkalinity was measured at each location using a Merck-Millipore MColortest Alkalinity Test. To measure DOC, 20 mL glass vials were acid cleaned and subsequently baked at 450°C for two hours prior to sampling and sealed tightly. Water samples were filtered through the same 0.45  $\mu\text{m}$  membrane mentioned above and the vials were filled such that there was no headspace and capped tightly for future analysis.

### **2.2.2 Discharge and Solute Mass Fluxes**

For all three sampling campaigns, the volumetric flow rate was measured at sample location 3 which is composed of a mixture of Melics Creek and the Victoria Mine effluent (Figure 2.5). The objective of this flow measurement was to calculate the elemental mass fluxes coming from the mine based on measured ion concentrations. These flow measurements were accomplished using a dissolved salt dilution method.

A nine-meter length of the stream was chosen as the mixing length for this method because it was (a) long enough to allow time for total mixing, and (b) did not have any contributing streams (i.e. water was conserved). Also, the end of the length created a natural funnel where all of the water flowed through, which increases the likelihood of consistent mixing and an accurate measurement (Figure 2.6(A)). This was the location of all conductivity measurements of the creek through time using the same conductivity meter described in section 2.2.1.

In a clean bucket, 50.0 g of pure NaCl was completely dissolved into 2.0 L of natural water taken from the measurement location (i.e. Melics Creek). The 2.0 L of saltwater was quickly poured into the upstream location of the nine-meter stream segment (i.e. saltwater slug), and conductivity at the downstream location was simultaneously measured through time. In 2019, conductivity was recorded every 20 seconds until the conductivity returned to background values. In 2020 and 2021, conductivity was recorded every 10 seconds until conductivity returned to background values.

Before data from these results can be used, a concentration-conductivity calibration was created. This is done in the form of a linear regression:

$$y = mx + b \quad (\text{Eq. 2.1})$$

where  $y$  is the salt concentration (mg/L),  $m$  is the slope ((mg/L)/(μS/cm)),  $x$  is the conductivity (μS/cm), and  $b$  is the y-axis intercept which depends on the intrinsic geochemistry of the water being used. To generate the linear calibration regression, water from sample-3 location was taken back to the laboratory. Using this natural water, four standard NaCl solutions were made via series dilutions beginning with a 25 g/L stock solution. The range of conductivity for the

standard solutions captured the range in conductivity measured in the field. The four calibration points were plotted in excel to generate a linear regression. Using the slope of the regression ( $m$ ) from Eq. 2.1, the following equation can be used to calculate discharge (Merz and Doppmann, 2006):

$$Q = \frac{S}{m \int (C_t - C_0) dt} \quad (\text{Eq. 2.2})$$

where  $Q$  is the volumetric discharge (L/s),  $S$  is the amount of salt injected (mg),  $m$  is the slope from Eq. 2.1,  $C_t$  is the conductivity after timestep  $t$  ( $\mu\text{S}/\text{cm}$ ),  $C_0$  is the base level conductivity ( $\mu\text{S}/\text{cm}$ ), and  $dt$  is the time interval (s). By integrating the area below the dilution curve (i.e. conductivity vs. time), the total discharge can be calculated. To calculate mass fluxes, volumetric discharge can be multiplied by the ion concentrations measured at the sample-3 location.

### **2.2.3 Water Chemistry Analyses**

The following elements were analyzed to determine their concentration in each acidified sample at the Scientific and Technological Center of University of Barcelona (CCiTUB): S, Mg, Zn, Ca, K, Na, Si, Fe, Sr, Mn, Al, Fe, Pb, Ni, Cr, Cu, Co, Li, Cd, Sb, Ti, and As. Each water sample was measured using inductively coupled plasma spectroscopy (ICP-OES). Minor elements were reported in ppb and measured using a Perkin Elmer NexION 350 (ICP-MS). Major elements were reported in ppm and measured using a Perkin Elmer Optima 8300 (ICP-OES). Detection limits are reported in supplementary information (Tables S1 and S2). Total analytical uncertainty is up to 4%. Several elements including Pb, Cr, Cu, Co, Mn, Cd, and Ti are not reported because the concentrations were below detection limits.

Filtered (not-diluted) samples for DOC measurement were analyzed using a Shimadzu TOC-V CSN Total Organic Carbon Analyzer. Immediately before measurement, each sample was acidified to a pH between 2.0 and 3.0 via pipette and 2.0 M trace-element grade HCl. Error for this method is  $\pm 0.05$  ppm.

### 2.2.4 Hydrozincite Characterization

Hydrozincite ( $Zn_5[CO_3]_2[OH]_6$ ) is a secondary zinc-carbonate mineral with a monoclinic structure (Ghose, 1964). It is found precipitating in four distinct morphologies in the Victoria Mine (Figure 2.8). Spherical nodules of hydrozincite (Figures 2.7(H) and 2.8(1)) were found throughout the mine ranging from 0.2 to 3 cm in diameter. Smoothly layered patinas of hydrozincite (Figures 2.6(D,E,F, and I), 2.7(B), and 2.8(2)) were ubiquitous in the mine, especially adjacent to flowing water. In semi-stagnant puddles, hydrozincite grew on the water surface and therefore named "floating skin" (Figures 2.6(H) and 2.8(3)). And botryoidal structures (Figure 2.8(4)) were found typically submerged under water. Each of these four morphologies was studied using XRD analysis, electron microprobe analysis accompanied by scanning electron microscope (SEM) imaging, and total acid digestion. Two additional samples, a stalactite (Figure 2.7(F)) and a powder sample from the terraces found at 280 m (Figure 2.7(D)) were analyzed with XRD to identify mineralogic composition.

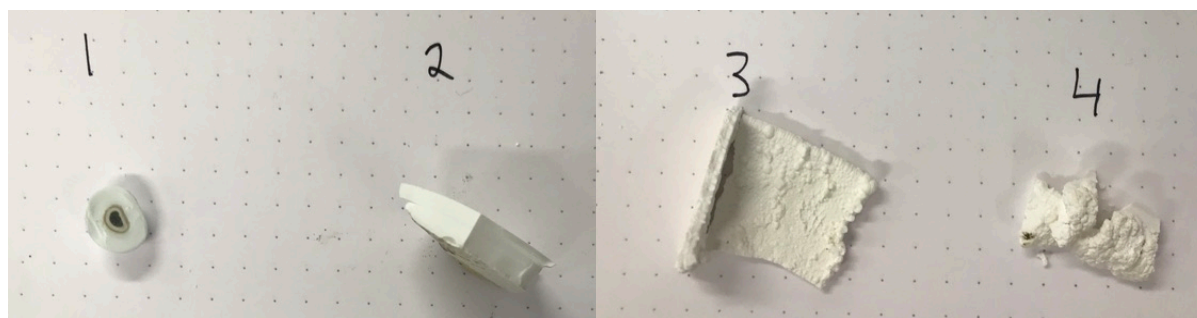


**Figure 2.8.** Photographs of four observed morphologies of hydrozincite found in the Victoria Mine. Morphologies are as follows: (1) nodular, (2) smooth layered, (3) floating skin, and (4) botryoidal. In this image, the distance between two horizontal or vertical dots represents 0.5 cm.

#### 2.2.4.1 XRD Analyses

Six samples of hydrozincite were analyzed via powder diffraction using a Bruker D8 A25 Advance X-ray diffractometer  $\theta$ - $\theta$ , with  $CuK\alpha_1$  radiation, Bragg-Brentano geometry, and a position sensitive LynxEyeXe detector. Diffractograms were obtained from  $4^\circ$  to  $120^\circ$  of  $2\theta$  with a step of  $0.015^\circ$  and counting time of 0.5 seconds and the sample in rotation at 15 revolutions/min. The crystalline phase identification was carried out by using the computer program "EVA" (produced by Bruker). The software TOPAS (Bruker, 2000) combined with the fundamental parameter approach was used for Rietveld refinement. The optimized parameters were background coefficients, zero-shift error, crystal size, peak shape parameters, scale factor and cell parameters. The values of the pattern dependence, Rwp, disagreement factor, and statistically reliability factor of Bragg, RB, are used to indicate that if peak fitting is satisfactory.



#### *2.2.4.2 Electron Microprobe Analyses*

A sample of each type of morphology was mounted in epoxy and subsequently cut to expose a flat surface of the mineral sample. The surface was then polished and coated with carbon before electron microprobe analysis was conducted at the CCI TUB. A JXA-8230 Electron Probe Microanalyzer with an accelerating voltage of 20.0 kV, electron current of  $6.0 \times 10^{-9}$  A, and beam diameter of 10  $\mu\text{m}$ , was used for compositional spot analyses of the following elements: Sr, Ca, Cd, Mg, Fe, Mn, Zn, and Ni. Additionally, elemental maps of each sample were created for Ca, Cd, Fe, Mg, and Zn using the same accelerating voltage and electron current as the spot analyses. In the method for spot analyses, elements are reported as oxide weight proportions (i.e. ppm) based on the assumption that the elements are in carbonate form (e.g.  $\text{CaOCO}_2$ ,  $\text{ZnOCO}_2$ ). The analyzer does not detect C, H or O. Therefore,  $\text{CO}_2$  mass is calculated based on the oxide analyses. Since the calculations assume that the mineral is not hydrated, any mass recovery below 100% can indicate the presence of OH or  $\text{H}_2\text{O}$  groups in the mineral.

Elemental distribution maps with a resolution of 200 x 400 (i.e. 800-point analyses) of the nodule and floating skin samples were generated using a 60.00 ms beam dwell time for each point analyses. Elemental distribution maps of the layered and botryoidal morphology samples used a 30.00 ms beam dwell time for each point analysis to generate an image with a resolution of 500 x 500 points.

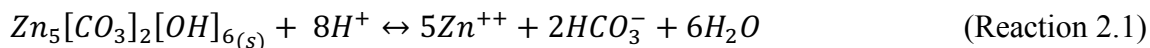
#### *2.2.4.3 Total acid Digestion*

A sample of each of the four morphologies was crushed into a powder and dried for 48 hours at 35°C. Then, 0.2500 g of the dried powder was added to an acid-cleaned Teflon bomb. Subsequently, 5.0 mL of 65% trace-metal grade nitric acid was added to the Teflon bomb containing the powdered samples, which was capped lightly to allow gas to escape. The acid dissolved the mineral for 24 hours. The remaining liquid was diluted to a final volume of 250.0 mL in a volumetric flask with ultrapure Milli-Q water (18.2 M $\Omega$ ) resulting in a final concentration of 1.3%  $\text{HNO}_3$ . Then, 10 mL aliquot of each dissolved sample was filtered through a nylon syringe filter (0.22  $\mu\text{m}$  membrane). The four samples were analyzed for cation concentrations using ICP spectroscopy identical to the method described in section 2.2.3.



### 2.2.5 Hydrozincite Solubility Experiment

To develop an appropriate geochemical model to simulate hydrozincite precipitation and dissolution in the Victoria Mine, an experiment was conducted to determine the mineral's equilibrium constant as a function of temperature according to the following reaction:



Additionally, the results could be used to determine metal availability as a function of dissolution. A sample of the floating skin morphology (Figure 2.8(3)) was used due to its flat geometry, allowing the surface area to be measured.

Two experiments using the same sample of hydrozincite were conducted; 3.7°C and 20.0°C. Before and after each experiment, the sample was dried for 48 hours at 35°C and then weighed on an analytical balance to determine the total dissolved mass. After weighing the sample, it was submerged into 500.0 mL of Milli-Q water that had previously been bubbled with filtered air for two hours to ensure that the water was at equilibrium with the air (Figure 2.9). The sample was suspended in the liquid using a section of clean tubing. The reaction vessel was constantly mixed and bubbled throughout the duration of the experiment. The reaction vessel was composed of four openings serving four purposes; (1) to allow a tube in to bubble the water, (2) allow the amended air to flow out, (3) to hold a pH electrode and (4) to hold a sample port.

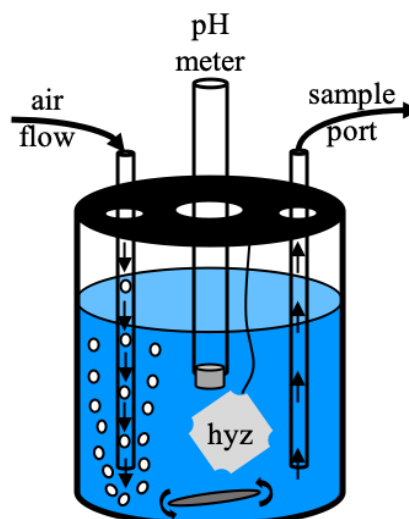


**Figure 2.9.** (left) A photo taken of the batch dissolution experiment at 3.7°C inside of a walk-in cooler. The white angular mineral suspended in the liquid is a sample of the floating skin hydrozincite (Figure 2.8(3)). (right) A schematic of the batch experiment showing the constant air bubbling and stirring, while the pH meter was fixed in position for in-situ measurements. The sample port was maintained closed while sampling was not occurring, and there was an outlet hole for air to escape so as not to build pressure within the vessel.

submerged in the water such that pH could be measured *in-situ* while sampling, and (4) to extract liquid samples.

A permanent tube fitted with a Luer Lock valve was placed into the liquid extraction port. This sampling tube was submerged at all times and the valve was used to seal the opening when not in use. At each sampling interval, a 0.2 mL purge volume was pulled from the sample port using a 1.0 mL syringe and discarded. This guaranteed that the sample is not mixed with water left in the tube from the previous sampling interval. Then, using a new 1.0 mL syringe, 1.0 mL of sample was extracted from the reactor, and subsequently filtered through a nylon-membrane (0.22  $\mu\text{m}$ ) syringe filter into a clean 1.7 mL microcentrifuge tube. The filtered sample was then pipetted (0.800 mL) into a clean 15 mL sample tube containing 9.200 mL of 2.0% trace-metal grade nitric acid. The pH of the liquid was simultaneously recorded. Sampling took place periodically over a  $\approx$ 10-hour period for the colder, 3.7°C experiment, while the warmer 20.0°C experiment was sampled until  $\approx$ 30 hours. The time frame of each experiment was determined based on the stability of the pH, such that once the pH stabilized, the experiment was terminated. Samples were analyzed using ICP-MS/OES as described in section 2.2.2.

This method was designed to observe the  $\text{Zn}^{++}$  concentration and pH at equilibrium (Reaction 2.1) for two different temperatures; 3.7°C and 20°C. Alkalinity (i.e.  $\text{HCO}_3^-$ ) was later calculated using a geochemical model under the assumption that the water was at equilibrium with the atmosphere because the water was constantly bubbled with air throughout the duration of the experiments. These calculations are discussed further in Chapter 3. Given the two temperatures, it is possible to extrapolate the equilibrium constant for a given temperature between the experimental range. These values can later be incorporated into geochemical models (see Chapter 3) to simulate the reaction occurring in the mine.

## 2.3 Results

### 2.3.1 Aqueous Chemistry Results

*In-situ* measurements (Figure 2.10) and ion concentrations (Figures 2.11, 2.12, Table S1 and S2) corresponding to sampling locations described in Table 2.1 and Figure 2.5 were plotted for the 2019, 2020, and 2021 sampling campaigns. Water flows from right to left in each plot (i.e. upgradient to downgradient). Further, the blue-shaded regions denote locations that were outside of the mine, while non-shaded regions denote locations within the 1330 Gallery. Concentration data for Zn, Cd, Ni and Fe from Marques *et al.* (2003) were incorporated into Figures 2.11 and 2.12 for comparison.

In 2019, alkalinity was measured only above and below the mine, and conductivity was not measured (Figure 2.10). The temperature of the water is strongly correlated to location. Inside the gallery (samples 5-10) the average temperature during the three consecutive years of sampling was  $6.4 \pm 0.5^\circ\text{C}$  (Figure 2.10). The pH at all sampling ranges from 6.9 to 8.0, with one measurement in 2021 at pH = 8.7 at sample location 6 (Figure 2.10). The average alkalinity during all three years for the upper catchment streams (upper Melics and Carné Creek) is  $181.0 \pm 7.6$  ppm  $\text{HCO}_3^-$ , while the same average for the lower Melics creek is  $99.7 \pm 7.6$  ppm  $\text{HCO}_3^-$ . In general, alkalinity decreases approximately 80 ppm as the water moves through the entire system. Dissolved organic carbon measurements in 2020 show low concentrations in the entire system ( $0.8 \pm 0.3$  ppm, Table S3), but DOC is slightly lower inside the mine than outside.

Conductivity does not follow the same patterns as alkalinity with regard to the upstream sampling locations (Figure 2.10). The critical difference between the two is that conductivity increases significantly between the upper catchment and the 280 m sample location (i.e. source water for the gallery), while alkalinity decreases by a small amount. It is important to note that sample-10 location represents gallery floor water that comes from deeper inside the mine. The flowing and dripping water from sample-9 location, immediately mixes with this water. As water flows downstream from the sample-9 location, the conductivity decreases as a function of distance in parallel with alkalinity. In general, the *in-situ* measurements over the course of three years show that alkalinity, conductivity, pH, and temperature do not vary significantly through time. However, of these properties, pH does show some variability, particularly within the gallery in 2021 (floor and drip water).

A notable characteristic is the concentration spike at the sample-9 location - water coming from the overlying host rock (Figure 2.11). As water enters the mine, zinc concentrations begin at 2.77 mM and quickly decrease to below 0.5 mM in the rest of the system. Calcium, magnesium, and sulfur all behave in the same fashion. Subsequently, all of these dissolved species decrease in concentration as they flow along the floor of the gallery and eventually leave the mine. This behavior is much less pronounced for Na, K, and Si, which show relatively low and stable concentrations across the entire system throughout the three years of measurement. For example, silicon concentrations average  $0.15 \pm 0.04 \mu\text{M}$  in all locations through time. The behavior of Ni, Sr, and Cd coincide with the behavior of major ions Ca, S, Zn, and Mg discussed above. Aluminum, aside from two data points, remains stable below  $0.50 \mu\text{M}$  (Figure 2.12).

Concentrations of Zn and Ni measured in this study are similar to those measured in 2002 by Marques *et al.* (2003) (Figures 2.12 and 2.13). However, Fe and Cd concentrations from 2019-2021 do not coincide when the same comparison is made. In 2002, the dissolved Fe concentration in the upper catchment (sample-11) is  $6.3 \mu\text{M}$ , while the average for this location from 2019 to 2021 is  $0.20 \pm 0.05 \mu\text{M}$ , indicating a significant decrease over the  $\approx 18$ -year period between measurements. It should be noted that Marques *et al.* (2003) also filtered their samples using a  $0.45 \mu\text{m}$  membrane. The dissolved Cd concentration measured in 2002 by Marques *et al.* (2003) was  $0.57 \mu\text{M}$  at the sample-3 location, while the average of the measured average in this study ( $0.28 \pm 0.06 \mu\text{M}$ ) at the same location. Iron concentrations appear to change very little at the sample-3 location over  $\approx 18$  years. At the upper catchment location, Cd concentrations remain below  $0.01 \mu\text{M}$  over  $\approx 18$  years. Generally speaking, the system is close to steady state with respect to water composition.

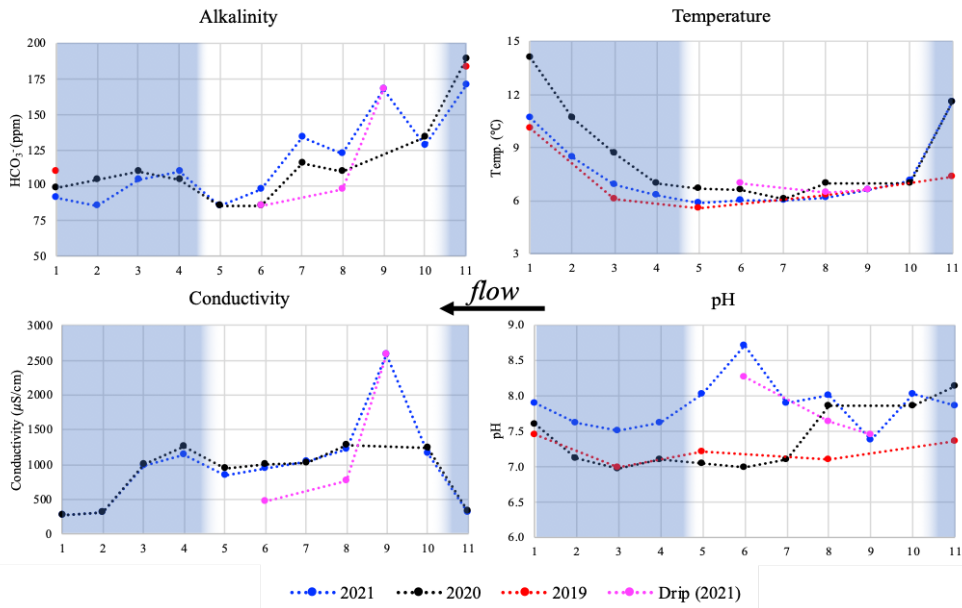


**Figure 2.10.** *In-situ* measurements of alkalinity, temperature, conductivity, and pH from 2019-2021. Flow moves from right to left. The blue-shaded regions denote locations outside of the mine while the non-shaded regions denote locations inside the mine. Numbers on the x-axis correspond to sampling locations as described in Table 2.1 and Figure 2.5. Conductivity was not measured in the gallery in 2019. See table S1 for uncertainty.

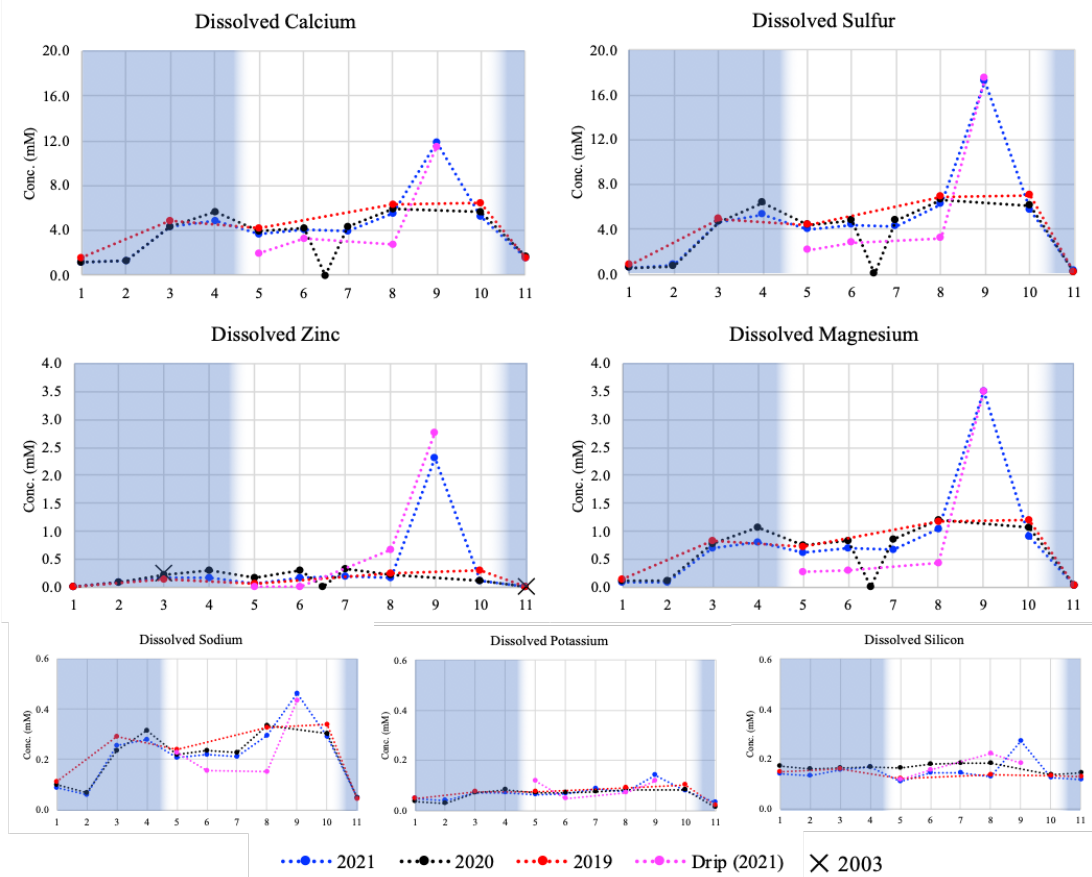


**Figure 2.11.** Major ion concentrations at sampling locations (mM). Analytical uncertainty is  $\pm 4\%$ . Here, flow moves from right to left. The highest measured concentrations are placed in the top row, and the lowest concentrations at the bottom. The blue-shaded regions denote locations outside of the mine while the non-shaded regions denote locations inside the mine. Numbers on the x-axis correspond to sampling locations as described in Table 2.1 and Figure 2.5. The "X 2003" in the legend above refers to the Zn measurements done by Marques et al. (2003).

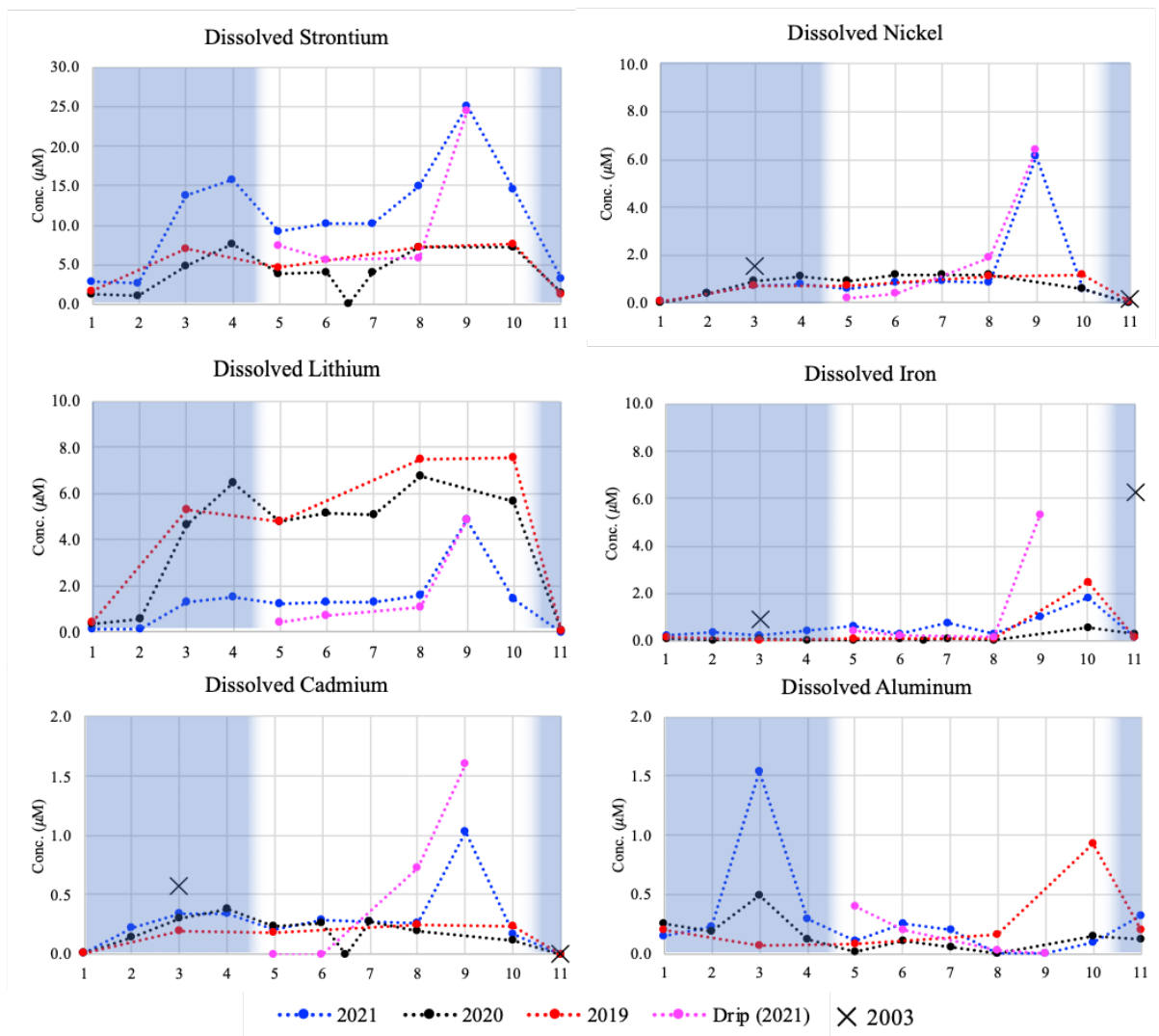


**Figure 2.12.** Minor ion concentrations at sampling locations given in  $\mu\text{M}$ . Water flows from right to left. The blue-shaded regions denote locations outside of the mine while the non-shaded regions denote locations inside the mine. Numbers on the x-axis correspond to sampling locations as described in Table 2.1 and Figure 2.5. The "X 2003" in the legend above refers to the Ni, Fe, and Cd measurements done by Marques et al. (2003). Analytical uncertainty is  $\pm 4\%$  for these values.

### 2.3.2 Discharge and Solute Flux Results

The volumetric discharge rate and associated elemental mass fluxes were determined for each sampling campaign. The conductivity measurements from the field and the calibration curve derived from the lab were used with Eq. 2.1 and Eq. 2.2 to make these calculations (Figure 2.13). The resulting discharge rates were 37.0, 40.4, and 23.1 L/min in 2019, 2020, and 2021, respectively. Using these discharge rates combined with the elemental concentrations, the daily mass fluxes of the dissolved species (Ca, SO<sub>4</sub>, Mg, Zn, Na, Si, K, Sr, Ni, Cd, Li) were calculated in grams per day (Table 2.2A) and moles per day (Table 2.2B). The relationship between mass flux and normalized volumetric discharge was also plotted (Figure 2.14). A linear regression of the normalized discharge versus the daily mass flux was calculated and the slope ( $m$ ) and  $R^2$  for each corresponding element was recorded for comparison (Figure 2.14). The discharge was normalized to highest discharge (40.4 L/min in 2021).

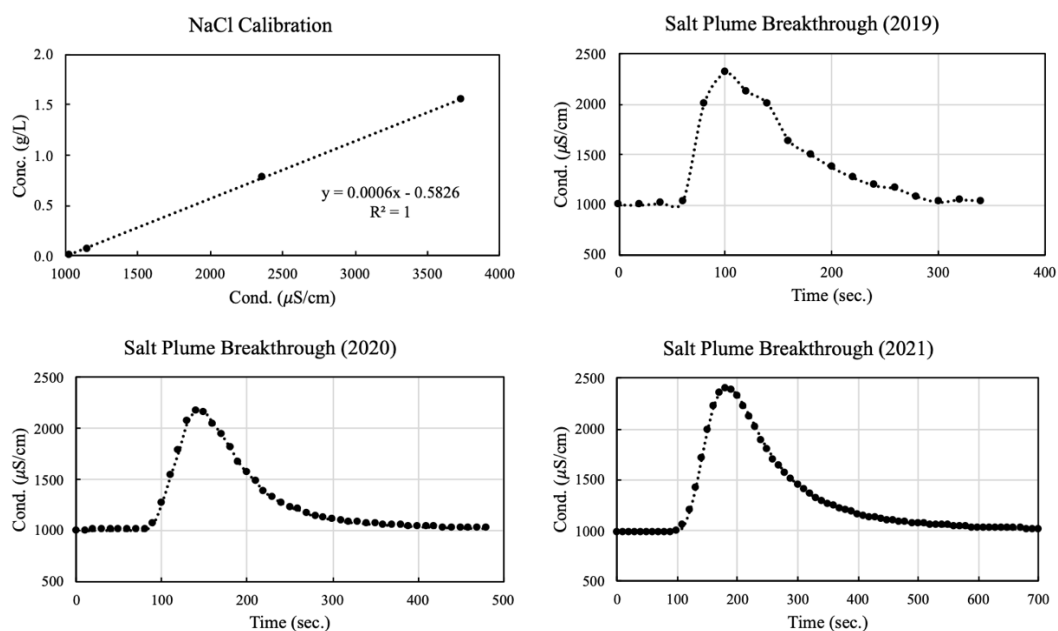


**Figure 2.13.** Salt calibration curve and breakthrough curves from field conductivity measurements during the three sampling campaigns. The linear regression (Eq. 2.1) can be viewed in the NaCl Calibration plot along with an  $R^2$  value, which is equal to 1.

A positive slope ( $m$ ) can be observed for all elements, indicating that mass flux increases with discharge. Further, some elements show similarity in their slopes. For example, Cd and Ni share the same  $m$  value (0.06). Sr and Li have a slope of 0.262 and 0.276, respectively. The most stable relationships (i.e.  $R^2 \geq 0.9$ ) are demonstrated by Ca, SO<sub>4</sub>, Si, Mg, K, and Li. The relatively high  $R^2$  value indicates a relatively stable linear relationship between discharge and mass flux between the aforementioned dissolved species.

Daily mass flux of elements (g/day)	2019 Q = 37.0 L/min	2020 Q = 40.4 L/min	2021 Q = 23.1 L/min
Ca <sup>++</sup>	10,480	10,014	5,822
SO <sub>4</sub> <sup>--</sup>	2,822	2,875	1,652
Mg <sup>++</sup>	1,060	1,102	567
Zn <sup>++</sup>	514	879	320
Na <sup>+</sup>	359	313	194
Si <sup>+</sup>	239	265	144
K <sup>+</sup>	156	159	90
Sr <sup>++</sup>	32.8	24.8	18.3
Ni <sup>+</sup>	2.3	3.0	1.41
Cd <sup>++</sup>	1.2	2.0	0.75
Li <sup>++</sup>	2.0	1.9	1.1

**Table 2.2A.** Daily elemental mass fluxes coming from the Victoria Mine at sample-3 location. Values are given in grams per day.

Daily mass flux of elements (Mol/day)	2019 Q = 37.0 L/min	2020 Q = 40.4 L/min	2021 Q = 23.1 L/min
Ca <sup>++</sup>	261.5	249.9	145.3
SO <sub>4</sub> <sup>--</sup>	33.1	34.4	17.7
Mg <sup>++</sup>	6.4	6.5	3.7
Zn <sup>++</sup>	7.9	13.5	4.9
Na <sup>+</sup>	15.6	13.7	8.5
Si <sup>+</sup>	8.5	9.4	5.1
K <sup>+</sup>	4.0	4.1	2.3
Sr <sup>++</sup>	0.37	0.28	0.21
Ni <sup>+</sup>	0.04	0.05	0.02
Cd <sup>++</sup>	0.03	0.05	0.02
Li <sup>++</sup>	0.28	0.27	0.16

**Table 2.2B.** Daily elemental mass fluxes coming from the Victoria Mine at sample-3 location. Values are given in moles per day.

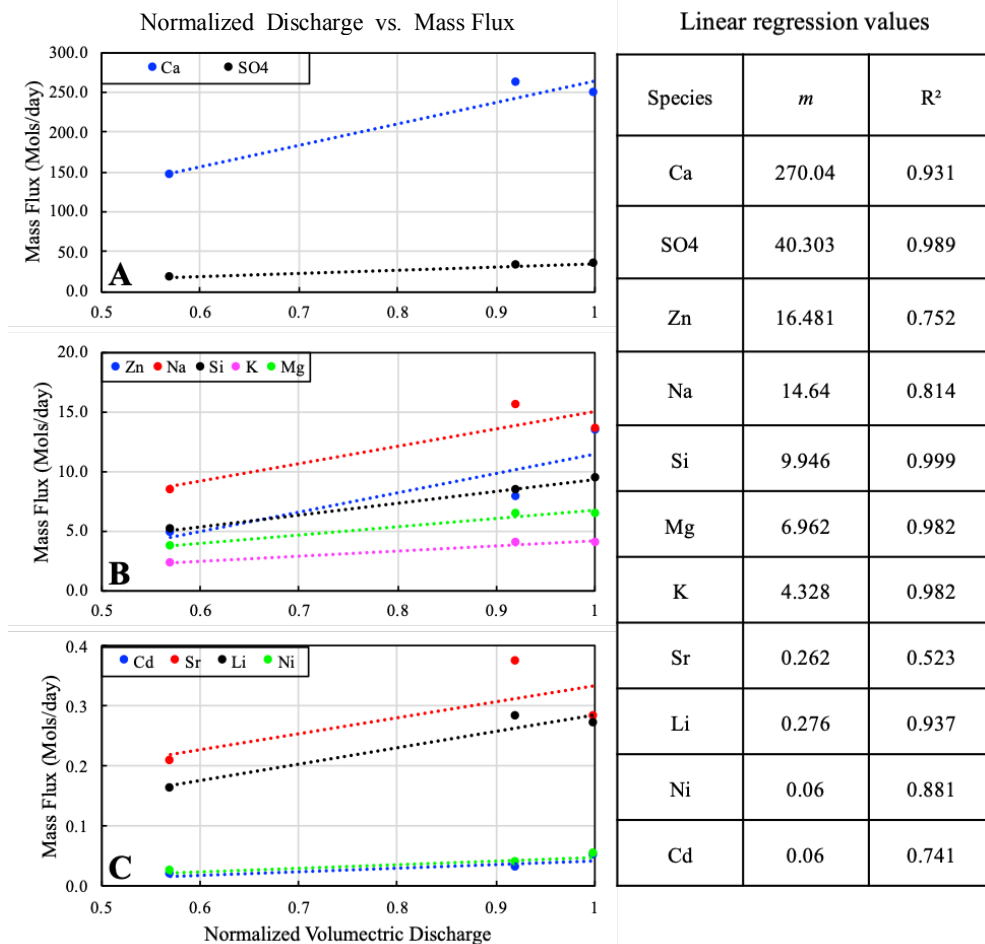


**Figure 2.14.** Three plots showing the relationship between volumetric discharge and elemental mass flux. Discharge was normalized to the highest value measured; 40.4 L/min in 2021. Each plot shows a dotted line that represents a linear best fit for the data. The slope (*m*) and R<sup>2</sup> from each regression was recorded in the table on the right. (A) Calcium and sulfate showing the two highest mass fluxes. (B) Zn, Na, Si, K, and Mg showing similar intermediate mass fluxes. (C) Cd, Sr, Li, and Ni showing the lowest mass fluxes.



### **2.3.3 X-ray Diffraction Results**

In total, six samples of hydrozincite and two samples of sphalerite ore, all from the Victoria Mine, were analyzed using X-ray diffraction analysis. These were qualitative analyses, which serve to identify which minerals are present and also give some information about each mineral's proportion relative to the whole sample. The hydrozincite samples include the four morphologies discussed previously, as well as a stalactite and an orange powder from the floor, both collected at the 280-meter sample-9 location. All six of the samples are pure hydrozincite (Figure 2.15). However, the floating skin morphology also shows trace amounts of the mineral brianyoungite ( $\text{Zn}_3[\text{CO}_3,\text{SO}_4][\text{OH}]_4$ ), another Zn-carbonate that incorporates sulfate into its crystal structure (Livingstone and Champness, 1993). Quantitative analysis of these samples could not be carried out because sample peaks were too wide, which would produce significant error. The wide peaks indicate that these samples are (a) not totally crystalline and/or (b) contain significant impurities.

Results from the two samples of sphalerite ore from the mine, Sphalerite Ore 1 and Sphalerite Ore 2, show that each is composed mainly of sphalerite (Figure 2.16), though other mineral phases are present. In the sample Sphalerite Ore 1, small amounts of quartz, illite, clinocllore, and calcite are present. In the sample Sphalerite Ore 2, there are small amounts of quartz, calcite, pyrrhotite, clinocllore, annite, and possibly grunerite.

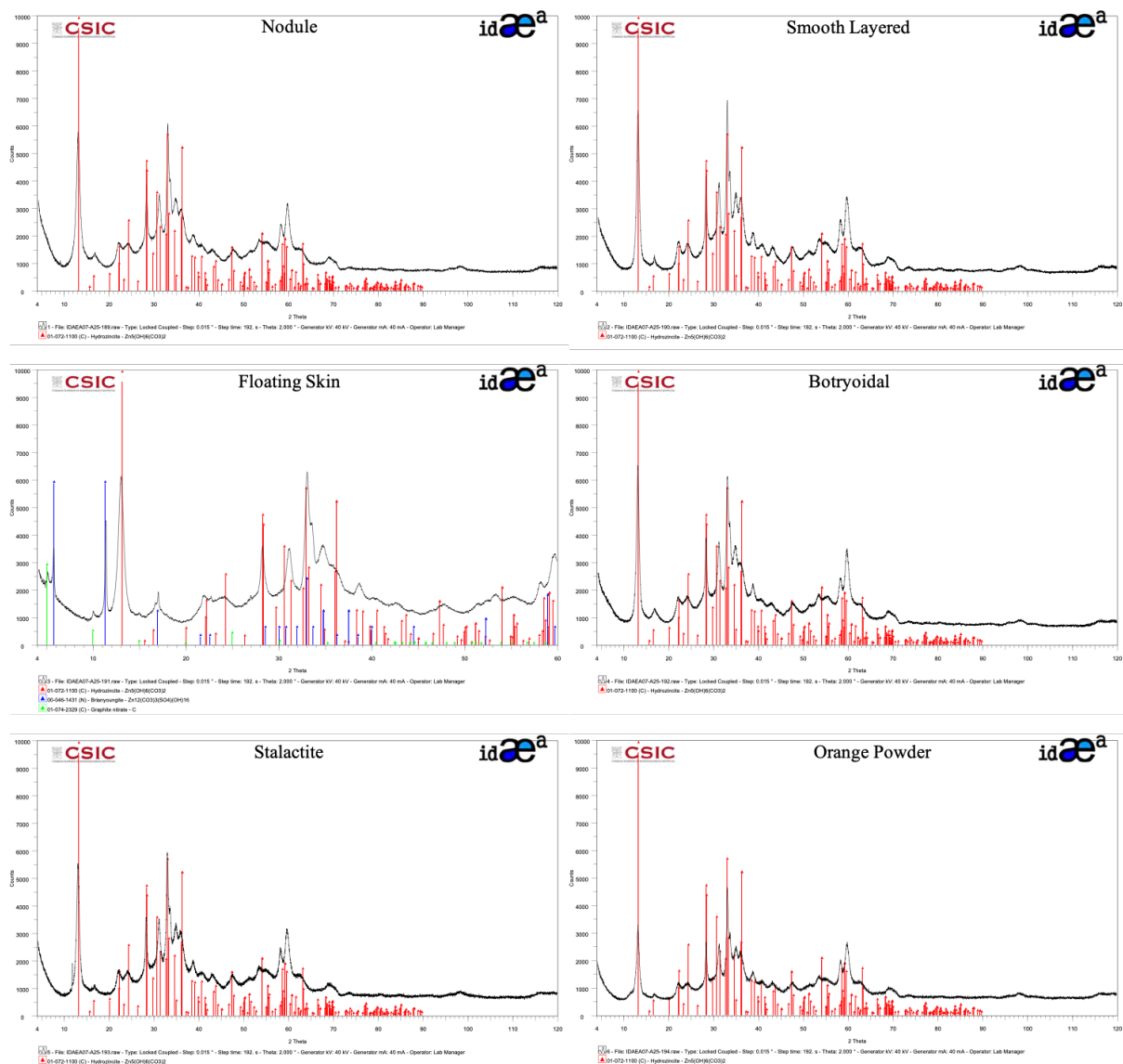


**Figure 2.15.** Qualitative X-ray powder diffraction analysis results (black line) overlaid over ideal crystal peaks (red lines) for six hydrozincite samples. These six samples are composed of pure hydrozincite; however, the peaks are relatively wide, suggesting that they are not completely crystalline or contain impurities. The floating skin sample shows a small amount brianyoungite ( $Zn_3[CO_3,SO_4][OH]_4$ ).

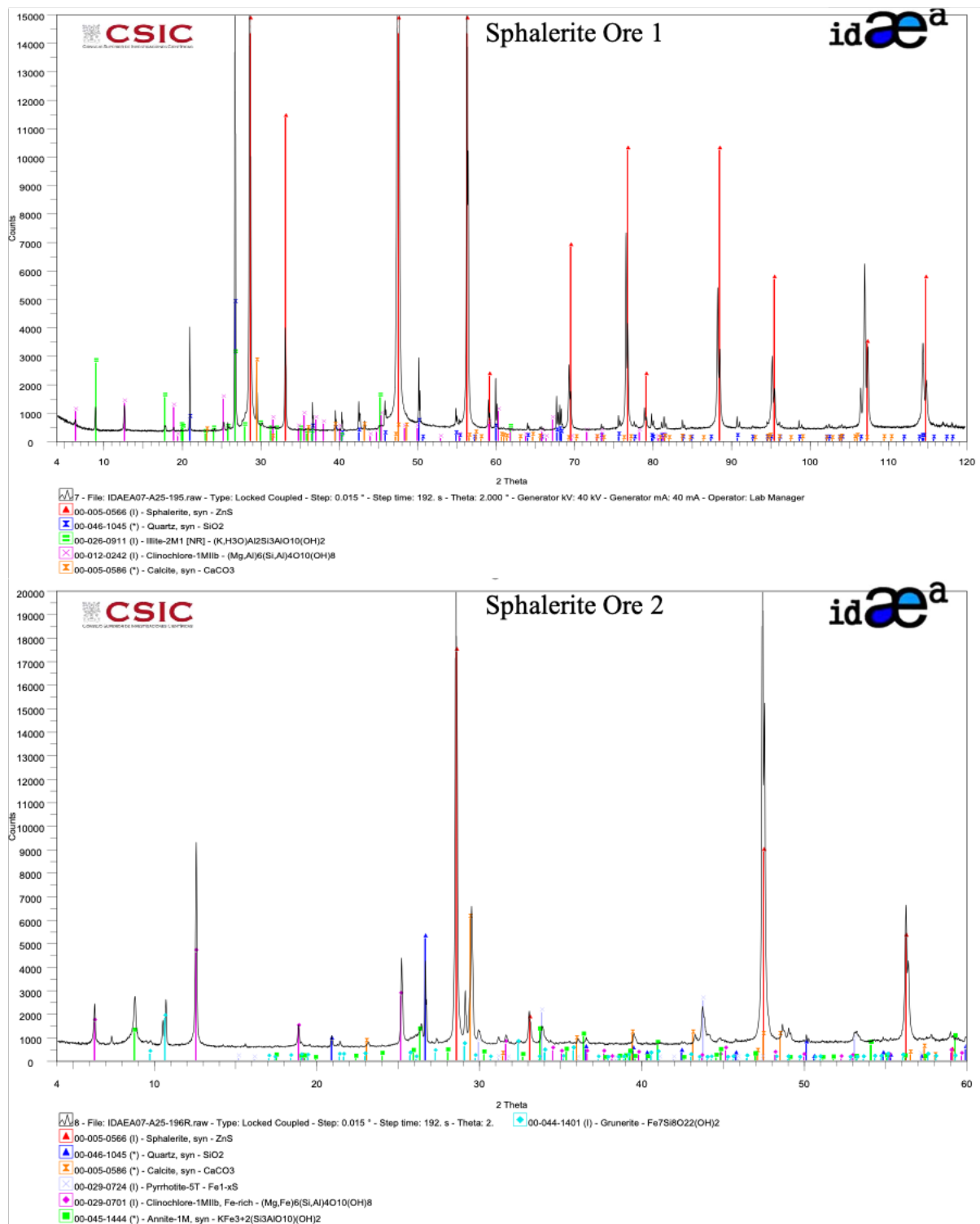


**Figure 2.16.** Qualitative X-ray powder diffraction analysis results (black line) overlaid over ideal crystal peaks (colored lines) for two sphalerite ore samples taken from the Victoria Mine. The samples are composed mainly of sphalerite, however, there are several other mineral phases present. In Sphalerite Ore 1, there are small amounts of quartz, illite, clinocllore, and calcite. Sphalerite Ore 2 contains small amounts of quartz, calcite, pyrrhotite, clinocllore, annite, and possibly grunerite.

### 2.3.4 Electron Microprobe and SEM Results

Backscattered electron imaging results demonstrate a zonation of heavy and light elemental compositions corresponding to the white and grey regions (Figure 2.17). This effect most pronounced in the nodule morphology (Figure 2.17(A and B)) and least pronounced in the smooth layered morphology (Figure 2.17(C)). This zonation is apparent in the floating skin (Figures 2.17(D-I)) and botryoidal (Figure 2.17(J-L)) morphologies. However, these two morphologies differ from the nodule and the smooth layered morphologies because they possess needle-like crystals.

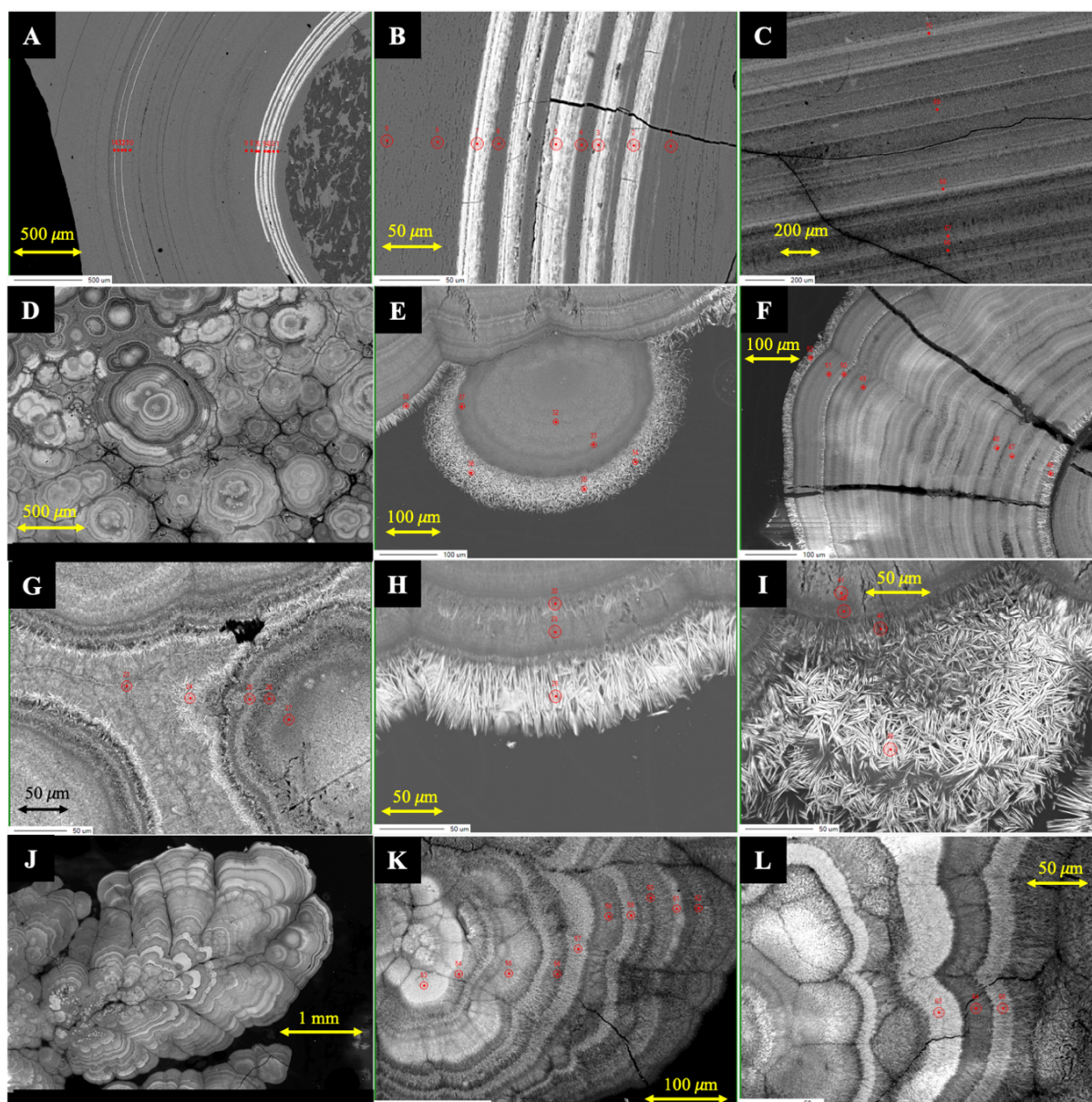


**Figure 2.17.** Backscattered electron images of four hydrozincite morphologies; Nodule (A-B), Smooth Layered (C), Floating Skin (D-I), and Botryoidal (J-L). Scale bars are shown at the bottom of each image. Each red dot represents the location of electron microprobe analysis. In general, white zones are richer in Zn than grey zones.



The floating skin samples often exhibit needles at the terminating edge of the crystal growth, while the botryoidal samples appear to be composed of needles. Comparing the needle structures between the two (i.e. Figure 2.17(I) vs. 2.17(L)), it is clear that the needle structures are significantly larger in the floating skin samples (up to 50  $\mu\text{m}$  along the long axis) than the botryoidal samples ( $\approx 5 \mu\text{m}$  along the long axis). Upon further inspection, the four morphologies can be grouped as two morphologies. The nodule and smooth layered show similar uniform layering patterns, such that both are planar and display similar zonation. Notably, elemental zonation is much more exaggerated in the nodule sample than in any other. Further, the botryoidal and floating skin samples both possess non-planar elemental zonations, often composed of needle structures.

These observed zonations were analyzed for Zn, Ca, Mg, Fe, Ni, and Cd concentrations via point analysis (Table S4) and elemental mapping (Figures 2.18(A-D)). It should be noted that the "level" (i.e. color scale) associated with each elemental scan is distinct for each sample. This level is a representation of the relative range in concentration for each element (e.g. Zn, Ca, Mg, Fe, and Ni) in each scan and does not represent an absolute concentration.

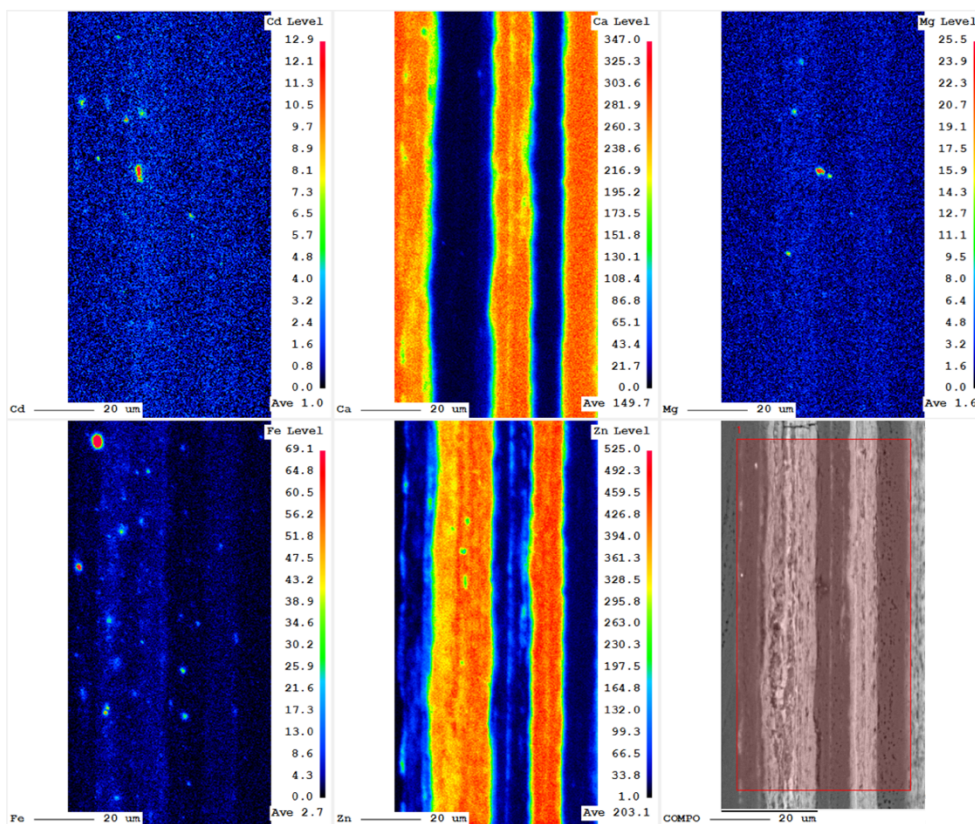


**Figure 2.18A.** Results from elemental scans of Cd, Ca, Mg, Fe, and Zn in the nodule morphology sample. The bottom right image is the backscattered electron image of the location where the scan was completed. The elemental "level" refers to a relative variation in concentration for a given scan, not an absolute concentration.

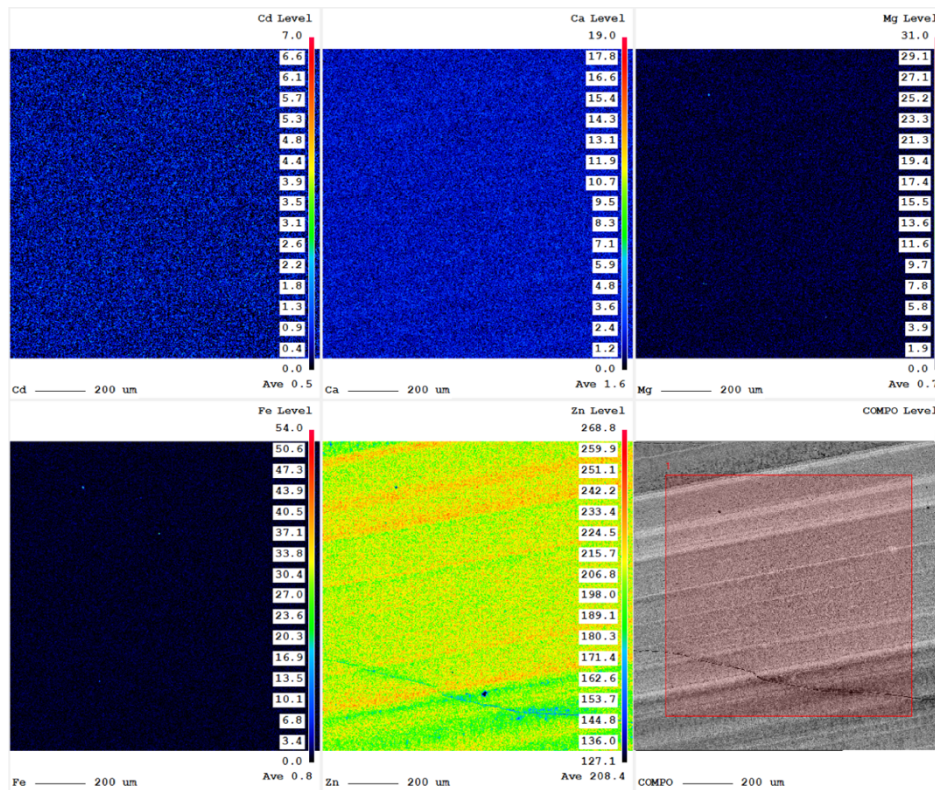


**Figure 2.18B.** Results from elemental scans of Cd, Ca, Mg, Fe, and Zn in the smooth layered morphology sample. The bottom right image is the backscattered electron image of the location where the scan was completed. The elemental "level" refers to a relative variation in concentration for a given scan, not an absolute concentration.

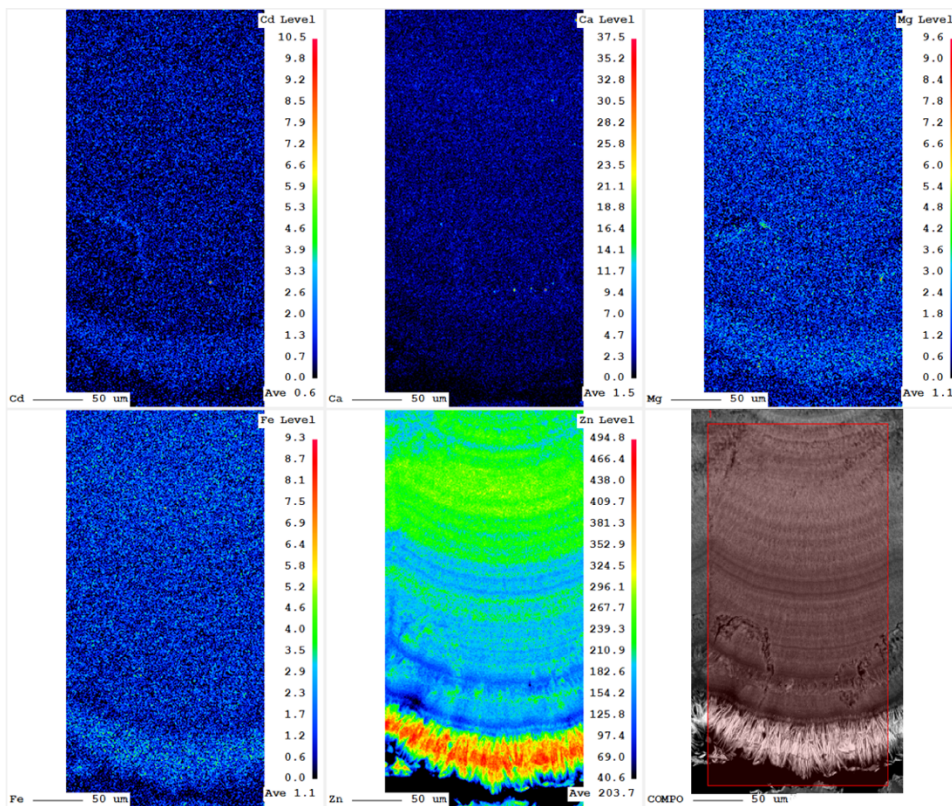


**Figure 2.18C.** Results from elemental scans of Cd, Ca, Mg, Fe, and Zn in the floating skin morphology sample. The bottom right image is the backscattered electron image of the location where the scan was completed. The elemental "level" refers to a relative variation in concentration for a given scan, not an absolute concentration.



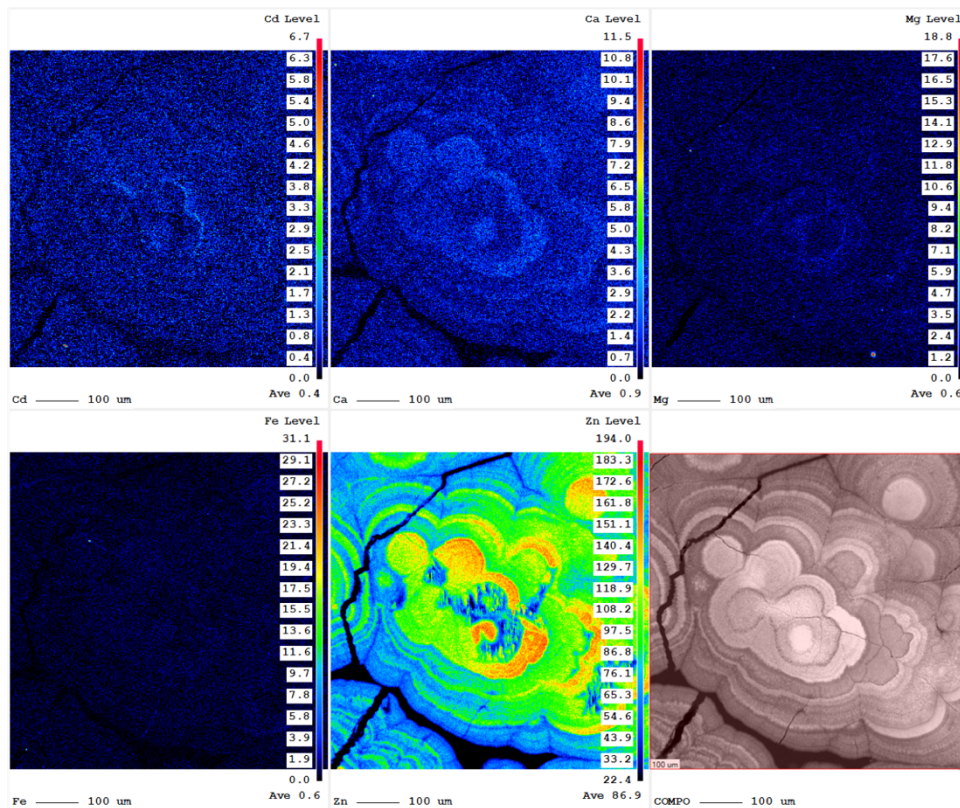


**Figure 2.18D.** Results from elemental scans of Cd, Ca, Mg, Fe, and Zn in the botryoidal morphology sample. The bottom right image is the backscattered electron image of the location where the scan was completed. The elemental "level" refers to a relative variation in concentration for a given scan, not an absolute concentration.

The elemental mapping of the nodule morphology sample (Figure 2.18(A)) indicates that the layering is primarily a zonation of Ca and Zn, although there is some slight zonation of Fe, such that there is more Fe in the Zn-rich areas. Most notably, Ca and Zn levels vary between 350 and 525 times that of their relative background concentrations, respectively. There are also some cadmium "hot-spots" that are in the Zn-rich layers where cadmium levels reach up to 13 times that of the background concentrations. The same is true for iron, such that Fe "hot-spots" approach 70 times that of background concentrations.

The elemental mapping of the smooth layered sample does not show significant zonation of Ca and Zn like that of nodule sample (Figure 2.18(B)). Instead, Ca exhibits a stable concentration throughout and Zn is also evenly distributed. This particular sample exhibits the least amount of elemental zonation when compared to the other three.

Elemental scan results of the floating skin sample exhibit strong Zn zonation in the outermost layer composed of large needle structures (Figure 2.18(C)). Zinc is most highly concentrated in the needle structures exhibiting  $\approx 500x$  concentrations relative to the

background. The needle structures also exhibit slightly higher concentrations of Cd, Mg, and Fe when compared to the rest of the scanned area. However, calcium is depleted in this area. In this sample, the needle structures indicate a higher concentration of all elements (excluding Ca) than the rest of the scanned area.

The results of the botryoidal elemental scan show the most consistent Ca and Zn zonation aside from the nodule sample (Figure 2.18(D)). However, unlike the nodule zonation patterns, which exhibited enrichment of Ca and Zn in different zones, the botryoidal shows high Ca and Zn levels in the same zones (i.e. the white zones). Further, there is slightly stronger Cd zonation in this sample than the others, although relative concentrations only vary by approximately 7x. Zinc concentration variability approaches 200x in the most concentrated white regions.

Elemental point analysis was done to determine relative concentrations of ZnO, CaO, SrO, CdO, NiO, FeO, and Mn (Table S4). The two most abundant elements in these analyses are Ca and Zn. A point analysis of the white and grey region of the nodule shows that the grey regions are composed of  $53.4 \pm 1.3$  wt. % CaO,  $2.1 \pm 1.2$  wt. % ZnO, and  $2,340 \pm 390$  ppm SrO. However, the white regions are composed of  $1.5 \pm 0.3$  wt. % CaO,  $66.7 \pm 2.7$  wt. % ZnO and  $22 \pm 22$  ppm SrO. In other words, Ca and Sr are enriched in the grey zones, while Zn is enriched in the white zones.

Observation of elemental compositions along a transect of the nodule shows a strong inverse correlation between Zn and Ca, meanwhile Ca and Sr are strongly correlated (Figure 2.19). Additionally, Ni and Zn are strongly correlated, such that Ni is only enriched in the Zn-bearing areas. Cd and Fe appear to increase towards the terminating boundary of the nodule, but do not appear to correlate with the Ca or Zn-rich zones. It should be noted that the percentage of ZnO in the grey areas of the nodule is approximately 2%, which is far below the theoretical mass fraction of ZnO in hydrozincite (74%). Further, the ZnO mass fraction in the white areas is approximately 67%, which is consistent with that of smithsonite (65%) In addition, the CaO concentration in the grey areas is approximately 53%, which agrees with the theoretical mass fraction of calcium in calcite (56%) (Table S4).



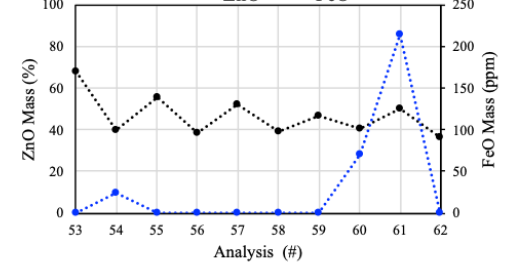
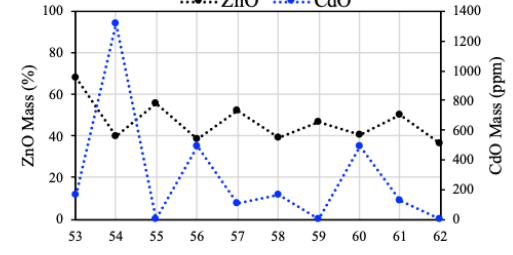
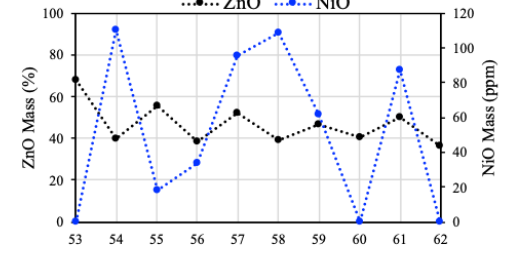
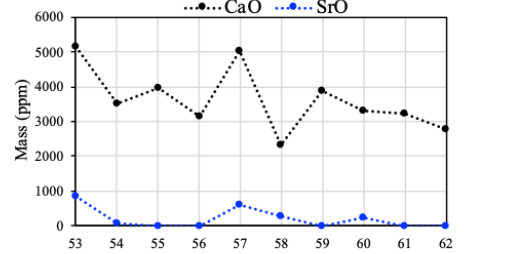
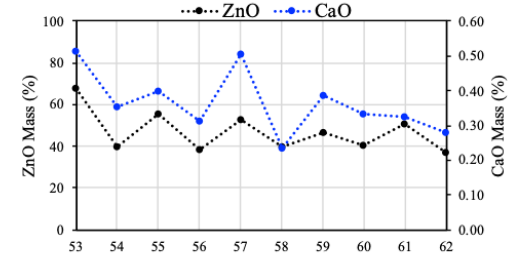
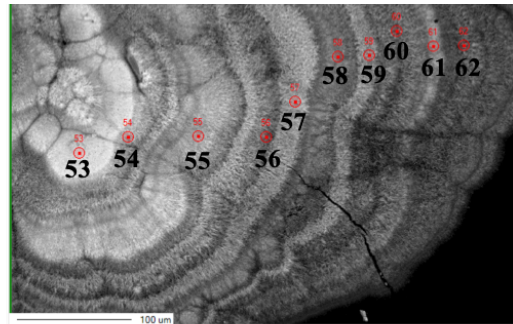
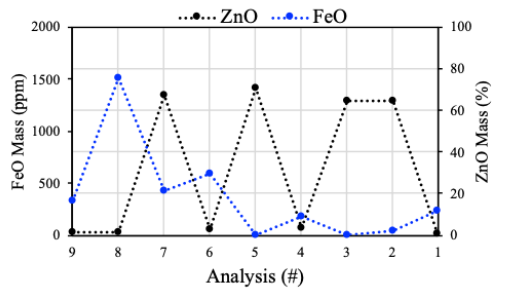
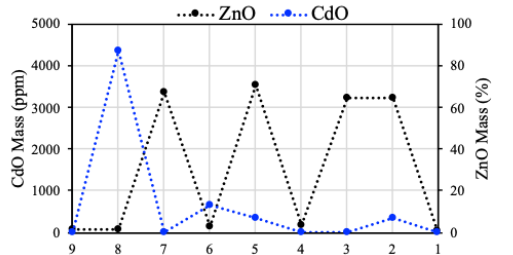
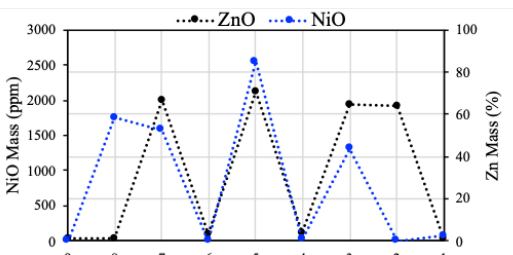
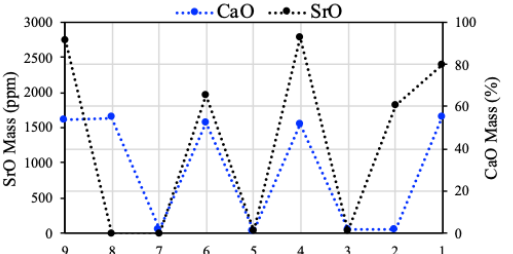
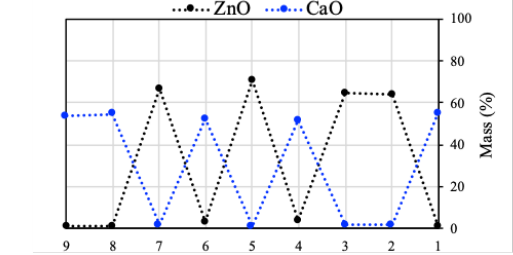
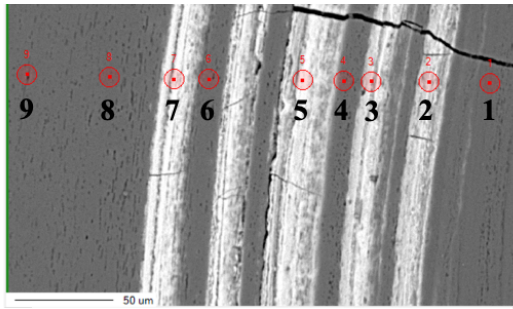


**Figure 2.19.** Results from electron microprobe point analysis of a transect of two samples. The left column is showing the analysis of the nodule morphology sample, and the right column corresponds to a botryoidal sample. The numbers on the SEM image correspond to the x-axis for each sample.

Elemental concentrations were measured along a transect of the botryoidal sample (Figure 2.19). The white zones (Figure 2.11 analysis #'s: 53, 55, 57, 59, Table S4) shows an average ZnO of  $55.63 \pm 7.72$  wt. % and CaO shows  $0.45 \pm 0.06$  wt. %. The darker colored zones (Figure 2.11 analysis #'s: 54, 56, 58, 60) exhibit average an average ZnO and CaO of  $39.60 \pm 0.79$  wt. % and  $0.31 \pm 0.05$  wt. %, respectively. This follows a similar trend when compared to the nodule sample zonations, such that Zn is higher in the white zones, though it is much less pronounced in the botryoidal sample than in the nodule sample. Further, CaO levels only reach a fraction of a percent in the whole botryoidal sample, while CaO reaches over 50% in the dark layers of the nodule. The principal difference is that Ca and Zn are positively correlated, unlike in the nodule. Considering Ni, Cd, and Fe, there is no clear zonation patterns related to the changing layers of white and grey (i.e. high and low Zn).

### ***2.3.5 Total Digestion Results***

Results from the total acid digestion of the four sample morphologies are shown in ppm (Table 2.3). The Zn concentration in all four digestions is  $544,388 \pm 16,143$  ppm, which agrees with that of theoretical hydrozincite (595,000 ppm). Further, since the other 40.5% of hydrozincite is hydrogen, carbon, and oxygen, this dissolved mass would appear as lost mass due to the inability to analyze these elements using the current method. The "Total (%)" is the percent sum of mass recovered from the four 0.2500 g samples, which averages  $55.5 \pm 1.9\%$ . This agrees with the theoretical mass that should be recovered (59.5%).

Sulfur and calcium concentrations indicate there are some impurities associated with the digested sample. Cadmium concentrations were determined to be  $87 \pm 22$  ppm, while nickel was the most abundant trace metal in the sample with a concentration of  $479 \pm 35$  ppm. The nodule sample shows the highest iron concentration at 343 ppm, while the smooth layered morphology only exhibits 26 ppm iron. There are significant amounts of copper in all samples, showing a mean of  $97 \pm 52$  ppm, although strontium is present in very small quantities in all samples exhibiting a concentration of  $13 \pm 1$  ppm. Additionally, arsenic is present in each sample, exhibiting an average of  $34 \pm 20$  ppm.

**Table 2.3.** Total acid digestion results from four 0.2500 g hydrozincite samples. The left table values are given in ppm. The "Total (%)" is the sum of mass recovered from the digestion given in %. Since hydrozincite is 60% Zn and 40% CO<sub>3</sub> and OH, a 60% recovered mass return would be expected because CO<sub>3</sub> was lost as CO<sub>2(g)</sub> and OH is lost during this analysis. All elemental concentrations are listed in descending order based on the average determined from the four samples. The standard deviation ( $\sigma$ ) showing the variability between the four samples is listed in the right column. Analytical uncertainty is  $\pm 4\%$ .

<b>Element</b>	<b>Nodule</b>	<b>Smooth Layered</b>	<b>Floating Skin</b>	<b>Botryoidal</b>	<b>Average</b>	<b><math>\sigma</math></b>
<b>Zn</b>	516,531	555,087	551,434	554,498	544,388	16,143
<b>S</b>	3,092	4,000	6,020	3,923	4,259	1,078
<b>Ca</b>	3,862	3,520	3,003	3,089	3,368	346
<b>Ni</b>	424	496	478	519	479	35
<b>K</b>	520	0	137	244	225	191
<b>Fe</b>	343	26	287	124	195	126
<b>Si</b>	131	159	186	179	164	21
<b>Mg</b>	198	129	176	150	163	26
<b>Pb</b>	126	23	305	162	154	101
<b>Cu</b>	129	162	30	65	97	52
<b>Cd</b>	98	107	50	94	87	22
<b>Al</b>	54	6	63	15	35	25
<b>As</b>	60	39	3	34	34	20
<b>Co</b>	27	20	25	35	27	5
<b>Mn</b>	29	0	30	28	22	13
<b>Sr</b>	15	12	12	12	13	1
<b>Total (%)</b>	52.6	56.4	56.2	56.3	55.4	1.9

### 2.3.6 Solubility Experiment Results

The purpose of this experiment is to determine the equilibrium constant ( $K_{eq}$ ) of hydrozincite at the temperatures observed inside of the Victoria Mine ( $6.5 \pm 0.4^\circ\text{C}$ ). This was accomplished via the dissolution of a solid sample of hydrozincite from the Victoria Mine mine in ultrapure Milli-Q water ( $18.2 \text{ M}\Omega$ ) at two temperatures;  $3.7^\circ\text{C}$  and  $20.0^\circ\text{C}$ . Zn concentrations and pH were measured, while the water was bubbled to maintain equilibrium with the atmosphere.

Equilibrium concentrations were based on pH observations, such that once the pH reaches steady state, the solution is assumed to be at equilibrium with the mineral. The results of this experiment demonstrate a steady state with respect to pH and Zn, and thus provide equilibrium concentrations at each temperature (Figure 2.20). For the  $20.0^\circ\text{C}$  condition, steady state with respect to Zn and pH is obtained after 4 hours (Figure 2.20) when the pH stabilizes at  $7.10 \pm 0.04$ . For the  $3.7^\circ\text{C}$  condition, steady state was obtained after 21 hours when the pH stabilized at  $6.98 \pm 0.01$ . Further, Zn concentrations stabilized at  $0.321 \pm 0.006 \text{ mM}$  and  $0.478 \pm 0.007 \text{ mM}$  for the  $20.0^\circ\text{C}$  and the  $3.7^\circ\text{C}$  conditions, respectively. Notably, in the  $20.0^\circ\text{C}$  dissolution, Ca results in a higher concentration than Zn at steady state, while this does not occur in the  $3.7^\circ\text{C}$  dissolution. Cd concentrations stabilize at  $0.06 \pm 0.01 \mu\text{M}$  and  $0.05 \pm 0.01 \mu\text{M}$  for the  $20.0^\circ\text{C}$  and  $3.7^\circ\text{C}$  conditions, respectively. Additionally, in the  $3.7^\circ\text{C}$  dissolution, Ni concentrations stabilize around  $0.4 \mu\text{M}$  while strontium concentrations stabilize around  $0.1 \mu\text{M}$ .

The change in mass of the solid sample before and after dissolution is compared to the calculated dissolved solute masses to further verify the results (i.e. mass recovery). The  $20.0^\circ\text{C}$  case resulted 0.0353 g loss, and the  $3.7^\circ\text{C}$  case resulted in a 0.0320 g loss. The masses of all solutes (e.g. Cd, Zn, Ca, Ni, and Sr) were summed for each experiment by multiplying the final concentrations by the final volumes and considering removed sample volume. The calculated dissolved mass in the  $20.0^\circ\text{C}$  case was 0.0269 g. The  $3.7^\circ\text{C}$  case resulted in 0.0232 g of solute mass. The calculated values are less than the weighed values because ideal hydrozincite is 59.5% Zn by mass, while H, C, and O are lost (i.e. cannot be calculated). If the assumption is made that the sample was pure hydrozincite (i.e. 59.5% Zn), then the  $20.0^\circ\text{C}$  case and the  $3.7^\circ\text{C}$  result in a 128% (0.0344 g) and 122% (0.0283 g) mass recovery, respectively. The consistency between experiments (within 6%) validates the experimental method.

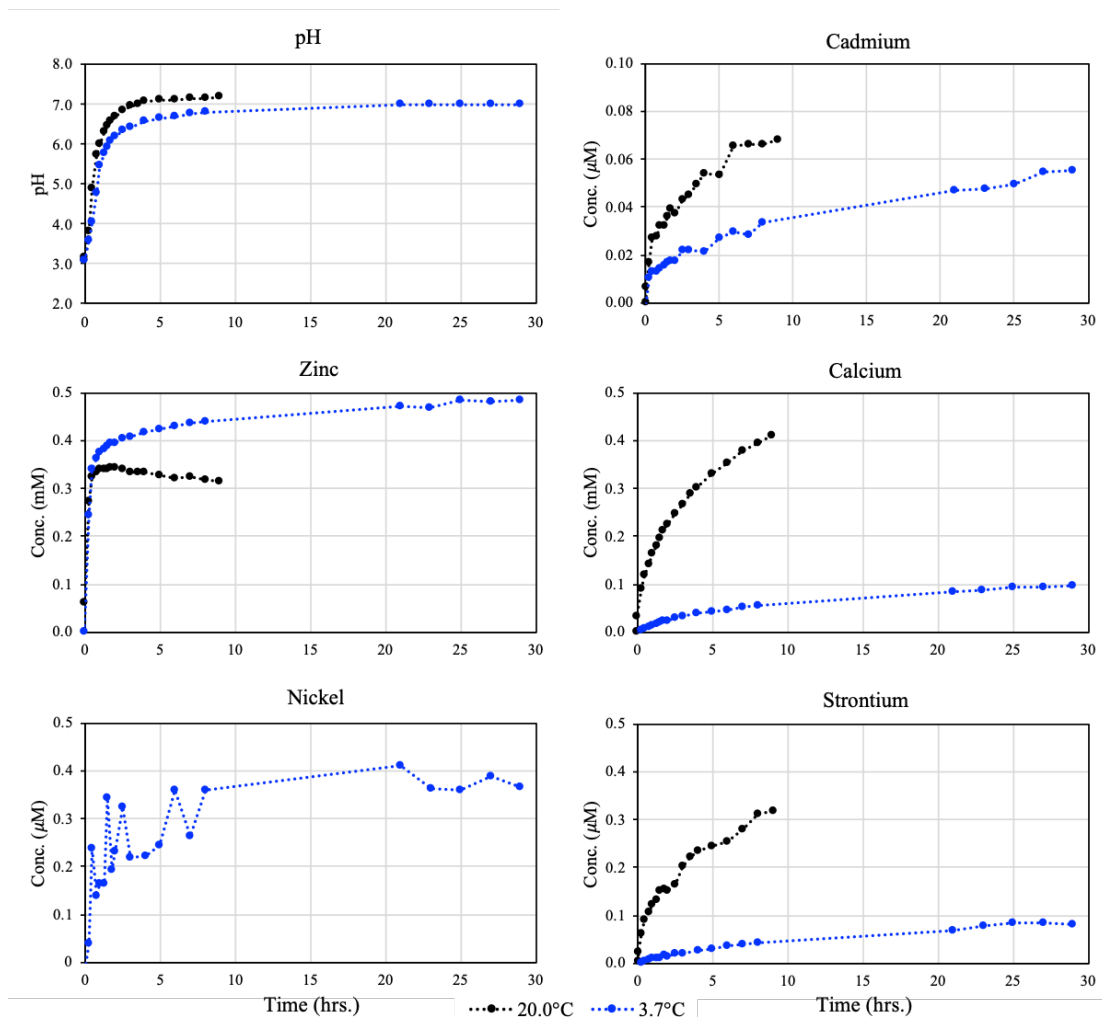


**Figure 2.20.** Concentration and pH results through time from the hydrozincite dissolution experiments. The black points represent the 20.0°C experiment and the blue points represent the 3.7°C experiment. Nickel was only measured during the 3.7°C experiment. It should be noted that the same 3.0 g piece of hydrozincite (floating skin morphology) was used for each temperature condition. The warmer 20.0°C condition was the first experiment, and later the colder 3.7°C condition was done. Analytical uncertainty is  $\pm 6\%$  for concentration values.

Although verified by XRD (Figure 2.15) to be hydrozincite with amorphous material, concentrations (Figure 2.20) and mass recovery calculations indicate that the sample is not pure hydrozincite. Nevertheless, the  $K_{eq}$  is calculated.

### 2.3.7 Equilibrium Constant for Hydrozincite

In accordance with the dissolution reaction of hydrozincite (Reaction 2.1) the corresponding equilibrium constant ( $K_{eq}$ ) is written as:

$$K_{eq} = \frac{(Zn^{++})^5 (HCO_3^-)^2}{(H^+)^8}$$

The activities of these species are calculated using the CrunchFlow geochemical modeling software package (Steeffel *et al.*, 2015). Further details of the code are found in chapter 3 (section 3.3). Solute concentrations given to the model correspond to those at steady state for both experiments (Table 2.4). Water is assumed to be at equilibrium with atmospheric oxygen (20.9%) and CO<sub>2</sub> (415 ppm).

**Table 2.4.** CrunchFlow input for solute concentrations (M), pH, and gas concentrations used to make speciation calculations for each experimental condition.

T = 20.0°C			T = 3.7°C		
Species	Conc. (M)		Species	Conc. (M)	
pH	7.13		pH	6.98	
K <sup>+</sup>	1.20E-04		K <sup>+</sup>	1.90E-04	
Mg <sup>++</sup>	3.00E-05		Mg <sup>++</sup>	4.12E-03	
SO <sub>4</sub> <sup>--</sup>	3.40E-04		SO <sub>4</sub> <sup>--</sup>	4.00E-05	
Ca <sup>++</sup>	3.70E-04		Ca <sup>++</sup>	9.00E-05	
SiO <sub>2</sub> (aq)	5.80E-06		SiO <sub>2</sub> (aq)	8.34E-06	
Zn <sup>++</sup>	3.20E-04		Zn <sup>++</sup>	4.80E-04	
Cd <sup>++</sup>	6.00E-08		Cd <sup>++</sup>	5.00E-08	
Sr <sup>++</sup>	2.80E-07		Sr <sup>++</sup>	8.00E-08	
Ni <sup>++</sup>	1.00E-10		Ni <sup>++</sup>	4.00E-08	
HCO <sub>3</sub> <sup>-</sup>	CO <sub>2</sub> (g)	0.000415	HCO <sub>3</sub> <sup>-</sup>	CO <sub>2</sub> (g)	0.000415
O <sub>2</sub> (aq)	O <sub>2</sub> (g)	0.209	O <sub>2</sub> (aq)	O <sub>2</sub> (g)	0.209

The speciation calculation reports a saturation index ( $SI = \log[IAP/K_{eq}]$ ) for hydrozincite with respect to a preexisting  $K_{eq}$  in the CrunchFlow thermodynamic database. Using this SI value, the new experimental  $K_{eq}$  is calculated by assuming that the water is in equilibrium with respect to hydrozincite (i.e.  $IAP = K_{eq}$  (new)), as this is the observation made from the experiments. Further, a linear relationship between the two temperature-dependent  $K_{eq}$ 's is used to find the  $K_{eq}$  at 7°C; the approximate temperature inside of the 1330 Gallery.

The new measured  $\log[K_{eq}]$  value of hydrozincite at 20.0°C and 3.7°C are 29.11 and 30.23, respectively. The interpolated  $\log[K_{eq}]$  value at 7°C is 30.01 This agrees with the only previously reported value for pure hydrozincite at 25.0°C ( $\log[K_{eq}] = 30.14$ , Schindler *et al.*, 1969).

### 2.3.8 Mineral Solubility along the Flow Path

The saturation indices (SI's) of hydrozincite, smithsonite, and calcite at every sampling location are determined using the CrunchFlow speciation feature (Figure 2.21). Additionally, the ionic strength resulting from these calculations is recorded from each calculation. Each calculation implements the  $K_{eq}$  of hydrozincite determined in this study ( $\log[K_{eq}] = 30.01$ ) and the water compositions at each sampling interval measured in 2020 and 2021 (Table S2). Further, the water is assumed to be in equilibrium with the atmosphere (415 ppm  $\text{CO}_2$  and 21%  $\text{O}_2$ ).

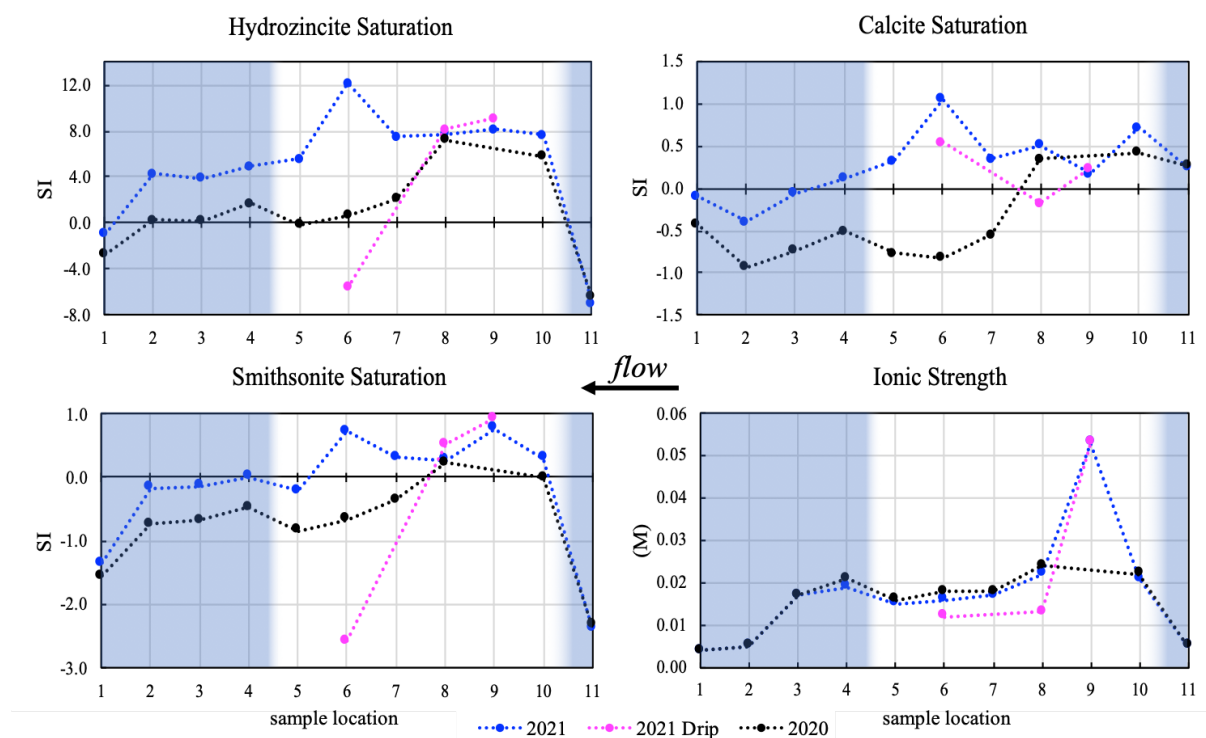


**Figure 2.21.** Resulting SI values and ionic strength (mol/L) from speciation calculations in CrunchFlow. Each calculation input has been adjusted to its corresponding measured water composition from the 2020 and 2021 sampling campaigns. Sample locations correspond to Table 2.1. The blue shaded regions represent sample locations outside of the mine, while non-shaded regions represent samples taken from inside the mine. Uncertainty here is  $\pm 6\%$  based on the analytical techniques.

The results of these calculations show that the SI values for all three minerals are generally higher in 2021 than 2020. Hydrozincite and smithsonite are undersaturated in the upper catchment (sample-11) before the water flows through the host rock and into the mine. In contrast, calcite is oversaturated above the mine. Once water enters the gallery (sample-9 and 10), smithsonite, calcite, and hydrozincite are all oversaturated, although hydrozincite is more oversaturated. For instance, smithsonite and calcite SI values do not surpass  $\sim 1.0$ , while hydrozincite SI values are always above 5 and reach 12 in the gallery.

When comparing all three minerals in 2020, a similar behavior can be observed, such that SI values decrease with distance once waters enter the mine. The same trend can be seen in 2021. However, in 2020 the mineral SI values more readily drop below zero, indicating that all three carbonates should dissolve towards the end of the gallery, and do not precipitate outside of the mine.

The SI values for hydrozincite and smithsonite in the drip water at sampling locations 8 and 9 are similar to those of the floor water below. This is not the case for the drip water sample at location 6, which is highly undersaturated in both hydrozincite and smithsonite. In the drip water at sampling locations 6 and 9, the SI value for calcite is similar to that of the underlying floor water. This is not the case for the sample-8 location, where calcite is undersaturated in the drip water and oversaturated in the underlying floor water.

The calculated ionic strength of the water is remarkably similar between 2020 and 2021. As expected, the ionic strength is low in the upper catchment before the water reacts with the host rock. Then the ionic strength increases through the host rock and enters the gallery. Along the gallery, the ionic strength generally decreases with distance. However, the ionic strength of the effluent appears to increase slightly and then decreases outside of the mine as the water flows down the catchment. It should be noted that ionic strength and conductivity are highly correlated (Figures 2.10 and 2.21).

These results demonstrate that the saturation state of minerals in the gallery is not at steady state. For instance, smithsonite and calcite are generally undersaturated in the gallery in 2020, and oversaturated in 2021, whereas hydrozincite in the gallery is almost always oversaturated regardless of the year. Hydrozincite precipitation would be expected to occur more readily than that of calcite and smithsonite in the gallery. This concept will be further discussed in chapter 3.



## 2.4 Discussion

### 2.4.1 Apparent Hydrozincite Solubility

Results from section 2.3.8 indicate that hydrozincite is highly oversaturated at several locations inside the mine (Figure 2.21). However, hydrozincite was seen as a secondary mineral precipitating wherever water was present, suggesting that the water is actively equilibrating ( $SI \rightarrow 0$ ) with respect to hydrozincite via precipitation. Considering this, it seems unlikely that that SI values would be readily above 5, and reach 12 in one case. Therefore, a potential variation in the solubility of hydrozincite is explored.

Equilibrium-constant values are generally assigned to pure endmember minerals. This means that the observable  $K_{eq}$  value can vary as a function of impurity content and crystallinity, like that seen here. Since minerals like hydrozincite in nature are rarely pure, experimentally determined and theoretically calculated  $K_{eq}$  values can be specific to the sample composition and morphology. In addition, a  $K_{eq}$  value for a mineral does not consider amorphous precursors that could lead to an increase in solubility (i.e. higher SI value) during initial formation. For instance, amorphous precipitates can act as more soluble precursors for La- and Nd-carbonates (Vallina *et al.*, 2015). This is in conjunction with Ostwald's step rule, which reasons that mineral formation can be a series of steps (i.e. Ostwald ripening) where thermodynamically less-stable phases occur first (e.g. amorphous precursors) (Van Santen, 1984). Such behavior would cause an apparent solubility higher than that of the pure mineral, which could cause high oversaturation to occur. This is consistent with the hydrozincite SI values associated with the mine (Figure 2.21).

Several hydrozincite morphologies were seen in the Victoria Mine, both visibly (Figure 2.8) and via backscattered electron images (2.17). Further, XRD results show amorphous material in all samples (Figure 2.15), and all samples analyzed via electron microprobe exhibit compositional heterogeneity (Figure 2.18(A-D), Figure 2.19, Table S4). Considering the variability in the mineral, the equilibrium constant would be expected to vary as well.

The equilibrium constant determined by experiments reflects the solubility of the solid sample. Considering the impurities found in the liquid and the theoretical recovered mass calculated for each temperature case (i.e. 122% and 128% mass recovery), the sample is not pure hydrozincite.

Under the assumption that the water inside the gallery at the sample-5 and sample-10 locations (2021) equilibrates via formation of hydrozincite, two new apparent equilibrium constants are calculated. Both of these samples represent locations where the water has had time to react, and therefore reach equilibrium. This is accomplished by solving the equation  $SI = \log(IAP/ K_{eq})$  for  $K_{eq}$  when  $SI = 0$  at each sample location. The IAP is calculated via the speciation feature in CrunchFlow using the water composition of each sample interval (Table S2) (Steefel *et al.*, 2015). The calculations also assume that the water is in equilibrium with atmospheric CO<sub>2</sub> (415 ppm) and O<sub>2</sub> (21%).

These calculations result in two new  $\log[K_{eq}]$  values for hydrozincite that are assumed to reflect processes involving amorphous precursors and impurity effects on crystallization. The sample-5 calculation gives  $\log[K_{eq}] = 35.53$ , and the sample-10 location gives  $\log[K_{eq}] = 37.68$ . These values, along with that found in the experiment ( $\log[K_{eq}] = 30.01$ ) represent a range that likely captures the variability in the solubility of hydrozincite at the Victoria Mine. Further, the new values suggest that hydrozincite is less soluble than the experiments predict (i.e. higher  $\log[K_{eq}]$  implies less soluble). The new equilibrium constants are used for the same speciation calculations to determine the new SI values along the flow path to show (Figure 2.22). The effects on mineral precipitation and solute mobility due to the apparent variability in hydrozincite solubility will be explored in chapter 3.

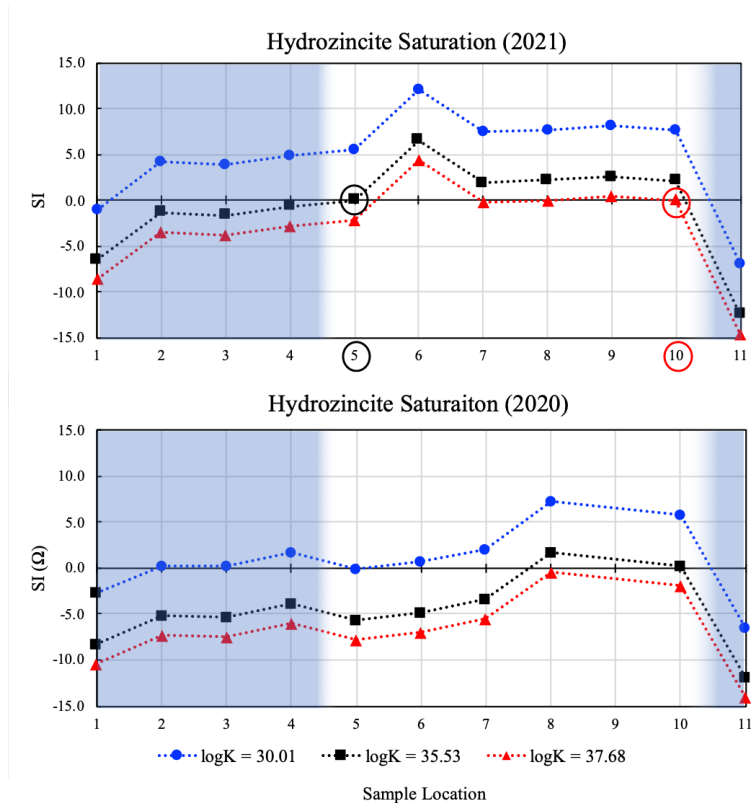


**Figure 2.22.** (top) Calculated SI values of hydrozincite based on 2021 water measurements plotted with respect to sampling locations (x-axis). Each line represents the SI for a given  $\log[K_{eq}]$ . The red circle denotes the location (sample-10) where a new  $\log[K_{eq}]$  was calculated to be 37.68 and corresponds to the red markers/lines. The black circle denotes the location (sample-5) where a new  $\log[K_{eq}]$  was calculated to be 35.53 and corresponds to the black markers/lines. These new  $\log[K_{eq}]$  values are calculated based on the assumption that the water at each sampling location is at equilibrium with respect to hydrozincite ( $SI = 0$ ). (bottom) The SI of hydrozincite based on the 2020 water measurements implementing the new  $\log[K_{eq}]$  values based on the 2021 measurements. Uncertainty is  $\pm 6\%$  for these values due to analytical uncertainty.

#### 2.4.2 Composition of the Mine Water

Characterization of the water through space and time at the Victoria Mine shows that the system has reached a relatively steady state with respect to water composition. This is based on the similarity of the ion concentrations, pH, temperature, and conductivity over the three years in almost all sampling locations (Figures 2.10, 2.11, and 2.12). However, SI calculations exhibit variability. To further validate the measurements made here, a comparison of Zn, Fe, Cd and Ni from Marques *et al.* (2003) shows that (a) these species concentrations are similar (Figures 2.11 and 2.12) and (b) the measurement methods are consistent with each other. In other words, two different measurement methods (EDXRF and ICP) returned similar results.

The sample-9 position (Figures 2.5 and 2.7(C-E)), represents what is assumed to be one of several points where water from the overlying catchment infiltrates into the mine. In the case of the 1330 Gallery, it appears to be one of two principal inputs along with the sample-10 location water input. Water in both locations was always flowing during three years of sampling. This suggests that the water coming from the sample-9 and sample-10 locations is a product of perennial flow, such that there is saturated porous media (i.e. a water table) above the mine acting as a reservoir (Arbel *et al.*, 2010; Druhan *et al.*, 2021; Oster *et al.*, 2021). In this flow regime, water has time to react with the surrounding host rock, resulting in an increase in solute concentrations from the initial input water, which is assumed to come from the creeks above the mine (sample-11). Since the initial water is essentially rainwater, it has few dissolved solids (Figures 2.11 and 2.10, sample-11). Therefore, it has more reactive potential to dissolve minerals as it infiltrates the host rock above the mine galleries. This process is what contributes to the increase in concentration from the upper catchment streams to the mine gallery. Measurements show an increase in sulfate, Ca, Zn, Mg, Ni, Sr and Cd concentrations indicating the dissolution of minerals that contain these elements (e.g. calcite, pyrite and sphalerite).

The Ca, Mg and Sr likely come from dissolving calcite, which is known to exist in abundance at this location (Figure 2.2 and Cardellach and Álvarez-Pérez, 1979). The Zn, Ni and Cd likely come from sphalerite. However, sphalerite is composed of a 1:1 molar ratio of Zn:S, and therefore it would be expected to see the same molar concentration of S, which would be in the form of sulfate because the waters are oxidized. Instead, molar sulfate concentrations are around 10x higher than those of zinc, implying that another sulfide mineral is dissolving. Since, pyrite is known to exist in these deposits, it is assumed to be contributing to the excess of observed sulfate (Figure 2.2 and Cardellach and Álvarez-Pérez, 1979). However, iron concentrations are in the micromolar range and thus do not account for the excess sulfate. This can be explained by the oxidative nature of the water and the pH. Since oxygen is in abundance where the samples are taken, and the pH is between 7.0 and 8.7, the dissolved iron as a product from pyrite dissolution is immediately oxidized to Fe(III), which is not soluble at this pH range. Thus, iron oxides such as ferrihydrite ( $\text{Fe}_2\text{O}_3 \cdot 5\text{H}_2\text{O}$ ) form. Therefore, it can be assumed that much of the sulfate is coming from pyrite dissolution in the host rock.

The dissolved species concentrations are significantly higher at the sample-9 location when compared to any other measured location within the mine. Subsequently, as water flows through the mine, concentrations decrease substantially, where the secondary mineral hydrozincite was observed wherever there was water. For this reason, it is reasonable to conclude that hydrozincite is acting as a sink for Zn, Ni, and Cd, which is most likely a product of sphalerite dissolution. The four hydrozincite morphologies were examined carefully to determine if this was the case and to what extent.

### ***2.4.3 Composition of Hydrozincite***

Results from electron microprobe analysis (Table S4) show that for the smooth layered and nodule samples, the mean total mass recovery is approximately 100%. A mass recovery below 100% indicates that the solid is hydrated (i.e. OH and/or H<sub>2</sub>O groups in the mineral). The floating skin and botryoidal sample have a mean mass recovery of approximately 50% and 75%, respectively. This suggests that the minerals in these samples are hydrated in accordance with hydrozincite. In contrast, the total mass recovery in the nodule and smooth layered samples indicates that the minerals present are not hydrozincite, but rather calcite and smithsonite.

In the white zones of the nodule the ZnO/CaO mass proportion of the nodule is  $46 \pm 16$  (Table S4). In the grey regions, the ZnO/CaO is  $0.04 \pm 0.03$ , indicating that there is more Ca than Zn, which is consistent calcite. The smooth layered sample exhibits a ZnO/CaO molar ratio of  $0.2 \pm 0.3$  (Table S4). Although there is high variability in the ZnO/CaO value, the result indicates that there is more calcium than zinc in the smooth layered sample, again indicating calcite.

Although confirmed by XRD analysis to be hydrozincite, the 100% mass recovery and high calcium content of the smooth layered and nodule samples suggest that both samples are not hydrozincite. The white layers in the nodule contain  $67 \pm 3\%$  ZnO by mass, which suggest that smithsonite is present as it has a theoretical ZnO mass of 65%. The dark layers of the nodule are composed of  $53 \pm 2\%$  CaO by mass, suggesting the presence of calcite, whose Ca mass proportion is 56%. The CaO levels in the smooth layered samples are  $47 \pm 11\%$ , suggesting that the sample is composed of calcite (56% CaO theoretical). Additionally, in both the smooth layered and nodule sample, strontium is incorporated into calcium bearing areas, consistent with the behavior of calcite (Table S4). These electron microprobe results suggest

that the solids are mineralogically heterogeneous, and contain hydrozincite, smithsonite and calcite. This is not in agreement with the XRD results. Although, XRD analysis demonstrates some amorphous material in all solids.

Another possible explanation for the lack of consistency between measurements is that samples for each analysis were selected by their visible morphologies. The assumption was made that each morphology possessed consistent chemical characteristics. As such, a different nodule was used for microprobe analysis, XRD analysis, and total acid digestion. Results suggest that morphology is not necessarily a good indication of chemical composition or crystal phase in the case of hydrozincite. This would be especially true for nodules and smooth layered morphologies found in the mine, as their XRD analyses show only hydrozincite, yet microprobe analyses indicate calcite and smithsonite. Further, microprobe analyses demonstrate elemental heterogeneity in all samples except for the smooth layered sample. This indicates that not all solid samples from the mine are equal, but the botryoidal and floating skin sample are hydrozincite.

Electron microprobe analyses of the botryoidal and floating skin samples demonstrate that there is more nickel than cadmium present, which agrees with the results of the total mineral digestion. Additionally, in several point analyses, there is no cadmium present, yet nickel is present everywhere. This shows that trace metal content is also heterogeneous.

A consistent feature of the white needle structures in the floating skin and botryoidal morphologies is that (a) they have higher ZnO/CaO mass ratios and (b) typically exhibit approximately 100% mass recovery (Table S4). This is especially true when the needles are located on a terminating mineral boundary. Whereas, the adjacent darker regions have significantly lower percent mass recovery (i.e. consistent with hydrozincite) and lower ZnO/CaO mass ratios. Based on this, the needle structures are most likely smithsonite.

There is evidence that calcite, hydrozincite, and smithsonite all form in the Victoria Mine based on SEM and electron microprobe analyses. Further, these three minerals appear to form intermittently, and hydrozincite tends to form with Zn-rich and Zn-poor layers. This is best visualized by the white and grey layers in the botryoidal samples (Figure 2.17(J-L)) and its corresponding elemental scan (Figure 2.18D).

Three years of sampling demonstrate that the flow rate appears to change in the system (section 2.3.2). A change in flow rate can be attributed to a rain event or a dry period. This could serve as one possible explanation for the mineral formation patterns seen in the 1330 Gallery. For example, if flow rate increases through the host rock before the water enters the mine, competing mineral dissolution kinetics (e.g. pyrite, sphalerite, and calcite), could result in water that is more saturated in calcite and/or smithsonite rather than hydrozincite. This change in water residence time will be explored further in Chapter 3.

The changes in Zn content between layers of hydrozincite, which are most pronounced in the botryoidal sample, are likely a result of the *in-situ* conditions during the formation of each individual layer. This could be explained by changes in precipitation rates. Sampling campaigns show some variability in solute concentrations (Figures 2.10, 2.11, 2.12), but it is conceivable that there was more variability that was not captured via sampling during the three campaigns. As conditions change, the rate of precipitation and the extent of impurity incorporation can change as well. The concept and likelihood of precipitation rates affecting mineral purity are discussed below in section 2.4.5.

#### **2.4.4 Metal Mobility**

The total acid digestion of four hydrozincite samples shows that the mineral contains significant amounts of sulfur and calcium (i.e. non-trace amounts). When added together, these two elements make up approximately 1% of the mass in the solid. However, XRD analysis shows the presence of only hydrozincite and no other mineral phase, except for a small amount of brianzincite in the floating skin morphology sample. Additionally, the peaks from these analyses are broad, indicating that some portion of the sample is not crystalline. Considering the lack of crystalline phases, it is reasonable to assume that these hydrozincite samples contain poorly crystalline material, composed of calcium, sulfur and trace metals. It should be noted that natural hydrozincite is often poorly crystalline (De Giudici *et al.*, 2009; Lattanzi *et al.*, 2020).

The mean Cd concentration in hydrozincite determined by acid digestion is  $87 \pm 22$  ppm (Table 2.3, Figure 2.12). In the mine water, Cd starts at approximately 105 ppb at the point source (sample-9 drip water) and decreases to a mean concentration of  $22 \pm 5$  ppb inside of the mine before eventually reaching approximately 1 ppb at the bottom of the catchment (Figure 2.5). Considering this, cadmium is over 800x more concentrated in the solid than in the liquid

by mass. This indicates that hydrozincite is acting as a sink for Cd, but does not appear to completely polish the water of Cd before it leaves the mine.

Nickel enters the mine at approximately 377 ppb (sample-9) and decreases to an average of  $54 \pm 8$  ppb inside the mine (Figure 2.12, Table S1). In the solid hydrozincite, the average Ni concentration is  $479 \pm 35$  ppm (Table 2.3). Nickel is over 1200x more concentrated by mass in the solid than in the liquid, indicating a metal polishing process. In fact, this same argument can be made for other potentially harmful metals found in the solid. For example, lead, arsenic, cobalt, were undetectable in the water, but can be measured in the solid (Table 2.3). Zinc is also being effectively polished by hydrozincite, which is to be expected due to its chemical composition. Zn begins at 150 ppm at it enters the mine (sample-9) and decreases to an average  $13 \pm 7$  ppm inside the mine, before decreasing to below 1 ppm at the bottom of the catchment (Figure 2.5, Figure 2.12, Table S1).

The calculated flux of elements out of the Victoria Mine (Tables 2.2A and 2.2B) show that calcium is the most abundant dissolved element, while alkalinity is around 100 ppm  $\text{HCO}_3^-$  and the pH is between 7.0 and 7.5 at this same location (Figure 2.5, sample-3). In other words, dissolution of calcite in the host rock is buffering the pH of the entire system. Therefore, calcite mineral dissolution is assumed to be the dominant geochemical reaction process taking place. The high magnesium discharge also suggests that there is magnesium-rich calcite present in the host rock. Additionally, the mean Ca/Mg molar ratio at each measurement (i.e. 2019, 2020, 2021) is  $\approx 40:1$  with a 2.5% variability between three years (Figure 2.14). The same molar ratio is reflected in the slopes ( $m$ ) of the two elements (Figure 2.14). This observation indicates that the molar Ca/Mg ratio is held constant independent of discharge, such that there is a direct linear relationship between discharge and mass flux for both elements. This implies that the processes controlling Ca and Mg mobility are fast and are not transport limited with respect to the range of measured discharge rates. Additionally, the persistent molar ratio, regardless of discharge rate, reflects a coupled Ca and Mg release proceeding in lock step, for example, the dissolution of Mg-bearing calcite.

The same behavior for dissolved Zn and Cd can be observed. The molar ratio of Zn/Cd at discharge rates of 37.0 and 40.4 L/min, were 263:1 and 270:1, respectively. Further, in 2021, at a discharge rate was 23.1 L/min, the corresponding Zn/Cd ratio was 245:1. This indicates a



persistent molar ratio between zinc and cadmium is released regardless of discharge rate. In other words, as discharge increases, so does the Zn and Cd flux out of the mine.

The consistent decrease in metal concentrations juxtaposed with the metal content in the solid indicate that the precipitation of hydrozincite is an effective metal polishing mechanism. As such, it is concluded that hydrozincite formation exhibits control on the observed metal attenuation in the Victoria Mine system. This in turn, substantially decreases any environmental impact as a product of anthropogenically enhanced metal-sulfide dissolution.

#### ***2.4.5 Comparison to Literature***

It can be argued that the precipitation of hydrozincite is the dominant control on zinc mobility after dissolved zinc enters the mine. However, since hydrozincite is not a Cd-carbonate (e.g. otavite ( $\text{CdCO}_3$ )), the same control over cadmium mobility would not be initially expected. This would apply to other trace metals as well. In a related study, Podda *et al.* (2000) measured metal uptake into naturally biomineralized hydrozincite samples from the Naracauli River (Sardinia, Italy). The study site at the upper part of the river receives drainage from both mine tailings and an abandoned gallery, which are relics of lead-sulfide and zinc-sulfide mining. The authors measured a significant decrease in metal concentrations along a 600-m transect of the river (see Table 2 in Podda *et al.*, 2000). Along this transect, the pH increased from 6.4 to 7.7, Zn decreased from 348 to 29 ppm, Cd from 3,280 to 420 ppb, Pb from 1,060 to 60 ppb, and Ni from 170 to 140 ppb. Thus, hydrozincite was acting as metal polishing mechanism as dilution was not a significant factor. Considering the 215-m transect in the Victoria Mine from sample-9 drip water to the mine effluent (sample-4) in 2021, pH increased from 7.5 to 7.6, Zn decreased from 155 to 10 ppm, there was no detectable Pb, Cd from 105 to 22 ppb, and Ni from 378 to 45 ppb (Table S1). The initial and change in metal concentrations in the upper Naracauli River is larger than that of the Victoria Mine system.

The natural biomineralized hydrozincite sediments from the Naracauli River were analyzed for metal content via acid digestion similarly to this study (see Table 1 in Podda *et al.*, 2000). The metal concentrations were as follows: Zn (51.9 %), Cd (540 ppm), Pb (6,500 ppm), and Ni (370 ppm). In comparison, the hydrozincite from the Victoria mine exhibited an average of the following concentrations: Zn (54.4 %), Cd (87 ppm), Pb (154 ppm), and Ni (479 ppm) (Table 2.3). Comparison of the solids from each site show that Cd is approximately 6.2x

more concentrated in the Naracauli River solid ( $Cd_{\text{Podda et al., 2012}}/Cd_{\text{Victoria Mine}} = 6.2$ ). In contrast, slightly more Ni is seen in the Victoria Mine solids (1.3x more) than in the Naracauli River solids. One likely explanation for variable trace metal concentrations in the solids is that the waters from each site have different compositions (e.g. different trace metal concentrations). Additionally, the Naracauli River solids are biomineralized.

To make comparisons between the liquid reactants and the solid products (e.g.  $Cd_{(s)}/Cd_{(l)}$ ), the maximum observed solute concentrations at both sites are considered. This refers to the beginning of the Naracauli River transect where concentrations are highest, and at the sample-9 location in the Victoria Mine.

The value of  $Cd_{(s)}/Cd_{(l)}$  (540 ppm/3.28 ppm) at the Naracauli River site is equal to 165. At the Victoria Mine, the value of  $Cd_{(s)}/Cd_{(l)}$  (87 ppm/0.105 ppm, Table S1) is equal to 828. The comparison of these ratios suggests that Cd is preferentially excluded from the solid as dissolved Cd concentrations increase. In other words, the value of  $Cd_{(s)}/Cd_{(l)}$  increases with decreasing dissolved Cd concentrations. Consequently, hydrozincite is less effective at polishing Cd as the dissolved Cd concentrations increase within the range examined here.

In the case for Ni, the value of  $Ni_{(s)}/Ni_{(l)}$  (370 ppm/0.17 ppm) at the Naracauli River site is equal to 2,176. At the Victoria Mine, the  $Ni_{(s)}/Ni_{(l)}$  (479 ppm/0.378 ppm, Table S1) value is equal to 1,267. The values of these ratios show a similar trend to that of Cd uptake. As dissolved Ni increases, Ni is preferentially excluded from the solid. In other words, the value of  $Ni_{(s)}/Ni_{(l)}$  increases with decreasing dissolved Ni concentrations. In conclusion, hydrozincite is less effective at polishing Ni as the dissolved Ni concentrations increase, within the range examined here.

Further comparison between the trace metals in the solids at both sites show that the  $Cd_{(s)}/Cd_{(l)}$  values (e.g. 168 and 828) are smaller than the  $Ni_{(s)}/Ni_{(l)}$  values (e.g. 1,267 and 2,176). The higher values exhibited by the Ni ratios indicate that hydrozincite, regardless of water the composition, uptakes Ni more readily than Cd. In other words, the liquid  $\rightarrow$  solid transition fractionates Ni more than Cd, thereby leaving more Cd than Ni in the liquid, relative to their respective concentrations.

It should be recalled that the water at the Naracauli River site was not of equal composition to that of the Victoria Mine. In comparison, the first sampling location at the Naracauli River transect had over double the Zn concentration, over 31x more dissolved Cd, and approximately 2x less Ni than the Victoria Mine water. Additionally, the pH at this point in the Naracauli River transect was 6.4, while the sample-9 location had a pH of 7.5. And, no dissolved Pb was seen at the Victoria Mine, whereas the Naracauli River had 1,060 ppb dissolved Pb. In general, the Naracauli River is more concentrated, perhaps due to a more acidic pH. Considering these differences in water compositions, the solid-to-liquid proportions for Ni and Cd may be controlled by other *in-situ* conditions aside from the concentration of the metal being incorporated.

#### **2.4.6 Mechanisms Controlling Hydrozincite Composition**

In highly oversaturated solutions, the extent to which impurities are incorporated into the solid is a result of rate at which the solid precipitates (Albon and Dunning, 1961; Davey, 1975; Sears, 1958). In highly oversaturated solutions, Sears (1958) describes a theoretical mechanism in which impurities adsorb to active crystal growth sites, thereby lowering the free energy required to for subsequent nucleation. However, this behavior is impurity specific, such that some impurities will not lower the free energy necessary for subsequent crystal growth, and therefore not be incorporated into the solid. In short, if a crystal is precipitating from a highly supersaturated solution (i.e. a fast rate), it would be more likely to incorporate more impurities as they are "buried" by subsequent atoms attaching to growth sites.

On the other hand, when the solution is slightly supersaturated, impurities can decrease the rate of precipitation via inhibition by adsorption (Albon and Dunning, 1961; Davey, 1975; Meyer, 1984; Sears, 1958; Wasylenski *et al.*, 2005). These precipitation-hindering effects have been quantified for calcite. For instance, Meyer (1984) evaluated the effect on calcite precipitation rates caused by the presence of several organic and inorganic impurities; Cd, Ni, sulfate, and Pb were among the impurities tested in the experiments. In this study, all but one impurity (an enzyme) added to a controlled calcite precipitation reaction (achieved by a constant oversaturation) resulted in slower calcite precipitation rates. In a solution oversaturated with respect to calcite, the authors determined the concentrations of each individual impurity required to reduce the calcite precipitation rate by 50%. This experiment was conducted at 20°C and a constant pH of 8.23. The impurity concentrations necessary for the 50% calcite precipitation rate reduction were 83 ppb lead, 352 ppb Ni, 787 ppb Cd, and 29

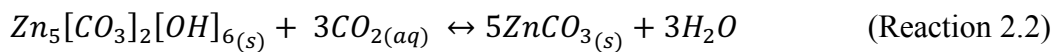
ppm sulfate. This study shows that, in general, when calcite is slightly oversaturated, increasing impurity concentration decreases the rate of calcite precipitation.

These studies illustrate competing mechanisms that could lead to more or less impurities in the solid. Nevertheless, as the rate of crystal growth increases (i.e. increasing oversaturation), the inhibitory effects of impurities are diminished, and those impurities can more readily be incorporated into the solid. This provides a plausible explanation for the heterogeneity and differences in impurity content observed in the hydrozincite in the 1330 Gallery. Calculated SI values for hydrozincite show that the water is highly oversaturated ( $SI < 12$ ), and that these values vary through time and space. For instance, under the mechanism described by Sears (1958), it would be expected that the hydrozincite would contain more impurities if it formed in 2021 than in 2020 because SI values are higher (Figure 2.21).

A possible explanation for the preferential exclusion of Cd in comparison to Ni in hydrozincite, regardless of the conditions in which it forms, is that each element may participate in a distinct incorporation mechanism. For instance, Lattanzi *et al.* (2010) demonstrates that Cd is not incorporated into the hydrozincite crystal structure, but instead bound to the surface of the mineral as an "amorphous surface precipitate". On the other hand, Ni and Zn have the same charge (+2) and similar ionic radii (Ni (149 pm), Zn (142 pm)). It is plausible that Ni is incorporated into the crystal structure of hydrozincite. Although, Cd has a +2 charge, its atomic radius is 162 pm. Therefore, Cd would be less likely to attach to vacant sites in the crystal structure due to steric hinderances. Furthermore, all XRD analyses show broad peaks for hydrozincite, indicating the existence of amorphous material in the sample (Figure 2.15). This is consistent with results from De Giudici *et al.* (2009), who showed that hydrozincite readily exhibits low crystallinity.

#### 2.4.7 Hydrozincite and Smithsonite

There exist two main secondary zinc-carbonate minerals: hydrozincite and smithsonite (Vagvokgui *et al.*, 2008; Hales and Frost, 2008). Further the likelihood of either mineral precipitating depends on the partial pressure of CO<sub>2</sub>, such that when pCO<sub>2</sub> is above 10<sup>-0.141</sup> (72.3%) smithsonite is the thermodynamically favored precipitate (Hales and Frost, 2008; Vágvölgyi *et al.*, 2008). The following reaction describes a transformation between the two minerals:



Considering this reaction is shifted to the right at high CO<sub>2(aq)</sub> concentrations, it is plausible that hydrozincite, once precipitated as a secondary mineral, could be altered via CO<sub>2</sub>-rich water into smithsonite, thus forming a tertiary mineral. However, this could not occur in a system in contact with the atmosphere because this water would degas CO<sub>2</sub> quickly and smithsonite would no longer be thermodynamically stable. Another possibility is that smithsonite is forming on top of hydrozincite intermittently due to a change in pCO<sub>2</sub>. This again, would require an environment not in contact with the atmosphere, such as a saturated porous media. Although CO<sub>2(g)</sub> was not measured in the mine, it can be assumed that CO<sub>2</sub> concentrations are at least that of the atmosphere, which at present are ≈ 415 ppm, according to the Mauna Loa Observatory in Hawaii. Since the water is entering the mine after dissolving carbonate rocks, it contains dissolved CO<sub>2</sub> that will readily degas as it enters the mine, thus increasing CO<sub>2(g)</sub> above 415 ppm. However, it would not reach 72.3% and cause smithsonite formation. This degassing process is ubiquitous in caves, and is also the process by which speleothems form (Fairchild and Baker, 2012).

A study by Sharma *et al.* (2018) successfully synthesized Zn-carbonate needles for fire-retardant fabric application. Results of the synthesized ZnCO<sub>3</sub> nanoneedles are remarkably similar to those seen by these analyses, both in shape and size (Figure 2.23). Figure 2.7(B) shows a blue coloration at the surface of the white precipitate. Since smithsonite readily forms a blue precipitate, it is plausible that this blue coloration seen in the Victoria Mine is smithsonite (Fairchild *et al.*, 2006).

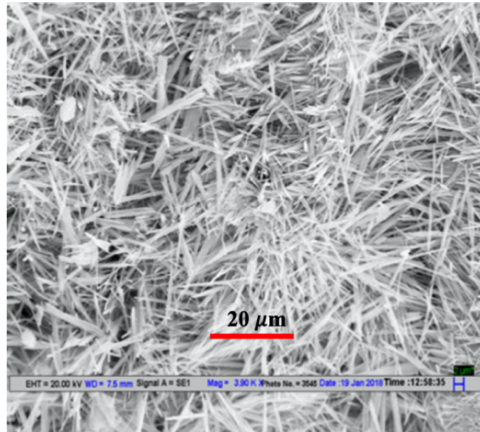


**Figure 2.23.** Secondary electron images of ZnCO<sub>3</sub> needle structures by Sharma et al. (2018). These needles are similar to those exhibited in the floating skin and botryoidal samples. Especially those found on the terminating mineral boundaries (Figure 2.17(H and I)).

## 2.5 Conclusions and Outlook

The geochemistry of the Victoria Mine was characterized with water and solids analyses over a three-year period from 2019 to 2021. The waters exhibit circumneutral to slightly alkaline pH values (7 - 8.7) and high calcium concentrations, suggesting that calcite dissolution is the dominant reaction. Second to carbonate dissolution is most likely the that of pyrite and sphalerite (and possibly other metal-sulfide minerals). The three-year assessment demonstrates that solute concentrations are relatively stable with respect to location, suggesting that the system is at a steady state.

The dissolved solute concentrations are highest when the water enters the mine at the sample-9 location, the dripping/flowing water site that is 280 m from the gallery entrance. The solute concentrations continue to decrease as they flow out of the mine and down the catchment (Figure 2.11 and 2.12). Specifically, dissolved Cd, Ni, and Zn decrease significantly through the system indicating that a natural attenuation process is occurring.

Based on the concentrations of metals found in hydrozincite, the precipitation of this mineral is controlling the attenuation of metals by incorporating them into the solid. This process has been observed in other abandoned mines where hydrozincite typically forms outside of the mine (De Giudici *et al.*, 2017; Lattanzi *et al.*, 2010; Podda *et al.*, 2000; Wanty *et al.*, 2013; Zuddas and Podda, 2005). However, the extent to which hydrozincite can polish Cd and Ni appears to be controlled by the composition of the water from which it forms.

The equilibrium constant of hydrozincite was determined by experiments ( $\log[K_{eq}] = 30.01$ ). This value, along with the measured water compositions, is used to calculate saturation indices of hydrozincite, calcite, and smithsonite (Figure 2.21). Hydrozincite shows variable and high oversaturation through space and time. The variability and magnitude of oversaturation (i.e. high oversaturation) provides one explanation for the variability in impurity content in hydrozincite. It would be expected that as saturation increases, so does impurity content in the solid.

The mineral is abundant in the mine, suggesting that the water would be actively approaching equilibrium with respect to the mineral (i.e.  $SI = 0$ ). Under the assumption that the water is at equilibrium, the water compositions at two sample locations (sample-5 and 10) in 2021 were chosen to calculate two new theoretical  $K_{eq}$  values. The new  $K_{eq}$  values for each

sample locations ( $\log[K_{eq}] = 35.53_{(\text{sample-5})}, 37.68_{(\text{sample-10})}$ ) suggest an apparent variability in the solubility of hydrozincite, which may be due to impurity incorporation, or the formation of amorphous phase with higher solubility (i.e. amorphous precursors). This is consistent with the theory of Ostwald's step rule, wherein more soluble amorphous solids could form before the less-soluble hydrozincite.

Based on solid-to-liquid ratio comparisons between field sites of Cd and Ni (e.g.  $Cd_{(s)}/Cd_{(l)}$ ), it is evident that the two metals are employed distinct mechanism of incorporation into the solid. For instance, Cd can form a "disordered amorphous surface precipitate" as reported by Lattanzi *et al.* (2010). This could be due to the fact that the ionic radius of Cd is significantly larger than that of Zn (12.4% larger), inhibiting its incorporation during crystal growth. This is consistent with the XRD analyses showing broad peaks, which are indicative of amorphous material. Further analyses would be necessary to confirm the existence of the amorphous Cd in these samples. For example, transmission electron microscopy (TEM), could determine if there were crystalline and amorphous regions within hydrozincite samples. In contrast, Ni concentrations in the solid appear to be less sensitive to dissolved Ni concentrations when compared to Cd. In addition to this, the atomic radius and charge of Ni would support incorporation into the hydrozincite crystal structure.

Although XRD analyses indicate that all four morphologies are hydrozincite, electron microprobe analyses indicate that the nodule and smooth layered samples contain smithsonite and calcite (i.e. mass recovery calculations). Further, the electron microprobe analyses demonstrate that these samples are highly heterogenous. The needle-like structures found at the terminating boundaries of hydrozincite do not contain OH groups according to electron microprobe analysis. Additionally, Sharma *et al.* (2018) found that  $ZnCO_3$  can form needles of a similar size to the ones image here (Figure 2.23). The blue coloration found on the surface of white patinas in the mine also support this hypothesis. Since one common feature of the needle structures is a lack of cadmium, the formation of these needles could increase the mobility of cadmium over time.

In conclusion, the potential environmental impact associated with the Victoria Mine is reduced by the precipitation of hydrozincite. It effectively polishes Cd, Ni, and Zn from the waters that enters the 1330 Gallery. However, based on solid comparisons to Podda *et al.* (2000) Cd is preferentially excluded from the solid as dissolved Cd increases. The same trend



is true for Ni. This suggests that the mineral may not be as effective at polishing metals at higher solute concentration, but further testing across a wider range of concentrations would confirm this behavior.

It appears that calcite and smithsonite are intermittently precipitating along with hydrozincite. Additional X-ray microdiffraction techniques could serve to confirm the existence of smithsonite, due to its relatively low amount in all samples. Nonetheless, these phases (e.g. needles) do not typically contain cadmium, which suggests that cadmium mobility is enhanced when smithsonite forms. Further sampling of the mine through time and more detailed analyses of the solids precipitation in the mine would be recommended to better confirm these hypotheses and more accurately predict cadmium mobility over time. Nevertheless, application of the present knowledge to geochemical reactive transport models can assist with such predictions. The quantification of the processes that affect metal mobility can be simulated to further advance this study. This will be discussed in Chapter 3.

## **CHAPTER 3 – MODELING OF THE VICTORIA MINE SYSTEM**

### **3.1 Introduction**

The Aran Valley was the site of large-scale Zn, Pb, Cu, Fe, and Ag mining from the late 19<sup>th</sup> century until approximately 1950. Although mining activities ceased over 70 years ago, some of the abandoned mining relics (e.g. tunnels, processing facilities, and tailings dumps) exhibit elevated concentrations of metals in the associated water systems. Thus, posing a health risk in the neighboring ecosystem. The largest underground Zn mine in the Aran Valley, the Victoria Mine, was chosen as a field site to showcase the processes affecting metal mobility in the environment. This mine is composed of 15 km of tunnel galleries, many of which are flooded today. The galleries are situated beneath a steep mountain slope. Moreover, the lowermost gallery, the Sinçay Gallery, exhibits a continuous output of water, whose composition reflects a flow path through the system.

In this continuous flow path, rainwater is collected in a catchment above the mine, subsequently infiltrates the overlying host rock, flows through the galleries, and eventually exits the mine. This effluent continues down the catchment, where it is diluted by other streams to safe concentrations. Sampling campaigns in 2019, 2020, and 2021 demonstrate that metal concentrations decrease with distance along a continuous 215-m stream on the floor of the 1330 Gallery. For instance, Zn, Cd, and Ni decrease from 155 to 10 ppm, 105 to 22 ppb and 377 to 32 ppb, respectively (Table S1). Hydrozincite was found covering the surface of the rocks in contact with the flowing water in the gallery. Additionally, two sampling locations in the gallery were identified as the principal sources of water for this 215-m flow path. The result of these gallery processes is such that the concentration of dissolved metals that leave the mine are low enough to be diluted to safe levels once the water travels further down the catchment.

### **3.2 Objectives and Model Overview**

Characterization of the secondary minerals found inside the mine demonstrate that hydrozincite incorporates Ni, Cd, Fe, Pb, As, and Co as it forms (Table 2.3). Thus, to some extent, acting as a sink for these metals. To quantify the evolution of solute concentrations and mineral reactions through the Victoria Mine system, a two-stage geochemical reactive transport model (RTM) is constructed based on a relevant set of parameter values (e.g. rock composition, gallery length, input water composition, hydrozincite solubility), and further constrained by ion concentration measurements (Figure 3.1).

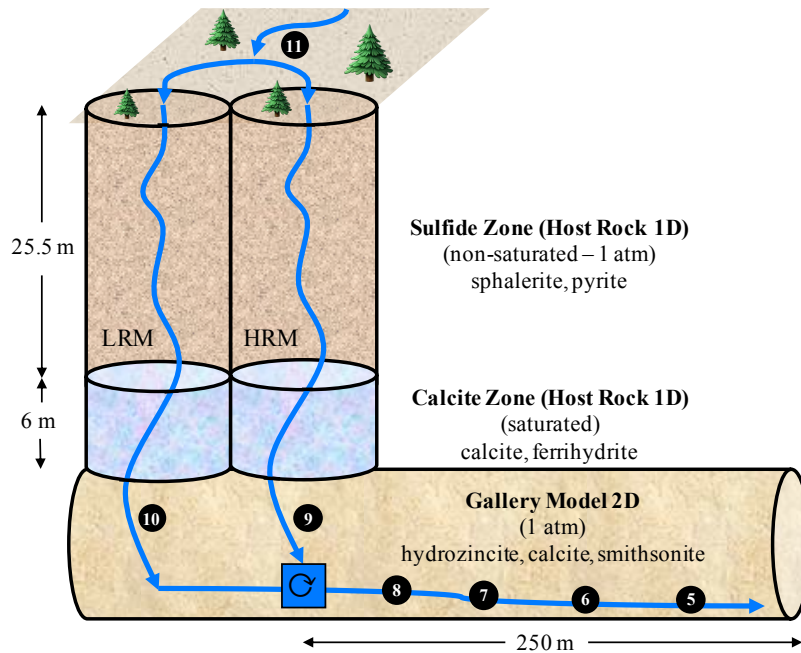


**Figure 3.1.** Conceptual diagram of the host rock and gallery models. The water composition at the end of the calcite zone (31.5 m) from the 1D high reactivity model (HRM) and the 1D low reactivity model (LRM) are used to inform the gallery model. Those two waters are mixed inside of the mixing cell (♻) before flowing down the 250-m domain. The flux/discharge proportion of LRM/HRM = 10. Numbers represent sampling intervals defined in Table 2.1 and the blue arrows denote flow direction.

These two stages are designed to simulate porous media flow through the host rock and surface water flow through the gallery. The RTM is separated into two stages primarily to solve the flow velocity problem that arises when porous media flow becomes surface water flow (i.e. water drips into a cave). The average linear velocity (ALV) of surface flow is typically several orders of magnitude larger than that of porous media flow.

The first stage of the RTM is designed to simulate rainwater infiltration through the overlying host rock along two flow paths. This promotes the dissolution of pyrite ( $\text{FeS}_2$ ), sphalerite ( $\text{ZnS}$ ), and calcite ( $\text{CaCO}_3$ ), the main minerals in the rock, which have been separated into two distinct zones – a "sulfide zone" and a "calcite zone". The decision to implement layered mineral zones will be discussed further in the host rock model setup and parameterization (section 3.4.1). Sampling of the two inlets in the gallery show different chemical compositions. Sample-9 water (drip water) is more highly concentrated with respect to all measured solutes than the sample-10 water (water flowing on the floor). Under the assumption that these two inlet waters originate in Melics and Carné creek (sample-11) and flow the same distance to reach the gallery, sample-9 water would be expected flow through a more reactive domain than sample-10. Bearing this in mind, the "host rock" models consist of two separate domains that simulate high-reactivity and low-reactivity flow paths to reproduce

the compositions of sample-9 and sample-10 water, respectively. From here on, the high-reactivity model is referred to as the "HRM" and the low-reactivity model is referred to as the "LRM", while the aggregate of the two will be referred to as the "host rock models".

These host rock models simulate a 1D flow path beginning in an unsaturated (i.e. 1 atm) pyrite and sphalerite zone (25.5 m long) followed by a saturated calcite zone (6 m long), and terminating in a short gallery zone where the water is allowed to equilibrate with the atmosphere (10 m long). Water flows at a realistic average linear velocity (ALV) of 1.5 m/day. This parameter will be discussed further (section 3.4.1.3). It should be noted that the short gallery zones in the host rock models are implemented only to make initial interpretations of geochemical behavior at this transition zone. More detailed and realistic simulations for the gallery geochemistry are done in the gallery-specific model.

The second stage of the RTM is designed to simulate flow down the 215-meter-long gallery floor – this will be referred to as the "gallery model". The 215 m corresponds to the distance from the sample-9 location to the sample-5 location. This enables comparison of measured concentrations with distance. The total length of the model domain was extended to 250 m to make additional observations. In the gallery model, water flows at a realistic yet slow surface water ALV of 0.48 m/min and is in contact with the atmosphere.

The gallery model is coupled to the host rock models via conservation of concentration. This is done by using the solute concentrations at the end of the calcite zone (31.5 m) in the host rock models as gallery model inputs. In practice, the gallery input composition is calculated by mixing the calcite zone output waters. To mix the two input concentrations from the HRM and LRM, a 2D mesh in the gallery model is constructed (Figure 3.2). This method allows for the adjustment of the 1D Darcy velocities of both the HRM ( $V_{HRM}$ ) and LRM ( $V_{LRM}$ ) into the mixing cell at the beginning of the gallery model domain. In a 3D context, this is comparable to adjusting the total volumetric discharge from each host rock flow path. Although the total volumetric discharge through the gallery domain is unknown, measurement data fitting via modification of the 1D Darcy fluxes from the HRM and LRM can help determine the relative volumetric discharges coming from each input. Once mixed, the water flows down

a 1D domain that is in contact with the atmosphere. Effectively, the gallery model is 1D, but employs a 2D grid to mix the two source waters.

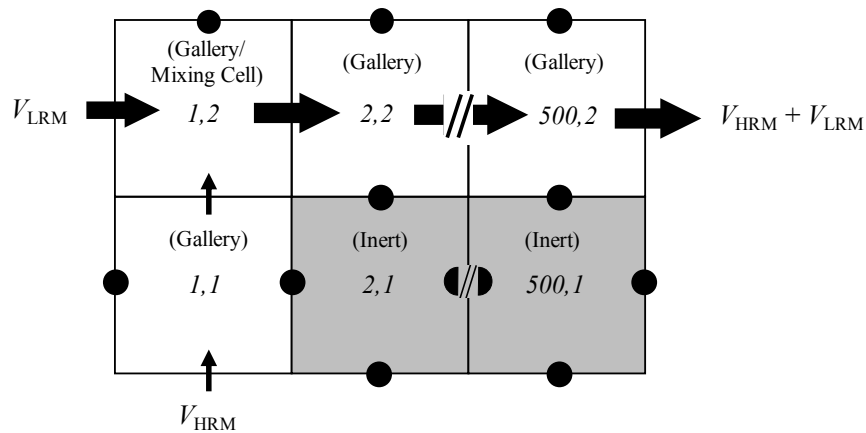


**Figure 3.2.** Sketch of the 2D grid implemented in CrunchFlow to simulate the mixing of the resulting HRM and LRM compositions and subsequent flow down the gallery. Each box is 0.5 m x 0.5 m. The numbers (e.g. 1,2) represent  $x,y$  indices in the 2D mesh. Arrows represent directional Darcy fluxes ( $V$ ) and the arrow size is proportional to the flux. Black circles represent no-flow boundaries. The grey "Inert" cells are composed of non-active minerals and a porosity of 0.001 to ensure no transverse flow.

The first objective of this RTM is to create a reference case where the coupled host rock and gallery models can reproduce the measured solute concentrations at both gallery inlets and along the gallery flow path with distance. Second, the RTM's sensitivity to four parameters will be evaluated in a series of four separate cases:

- Case 1 examines a change in flow velocity through both stages of the RTM.
- Case 2 examines the observed variability in the solubility of hydrozincite (i.e. change in  $K_{eq}$ ). This is applied only to the gallery model.
- Case 3 examines a change in dispersivity in the gallery model.
- Case 4 considers the possibility that the host rock is a homogenous mixture of calcite, pyrite, and sphalerite instead of two distinct mineralogical zones, as presented in the reference model. The non-saturated and saturated zones are maintained such that they reflect that of the reference case.

The detailed model setup and parametrization for these cases will be discussed below in section 3.4. Lastly, an effort to demonstrate the RTM's ability to predict the solute mass flux (mol/day) and discharge relationships (L/min) like those described in section 2.3.2 conclude the examination of the model. The results of each case, excluding case 4, include a flux vs.

discharge comparison. This relationship is accomplished via assignation of an estimated discharge from the gallery (described in further detail below).

An RTM of the Victoria Mine that tests these cases can be used to examine how mineral reaction rates and salute concentrations change through the system. For instance, understanding the extent of hydrozincite precipitation, and the possibility of calcite and smithsonite formation as conditions are perturbed according to the different model cases. This can aid in the quantification of the extent of natural attenuation of metals via secondary mineral precipitation, which serves to assess the environmental risk posed by the mine effluent.

Further, there are several active and abandoned mines in the French and Spanish Pyrenees that target(ed) minerals such as pyrite, galena, and sphalerite for their metals. These mines and mineralizations are often situated in geologic formations that are similar to that of the Victoria Mine. Therefore, the RTM of the Victoria Mine system could be adapted to other similar systems to simulate metal mobility. Such application could assist in strategic reclamation of these related systems, reducing remediation costs and potential environmental risks.

### 3.3 Description of the RTM Code

Geochemical and reactive transport simulations are done using the CrunchFlow software (Steeffel *et al.*, 2015). CrunchFlow is a multicomponent and multidimensional RTM code that can simulate solute transport, mineral reactions (i.e. solid  $\leftrightarrow$  liquid) and aqueous reactions (i.e. liquid  $\leftrightarrow$  liquid) using a thermodynamic and kinetic database. All of this can be done in a through-flowing context typically of porous media. Here, only a few components of the model that are most relevant in the context of this work are described. The numerical model solves the advection-dispersion-reaction equation (ADRE), which is based on the conservation of solute mass (Steeffel and Lasaga, 1992; Steeffel and Lasaga, 1994) and takes the form

$$\frac{\partial}{\partial t}(\phi C_j) = \nabla(\mathbf{D}\nabla C_j) + \nabla(\mathbf{q}C_j) + R_j \quad (j = 1, 2, \dots, N_{tot}) \quad (\text{Equation 3.1})$$

where  $C_j$  is the concentration of a primary species  $j$  in solution ( $\text{mol}/\text{m}^3$ ),  $\mathbf{q}$  is the Darcy velocity ( $\text{m}^3/\text{m}^2/\text{s}$ ),  $\mathbf{D}$  is the combined dispersion-diffusion coefficient ( $\text{m}^2/\text{s}$ ),  $R_j$  is the total reaction rate

(mol/m<sup>3</sup> rock/time) affecting component  $j$ ,  $t$  is time,  $N_{tot}$  is the total number of primary species, and  $\phi$  is porosity.

In the present simulations, the rate laws used for a mineral reaction take the following form:

$$R_m = A_m \sum k_{25} \exp \left[ \frac{E_a}{R} \left( \frac{1}{T_{25}} - \frac{1}{T} \right) \right] \left( \prod_i a_i^{n_i} \right) f_m(\Delta G) \quad (\text{Equation 3.2})$$

where  $R_m$  is the reaction rate (mol/m<sup>3</sup>rock/s) for a given mineral  $m$ ,  $A_m$  is the surface area of the mineral (m<sup>2</sup>/m<sup>3</sup> rock),  $k_{25}$  is the reaction rate constant (mol/m<sup>2</sup>/s) at 25°C,  $\prod_i a_i^{n_i}$  describes the effect of any species  $i$  on the overall rate (i.e. inhibition or catalysis),  $R$  is the gas constant (8.3144 J/mol/K),  $E_a$  is the activation energy (J/mol),  $T$  is temperature (K), and  $f_m(\Delta G)$  is a function that describes the dependence of the rate on the solution saturation state with respect to that mineral. It should be noted that the summation term indicates that  $R_m$  may depend on other parallel rate laws for the reaction. For example,  $R_m$  can depend on the pH and/or the O<sub>2(aq)</sub> concentration. The function  $f_m(\Delta G)$  is described as

$$f_m(\Delta G) = [1 - \exp(m_2 g^{m_3})]^{m_1} \quad (\text{Equation 3.3})$$

where

$$g = \frac{\Delta G}{RT} = \ln \frac{IAP}{K_{eq}} \quad (\text{Equation 3.4})$$

and  $\Delta G$  is the Gibbs free energy of the reaction (J/mol), IAP is the ion activity product of the solution with respect to the mineral and  $K_{eq}$  is the equilibrium constant for that mineral reaction. Equation 3.4 serves to calculate the saturation index (SI = log[IAP/ $K_{eq}$ ]) of the mineral depending on the IAP. The parameters  $m_1$ ,  $m_2$  and  $m_3$  define the shape of the  $f_m(\Delta G)$  function and are determined empirically through experiments. Otherwise, they are assumed to be 1 (Lasaga, 2014).



### **3.4 Model Setup and Parameterization**

#### ***3.4.1 Host Rock Reference Models***

The solute concentrations at the gallery input locations (sample-9 and 10) suggest that the upper catchment water (sample-11) takes at least two different flow paths through the host rock before arriving to the sampling transect to 1330 Gallery (Figures 2.5, 2.11 and 2.12). Considering this, two gallery inlet sources were selected; one source with sample-9 composition and the other with sample-10 composition. Sample-9 water reflects a more reactive flow path through the host rock than sample-10 water because sample-9 water is more highly concentrated.

Since little constraint on the physical parameters of the flow path through the overlying host rock and into the gallery exist (e.g. path length, flow rate, porosity, and detailed mineral composition and distribution), the objective of the host rock models is to compare mineral reactivity between the two conceived flow paths while maintaining realistic physical conditions. To reproduce the sample-9 water composition, a 1D high-reactivity model (HRM) is developed. To reproduce the sample-10 water composition, a 1D low-reactivity model (LRM) is developed.

##### ***3.4.1.1 Flow Path Length***

The length of the flow path is based on the vertical displacement between the 1330 Gallery and the upper streams where samples were taken. This vertical displacement is approximately 100 meters. However, water flows down the steep catchment on the creek beds for 10's of meters before presumably infiltrating the host rock. In reality, the creek water most likely does not infiltrate the host rock at one or two locations, but rather simultaneously flows along the creek bed and infiltrates the rock below. An attempt to quantify the innumerable flow paths along the creek bed where water infiltrates is out of the scope of this study and does not serve to enhance the study as currently presented. Nevertheless, it can be inferred that this surface water begins to infiltrate the host rock at a height less than 100 meters above the 1330 Gallery. It should be noted that in the context of reactivity, changing the path length yields the same results as changing the mineral reactivity (surface area in this case), which is an unknown parameter. Therefore, an accurate length assigned to the flow path is not critical considering the objectives of this exercise for comparing relative mineral reactivities between the LRM and HRM. Further, a fixed flow path length in the host rock model simulations allows for

straightforward comparisons of mineral reaction rates. The total flow path length through the host rock is 31.5 m.

### 3.4.1.2 Mineral Distribution and Reactions

The mineral reactions determined to be most relevant to the system, and therefore implemented into the model include; hydrozincite, smithsonite, calcite, ferrihydrite, pyrite and sphalerite (Table 3.1). Based on previous work (e.g. Álvarez-Pérez *et al.* (1977) and Cardellach *et al.* (1996)) and the measured composition of the water in the mine (e.g. elevated zinc and sulfate concentrations), it is assumed that sphalerite and pyrite are the most abundant/reactive metal-sulfide minerals present. It should be noted that galena (PbS) is known to exist in the Victoria Mine system. However, no significant lead concentrations were found and, therefore, galena is excluded from the model. Pyrite readily dissolves in the presence of oxygen and subsequently lowers the pH due to its dissolution products (Descostes *et al.*, 2004; Palandri and Kharaka, 2004). Two parallel pyrite reaction rate laws are used to account for effects of aqueous oxygen concentrations, Fe(III) concentrations, and pH (Table 3.2). In the case of sphalerite, two parallel sphalerite dissolution rate laws are also implemented. One to describe the normal pH-dependent dissolution (Table 3.2, Acero *et al.*, 2007), and a second "neutral mechanism" to avoid dissolution in alkaline conditions.

**Table 3.1.** Equilibrium constants ( $\log K_{eq}$ ) at 7°C for all mineral reactions. Minerals with \*\* are fake minerals used to maintain a partial pressure of CO<sub>2</sub> and O<sub>2</sub> in non-saturated and gallery domains.

Mineral Name	Mineral Reaction	$\log(K_{eq})$
Hydrozincite	$Zn_5(CO_3)_2(OH)_6 + 8H^+ \Leftrightarrow 5Zn^{++} + 2HCO_3^- + 6H_2O$	30.01, 35.53, 37.68
Smithsonite	$ZnCO_3 + H^+ \Leftrightarrow Zn^{++} + HCO_3^-$	0.793
Sphalerite	$ZnS + 2O_{2(aq)} \Leftrightarrow Zn^{++} + SO_4^{2-}$	136.17
Calcite	$CaCO_3 + H^+ \Leftrightarrow Ca^{++} + HCO_3^-$	2.123
Pyrite	$FeS_2 + 3.5O_{2(aq)} + H_2O \Leftrightarrow Fe^{++} + 2SO_4^{2-} + 2H^+$	233.12
Ferrihydrite	$Fe(OH)_3 + 2H^+ \Leftrightarrow Fe^{++} + 0.25O_{2(aq)} + 2.5H_2O$	-4.678
AtmiteO2**	$O_{2(s)} \Leftrightarrow O_{2(g)}$	-0.678 (21%)
AtmiteCO2**	$CO_{2(s)} \Leftrightarrow CO_{2(g)}$	-3.38 (415 ppm)

**Table 3.2.** Parameters for the mineral reaction rate laws. AtmiteCO2 and AtmiteO2 are fake minerals used to maintain an atmosphere of CO<sub>2(g)</sub> and O<sub>2(g)</sub> in non-saturated and gallery domains.

Mineral	$k_{25}$ (mol/m <sup>2</sup> /sec)	$E_a$ (kcal/mol)	$(a_{H^+})^n$	$(a_{Fe^{+++}})^n$	$(a_{O_2(aq)})^n$	$m_1$	$m_2$	$m_3$	Reference
Calcite	-5.81	5.62	0	0	0	3	1	1	Palandri and Kharaka, 2004; Xu et al., 2012
Calcite	-0.3	3.44	1	0	0	3	1	1	same as above
Sphalerite	-6.49	15	0.54	0	0	1	1	1	Acero et al., 2007
Sphalerite	-9.73	15	0	0	0	1	1	1	Assumed neutral mechanism
Hydrozincite	-6	15	0	0	0	1	1	1	assume local equilibrium (fast kinetics)
Pyrite	-7.52	13.6	-0.5	0.5	0	1	1	1	Palandri and Kharaka, 2004
Pyrite	-4.55	13.6	0	0	0.5	1	1	1	same as above
Smithsonite	-6	15	0	0	0	1	1	1	assume local equilibrium (fast kinetics)
Ferrihydrite	-5	0	0	0	0	1	1	1	assume local equilibrium (fast kinetics)
AtmiteCO2	-5	0	0	0	0	1	1	1	assume local equilibrium (fast kinetics)
AtmiteO2	-5	0	0	0	0	1	1	1	assume local equilibrium (fast kinetics)

Metal-sulfide minerals have been found to coexist in the same geologic formations in the Aran Valley (Álvarez-Pérez *et al.*, 1977; Cardellach & Álvarez-Pérez, 1996; López *et al.*, 1977). Accordingly, sphalerite and pyrite are assumed to coexist in the same formation. This is somewhat consistent with the observed geologic configuration associated with the catchment, where a geological layer of pyrite rich shale can be seen on overlying the Victoria Mine (Figure 2.2). It is conceivable that a stratiform sphalerite deposit also resides in the overlying formation. Since the relative volumetric proportions of sphalerite and pyrite in the system are unknown, their respective proportions were set as equal values to make straightforward comparisons of their reactive surface areas (Table 3.3). It should be noted that iron is not soluble at the observed pH range (pH = 7-8) and readily precipitates as an iron oxide in these conditions (Schwertmann, 1991). To account for this process, ferrihydrite is implemented throughout the entire model domain under a local equilibrium assumption, such that it precipitates very quickly. As a result, only measured sulfate concentrations may be used to determine the extent of pyrite dissolution.

**Table 3.3.** Mineral volume fractions and bulk surface areas (m<sup>2</sup>/m<sup>3</sup> rock) used in all CrunchFlow simulations for the 1D host rock and 2D gallery models. The lower table corresponds only to the homogeneous host rock case, where the 2D gallery model is not considered.

Model:	Host Rock 1D (reference)							Gallery 2D	
Domain:	Sulfide Zone	HRM	LRM	Calcite Zone	HRM/LRM	Gallery Zone	HRM/LRM	Gallery	
Parameter:	vol. frac.	bsa	bsa	vol. frac.	bsa	vol. frac.	bsa	vol.frac	bsa
Hydrozincite	0	0.01	0.01	0	0.01	0	0.01	0	0.1
Smithsonite	0	0.01	0.01	0	0.01	0	0.01	0	0.1
Sphalerite	0.3	400	100	0	0	0.6	0	0.6	0
Calcite	0	0	0	0.6	1.5	0	0.01	0	0.1
Pyrite	0.3	12	4	0	0	0	0	0	0
Ferrihydrite	0	0.01	0.01	0	0.01	0	0.01	0	0.01
AtmiteO2*	0.01	5	5	0.01	0	0.01	5	0.01	5
AtmiteCO2*	0.01	5	5	0.01	0	0.01	5	0.01	5
porosity	0.38	-	-	0.38	-	0.38	-	0.38	-

Model:	Host Rock 1D (homogeneous case)							
Domain:	Sulfide Zone	HRM	LRM	Calcite Zone	HRM	LRM	Gallery Zone	HRM/LRM
Parameter:	vol. frac.	bsa	bsa	vol. frac.	bsa	bsa	vol. frac.	bsa
Hydrozincite	0	0.01	0.01	0	0.01	0.01	0	0.01
Smithsonite	0	0.01	0.01	0	0.01	0.01	0	0.01
Sphalerite	0.25	333.33	83.33	0.25	333.33	83.33	0.6	0
Calcite	0.1	0.25	0.25	0.1	0.25	0.25	0	0.01
Pyrite	0.25	10	3.33	0.25	10	3.33	0	0
Ferrihydrite	0	0.01	0.01	0	0.01	0.01	0	0.01
AtmiteO2*	0.01	5	5	0.01	0	0	0.01	5
AtmiteCO2*	0.01	5	5	0.01	0	0	0.01	5
porosity	0.38	-	-	0.38	-	-	0.38	-

Field measurements show that gallery waters are pH-buffered by bicarbonate (e.g. pH > 7.0 and high alkalinity) and contain dissolved calcium. Given the existence of several limestone formations overlying the gallery (Figure 2.2), it can be reasonably assumed that calcite exists along the host rock flow path. Calcite is added to the model to reproduce these observations. Two parallel calcite reaction rate laws are implemented in the model to account for both acidic and neutral dissolution mechanism as described in Palandri and Kharaka (2004) and Xu *et al.* (2012) (Table 3.2). Further, calcite dissolution increases the pH and thereby inhibits pyrite and sphalerite dissolution. Therefore, calcite was placed after pyrite and sphalerite in a distinct zone.

Kinetic parameters (e.g. rate constants) for hydrozincite and smithsonite have not been previously determined for the conditions at the Victoria Mine. Therefore, like ferrihydrite, they react under the assumption of local equilibrium, such that their reaction rates are generally fast and controlled by their solubility (i.e. Equation 3.3).

The calculated  $\log[K_{eq}]$  of hydrozincite at 7.0°C based on experiments in this study is 30.01 (section 2.3.7). However, using this experimentally derived value, bicarbonate measurements cannot be reproduced in the model. During preliminary calculations using this solubility, bicarbonate concentrations fell to effectively zero in the presence of excess zinc, whereas measured alkalinity values were between 1.4 and 2.8 mM in the gallery. This decrease in bicarbonate was caused by the precipitation of hydrozincite. Since the smithsonite and calcite precipitation are also key to this study, reproducing observed bicarbonate concentrations is critical.

To construct a model that could reproduce measured bicarbonate concentrations, a new  $\log[K_{eq}]$  was selected based on a speciation calculation carried out for the sample-10 location geochemistry (see section 2.4.1). The assumption is that water at the sample-10 location has reacted to equilibrium with respect to hydrozincite. This assumption is based on two observations. First, the water at this location has been flowing along the gallery floor allowing time for mineral reactions to take place. Second, hydrozincite was seen at this location, indicating that the water is likely equilibrating via mineral precipitation. Using the equation,  $SI = \log[IAP/K_{eq}]$ , the apparent  $\log[K_{eq}]$  was calculated in order to satisfy the  $SI = 0$  (i.e. equilibrium with respect to the mineral), such that  $K_{eq} = IAP$ . Accordingly, the new  $\log[K_{eq}]$  of hydrozincite used in the reference models was 37.68 at 7.0°C. Implementing this value as the new  $\log[K_{eq}]$  in the model effectively increased hydrozincite solubility and allowed for more bicarbonate to remain in solution – consistent with the measurements in the gallery. The new  $\log[K_{eq}]$  serves as the reference value for both the host rock and gallery models and results and discussions will be centered around this value.

In the context of mineral distribution in space, natural systems are rarely homogenous. In the 100's of meters of vertical displacement in the Victoria Mine system, the geologic formations are composed of layers of distinct rock types (Figure 2.2). Therefore, the associated flow path was treated as layers of rock rather than a homogeneous porous media. Further, it is essential that waters containing dissolved oxygen reach the pyrite and sphalerite to promote their dissolution. Therefore, the "sulfide zone" is configured as a non-saturated zone closest to the surface, such that atmospheric oxygen is available for the dissolution of these minerals.

The sample-9 and 10 locations were flowing all three years indicating perennial flow. This suggests that there is a reservoir from which this water comes (e.g. a water table). Due to the steep topography ( $\sim 45^\circ$ ), it is assumed that during non-rainy periods, the water table is deep below the surface, such that the phreatic level is not far above the gallery. Thus, the saturated zone is assumed to be thin relative to the total depth of the system. This saturated zone is chosen to coincide with the calcite zone, as oxygen is not required for the dissolution of calcite.

#### 3.4.1.3 Water Flow Velocity

No constraint on the flow velocity, porosity, or water residence time in the host rock is known for the Victoria Mine system. Therefore, an accurate value cannot be implemented and a reasonable value is inferred based on previous studies. Accordingly, both 1D host rock models have the same ALV in order to maintain the same residence time between the two. Vertical flow velocities are most often measured in a karst context, where tracers (e.g. Br<sup>-</sup>, Cl<sup>-</sup>, uranine) are injected at the surface and subsequently captured in the drip water in an underlying cave. Although this vertical drainage flow velocity can vary widely for any system, and even more between systems, one basic assumption made here is that the water coming from sample-9 and 10 locations reflects perennial flow as it was never dry. According to a study by Arbel *et al.* (2010), four different types of drip water infiltrating a 27-m vertical section of rock before entering a cave were identified: post-storm, seasonal, perennial, and overflow. These four drips were assigned ALVs, and the dominant/most frequent flow velocity for perennial flow was  $\sim 5.8$  m/day. Considering this value, the assumption is made that the ALV at the mine is within the same order of magnitude (e.g. 1 - 10 m/day). The reference host rock models are assigned an ALV of 1.5 m/day. This corresponds to Darcy velocity of 0.57 m/day in the model.

### 3.4.1.4 Initial and Input Water Composition

The amending water and initial composition in both the HRM and LRM simulations are adjusted to the sample-11 geochemistry (Table 3.4). This includes 14 primary species and eighty-six secondary species (Table 3.5). These primary and secondary species are incorporated into all simulations in this study. Further, since the upper catchment water is in contact with the atmosphere, the input water is forced to be in equilibrium with atmospheric oxygen and CO<sub>2</sub> before entering the rock. It should be noted that the initial water in the domain is not of critical importance, as is completely washed out of the system as flow proceeds.

**Table 3.4.** Initial and amending water compositions used for all CrunchFlow simulations given in mol/L. These are the pH and total concentrations of the primary species assigned in the input file. The "Sample 10/11" columns reflect the composition of the measured values from the corresponding sampling points. The "HRM/LRM input" labels reflect the composition of the water at the end of the calcite zone (31.5 m) when the host rock model simulations are completed (e.g. 60 days for the reference case).

Condition:	Initial (mol/L)		Input (mol/L)						
	Host Rock 1D	Gallery 2D	Host Rock (ref.)	Gallery (ref.)		Gallery (low flux case)		Gallery (high flux case)	
Model:	Sample 11	Sample 10	Sample 11	HRM input	LRM input	HRM input	LRM input	HRM input	LRM input
pH	7.90	8.00	7.90	6.48	7.18	6.42	7.02	6.47	7.44
Na+	5.07E-05	2.92E-04	5.07E-05	5.07E-05	5.07E-05	5.07E-05	5.07E-05	5.07E-05	5.07E-05
K+	3.07E-05	7.66E-05	3.07E-05	3.07E-05	3.07E-05	3.07E-05	3.07E-05	3.07E-05	3.07E-05
Mg++	3.40E-05	9.21E-04	3.40E-05	3.40E-05	3.40E-05	3.40E-05	3.40E-05	3.40E-05	3.40E-05
Ca++	1.54E-03	5.29E-03	1.54E-03	1.30E-02	5.48E-03	2.47E-02	1.00E-02	6.79E-03	3.01E-03
Zn++	1.80E-07	9.01E-05	1.80E-07	3.61E-03	4.50E-04	9.47E-03	1.29E-03	1.23E-03	9.93E-05
Cd++	1.10E-10	1.70E-07	1.10E-10	1.10E-10	1.10E-10	1.10E-10	1.10E-10	1.10E-10	1.10E-10
Sr++	3.15E-06	1.45E-05	3.15E-06	3.15E-06	3.15E-06	3.15E-06	3.15E-06	3.15E-06	3.15E-06
Fe++	1.43E-07	1.80E-06	1.43E-07	1.57E-07	9.25E-08	1.65E-07	9.84E-08	1.60E-07	8.59E-08
Li+	2.07E-09	1.40E-06	2.07E-09	1.10E-10	1.10E-10	1.10E-10	1.10E-10	1.10E-10	1.10E-10
Ni++	1.12E-07	5.93E-07	1.12E-07	1.12E-07	1.12E-07	1.12E-07	1.12E-07	1.12E-07	1.12E-07
SO4--	2.86E-04	5.71E-03	2.86E-04	1.50E-02	4.60E-03	3.18E-02	9.36E-03	7.03E-03	2.30E-03
SiO2(aq)	1.16E-04	1.22E-04	1.16E-04	1.16E-04	1.16E-04	1.16E-04	1.16E-04	1.16E-04	1.16E-04
HCO3-	2.00E-03	2.10E-03	2.00E-03	4.84E-03	2.44E-03	7.86E-03	4.06E-03	2.64E-03	1.15E-03

**Table 3.5.** The equilibrium constants ( $\log K_{eq}$ ) at 7°C for the equilibria of 86 secondary species in solution. Reactions are written as the destruction of 1 mole of the species using the following the primary species:  $H^+$ ,  $Na^+$ ,  $K^+$ ,  $Mg^{++}$ ,  $Fe^{++}$ ,  $SO_4^{2-}$ ,  $Ca^{++}$ ,  $Zn^{++}$ ,  $Cd^{++}$ ,  $Sr^{++}$ ,  $Ni^{++}$ ,  $SiO_{2(aq)}$ ,  $HCO_3^-$ ,  $O_{2(aq)}$ .

Species	$\log K_{eq}$	Species	$\log K_{eq}$	Species	$\log K_{eq}$
CO2(aq)	-6.49E+00	Cd(OH)4--	4.73E+01	SrCO3(aq)	7.85E+00
CaHCO3+	-1.06E+00	Cd2OH+++	9.39E+00	SrOH+	1.33E+01
CaSO4(aq)	-2.07E+00	CdCO3(aq)	7.33E+00	Zn(OH)2(aq)	1.73E+01
CdHCO3+	-1.50E+00	CdOH+	1.01E+01	Zn(OH)3-	2.88E+01
CdSO4(aq)	-4.03E-03	Fe(OH)2(aq)	2.06E+01	Zn(OH)4--	4.16E+01
FeHCO3+	-2.72E+00	Fe(OH)3-	3.10E+01	ZnCO3(aq)	6.43E+00
FeSO4(aq)	-2.20E+00	Fe(OH)4--	4.60E+01	ZnOH+	9.24E+00
KSO4-	-8.70E-01	FeCO3(aq)	5.60E+00	S2--	2.60E+02
MgHCO3+	-1.05E+00	FeOH+	9.50E+00	S2O4--	1.27E+02
MgSO4(aq)	-2.21E+00	H2SO4(aq)	1.02E+00	S2O6--	5.54E+01
NaHCO3(aq)	-3.09E-01	H2SiO4--	2.30E+01	S2O8--	2.46E+01
NaSO4-	-8.20E-01	H4(H2SiO4)4-	3.59E+01	S3O6--	1.57E+02
NiSO4(aq)	-2.11E+00	H6(H2SiO4)4-	1.36E+01	S4O6--	2.42E+02
SrSO4(aq)	-2.30E+00	HO2-	2.98E+01	Fe(OH)2+	-3.90E+00
ZnHCO3+	1.28E+00	HS2O3-	1.32E+02	Fe(OH)3(aq)	2.43E+00
ZnSO4(aq)	-2.16E+00	HSO4-	-1.78E+00	Fe(OH)4-	1.20E+01
HS-	1.48E+02	HSiO3-	1.02E+01	Fe(SO4)2-	-1.28E+01
S2O3--	1.43E+02	KHSO4(aq)	-5.23E-01	Fe2(OH)2++++	-1.62E+01
CO(aq)	4.48E+01	KOH(aq)	1.45E+01	Fe3(OH)4(5+)	-2.24E+01
Fe+++	-9.57E+00	Mg4(OH)4++++	3.98E+01	FeCO3+	-9.55E+00
H2(aq)	4.92E+01	MgCO3(aq)	7.63E+00	FeOH++	-7.38E+00
HSO5-	1.88E+01	NaCO3-	9.80E+00	FeSO4+	-1.12E+01
SO3--	4.96E+01	NaHSiO3(aq)	8.39E+00	H2S(aq)	1.41E+02
CO3--	1.05E+01	NaOH(aq)	1.54E+01	H2SO3(aq)	4.04E+01
CaCO3(aq)	7.35E+00	Ni(OH)2(aq)	2.00E+01	HSO3-	4.25E+01
CaOH+	1.29E+01	Ni(OH)3-	3.10E+01	S--	1.62E+02
Cd(CO3)2--	1.43E+01	Ni2OH+++	1.07E+01	S2O5--	8.98E+01
Cd(OH)2(aq)	2.03E+01	Ni4(OH)4++++	2.77E+01	SO2(aq)	4.08E+01
Cd(OH)3-	3.33E+01	OH-	1.46E+01		

### 3.4.1.5 Construction of the Host Rock Models

The host rock models consist of a 41.5 m domain and three zones. The first zone is a 25.5 m unsaturated "sulfide zone", which is composed of 500x5.0 cm grid cells and terminates with and additional 50x1.0 cm grid cells. The second zone is a 6-m saturated "calcite zone", which is composed of 100x5.0 cm grid cells and surrounded on both ends by 50x1.0 cm grid cells. Finally, a short 10-m "gallery zone" was implemented in this host rock model as a means to make initial observations of mineral reactions in the gallery before parameterizing the 2D gallery model discussed in the following section. This gallery zone is composed of 50x1 cm grid cells followed by 200x5 cm grid cells. The finer mesh provided at the interface of the zones is advantageous for model functioning because concentrations can change quickly at these interfaces. Another solution to manage this effect is to decrease time stepping, but this



can increase model run times substantially. The water residence time through the host rock model is ~30 days. The runtime of each model is 60 days, such that the system experiences approximately two total volume displacements. The temperature for all simulations was chosen to be 7.0°C based on the temperature of water deep in the gallery (Figure 2.10).

The sulfide zone is composed of 30% pyrite and 30% sphalerite by volume (Table 3.3). The water in this domain is in equilibrium with the atmosphere (415 ppm CO<sub>2</sub> and 21% O<sub>2</sub>), thus simulating an unsaturated zone (i.e. vadose zone). This is accomplished by creating two fake minerals, CO<sub>2(s)</sub> and O<sub>2(s)</sub> that occupy very little volume. The two fake minerals dissolve and precipitate to maintain a constant atmosphere wherever they are present. This promotes sphalerite and pyrite dissolution.

The calcite zone is composed of 60% calcite by volume to maintain porosity and therefore, the ALV between zones. Here, water is not at equilibrium with the atmosphere, thus simulating a water table above the gallery.

In the gallery zone, the smithsonite, hydrozincite, calcite and ferrihydrite are secondary minerals because simulations begin with a 0% volume fraction for all. The geochemistry of an open tunnel incorporates an atmosphere similar to that of earth's surface. Therefore, the same technique used to simulate the non-saturated zone is applied. As mentioned previously, the gallery zone in the host rock models is for preliminary observations because the ALV is unrealistic for surface water. Nonetheless, the effects of CO<sub>2</sub> degassing as water enters the mine can be observed. Notably, water from both sample-10 and 9 locations had some time to equilibrate with the air before sampling. This is especially true for the sample-10 location as it came from a stream on the floor and not directly from a dripping source like sample-9. More detailed modeling efforts towards the gallery geochemistry will be carried out in the gallery-specific model described in the next section.

In the host rock models, the resulting solute concentrations are a function of water residence time and mineral reaction rates. The former is a function of path length and flow rate. As these values are not constrained, there is no merit to altering them between the LRM and HRM. Therefore, their parameter values are held constant in both 1D reference simulations, while only the bulk surface areas (m<sup>2</sup>/m<sup>3</sup>rock) of pyrite and sphalerite are different between the HRM and LRM.

In summary, the HRM and LRM are constructed to quantify the variation in reactivity between two perceived flow paths and reproduce gallery input water concentrations. These flow paths simulate water from the upper catchment infiltrating the host rock, and eventually flowing into the 1330 Gallery where solute concentrations were measured over three years. The flow path is composed of a 25.5 m unsaturated sulfide zone where pyrite and sphalerite exist in equal proportions, yet their reactive surface reactivities vary. This is followed by a 6-m saturated calcite layer, where calcite has a constant reactive surface area between the HRM and LRM. Finally, a short 10-m gallery zone where the water can re-equilibrate with atmospheric oxygen and CO<sub>2</sub> is implemented to make initial interpretations about mineral reactions and solute concentrations. The water residence time is constant between both models, thereby controlling resulting solute concentrations via mineral surface areas. The surface areas in the HRM and LRM are adjusted to reproduce the sample-9 and sample-10 compositions, respectively.

### ***3.4.2 Gallery Reference Model***

A separate gallery model serves to simulate both mixing of host rock input waters and generate a realistic ALV of surface water. One objective of the gallery model is to simulate the relative mineral reaction rates of hydrozincite, smithsonite and calcite along the gallery floor once the two source waters have mixed. In the model, hydrozincite and smithsonite precipitate under local equilibrium, therefore their reaction rates are principally controlled by their respective solubilities and the concentrations of their reactants (Equations 3.3 and 3.4). Considering this, it is necessary to reproduce solute concentrations (e.g. Ca, Zn, and HCO<sub>3</sub>) and pH along the a 215-m interval of the gallery domain. In order to make straightforward comparisons, the reactive surface areas of the minerals are equal (Table 3.3). Comparison of precipitation rates and associated mineral solubilities can demonstrate which minerals are expected to dominate the composition of the solids found in the mine. Observations demonstrate that they are highly heterogeneous.

Mixing two water sources in CrunchFlow requires a 2D domain (Figure 3.2). This allows for the application of a "mixing cell", where waters with distinct chemical compositions can be transported into this cell. From this mixing cell, the water flows down a 1D domain while remaining in equilibrium with the atmosphere (415 ppm CO<sub>2(g)</sub> and 21% O<sub>2(g)</sub>). The domain used in this exercise consists of 500 x 2 grid cells, each measuring 0.5 m x 0.5 m,

resulting in a 250-m flow path. The two rows of 500 cells are stacked, such that y-coordinates are defined by a 1 or 2 ( $x, 1-2$ ) and x-coordinates are defined as 1 to 500 ( $1-500, y$ ). The gallery domain is defined as ( $2, 1-500$ ), which is effectively a 1D matrix stacked on top of another 1D matrix defined as ( $1, 1-500$ ). The gallery domain ( $2, 2-500$ ) is composed of an inert mineral resulting in a porosity of 0.38. Hydrozincite, smithsonite, calcite are the only minerals that exist in the model. All of which are secondary minerals, such that their initial mineral proportion is 0, but they retain a reactive bulk surface area of  $0.1 \text{ m}^2/\text{m}^3$  rock (Table 3.3). This allows the minerals to react although they are not present at the initiation of the simulation. The underlying "ghost domain" ( $1, 2-500$ ) is composed of an inert mineral with porosity of 0.001 (i.e. effectively solid), which diminishes the possibility of transverse flow. However, the first cell in the ghost domain ( $1, 1$ ) has a porosity of 0.38, identical to that of the overlying cells, and contains only an inert mineral. This cell serves as one input.

Darcy velocities ( $V$ ) are defined at the border of each grid cell, such that flow can only occur along the gallery (left to right), and up through the  $1, 1$  cell. In other words, this is a "ghost cell" as it serves only to transport water and solutes into the first cell (i.e. the mixing cell) of the overlying 1D gallery domain. The sum of the two input Darcy velocities into the mixing cell ( $1, 2$ ) must be equal to the output Darcy velocity for the mixing cell and all subsequent cells as all cells are of the same size ( $0.5 \text{ m} \times 0.5 \text{ m}$ ). Further, all transverse flow velocities are set to zero in the model and no flow can be lost to the underlying ghost domain ( $1, 2-500$ ). This ensures mass conservation down the 1D gallery domain. The solute concentrations for each input are informed by the water compositions of the LRM ( $V_{\text{LRM}}$ ) and HRM ( $V_{\text{HRM}}$ ) at the calcite zone-gallery zone interface ( $31.5\text{m}$ ) (Table 3.4). In the case of this model, the 1D Darcy velocity through gallery is a fixed  $11.0 \text{ m/hour}$ , such that  $V_{\text{HRM}} + V_{\text{LRM}} = 11$ . This number was selected to produce a realistic ALV of  $0.48 \text{ m/min}$  while incorporating the 0.38 porosity value (Table 3.3). This was a slow-moving stream upon observations in the field. The relative proportion of the two inputs is adjusted to fit the measurement data. Specifically,  $V_{\text{LRM}}/V_{\text{HRM}}$  is set to a value reproducing sulfate concentrations, as this solute is conserved in the model.

### **3.4.3 Case 1: Flow Velocity**

The nature of an underground mine tunnel implies that the physical conditions are relatively constant through time (e.g. temperature, gas concentrations, input source locations). However, based on the measurements of the mine effluent and adjacent Melics Creek, it is evident that volumetric discharge can change. For instance, the volumetric discharge of the

stream composed of the mine effluent and Melics creek (Figure 2.5) showed different values in 2019 (37.0 L/min), 2020 (40.4 L/min), and 2021 (23.1 L/min) (section 2.3.2). This could be attributed to dry and rainy seasons and rain events. Ultimately, this could affect the volumetric flux through the system, thereby changing the ALVs, and perturbing water residence time.

This is conceptually a 1D model, and therefore simulation of changes in volumetric discharge translates to changes in flow velocities, assuming a fixed flow path (i.e. a tube). A flow velocity of half the reference ALV and a fast flow velocity of twice the reference is tested. The slow flow case referred to as the "low flux" case, and the fast flow case is referred to as the "high flux" case. These two cases are applied to both the host rock and gallery models. In practice, the high flux case doubles the ALV through the host rock models and gallery models. The low flux case halves the ALV through the host rock and gallery models. It should be noted that the goal of this exercise is not to precisely determine the water infiltration rate above the Victoria Mine, but to explore the effects due to different flow velocities. This case generates six new sets of results: Two in the LRM, two in the HRM, and two in the gallery model.

#### **3.4.4 Case 2: Hydrozincite Solubility**

Under the assumption that hydrozincite was precipitating under local equilibrium conditions in the gallery (i.e.  $SI = 0$ ), the  $K_{eq}$  determined by the speciation calculation for the 2021 sample-10 water composition is used for the reference model ( $\log[K_{eq}] = 37.68$ ) (see section 2.3.6). However, the experimental  $\log[K_{eq}]$  and  $\log[K_{eq}]$  based on sample-5 speciation calculations suggest that the apparent  $\log[K_{eq}]$  of hydrozincite shows some variability (see section 2.3.6).

One explanation for the apparent change in solubility is the observation that the hydrozincite found in the Victoria Mine was both highly heterogeneous and contained significant impurities. As impurities can alter the apparent  $K_{eq}$  of a mineral (Druhan *et al.* 2021; Maher *et al.*, 2006), it is reasonable to assume that samples from the mine could exhibit behavior such that the experimentally determined  $K_{eq}$  reflects an impure mineral. Further, the heterogeneous nature of the samples suggests that this effect could be different for distinct samples, where an apparent  $K_{eq}$  would be seen for each different sample.

The  $\log[K_{eq}]$  of hydrozincite based on these experiments (31.12) and the 2021 sample-5 speciation calculation (35.53) are examined in comparison to the reference case (37.68), as this represents a relevant range of hydrozincite solubilities. The apparent hydrozincite solubilities are implemented into the gallery model allowing generating two new sets of results.

### ***3.4.5 Case 3: Dispersivity***

Hydrodynamic dispersion (dispersivity) attempts to account for the effects resulting from variation in the water flow velocity along a flow path (Equation 3.1). This translates to the stretching of the solute curve in the flow direction during advection. The parameter itself is a simplification of the processes at work. Therefore, it is often used as a fitting parameter.

The model sensitivity to changes in dispersivity are examined. A typical value assigned for porous media is a distance equal to 10% the domain length, but the gallery is a surface water and therefore could reasonably differ. As such, the reference case dispersivity is selected to be 1% of the domain length (2.5 m). A high dispersivity case is given a value equal to 10% of the domain length (25 m), and a low dispersivity case is given a value equal to 0.1% of the domain length (0.25 m).

Since no data exists along the host rock flow path to constrain the shape of the solute concentration curve, this case will not be applied to the host rock models. Instead, the three dispersivity values will be compared only in the gallery model domain, where concentrations with distance were constrained with measurements. This case generates two sets of new results in the gallery model.

### ***3.4.6 Case 4: Homogeneous Host Rock***

Previous geological mapping shows that distinct rock formations exist above the Victoria Mine (Figure 2.2). However, little is known about the physical distribution of minerals along the flow path(s) taken by waters that infiltrate the mine. When mineral distribution in porous media is unknown, it is often assumed to be homogeneous. Generally, this would be considered the most basic assumption. Comparing a homogeneous case to the layered reference case can give insight towards the real mineral distribution that exists in the host rock at the Victoria Mine.

In this case, the assumption remains that there are non-saturated and saturated zones above the mine. Therefore, the two zones defined in the reference case will be maintained, such that the first 25.5 m is non-saturated porous media, while the remaining 6 m is saturated porous media. The gallery zone is not altered in any way, as it does not contain any initial volume of reactive minerals.

The fundamental modification is such that the total volume fraction and reactive surface area of pyrite, calcite, and sphalerite in the reference case are mixed uniformly across the 31.5 m domain. Specifically, the total surface reactivity ( $m^2/m^3$  rock) assigned to each mineral in the LRM and the HRM is conserved in the homogeneous case of each model (Table 3.3). Further, the flow and initial and input conditions are identical to that of the reference case (Table 3.4). This case results in two new sets of results; the mixed HRM and the mixed LRM.

#### ***3.4.7 Solute Mass Flux and Discharge***

An important goal of this modeling study is to quantify solute mass flux out of the gallery based on the various conditions imposed on the system, and compare the solute flux vs. discharge relationships to those measured outside of the mine (section 2.3.2). This translates to understanding the metal mobility through the Victoria Mine. Although this is a 1D model, the concentrations at the end of the gallery model in all cases can be multiplied by an estimated volumetric discharge to produce a solute mass flux.

The only data that exists to support a realistic estimation for the gallery discharge rate are the discharge measurements described in section 2.3.2, which constitute a combined discharge from the mine effluent and the adjacent Melics Creek. Using this data, two assumptions must be made to assign a reference discharge to the gallery: (1) the mine effluent and Melics Creek discharges are equivalent and (2) the mine effluent discharge is equal to that of the 1330 Gallery discharge. The minimum measured discharge was 23.1 L/min in 2021 and the maximum was 40.4 L/min, therefore the average is 31.75 L/min. Based on the assumptions, the assigned gallery discharge is 15.9 L/min. This value is changed only in the flow velocity test (case 1), in which the discharge is 31.8 L/min and 7.95 L/min in the high and low flux cases, respectively.

### 3.5 Simulation Results and Discussion

#### 3.5.1 Host Rock Reference Model Results

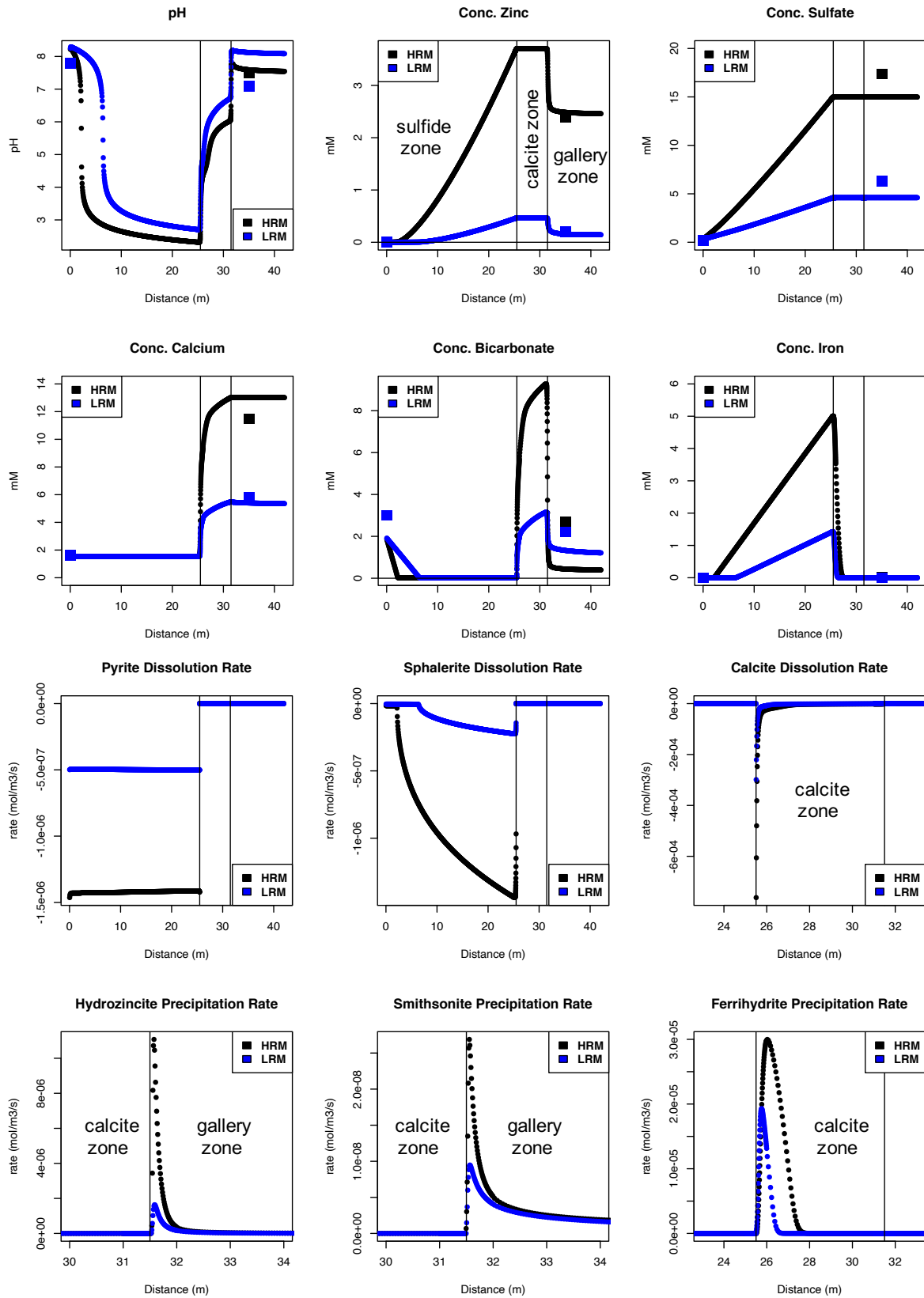
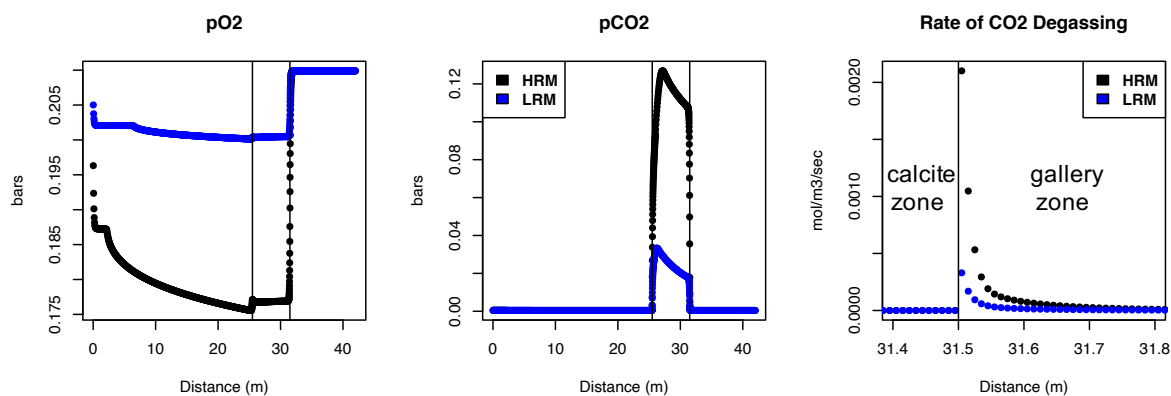


Figure 3.3. See following page for caption.



**Figure 3.3.** CrunchFlow simulation results of the host rock reference case. Flow goes from left to right with an ALV of 1.5 m/day. The high reactivity model (HRM) and low reactivity model (LRM) are plotted as a function of distance at  $t = 60$  days, where the residence time of the system is 30 days. The vertical lines divide the three zones as described in the "Conc. Zinc" plot. The non-saturated sulfide zone exists from 0 to 25.5 m, the saturated calcite zone exists from 25.5 m to 31.5 m, and the gallery zone exists from 31.5 m to 41.5 m. This is the same for all host rock models. measured sample 9 and 10 water compositions are plotted at 35 m with black and blue squares, respectively. The sample 11 data are plotted at 0 m. The plots for calcite, hydrozincite, smithsonite, and CO<sub>2</sub> degassing rates have been scaled on the x-axis to more clearly visualize the model behavior. These five rates remain at zero outside of the visible range.

The results of the LRM and HRM (Figure 3.3) are produced by altering the bulk surface areas assigned to pyrite and sphalerite (Table 3.3), while all other parameters remained constant. Model fitting for the LRM is accomplished with a bulk surface area of 4.0 and 100.0 m<sup>2</sup>/m<sup>3</sup>rock for pyrite and sphalerite, respectively. Model fitting for the HRM is accomplished by assigning a bulk surface area of 12.0 and 400.0 m<sup>2</sup>/m<sup>3</sup>rock for pyrite and sphalerite, respectively. The pyrite in the HRM is 3 times more reactive than that of the LRM, and the sphalerite in the HRM is 4 times more reactive than that of the LRM. Notably, calcite reactivity is not altered (1.5 m<sup>2</sup>/m<sup>3</sup>rock, Table 3.3) and the calculated calcium concentrations are consistent with measured values.

In general, pH, zinc, sulfate, bicarbonate, and total iron concentrations measured in the field are reproduced by the model. Specifically, the LRM reproduced solute concentrations that correspond to those of sample-10, while the HRM reproduced solute concentrations that correspond to those of sample-9. Further, the results from the LRM and HRM follow the same patterns, and differ only in that the mineral reactions are faster in HRM.

Each model displays a distinct yet constant pyrite dissolution rate despite the large changes in pH and iron concentrations. The constant rates indicate that oxidative dissolution of pyrite ( $k_{25} = 10^{-4.55}$ , Table 3.2) dominates the overall dissolution rate of pyrite, while the pH-



dependent rate law ( $k_{25} = 10^{-7.52}$  mol/m<sup>2</sup>/sec, Table 3.2) plays a minor role. The rate of oxygen consumption due to the reaction can be visualized in the pO<sub>2</sub> plot. This is because and oxygen gas in the model is supplied by a false mineral (O<sub>2(s)</sub>) that attempts to maintain a constant 21% oxygen gas in the system using a kinetic rate law ("AtmiteO2", Table 3.2). Considering this, the deviation from 21% pO<sub>2</sub> can be interpreted as oxygen consumption, where the magnitude of this deviation is proportional to the rate of consumption.

In the case for sphalerite, the acidic dissolution mechanism ( $k_{25} = 10^{-6.49}$  mol/m<sup>2</sup>/sec, Table 3.2) dominates over the neutral mechanism ( $k_{25} = 10^{-9.73}$  mol/m<sup>2</sup>/sec, Table 3.2). This explains the increasing dissolution rate with distance for sphalerite. As the pH decreases, due to the dissolution of pyrite, the acidic dissolution mechanism for sphalerite takes over, thereby increasing the overall rate. This also explains the non-linear oxygen consumption curve. The total deviation from 21% pO<sub>2</sub> is due to both sphalerite and pyrite dissolution, but sphalerite dissolution consumes more oxygen as pH increases, causing the non-linearity of the curve.

In both models, the acidic waters from the sulfide zone enter the calcite zone causing calcite to dissolve rapidly in accordance with the acidic mechanism ( $k_{25} = 10^{-0.3}$  mol/m<sup>2</sup>/sec, Table 3.2). The carbonate product serves to neutralize the acid while simultaneously increasing the pH. Once the pH increases above  $\approx 5$ , the rate of calcite dissolution slows as the neutral/slower dissolution mechanism ( $k_{25} = 10^{-5.81}$  mol/m<sup>2</sup>/sec, Table 3.2) becomes more relevant as the water equilibrates with calcite. This can be observed by the change in the shape of the pH curve, where the pH increases rapidly (steep curve) until pH  $\approx 5$ , and then increases more slowly until the water reaches the gallery zone. Ferrihydrite begins to precipitate rapidly once the water enters the saturated calcite zone because the pH increases and there is dissolved iron in solution. The rate of ferrihydrite formation subsequently falls to zero because iron is consumed.

The pCO<sub>2</sub> plot can be interpreted in similar fashion as the pO<sub>2</sub> because the gas is supplied by a fake mineral (CO<sub>2(s)</sub>, "AtmiteCO2"). In the sulfide zone and the gallery zone, this "mineral" can precipitate or dissolve to maintain a constant 415 ppm CO<sub>2(g)</sub>, which is why it is constant in non-saturated domains. In the calcite zone, no atmosphere-maintaining minerals exist. Here pO<sub>2</sub> does not change because there are no oxygen consuming reactions occurring. In the case for pCO<sub>2</sub>, high partial pressures indicate a solution that is highly saturated in CO<sub>2(aq)</sub>.

This is confirmed by the bicarbonate concentrations through the calcite zone, showing a solution highly saturated with respect to bicarbonate.

The gallery zone marks a transition from a saturated zone to a non-saturated zone where an O<sub>2</sub>/CO<sub>2</sub> atmosphere is imposed. This simulates water oversaturated in CO<sub>2</sub> entering the open gallery. This process can be observed via the rapid rate of CO<sub>2</sub> degassing, which is analogous to the water re-equilibrating with the atmosphere. This effect is the cause for precipitation of hydrozincite and smithsonite. A small amount of calcite precipitates as well, but the rate is slow compared to hydrozincite. Therefore, hydrozincite consumes bicarbonate before any significant calcite can form. This explains the "flat" calcium concentration curve in the gallery. One initial observation in the gallery zone is that the rate of hydrozincite precipitation is approximately 100x faster than that of smithsonite. However, this is further discussed in the next section in the gallery model.

The precipitation of these two carbonate minerals is controlling the zinc and bicarbonate concentrations in the gallery zone. Though hydrozincite precipitation is the dominant control because it has a faster rate. Therefore, the resulting bicarbonate and zinc concentrations reflect the solubility of hydrozincite. This is the result of the local equilibrium assumption, such that precipitation rate is controlled primarily by the solubility (i.e. oversaturation) of the mineral, rather than kinetic parameters. Based on the rates of hydrozincite and smithsonite precipitation, it appears that hydrozincite reaches equilibrium with respect to the water faster than smithsonite because smithsonite continues precipitating further down the gallery zone.

### ***3.5.2 Gallery Reference Model Results***

The results of the gallery reference model (Figures 3.4 and 3.5) were produced by a mixing the LRM and HRM water compositions at the end of the calcite zone (Table 3.4) at a proportion of 10:1, such that  $V_{LRM}/V_{HRM} = 10$ . In a 3D context, this implies that the volumetric discharge of the LRM is 10-times greater than that of the HRM into the gallery. This proportion was principally determined based on the assumption that sulfate is conserved through the gallery. In other words, mixing and dilution are the only processes that can affect its concentration, not reaction. In general, the measured concentrations of bicarbonate, zinc, calcium, sulfate, and pH were reproduced by the model. Although, bicarbonate measurements are slightly higher than what the model predicts. The measured values plotted in these figures

correspond to real distances along the gallery. Samples 8, 7, 6, and 5 correspond to 90, 120, 140, and 215 m from the sample-9 (drip water) location, respectively.

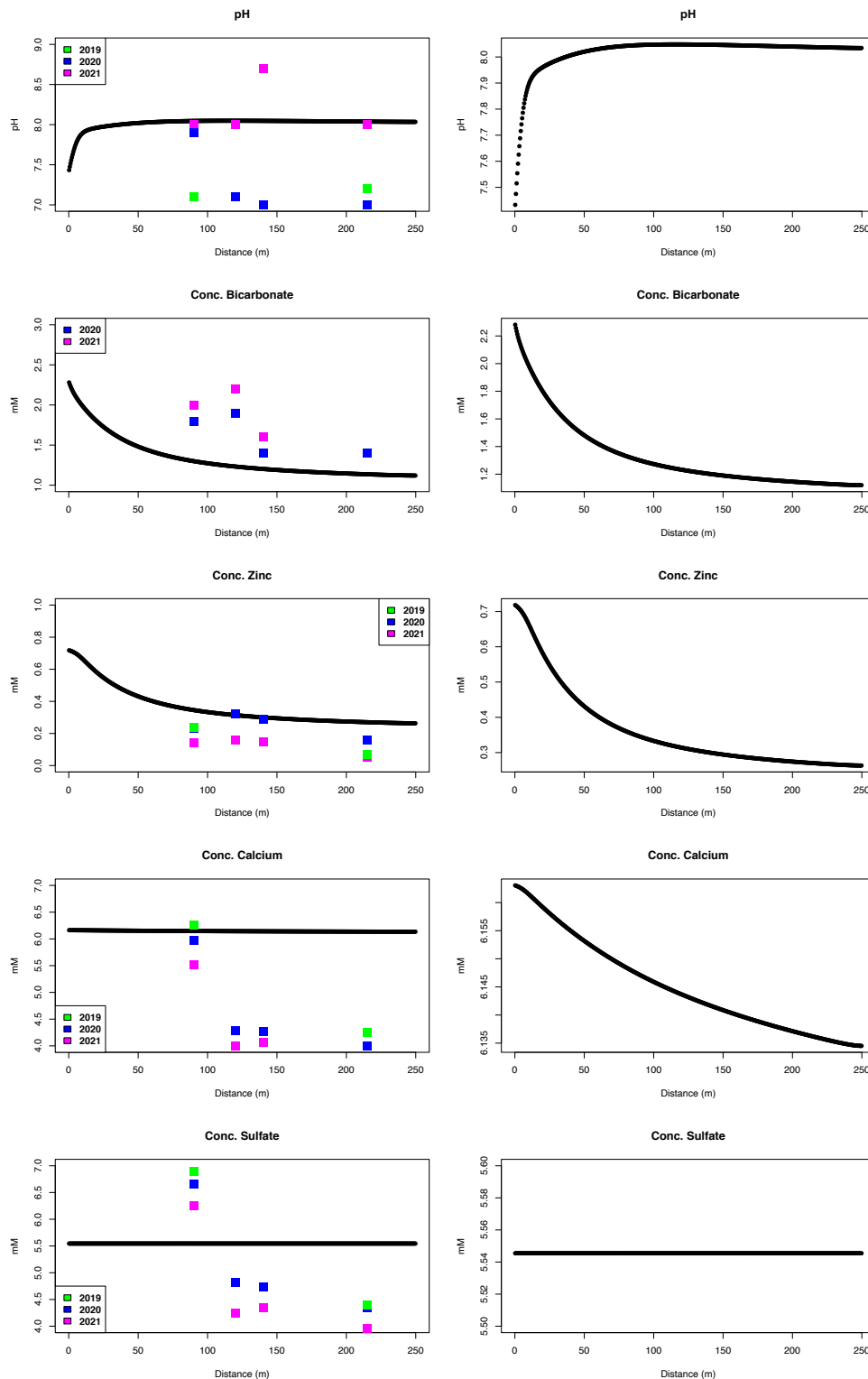


**Figure 3.4.** CrunchFlow simulation results for the gallery model reference case plotted as a function of distance at  $t = 5$  days. Flow goes from left to right at an  $ALV = 0.48$  m/min. (right) Simulation results showing data plotted from three years of sampling. (left) The same simulation results scaled to more clearly show model behavior.

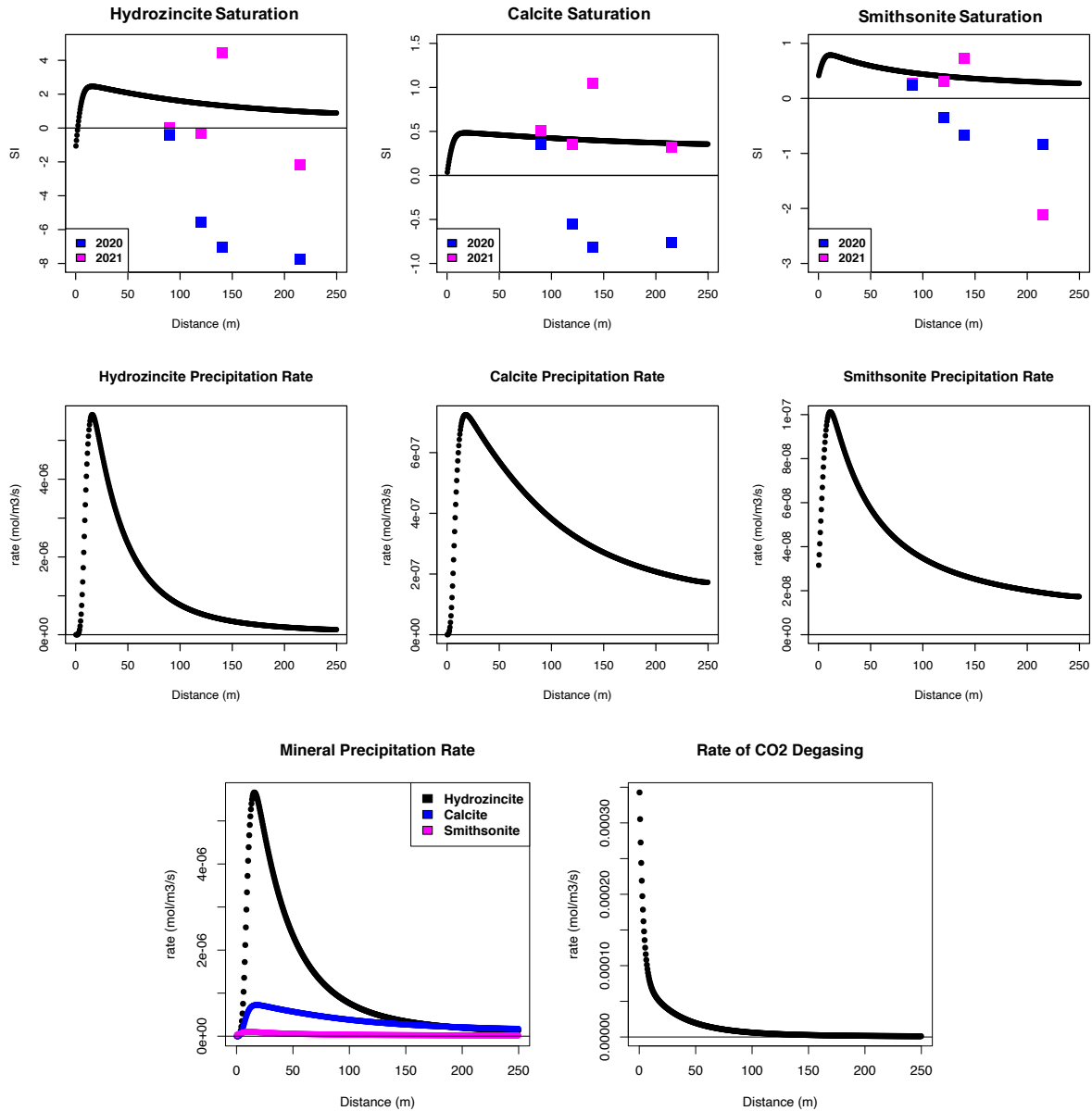


**Figure 3.5.** CrunchFlow simulation results for the gallery model reference case plotted as a function of distance at  $t = 5$  days. Flow goes from left to right with an ALV = 0.48 m/min resulting in a water residence time of 8.7 hours. The calculated SI values from the 2020 and 2021 water measurements are done using a  $\log(K_{eq}) = 37.68$  for hydrozincite and plotted on the solubility diagrams.

The measured calcium and sulfate concentrations decrease in a similar fashion after  $\sim 100$  m and remain fairly constant after the initial decrease. The model does not reproduce this behavior because no sulfate mechanism is considered, and calcite precipitation is slow and contributes to a  $\sim 0.02$  mM decrease across the gallery domain. Gypsum ( $\text{CaSO}_4 \cdot 2\text{H}_2\text{O}$ ) was considered in the model and showed that it was always highly undersaturated, and therefore would not precipitate inside of the Victoria Mine. This consistent decrease of calcium and sulfate the sample-8 location suggests dilution and/or mixing with another water beyond this point.

The calculated SI values for hydrozincite, calcite, and smithsonite generally show a decrease with distance (Figure 3.5). The model reproduces this behavior. This is due to the precipitation of all three minerals, forcing the water closer to equilibrium. In these simulations, hydrozincite precipitation controls the concentrations of zinc and bicarbonate as it precipitates approximately 10 times faster than calcite, and almost 20 times faster than smithsonite. The "Mineral Precipitation Rate" plot (Figure 3.5) illustrates these three rates relative to one another. This is consistent with the analyses of solid samples from the mine, which were composed almost exclusively of hydrozincite. Further, hydrozincite and smithsonite share the same rate constants and bulk surface areas ( $k_{25} = 10^{-6}$  mol/m<sup>2</sup>/sec, Table 3.2 and  $bsa = 0.01$  m<sup>2</sup>/m<sup>3</sup>, Table 3.3). This further illustrates that their relative rates in the model are determined by solubility according to equations 3.3 and 3.4 (i.e. local equilibrium assumption).

The model most accurately reproduces the saturation state of all three minerals in 2021. However, the model does not predict negative SI values, which are apparent in both 2020 and 2021. Further, the SI values calculated from measurements typically result in negative values after 100 m. This is especially true in 2020, as SI values for all minerals are typically lower for that year.

The mechanism for the precipitation of these carbonate minerals relies on the degassing of the water as it enters the gallery. Prior to this transition (i.e. saturated porous flow → drip/surface water), water is highly saturated with respect to CO<sub>2</sub>. Thus, it has a lower pH ( $pH_{LRM} = 7.18$  and  $pH_{HRM} = 6.48$ , Table 3.4). As the water enters the open tunnel and CO<sub>2</sub> degasses, the pH increases rapidly (Figure 3.4), thus decreasing the carbonate mineral solubility and forcing precipitation.

The rate of CO<sub>2</sub> degassing approaches zero and the pH stabilizes at about 100 m, implying that these processes are coupled. This is a confirmation of proper model functioning. The distance over which this process occurs is a result of the flow velocity and rate parameters assigned to the to the CO<sub>2(s)</sub> "mineral" ( $k_{25} = 10^{-5}$  mol/m<sup>2</sup>/sec,  $bsa = 5.0$  m<sup>2</sup>/m<sup>3</sup> rock, Tables 3.2 and 3.6). The mineral will precipitate to maintain an aqueous CO<sub>2</sub> concentration that reflects equilibrium with the atmosphere. These rate parameters generally reflect a fast rate, increasing the overall rate by modifying them would result in the degassing to occur over a shorter distance assuming the same flow velocity.

### 3.5.3 Case 1 Results: Flow Velocity

#### 3.5.3.1 Host Rock Model Sensitivity

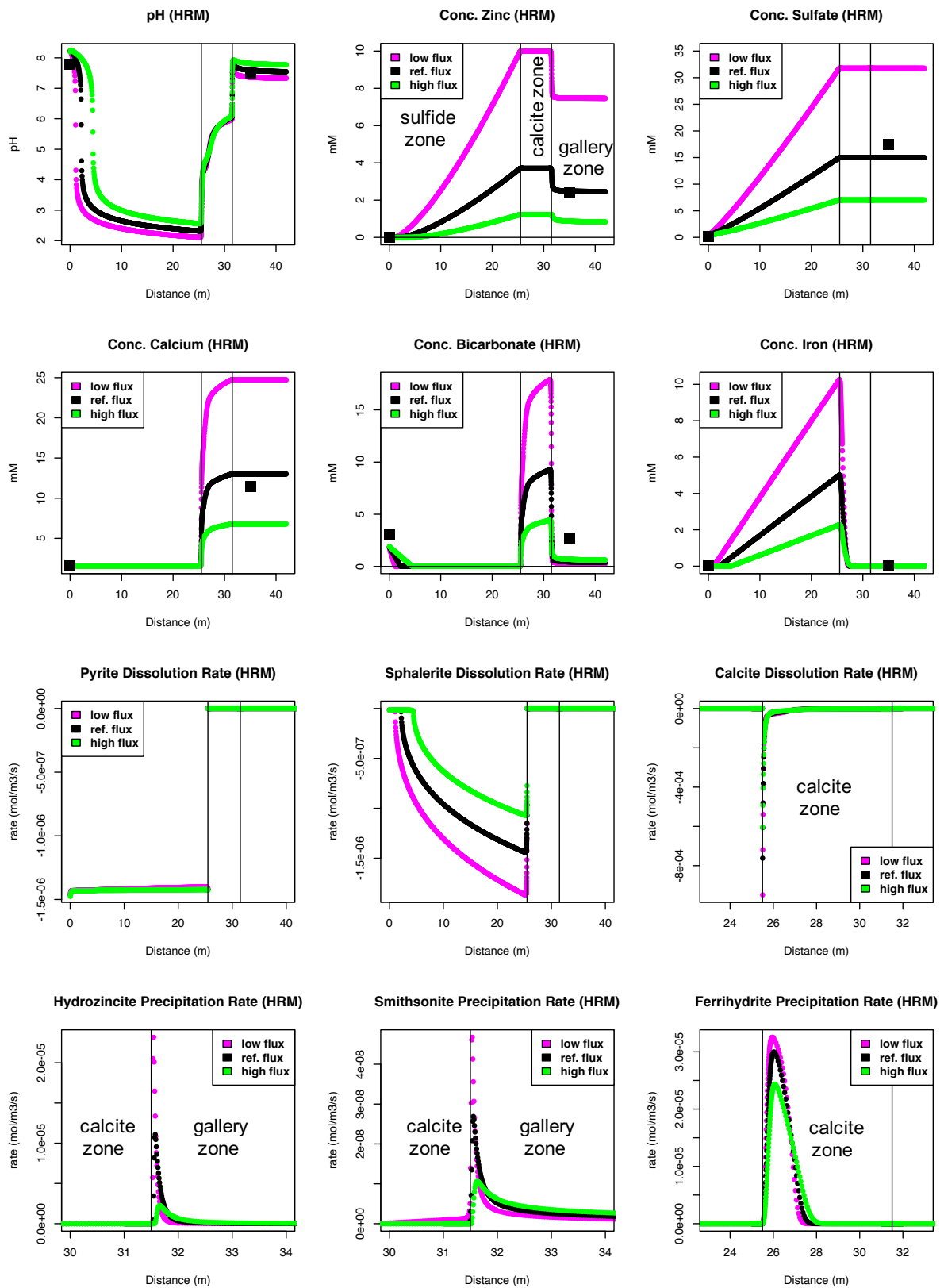
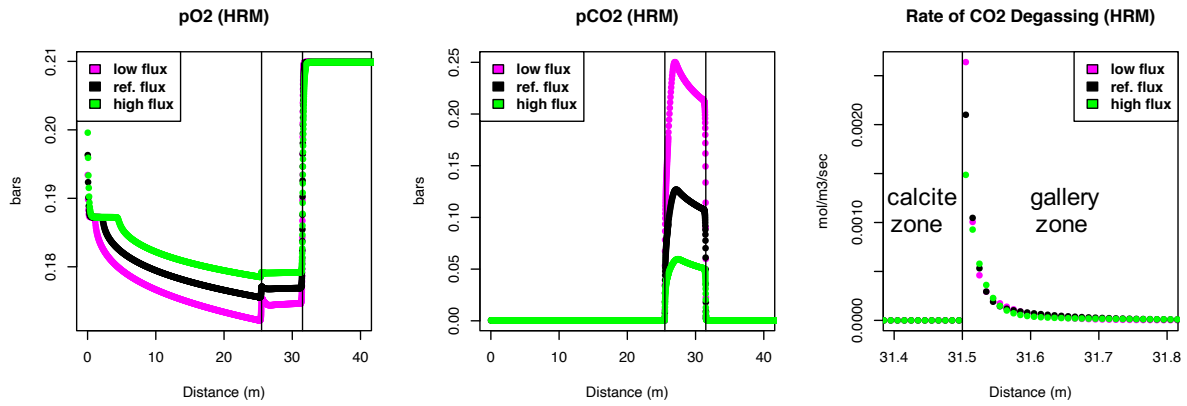


Figure 3.6. See following page for caption.



**Figure 3.6.** High reactivity model (HRM) simulation results for the high flux case and low flux case. Flow goes from left to right at 0.75 and 3.0 m/day for the low and high flux case, respectively. The HRM reference case is also plotted and corresponds to the HRM results (blue) in Figure 25. In the high flux case, results are plotted as function of distance at  $t = 30$  days, where the residence time for the model is 15 days. The low flux results are plotted as a function of distance a  $t = 120$  days, where the residence time for the model is 60 days. The sample 11 data are plotted at 0 meters and the sample 9 data is plotted at 35 m as black squares. The plots for calcite, hydrozincite, smithsonite, and  $\text{CO}_2$  degassing rates have been scaled on the x-axis to more clearly visualize the model behavior. These five rates remain at zero outside of the visible range, except for smithsonite, which is slightly above zero ( $\sim 5.0 \times 10^{-9}$  mol/m<sup>3</sup>/sec).

The ALV through the host rock models is doubled (3.0 m/day, "high flux" case) and halved (0.75 m/day, "low flux" case) with respect to the reference case generating two new results in the HRM (Figure 3.6) and the LRM (Figure 3.7). For each flow velocity case, the concentrations at the calcite-gallery interface (31.5 m) are used as the two input water concentrations for the gallery model. Similar to the reference case, the input concentrations are mixed such that  $V_{LRM}/V_{HRM} = 10$ . However, the 1D Darcy velocities are doubled and halved for the high and low flux cases, respectively. This results in an ALV in the gallery of 0.24 m/min (residence time = 17.4 hours) and 0.96 m/min (residence time 4.3 hours) in the low and high flux cases, respectively. This is consistent with the assumption that increasing the volumetric flux also increases the ALV in the gallery stream. Further, this method serves to couple the host rock and gallery models allowing the comparison of the solute mass flux and volumetric discharge relationships discussed in section 3.5.7.

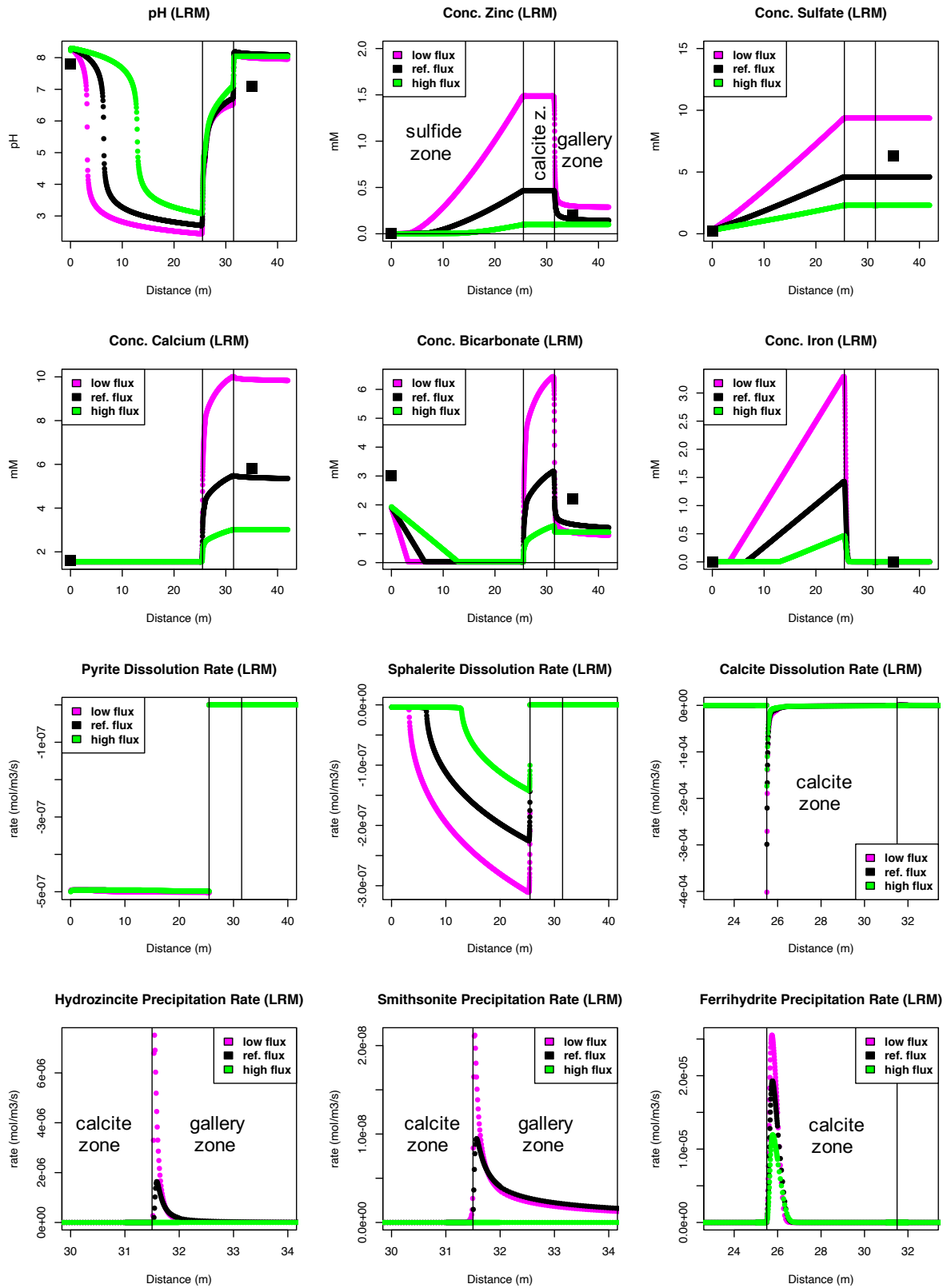
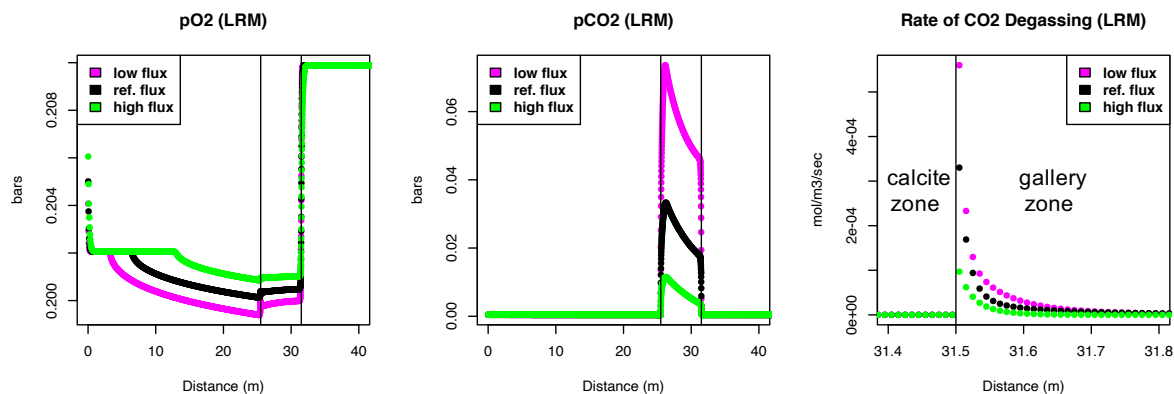


Figure 3.7. See following page for caption





**Figure 3.7.** Low reactivity model (LRM) simulation results for the high flux case and low flux case. Flow goes from left to right at 0.75 and 3.0 m/day for the low and high flux case, respectively. The LRM reference case is also plotted and corresponds to the LRM results (black) in Figure 25. In the high flux case, results are plotted as function of distance at  $t = 30$  days, where the residence time for the model is 15 days. The low flux results are plotted as a function of distance at  $t = 120$  days, where the residence time for the model is 60 days. The sample 11 data are plotted at 0 meters and the sample 10 data is plotted at 35 m as black squares. The plots for calcite, hydrozincite, smithsonite, and CO<sub>2</sub> degassing rates have been scaled on the x-axis to more clearly visualize the model behavior. These five rates remain at zero outside of the visible range, except for smithsonite, which is slightly above zero ( $\sim 5.0e-09$  mol/m<sup>3</sup>/sec).

In both the LRM and the HRM, the pyrite dissolution rate remains constant regardless of the flow velocity. This indicates that at these flow velocities, the oxidative dissolution mechanism exhibits most of the control the overall rate. However, even though the dissolution rate is constant in each model, the high flux cases produce lower sulfate and iron concentrations, while the low flux cases produces higher sulfate and iron concentrations when compared to the reference cases. This is a textbook demonstration of the relationship between water residence time and solute concentration resulting from a reaction. Although the rate of sulfate and iron liberation from pyrite dissolution remains unchanged, the time spent by a volume of water adjacent to the reaction increases as a result of increased residence time. Therefore, the water has more time to accumulate solute as it passes over the reactive mineral surfaces. This can also explain the linear shape of the sulfate and iron curves, such that a constant flux of solute mass is being added to the water, regardless of flow velocity.

The rate of sphalerite dissolution appears to be affected by flow velocity because slow flow produces high rates and vice versa. However, this is an indirect effect. The rate of sphalerite dissolution at these conditions is dominated by the pH as described in section 3.5.1. Therefore, the decrease in pH due to pyrite dissolution remains dominant mechanism by which sphalerite dissolves. Further, as the pH decreases with decreasing flow velocity (i.e. increased residence time), the rate of sphalerite dissolution would be expected to increase. This occurs in both host rock models, confirming that they behave correctly. Additionally, non-linear

sphalerite rate curves can explain the corresponding non-linear zinc concentration curves for all cases in the host rock models.

The initial rate of calcite dissolution is faster in the low flux case and slower in the high flux case when compared to the reference case. This can be explained by the pH of the water entering the calcite zone since the dominant dissolution rate law is pH dependent (Table 3.2). However, within ~2 m, rates in all three cases become almost indistinguishable, suggesting that the slower, neutral mechanism becomes relevant to the overall dissolution rate. This is true in both host rock models. The effect of residence time on the calcium and bicarbonate concentrations is demonstrated here, similar to the pyrite scenario. For instance, relatively constant calcite dissolution rates result in three different bicarbonate and calcium concentrations in both host rock models.

In conclusion, the host rock models behave similarly in the high and low flux cases. The low flux case results in higher concentrations at the end of the calcite zone in both models. This is attributed to the increase of water residence time, which demonstrates these models are sensitive to flow velocity.

### 3.5.3.2 Gallery Model Sensitivity

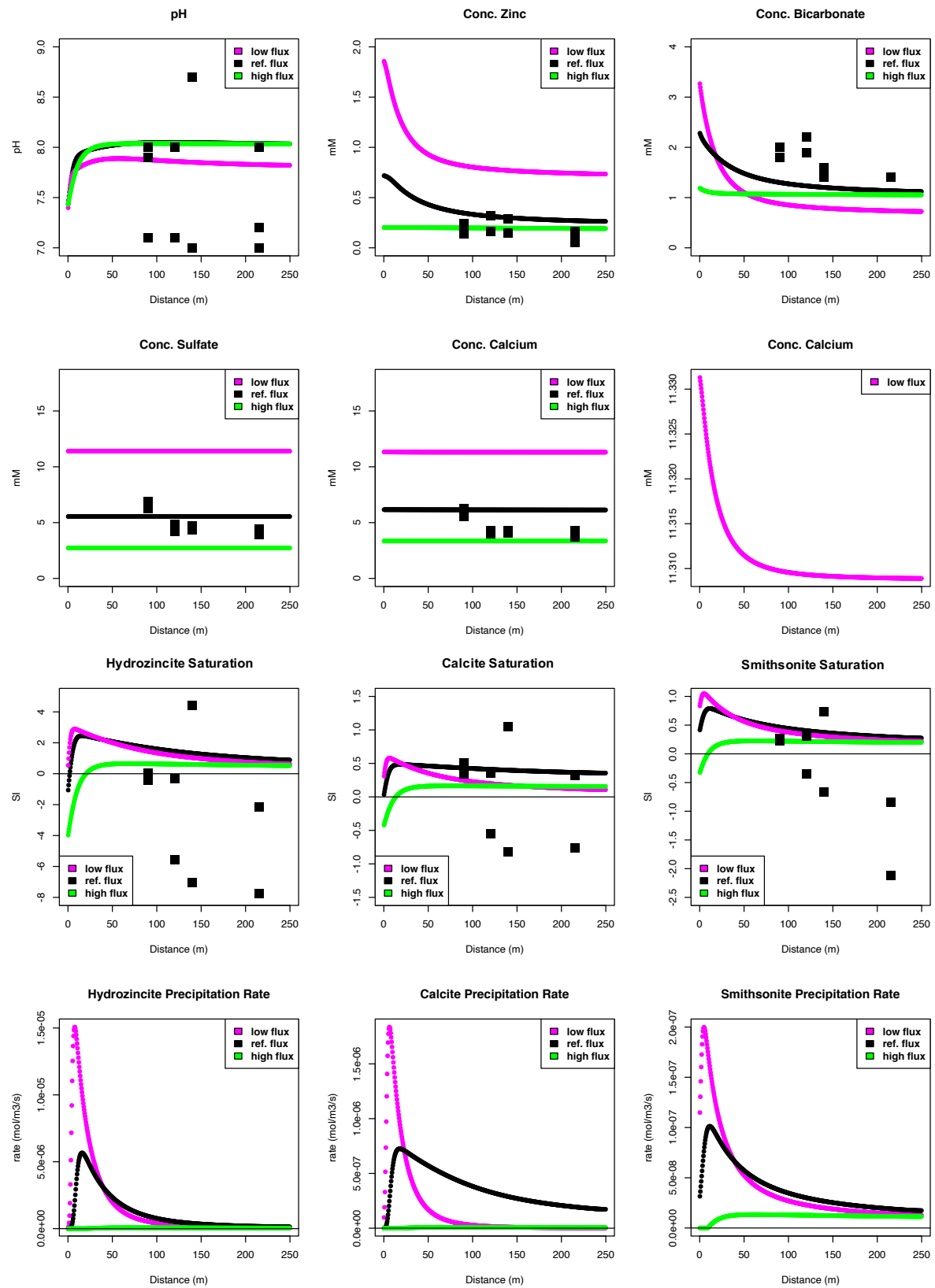
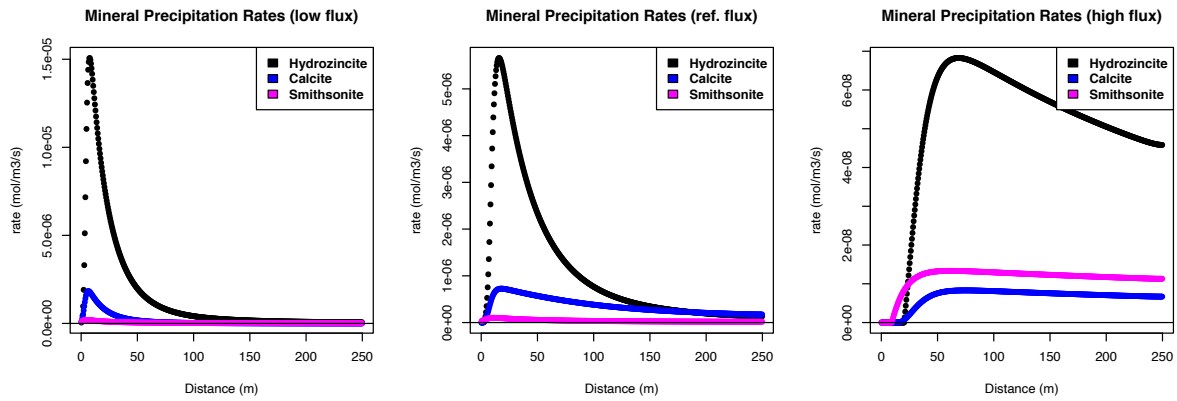


Figure 3.8. See following page for caption.



**Figure 3.8.** Results of the 2D gallery model informed by the low and high flux host rock cases. Results are plotted as function of distance at  $t = 5$  days. Flow goes from left to right. The ALV is 0.24, 0.48, and 0.96 m/min for the low, ref., and high flux cases, respectively. The data from all sampling campaigns are shown with black square markers.

The high flux case brings water into the gallery with lower solute concentrations and the flow velocity is doubled ( $ALV = 0.96$  m/min). As a result, smithsonite, hydrozincite, and calcite precipitation rates decrease by approximately 2 orders of magnitude when compared to the reference (Figure 3.8). On the other hand, the low flux case brings water into the gallery with higher solute concentrations, while the flow velocity is halved ( $ALV = 0.24$  m/min). In this case the, the mineral precipitation rates increase by a little more than one order of magnitude ( $\sim 40$  times faster). In the context of mineral rates, the low flux and reference cases show similar patterns, such that the rate of hydrozincite  $>$  calcite  $>$  smithsonite (Figure 3.8). Alternatively, in the high flux case, smithsonite precipitation is faster than that of calcite.

The high and low flux cases also result in changes to the relative mineral precipitation rates. For instance, in the high flux case, smithsonite and calcite make up a larger proportion of the total mineral precipitation (i.e. total rate = rate of hydrozincite + rate of smithsonite + rate of calcite). In contrast, in the low flux case, calcite and smithsonite contribute less to the total mineral precipitation in the gallery (Figure 3.8). In reality, this suggests that the mineralogical composition of a theoretical solid forming in the gallery would change water flux through the system. Specifically, as discharge increases, so does heterogeneity, as more smithsonite and calcite would be expected to form with respect to hydrozincite. Congruently, as discharge decreases, the theoretical solid would contain less calcite and smithsonite, resulting in a more homogenous hydrozincite solid.

In the low flux case, mineral rates stabilize around 150 m, while in the reference case, mineral stabilize at the end of the domain (250 m). The high flux case does not show mineral rate stabilization within the domain. These patterns are primarily due to the ALV, such that faster flowing water does not allow time for the minerals to reach equilibrium with respect to the fluid.

All measured concentrations of sulfate are captured by changing the flow velocity (Figure 3.8). Specifically, the post-100 m data points fall between the high flux and reference cases, while the pre-100 m data points fall between the reference and the high flux cases. All measured calcium concentrations are captured by the high flux and reference case. Further, several measured zinc concentrations are reproduced by the high flux case, that were not reproduced by the reference case. In general, the high flux case is a more accurately reproduces zinc, sulfate and calcium measurements.

The low flux case shows a lower pH than the reference and high flux case, which are similar. This is mainly due to the higher zinc concentrations at the input. The excess zinc promotes hydrozincite precipitation, which consumes more bicarbonate (reaction 2.1). The flattening of the zinc and bicarbonate curves reflects the fluid approaching equilibrium with respect to hydrozincite. Notably, the carbonate and zinc curves all reflect the fluid approaching equilibrium with respect to hydrozincite.

### 3.5.4 Case 2 Results: Hydrozincite Solubility

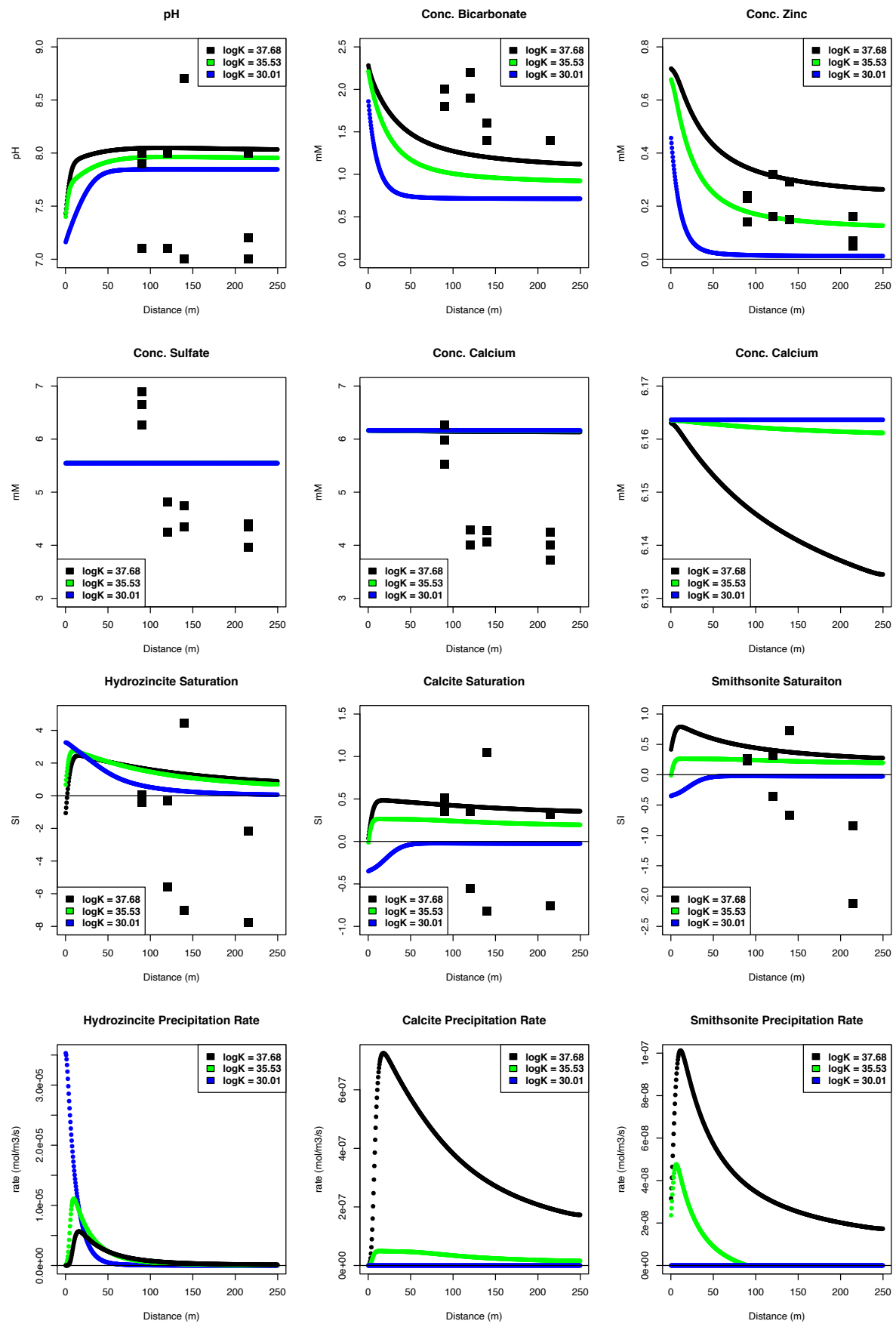
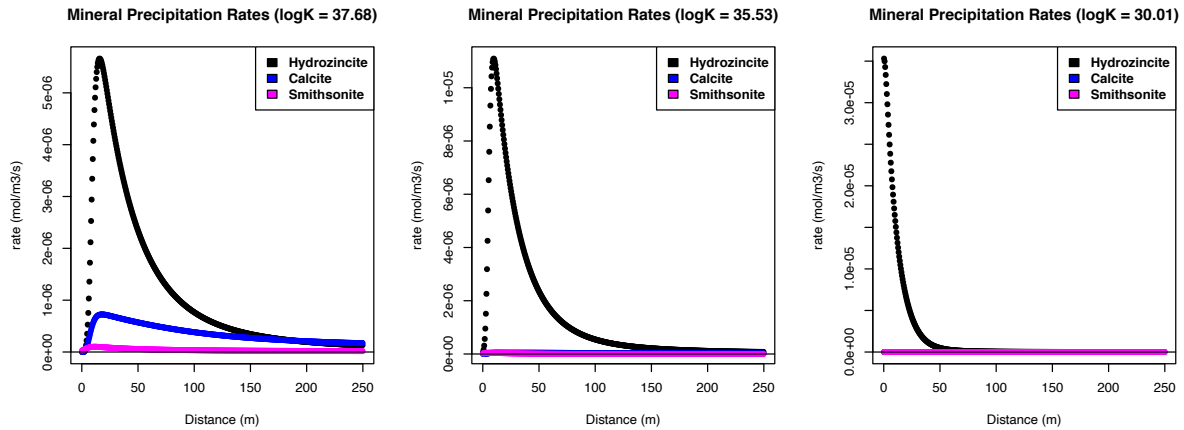


Figure 3.9. See following page for caption.



**Figure 3.9.** Results of the variable  $K_{eq}$  of hydrozincite cases in the 2D gallery model plotted with distance at  $t = 5$  days. Flow goes from left to right at an ALV of 0.48 m/min. The SI of hydrozincite, calcite, and smithsonite calculated from 2020 and 2021 field measurements are plotted with black squares. The SI of hydrozincite for these data points is based on a  $\log(K_{eq}) = 37.68$ .

Two distinct  $\log[K_{eq}]$  values for hydrozincite at  $7^\circ\text{C}$  are applied to the gallery model and compared to the reference case. No other parameters are altered. The first is the experimentally determined value ( $\log[K_{eq}] = 30.01$ ). The second is a value calculated under the assumption that the water at the sample 5 location was in equilibrium with hydrozincite ( $\log[K_{eq}] = 35.53$ ). This produces two new sets of results (Figure 3.9).

The  $K_{eq}$  for hydrozincite is calculated according to equation 2.3, meaning that decreasing the  $\log[K_{eq}]$  value decreases solubility. In the reference case ( $\log[K_{eq}] = 37.68$ ), hydrozincite is the most soluble, while it is least soluble using the experimentally determined value ( $\log[K_{eq}] = 30.01$ , section 2.3.6). Two model behaviors are expected based on this observation. First, as solubility decreases, the rate of precipitation increases under the local equilibrium assumption, given that the initial concentrations remain constant (equations 3.3 and 3.4). Second, zinc and bicarbonate would approach lower concentrations as the water approaches equilibrium with respect to hydrozincite.

The rate of hydrozincite precipitation doubles when the experimental  $\log[K_{eq}]$  is applied (Figure 3.9). This drives the bicarbonate to  $\sim 0.75$  mM and zinc to below 0.1 mM before 100 m down the gallery, wherein hydrozincite precipitation slows to effectively zero. The consumption of bicarbonate to this concentration effectively inhibits calcite and smithsonite precipitation. This can be more clearly seen in the "Mineral Precipitation Rates" plots. As the solubility of hydrozincite decreases, the calcite and smithsonite precipitation becomes less

dominant. Calcium and sulfate concentrations remain approximately the same as the reference case. There is, however, a small decrease in calcium due to calcite precipitation.

Most importantly, this analysis demonstrates that as hydrozincite solubility decreases, calcite and smithsonite precipitation becomes less relevant. In other words, hydrozincite precipitation increasingly dominates geochemistry of the gallery as its solubility decreases. Given this, using the  $\log[K_{eq}]$  from these experiments effectively shuts-off calcite and smithsonite precipitation.



### 3.5.5 Case 3 Results: Dispersivity

The changes to the gallery reference case based on a variation in dispersivity (0.25 m, 2.5 m, 25 m) produce two new sets of results (Figure 3.10). The results of these parameter changes show that concentration, solubility, and reaction rate curves tend to "flatten" across the domain. This exercise demonstrates that dispersivity is a relatively insensitive parameter, such that no significant change to solute concentrations or mineral reaction rates was observed.

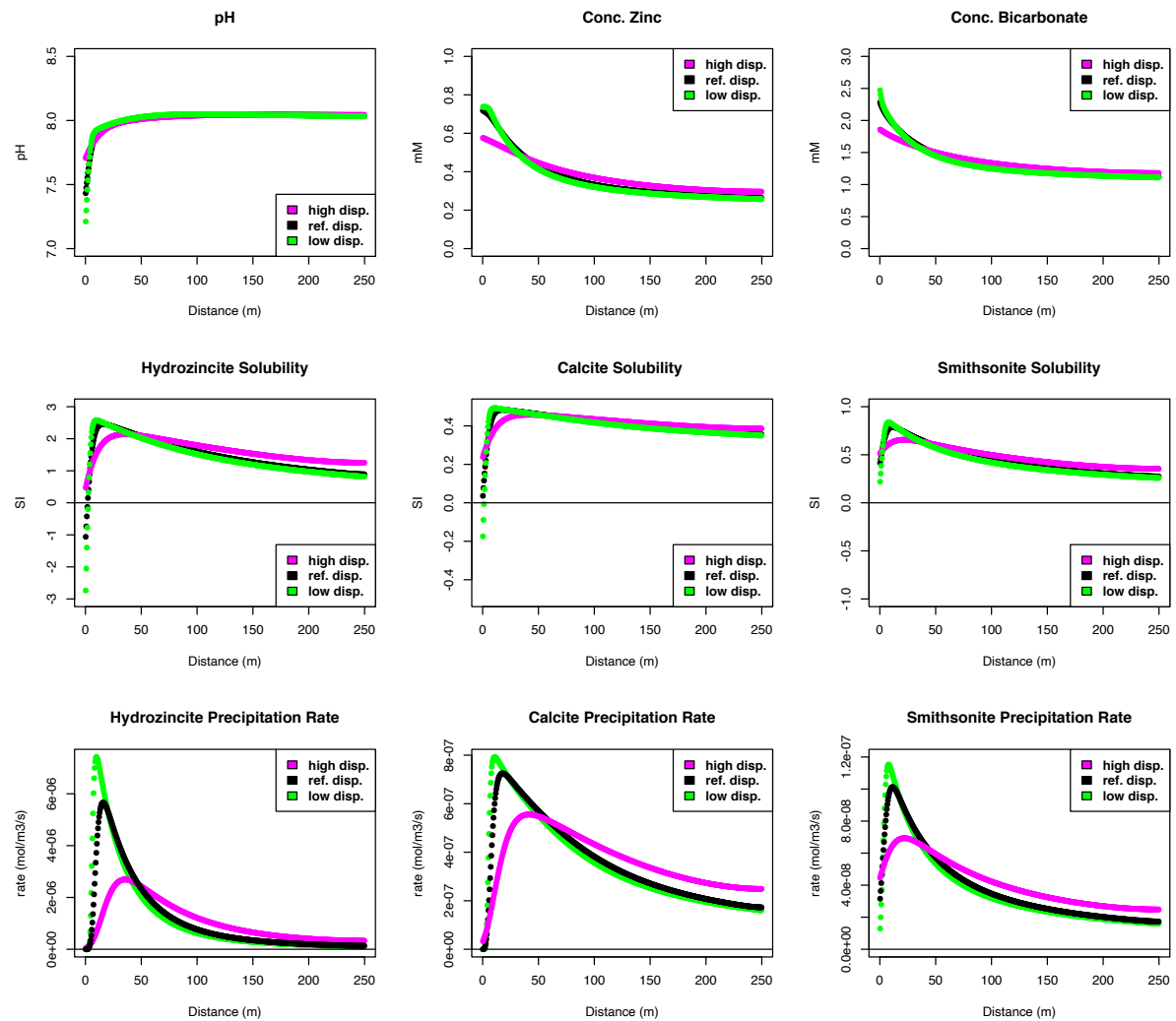


**Figure 3.10.** The results plotted as a function of distance at  $t = 5$  days of three 2D gallery model simulations where only the dispersivity values were changed. Flow goes from left to right with an ALV of 0.48 m/min. The "high disp." case refers to the dispersivity set to 25 m, or 10% of the domain length. The "ref. disp." case refers to a dispersivity set to 2.5 m, or 1% of the domain length. Finally, the "low disp." case refers to the dispersivity set to 0.25 m, or 0.1% of the domain length. Data from sampling campaigns is not plotted.

### 3.5.6 Case 4 Results: Homogeneous Rock Case

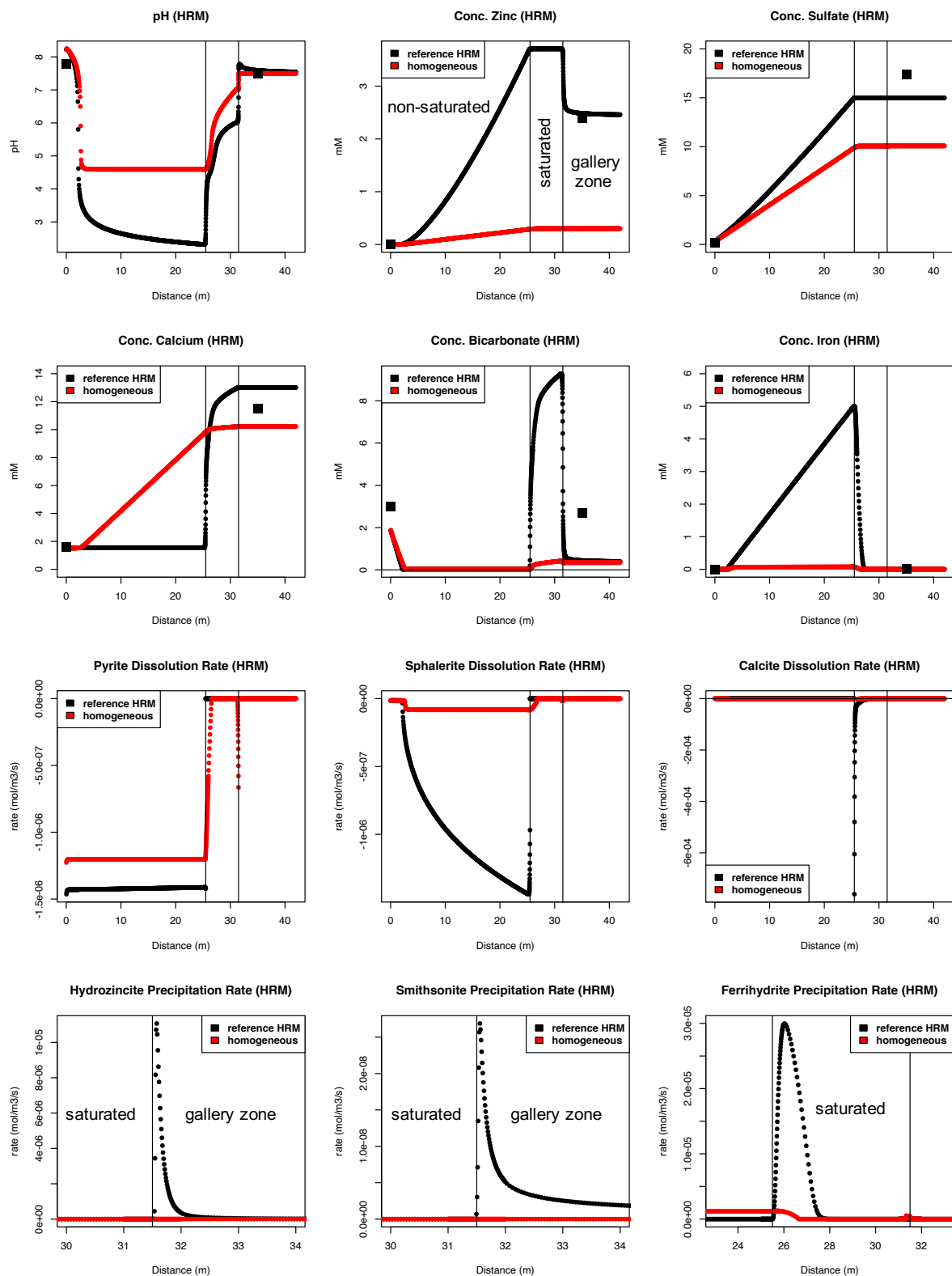
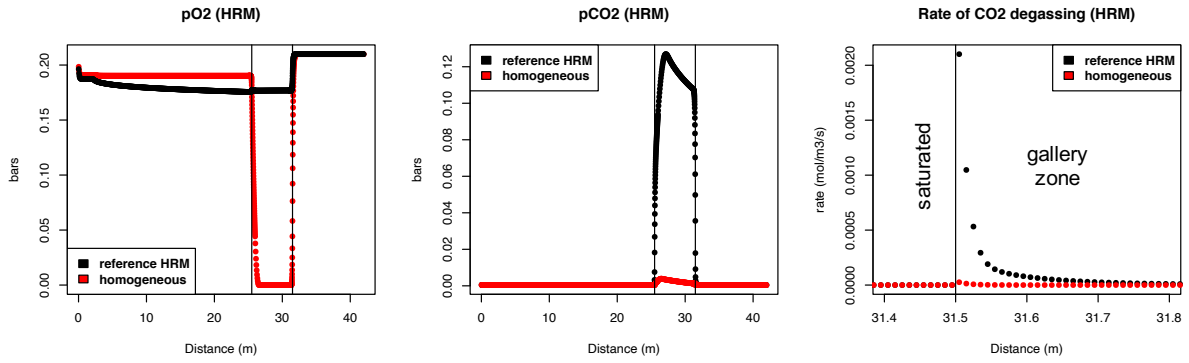


Figure 3.11. See following page for caption.



**Figure 3.11.** CrunchFlow simulation results in the high reactivity host rock model (HRM) comparing the homogeneous host rock case and the layered host rock (reference) case. Results are plotted as a function of distance at  $t = 60$  days. Flow goes from left to right with an ALV of 1.5 m/day. The vertical black lines represent zones of saturated and non-saturated rather than mineralogic composition since this model is mineralogically homogeneous. The gallery zone was not changed in this simulation, such that it is still effectively a non-saturated zone where flowing water is in contact with the atmosphere. The plots for calcite, hydrozincite, smithsonite, and CO<sub>2</sub> degassing rates have been scaled on the x-axis to more clearly visualize the model behavior. These five rates remain at zero outside of the visible range, except for smithsonite, which is slightly above zero ( $\sim 5.0 \times 10^{-9}$  mol/m<sup>3</sup>/sec) in the reference model. The ferrihydrite precipitation rate  $1.2 \times 10^{-6}$  mol/m<sup>3</sup>/sec from 0 to 27 meters and then drops to zero.

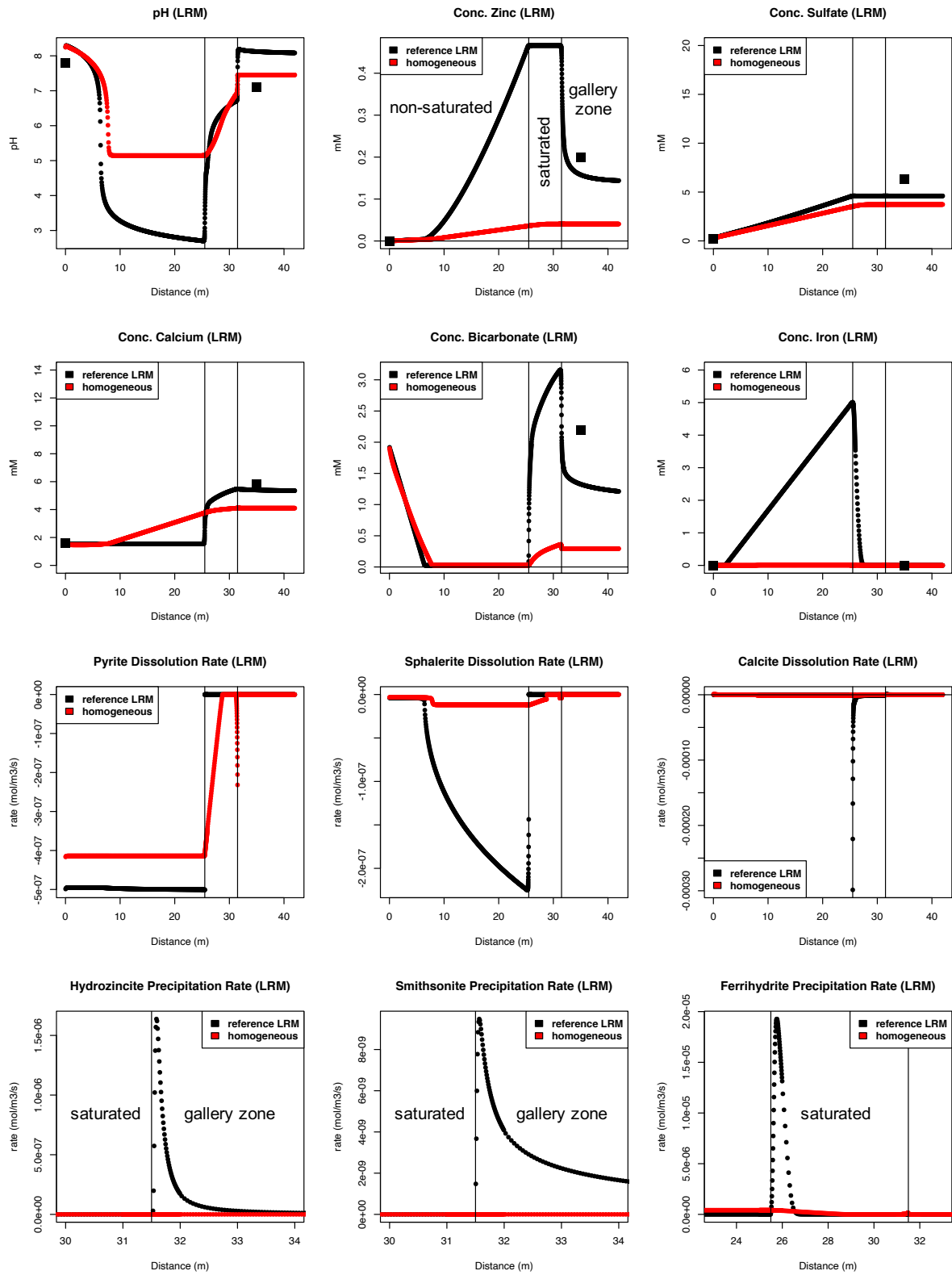
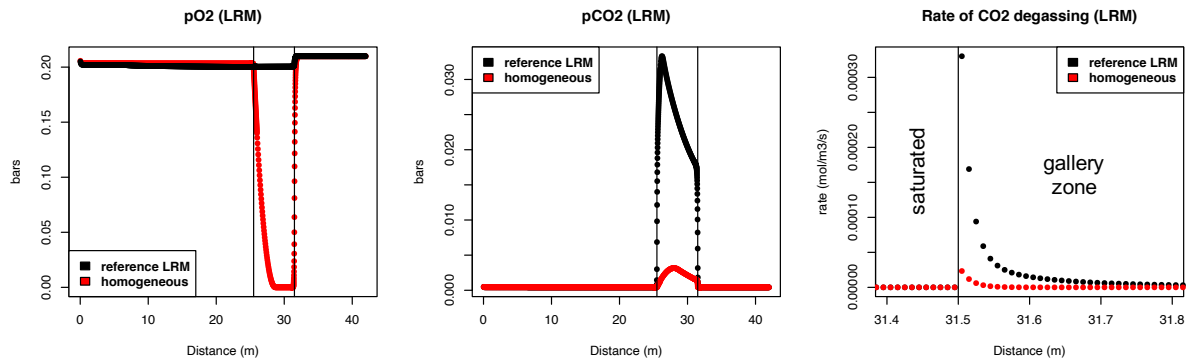


Figure 3.12. See following page for caption.



**Figure 3.12.** CrunchFlow simulation results from the low reactivity host rock model (LRM) comparing the homogeneous host rock case and the layered host rock (reference) case. Results are plotted as a function of distance at  $t = 60$  days. The vertical black lines represent zones of saturated and non-saturated rather than mineralogical composition. The gallery zone was not changed in this simulation, such that it is still effectively a non-saturated zone where flowing water is in contact with the atmosphere. The plots for calcite, hydrozincite, smithsonite, and CO<sub>2</sub> degassing rates have been scaled on the x-axis to more clearly visualize the model behavior. These five rates remain at zero outside of the visible range, except for smithsonite, which is slightly above zero ( $\sim 5.0 \times 10^{-9}$  mol/m<sup>3</sup>/sec) in the reference model. The ferrihydrite precipitation rate is  $4.1 \times 10^{-7}$  mol/m<sup>3</sup>/sec from 0 to 27 meters and then drops to zero.

A new host rock model case is constructed by creating a homogeneous mixture from the calcite, sphalerite, and pyrite. This refers to the reactive solids from the beginning of the sulfide zone to the end of the calcite zone (31.5 m), such that the mineral total mineral volume and reactive surface area from the reference case is maintained. This creates a new homogeneous case result in the HRM (Figure 3.11), and a homogeneous case result in the LRM (Figure 3.12).

The dominant effect of the homogeneously distributed minerals is the slower mineral dissolution rates, namely sphalerite. The reduced reaction rates result in lower resulting solute concentrations once the water enters the gallery zone. This is shown by the pH plots in both host rock models (Figures 3.11 and 3.12), such that the lowest pH values are much higher than the reference case, and both reach a constant value.

The pyrite rate is not affected as much at the sphalerite rate because pyrite's fastest reaction mechanism in the model is oxidative dissolution. This process is particularly evident in the pyrite rate plot. As water reaches the saturated zone, no oxygen source is present causing pO<sub>2</sub> to fall to zero due pyrite dissolution, which shuts down pyrite dissolution.

On the other hand, the overall sphalerite rate is much slower because the acidic (pH dependent) mechanism dominates the sphalerite dissolution (Table 3.2). The cause of this discrepancy in the sulfide-mineral rates is simultaneous calcite dissolution. As calcite dissolves

and produces  $\text{CO}_3^{2-}$ , it instantaneously forms  $\text{HCO}_3^-$  using the  $\text{H}^+$  that comes primarily from pyrite dissolution. Since sphalerite dissolution is a kinetically limited reaction, it cannot use the  $\text{H}^+$  as quickly as the equilibrium bicarbonate forming process. The main result is that pyrite and calcite dissolve to a similar extent when compared to the reference case, but sphalerite does not.

Hydrozincite, smithsonite, and calcite do not precipitate in the gallery zone as a result of the low bicarbonate and zinc concentrations in the water. Therefore, using a homogeneous mineral distribution does not reproduce the behavior seen in the Victoria Mine. This implies that the real flow path likely contains layers of rock, similar to those applied to the host rock reference case.

### 3.5.7 Solute Mass Flux and Discharge

Under the assumption that the gallery model reference case exhibits a discharge of 15.9 L/min, the concentrations at the end of the domain (250 m) are used to calculate solute mass fluxes (Table 3.6). Further, the volumetric discharge and mass fluxes of zinc, calcium and sulfate measured in the field over three years (see section 2.3.2) are compared to the results of the model (Figure 3.13). It should be noted that these flux vs. discharge relationships predicted by the model are qualitative. In other words, based on the assumptions necessary to generate these values, there is a high degree of uncertainty.

**Table 3.6.** Solute mass flux (mol/day) leaving the gallery model for seven different simulations.

Discharge (L/min)	15.9	7.95	31.8	15.9	15.9	15.9	15.9
Model Case	reference	low flux	high flux	logK= 30	logK= 35	high disp.	low disp.
Zinc	6.0	8.4	8.8	0.5	2.9	6.8	5.9
Bicarbonate	25.7	8.3	48.2	16.7	21.1	27.0	25.4
Calcium	140.5	129.5	153.6	141.1	141.1	140.4	140.5
Sulfate	127.0	130.5	125.0	127.0	127.0	127.0	127.0

Zinc mass flux does not show a strong correlation with discharge when considering the high and low flux cases. The reference discharge shows the lowest zinc flux, while the high and low flux cases show higher zinc fluxes than the reference case (Table 3.6). However, zinc flux is not highly dependent on flow rate in the model. This does not capture entirely the natural behavior from the mine, which shows an increase of zinc with discharge (Figure 3.13). Notably, using the estimated 15.9 L/min discharge, the zinc flux from the model is similar to that of the measured values.

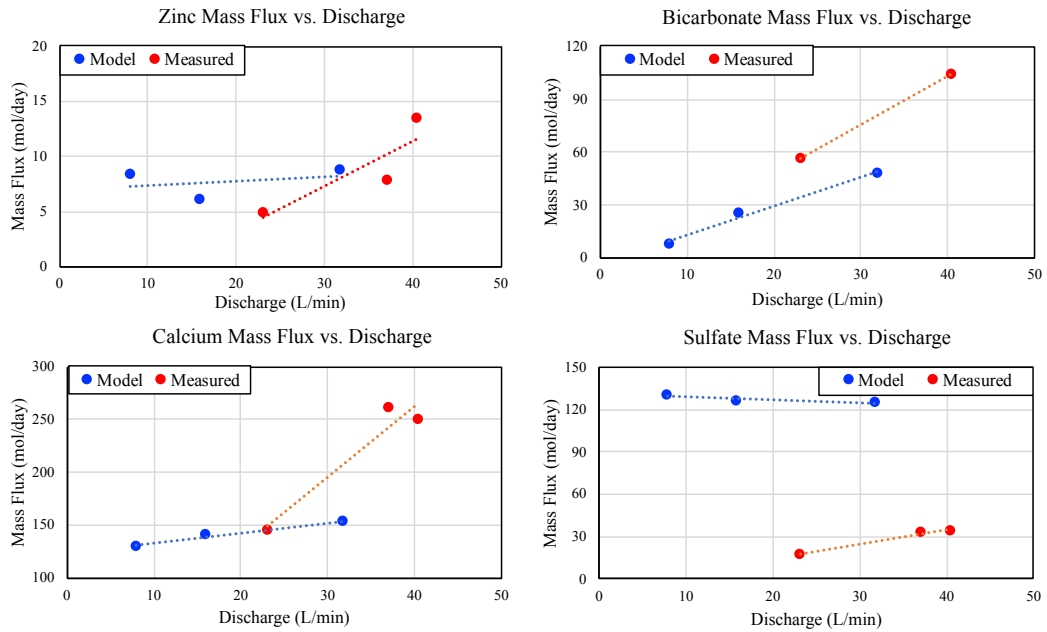


**Figure 3.13.** Flux discharge relationships plotted from measurements (red) and the model (blue) for zinc, bicarbonate, calcium, and sulfate. Concentrations at 250 m in the gallery model were used in these calculations. The measured values are reported in section 2.3.2.

The bicarbonate mass flux and discharge relationship from both the model and measurements show a similar trend (Figure 3.13). That is, as discharge increases, so does bicarbonate mass flux. Further, the slopes of the lines are similar, indicating that the model is capturing the behavior of the Victoria Mine in this context. It should be noted that only mass flux data from 2020 and 2021 are available.

Calcium mass flux increases with increasing discharge in both the model and at the Victoria Mine (Figure 3.13). The calcium fluxes produced by the model are similar to those produced by the mine at the lower range of discharge. However, at the mine, more calcium leaves the mine per unit increase in discharge.

Sulfate mass flux from the model is significantly higher than what is observed at the Victoria Mine; approximately 100 mol/day more. Further, the sulfate flux tends to decrease with increasing discharge in the model, while the opposite is true at the mine. Notably, sulfate is conserved through the gallery model, and its concentration is a result only of the pyrite dissolution in the host rock models. In contrast, zinc, calcium, and bicarbonate form part of mineral reactions through the gallery model. In general, the model does not capture the sulfate flux or discharge relationships.

### 3.6 Summary and Conclusions

A reactive transport model to simulate the geochemical processes at the Victoria Mine system provides a framework to test different conditions that can affect solute mobility. Predictions towards what can affect said mobility are made primarily through quantification of the mineral precipitation-dissolution reactions. Further, as trace metals were not considered in the model, zinc was used to make interpretations towards metal mobility, as trace metal mobility is directly linked with hydrozincite precipitation, the dominant metal attenuating mineral in the Victoria Mine.

Fitting of the gallery model to data (i.e.  $V_{LRM}/V_{HRM} = 10$ ) implies that total volumetric discharge through the gallery is composed mainly of the water coming from the sample-10 location, while the sample-9 drip water contributes to approximately one tenth of the total discharge. The model demonstrates that the addition of the concentrated sample-9 drip water enhances the precipitation of secondary carbonate minerals because it is rich in bicarbonate, Ca, and Zn. In essence, the more concentrated/toxic water serves to increase the saturation state of the water with respect to hydrozincite, which in turn, causes attenuation of these metals via precipitation.

Sulfate concentrations decrease after the sample-8 (90 m) location during all three years (Figure 3.4) and no gypsum or significant quantity of other sulfate bearing minerals were found in the 1330 Gallery. Further, preliminary model simulations show that gypsum is highly undersaturated at the conditions in the mine, and therefore would be expected to form. Calcium concentrations show a decrease similar in magnitude to that of sulfate after the sample-8 location, and model simulations in all cases predict no significant decrease in calcium. A likely explanation for this lends to a compositionally distinct water source between 90 m (sample-8) and 120 m (sample-7). This water source would be more dilute with respect to sulfate and Ca, and perhaps Zn, which could cause the negative SI's beyond 90 m (Figures 2.22 and 2.23).

X-ray diffraction of the solids identifies hydrozincite as the only mineral present in the Victoria Mine. Although, the method used (see section 2.2.4.1) is not sensitive enough to recognize phases that exists in volume fractions less than approximately 5%. This implies that a small amount of, for example, smithsonite or calcite, could go unrecognized. Further, electron microprobe analyses strongly suggest the existence of calcite and smithsonite in the sample, and backscattered electron images show morphologies consistent with that of smithsonite



(section 2.3.4). The model predicts, in all cases, some precipitation of calcite and smithsonite alongside hydrozincite. For instance, in the reference case, the maximum calcite precipitation rate is approximately 10 times slower than that of hydrozincite, and smithsonite is approximately 15 times slower. These rates indicate that, although composed mostly of hydrozincite, a theoretical solid would contain some smithsonite and calcite. Given this, the reference case model reproduces a theoretical solid that would reflect what was found in the gallery.

Applying this logic to precipitation rates, the low flux case (i.e. slow flow velocity, dry period) would produce a theoretical solid containing some calcite, whereas smithsonite would likely be undetectable. On the other hand, the high flux case (i.e. rainy period) would produce proportionately significant amounts of both, and smithsonite would be more abundant than calcite. In the case testing the variability in hydrozincite solubility, any solubility below that applied in the reference case would produce a theoretical solid that would be almost completely hydrozincite. This strongly suggests that amorphous solid precursors are forming prior to the structured mineral. A change in the hydrodynamic dispersivity would not induce significant changes to the theoretical solid.

The solute mass flux calculations based on the model results show that flow velocity (i.e. discharge) and metal mobility are not closely related. This is because Zn mass flux does not appear to increase or decrease with discharge (Table 3.6, Figure 3.13), and Zn and other trace metals (e.g. cadmium) are controlled by hydrozincite precipitation. Instead, modeling results suggest that there are specific flow velocities that increase and decrease metal fluxes. However, this conclusion is based on three simulations. Further testing of flow velocities could lead to a better understanding of the relationship between discharge and mass flux through the Victoria Mine system. Again, this is a qualitative examination of the flux vs. discharge relationships and is associated with a large amount of uncertainty.

Metal mobility was most affected by a change imposed to the solubility of hydrozincite. For instance, when the equilibrium constant found in the experiments in this study are applied to the model ( $\log[K_{eq}] = 30.01$ ), the zinc flux out of the mine is 12x less than the reference case at the same discharge (Table 3.9), yet observed concentrations cannot be reproduced. The apparent solubility of hydrozincite appears to change based on the environment in which it is precipitating. Since this effect exhibits significant control over metal mobility, more

investigation to understand what conditions may perturb hydrozincite solubility should be done.

The flux-discharge relationship for bicarbonate at the Victoria Mine are captured by the model; as discharge increases, so does bicarbonate mass flux (Figure 3.13). The same is true for Ca. This indicates that calcite dissolution is fast relative the flow velocities imposed by the model. Although the model reproduces the observed behavior at the mine (Figures 2.14 and 3.13), a more extensive modeling study of flow velocities could serve to determine the flow conditions that lead to maximum and minimum bicarbonate and calcium fluxes.

In conclusion, the RTM created for the Victoria Mine system reproduces concentrations seen in the gallery via implementation of realistic mineral reactions and flow velocities. Hydrozincite, smithsonite, and calcite precipitate in the gallery due to CO<sub>2</sub> degassing as the water enters the gallery, analogous to the formation of carbonate speleothems. The host rock model uses mineralogically distinct zones and saturated/non-saturated flow to reproduce solute compositions measured at the input of the gallery. Case 4 demonstrates that a homogeneous mineral distribution in the host cannot reproduce the observed water compositions.

Flow velocities disproportionately affect mineral precipitation rates, indicating that the resulting theoretical solid would have more smithsonite in a fast flow regime, and more calcite in a slow flow regime. Furthermore, as flow velocity increases, so does the overall proportion of calcite and smithsonite in the solid with respect to hydrozincite. This explains some of the heterogeneity observed in the hydrozincite samples (Figure 3.8). Although, determination and implementation of the kinetic parameters of smithsonite and hydrozincite would strengthen this argument.

Hydrozincite solubility is the most sensitive parameter because metal fluxes and patterns of precipitation for all three minerals are dominantly controlled by the  $K_{eq}$  of hydrozincite (Table 3.6).

The model captures a range of behaviors observed at the Victoria Mine, and explains to some extent why the solids are highly heterogeneous. Additionally, more is known about the reactivity and distribution of the minerals host rock, such that further parameterization of the flow rates and flow paths could be used to make this model more accurate. The model

predicts that an increase in discharge does not necessarily increase metal mobility, although more work would be necessary to make a definitive statement on this matter.

The model presented here is not particularly well-constrained. For instance a detailed mineralogic distribution and associated reactivities, information regarding the water residence time and volumetric discharge is not well known. Nevertheless, the conceptual framework and sensitivity analyses of these parameter values serves to help understand and quantify the geochemical processes that affect both mineral precipitation and metal mobility at the Victoria Mine. The model predicts solute concentrations and mineralogy that agree with the observations using reasonable assumptions and applying realistic ranges to several of the unknown parameter values. The model also explains why heterogeneity is observed in solid samples (i.e. changing oversaturation values). Additional sampling of the mine, characterization of the host rock, volumetric measurements inside the mine, and experimental work to determine the kinetic values associated with hydrozincite and smithsonite formation (and dissolution) would serve to enhance the accuracy of this work. Nevertheless, the model succeeds in capturing the overall geochemical behavior of the system. It serves as a first approach towards making realistic predictions about mineral formation and metal mobility at the Victoria Mine considering several system variables.



## CHAPTER 4 – MICROBIOLOGY OF THE VICTORIA MINE

### 4.1 Introduction

In all ecosystems, microorganisms contribute to the cycling of both organic and inorganic materials by mediating chemical transformations (Madsen *et al.*, 2011). It has been proposed that the majority of biomass on earth is composed of microorganisms (Whitman *et al.*, 1998). Microorganisms that live in energy-poor conditions (oligotrophic) with limited carbon and nutrient availability often catalyze these reactions more slowly than a system with more energy and organic carbon (eutrophic) (Bethke *et al.*, 2011; Qin *et al.*, 2013). Subterranean and hypogean (e.g. caves) environments are typically oligotrophic, and are therefore expected exhibit slow reaction rates (Groth and Saiz-Jimenez, 1999). The Victoria Mine is no exception as dissolved organic carbon (DOC) concentrations are low ( $0.8 \pm 0.3$  ppm; Table S3).

One process by which microbial communities can affect elemental cycling is via biomineralization, wherein the organisms catalyze the formation of a mineral that may not otherwise occur abiotically or affect the rate of precipitation (Lian *et al.*, 2006; Braissant *et al.*, 2003; Fang and Achal, 2019). This process often results in the sequestration of solutes (e.g. metals) acting as a natural metal attenuation mechanism (i.e. inhibiting metal mobility).

Podda *et al.* (2000) found *cyanobacteria* (*Scytonema* sp. strain ING-1) and microalga (*Chlorella* sp. strain A1) responsible for catalyzing hydrozincite precipitation in the Naracauli River in Sardinia, Italy. The result of the bioprecipitation was an enhanced attenuation of dissolved metals (e.g. Zn, Cd, Pb, Ni, and Cu) coming from the effluent of the Ingurtosu Mine, an abandoned mine in Sardinia (Italy).

Similar to the Ingurtosu Mine, the Victoria Mine is associated with drainage conditions conducive for sphalerite and pyrite dissolution resulting in increased mobility of harmful metals (e.g. Cd, Zn, and Ni) as demonstrated in chapters 2 and 3. Fortunately, the precipitation of hydrozincite significantly reduces the mobility of these dissolved metals. And, although model simulations predict that hydrozincite precipitates abiotically in the mine (see chapter 3), it is important to evaluate the effect that the local microbial communities may have on the metal attenuation process. Therefore, the bacterial communities inside and outside of the mine were

sampled and analyzed to determine if bacteria associated with hydrozincite formation are present.

An effective tool used to characterize a bacterial community is DNA sequencing (Janda *et al.*, 2007). More specifically, metagenomic sequencing, which identifies the taxonomy of the bacterial community and gives the relative abundance of each bacteria in that community. The bacterial genome is composed of DNA sequences that can range from approximately 130,000 to 14,000,000 base pairs. The genome serves to provide the instructions for life and is unique to each bacterial species. A critical function inscribed in every bacterial genome is the ability to make proteins, the building blocks of life (Woese, 1987). Although, microbial genomes possess several genes that serve to make proteins, there is one distinct gene sequence that can be found in all bacteria (i.e. a conservative gene) – the 16s ribosomal ribonucleic acid (16s rRNA) gene (Acinas *et al.*, 2004).

The 16s rRNA gene is made up of approximately 1,500 base pairs and can be found in all bacteria. It provides essential instructions to help build proteins in the cell, and therefore bacterial life does not occur without it. Due to its essential nature, the gene is highly conserved across species genomes, which means that it can be easily targeted, amplified (i.e. copied), and eventually identified via comparison to a 16s rRNA taxonomic database (Jonasson *et al.*, 2002; Van de Peer *et al.*, 1996). In other words, there are segments of the 16S rRNA gene that are identical, such that they can be found routinely using established techniques like PCR amplification (Janda *et al.*, 2007). Additionally, the gene carries phylogenic markers unique to each species, such that it acts as a unique taxonomic identifier. At present, the taxonomic identification of bacterial species is most commonly accomplished through the sequencing of the 16s rRNA (Lane *et al.*, 1985). DNA sequencing and taxonomic identification of the communities present at the Victoria Mine can serve to make comparisons to previously characterized mining sites and make an ecological health assessment.

## 4.2 Objectives

The goal of this study is to examine the effects that the bacterial communities at the Victoria Mine have on both metal attenuation and aqueous geochemistry. This is relevant because previous studies have demonstrated that biomineralization of hydrozincite can enhance metal attenuation in a similar abandoned mine setting (De Giudici *et al.* (2009); De Giudici *et al.* (2017), Podda *et al.* (2000), and Wanty *et al.*, 2013). This is done via three methods.

First, taxonomic comparisons between the bacteria at the Victoria Mine and the bacteria responsible for biomineralization of hydrozincite are made. Notably, the responsible organisms were photosynthetic (Podda *et al.*, 2000), which would not thrive in a dark tunnel. Second, SEM images of hydrozincite from De Giudici *et al.* (2009), verified to be a product of biomineralization, are compared to SEM images of the hydrozincite inside of the Victoria Mine. Third, bioreactor experiments using indoor and outdoor communities are done to examine the relative activities and responses of these communities under normal and carbon-stimulated conditions. Thus, illustrating the extent to which microbial activity may affect the geochemistry at the mine, and the response to secondary carbon stimulation. In addition to these methods, the information obtained from metagenomic sequencing is used to give a brief characterization of the bacterial populations at the Victoria Mine.

## 4.3 Methods

### 4.3.1 Bioreactor Experiments

The purpose of these experiments is to observe the indoor and outdoor bacterial community response to eutrophic conditions since mine is an oligotrophic environment (i.e. DOC =  $0.8 \pm 0.3$  ppm, Table S3). The communities were collected during the 2021 sampling campaign. This was accomplished via two sets of two reactors (four in total); two inoculated with an indoor community using sediments from the sample-9 location, and two inoculated with an outdoor community using sediments from the sample-3 location (Table 2.1). One of the two bioreactors from each indoor and outdoor set were amended with yeast extract, a carbon and nutrient source. Periodic sampling of the reactions over a 22-day period from inoculation was done to monitor solute concentrations.

Four 500-mL glass bottles were cleaned, sterilized via autoclave, and sealed with a screw cap before taken to the Victoria Mine. Using a sterilized metal spatula, sediment samples from sample-3 and sample-9 locations were scooped to fill a sterile 15-mL sterile falcon centrifuge tube and then transferred into the glass reactor bottle. Subsequently, the bottles were filled completely with the water in contact with the sediments and sealed. The sample-3 solid was a dark sediment from the creek bed. The sample-9 solid was a fine orange powder determined to be hydrozincite by XRD (Figure 2.15, "Orange Powder"). The non-stimulated reactors were sealed immediately, and the stimulated reactors were amended 0.5 mL of a filter-sterilized ( $0.22 \mu\text{m}$ ) solution of 1g/100 mL yeast extract and Milli-Q water. The sealed bottles from the indoor location were covered in aluminum foil to prohibit light from contacting the bacteria. At this point, a 10.0 mL aliquot of each reactor was removed and filtered ( $0.22 \mu\text{m}$ ) to measure pH, alkalinity, and to be acidified for ion concentration measurements (see methods section 2.2.3).

The bioreactors were kept in a cooler with ice for ~48 hours before being brought back to the laboratory for further observations. After the initial sampling interval (0 days), subsequent sampling intervals took place at 6, 12, 17 and 22 days. The air temperature of the laboratory in which these reactions took place was  $20.0^\circ\text{C}$  and the bioreactors remained sealed except for ~20-minute periods during each sampling interval.



Each sampling was done by removing 10.0 mL from the open bioreactor while a Bunsen burner was ignited next to the bottle to avoid outside contamination. The 10.0 mL were filtered (0.22  $\mu\text{m}$ ) and the pH and alkalinity were measured immediately. A 0.80 mL sample was then diluted to 10.0 mL with 2% trace-metal grade  $\text{HNO}_3$  and measured with ICP-MS/OES (see section 2.2.3). Analytical uncertainty for this method is  $\pm 4\%$ .

#### **4.3.2. Sampling, DNA Extraction, and PCR**

During the 2019 sampling campaign, sediment samples from two locations inside of the 1330 Gallery (sample-5 and 10, Table 2.1) and two locations outside of the mine (sample-3 and 11, Table 2.1) were collected. Approximately 10g of soil/sediment from each sample location were placed inside sterile (RNase-/DNase-free) 15-mL Corning centrifuge tubes. This was done using a stainless-steel spatula sterilized three consecutive times via 99% ethanol soaking and subsequent igniting with a butane lighter. Immediately after the sample was placed in the tube, it was capped tightly and slowly lowered into a liquid nitrogen dewar. The frozen samples were later preserved in a  $-80^\circ\text{C}$  freezer for future processing.

The DNA of the 2019 samples 3, 5, 10, and 11 (Table 2.1) was extracted using DNeasy PowerMax Soil Kit and following the manufacturer's instructions (Qiagen, Germany). DNA concentration was measured using a *Nanodrop* (Thermo Fisher Scientific) spectrophotometer. In order to verify the presences of microbial DNA, a 10.0  $\mu\text{L}$  aliquot of each pure extracted DNA sample was put through a polymerase chain reaction (PCR) targeting a 16S rRNA sequence using an Illustra Ready-to-go PCR kit (GE Healthcare, United States). The universal primers 27F (forward) and 1492R (reverse) were used to do the PCR and a pure sample of sulfate reducing bacteria genome was used as positive control (Frank *et al.*, 2008). The negative control was ultrapure DNA-free Milli-Q water (18.2 M $\Omega$ ). All microbiological laboratory work was conducted in a UV sterilized horizontal air flux chamber (i.e. positive pressure laminar air flow) to minimize contamination. The PCR thermo cycling was done with an Eppendorf Mastercycler machine. The thermal cycling profile used was following; 2 min. at  $50^\circ\text{C}$  and 10 min at  $95^\circ\text{C}$ , following by 30 cycles of 20 sec. at  $95^\circ\text{C}$ , 20 sec. at  $50^\circ\text{C}$ , and 3 min. at  $72^\circ\text{C}$ , followed by 10 min. at  $72^\circ\text{C}$ .

The PCR products from the natural DNA samples were compared to that of the known sulfate reducing bacteria to determine if the 16S rRNA gene was present. This was accomplished by way of a 1% agarose gel electrophoresis mixed with Syber red DNA fluorescent dye. This method separates DNA fragments by the relative length of the copied sequences. Each PCR product was placed into a separate pre-cast well in the agarose gel plate. Once the DNA is loaded into the wells and mixed with a loading buffer, a voltage is induced across the agarose gel plate. The voltage causes the negatively charged DNA fragments to move through the gel at a velocity inversely proportional to length of the fragment (e.g. 1500 base pairs for 16s rRNA gene). Once the electrophoresis is completed, the distance traveled by the DNA segments on the gel plate can be visualized using UV light. This was imaged in a GELDOC XR imaging system (BioRad, United States) (Figure 4.1). Through this method, the presence of 16s rRNA (i.e. bacteria) was verified. Therefore, the pure extracted DNA samples were later sequenced to characterize the microbial taxonomy.

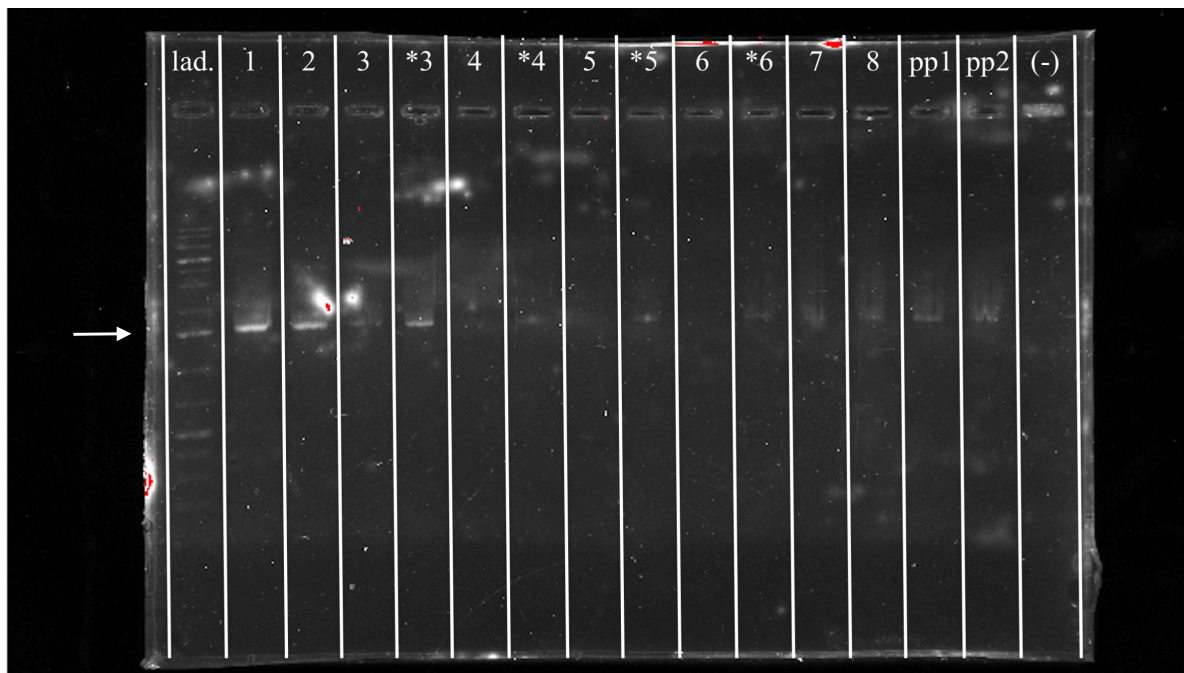


**Figure 4.1.** Image of the agarose gel plate after electrophoresis. DNA fragment travel direction is top to bottom. a separate sample of the PCR products. The PCR products were died with a fluorescent dye such that UV light can be visible; shown as the lightly colored horizontal lines. The pre-cast wells are the rectangles immediately below and voltage-driven DNA migration was induced from top to bottom, although the gel plate was perfectly horizontal. The “lad.” column contains the standard sulfate reducing bacteria DNA. The white arrow denotes the location of the DNA fragment containing the microbial 16s rRNA sequence. Each number is a natural sample and the products of a second PCR on the same DNA sample. The “pp1” and “pp2” refer to samples that are not a PCR and “(-)” represents the negative control (i.e. Milli-Q water).

### 4.3.3 MiSeq-Sequencing and Bioinformatics

The pure extracted DNA samples were shipped to Macrogen Inc. (Seoul, Korea) for sequencing. Sequencing was performed with the MiSeq-Illumina platform targeting the V3-V5 region of the 16S rRNA gene implementing 2x300 cycles and 100,000 reads.

The metagenomic analysis of the MiSeq-Illumina sequencing data was performed using Mothur via Galaxy Ecology platform web-based software package (Afgan *et al.*, 2018). This tool (1) filtered low quality sequence readings, (2) filtered duplicate sequences, (3) and compared the remaining sequences to a microbial 16S database known (trainset9\_032012.pds.tax - Hiltmann *et al.*, 2019) to identify the operational taxonomic units (OTUs) in each sample. Using the same tutorial, Krona diagrams were generated for each sample to visualize the OTUs. In addition, the inverse Simpson diversity index ( $1/D_{simpon}$ ) of each community is calculated to quantify the species richness at each sampling location. The Simpson diversity index is calculated using the formula

$$D_{simpon} = \frac{\sum_{i=1}^{S_{obs}} n_i(n_i-1)}{N(N-1)} \quad (\text{Equation 4.1})$$

where  $S_{obs}$  is the number of observed OTUs,  $n_i$  is the number of individuals in the  $i^{\text{th}}$  OTU, and  $N$  is the total number of individuals in the community.

The result of this calculation is such that a community with more diversity returns a smaller value for  $D_{simpon}$ . Since this is not intuitive, the inverse is reported (i.e.  $1/D_{simpon}$ ); the larger the inverse Simpson index, the more biodiversity is present in the sample. The Simpson index considers both the "richness" and "evenness" of a sample. The richness refers to the number of different OTUs in a sample. Evenness considers the relative abundance of each OTUs.

## 4.4 Results

### 4.4.1 Bioreactor Experiment Results

The results of the four bioreactors demonstrate that stimulating the microorganisms with yeast extract (a source of organic carbon) did not result in faster metabolism (Figure 4.2). In all reactors, the concentrations of sulfate, Ca, Sr, and Cd remain constant throughout the duration of the experiment. The Cd appears to increase and decrease slightly, but the net change is negligible over the 22-day period. The pH is also relatively stable for all reactors. Alkalinity increases about 2 mM ( $\text{HCO}_3^-$ ) for both outdoor community reactors. In contrast, the non-stimulated indoor community loses approximately 1.6 mM of bicarbonate, while the stimulated indoor community loses approximately 0.75 mM bicarbonate. Of the trace metals, only Ni shows a significant change in concentration.

Solutes appear to be consumed in the non-stimulated indoor. For example, Zn decreases 0.7 mM and alkalinity decreases 1.6 mM. This suggests that there could be hydrozincite precipitation, but the relative molar ratios of reactant consumption do not reflect that of hydrozincite ( $\text{Zn}:\text{CO}_3 = 5:2$ ). Further, Ni decreases 1.5  $\mu\text{M}$ , which is consistent with hydrozincite as it tends to incorporate Ni when it precipitates (this study Table 2.3 and Podda *et al.*, 2000).

The outdoor community reactors show an increase in solute concentrations through time. This is true for Zn, bicarbonate and Ni, suggesting mineral dissolution. In general, the indoor communities may exhibit mineral dissolution, while the outdoor communities, especially the non-stimulated community, indicate mineral precipitation. Considering the indoor communities, the yeast extract appears to have inhibited the Zn, bicarbonate, and Ni consuming processes that would have occurred otherwise.

In conclusion, the geochemistry of all the reactors does not change substantially as would be expected from microbial reactions. Further, there is no evidence that yeast extract (a carbon and nutrient source) stimulates the metabolism of the either community, but rather inhibits metabolism for the indoor communities of the Victoria Mine.

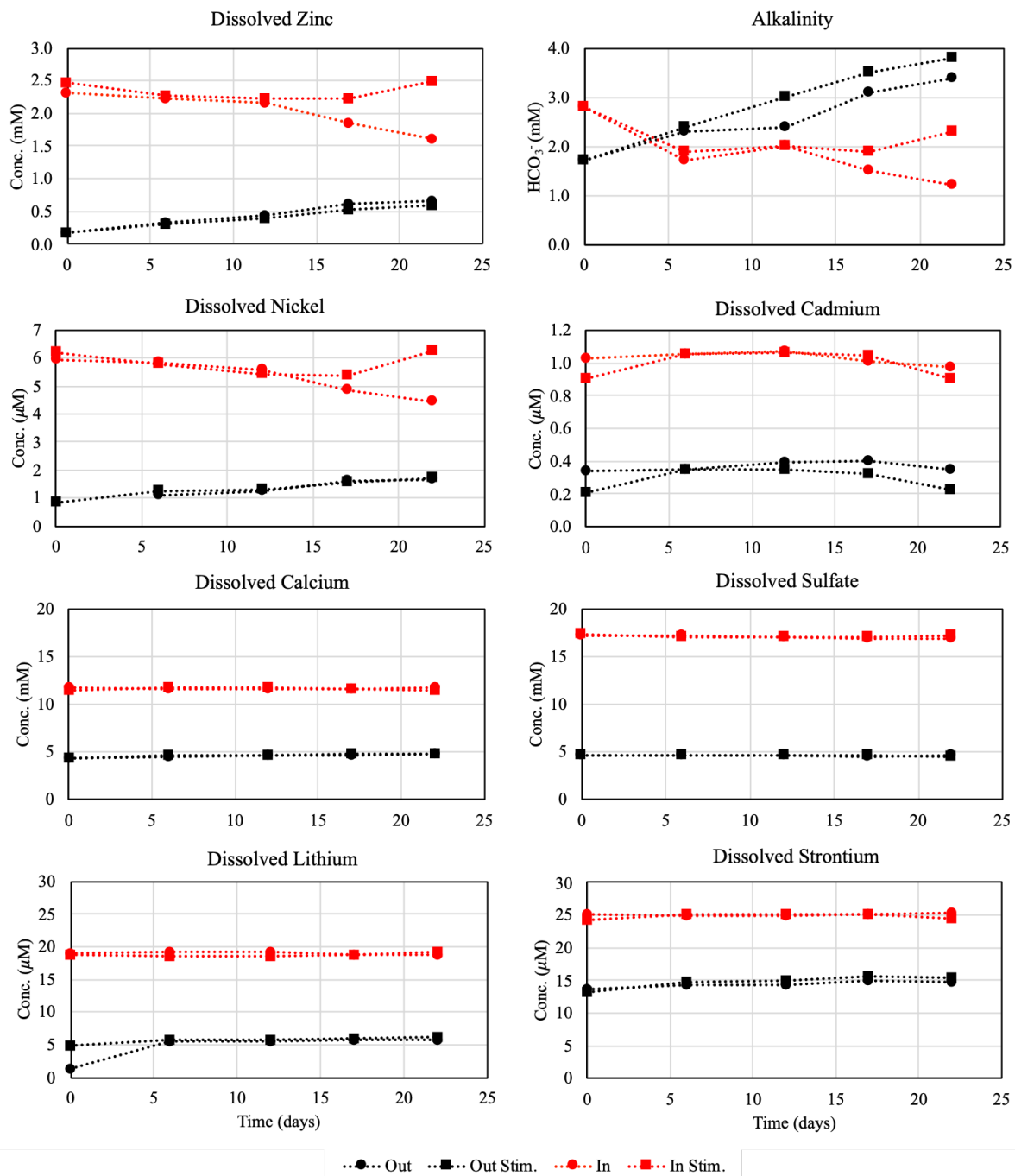


**Figure 4.2.** Solute concentrations through time of the four bioreactor experiments. In the legend, "Out" refers to the outdoor sample-3 location, and "In" refers to the indoor sample-9 location. "...Stim." denotes the reactors that were amended with yeast extract. Analytical uncertainty for these measurements is  $\pm 4\%$ .

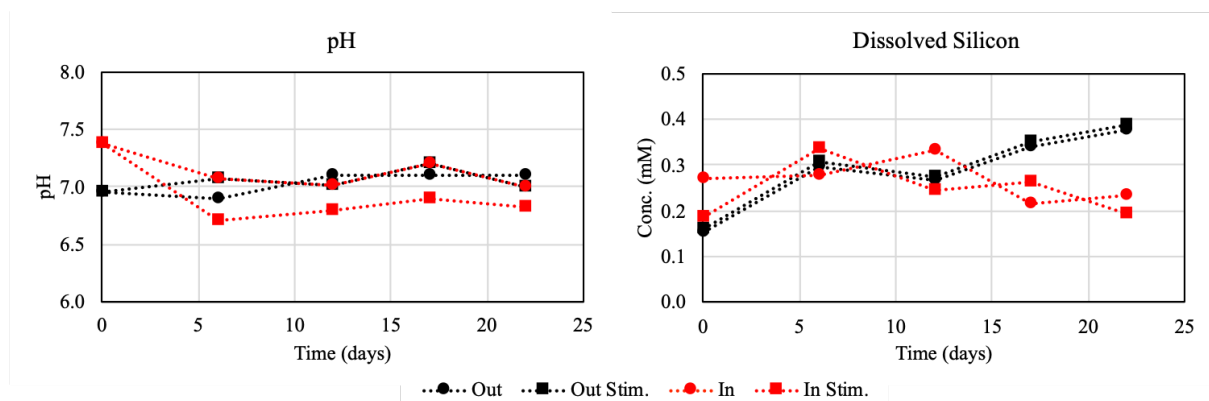


**Figure 4.2.** See previous page for caption.

#### 4.4.2 Sequencing and Bioinformatics Results

The microbial communities along the water flow path of the Victoria Mine are sequenced and classified by their OTUs according to a preexisting taxonomic database. Additionally, the relative abundance of each taxonomic rank is calculated. The accuracy of the assigned abundance values is quantified by the sequencing coverage (%). The result for these data is that abundance values are reported at >95% confidence for each sample (Table 4.1). Rarefaction curves are generated to visualize sequencing coverage (Figure S1).

Each community can be visualized with a Krona diagram (the URLs to the Krona diagrams can be found in the supplementary information to view the detailed metagenomic analyses of each sample). Krona diagrams are in order from the upper stream (Figure 4.3A), to 310 m from the entrance of the mine (Figure 4.3B), to 65 m from the entrance of the mine (Figure 4.3C), and finally at the confluence of Melics Creek and the mine effluent (Figure 4.3D). The results are centered around the phylum level of each community; both the specific phyla and their respective abundances. As proteobacteria are of great interest in the field of microbial ecology (Brenner *et al.*, 2005), special attention is given to the classes of Proteobacteria present (*Alpha-*, *Beta-*, *Gamma-*, and *Deltaproteobacteria*). The well-known bacterial associated with heavy metal environments, such as mines, belong to this phylum (Bruneel *et al.*, 2006). It should be noted that no cyanobacteria, including *Scytonema*, was not found in any of the samples - the bacteria associated with biomineralization of hydrozincite (Podda *et al.*, 2000).

**Table 4.1.** Results from bioinformatics on the four sequenced samples. The grey-shaded columns represent sampled locations inside of the 1330 Gallery where there is no sunlight. Phylum are listed in order of abundance with respect to the sample-11 community.

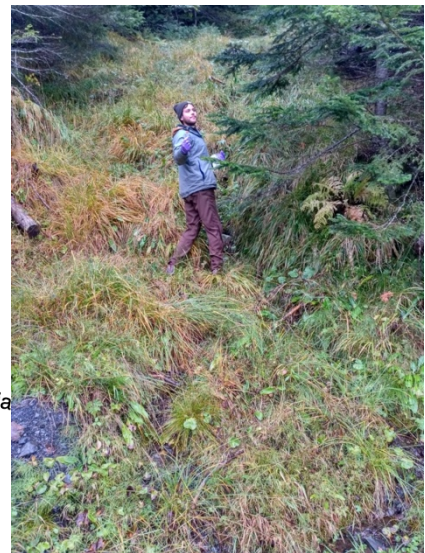
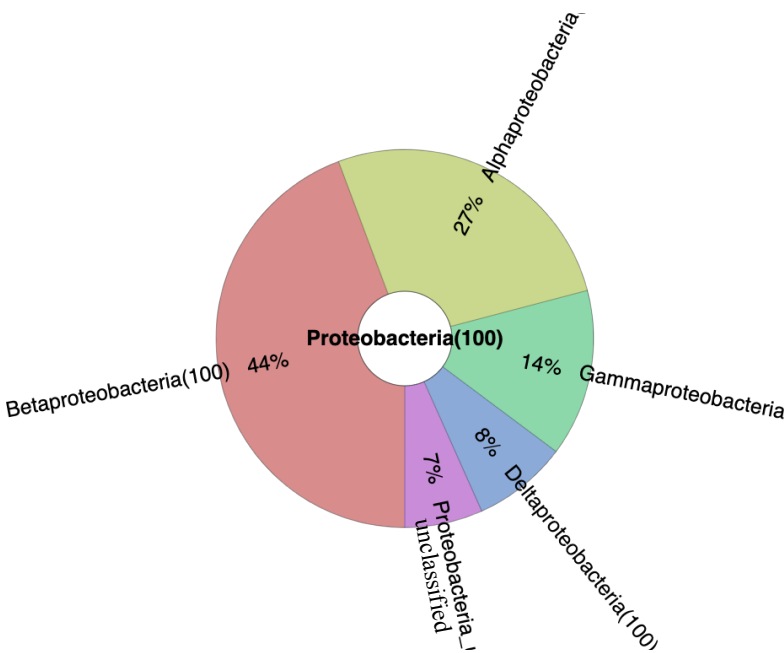
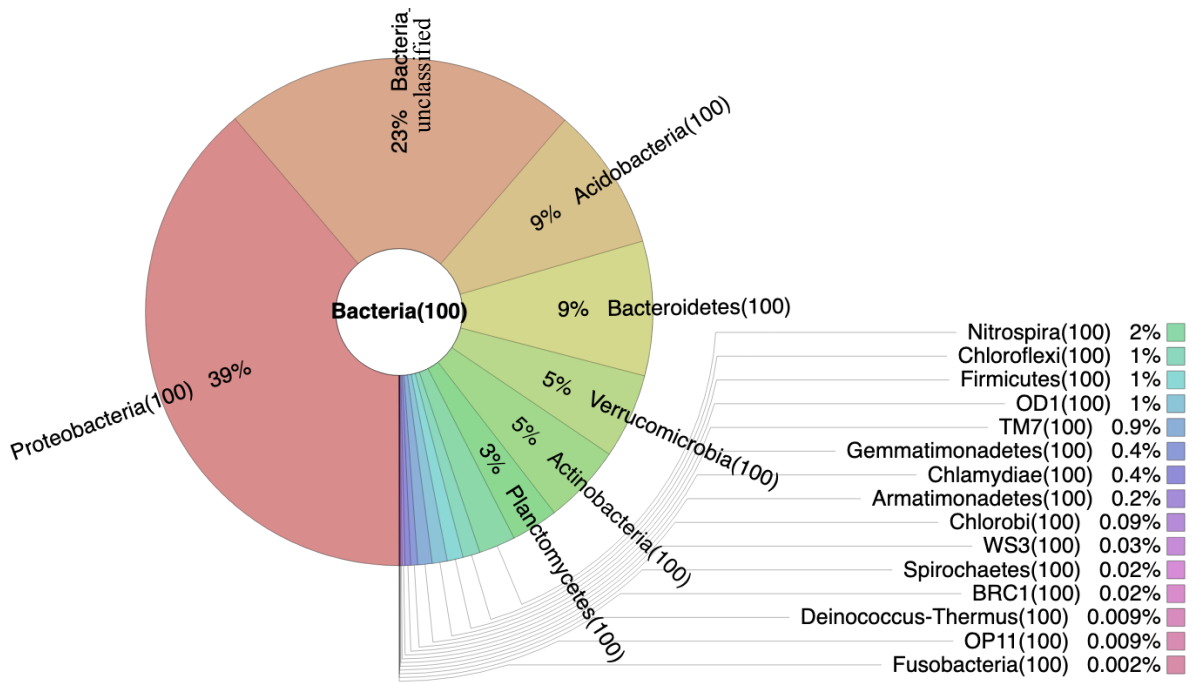
Location	sample-11	sample-10	sample-5	sample-3
# of sequences	78,960	79,551	94,343	76,335
# of OTUs	7,828	899	1,492	7,029
Coverage (%)	95.9	99.2	99.4	95.5
Inverse Simpson	498.4	9.98	47.71	272.6

**Phylum (% total abundance)**

<i>Proteobacteria</i>	39	40	44	43
<i>Acidobacteria</i>	9	2	8	10
<i>Bacteroidetes</i>	9	3	3	14
<i>Verrucomicrobia</i>	5	0.1	0.5	3
<i>Actinobacteria</i>	5	2	4	3
<i>Planctomycetes</i>	3	0.2	1	2
<i>Nitrospira</i>	2	0.6	3	3
<i>Chloroflexi</i>	1	0.3	1	0.9
<i>Firmicutes</i>	1	46	9	0.6
Unclassified	23	3	18	15

***Proteobacteria* (% total abundance)**

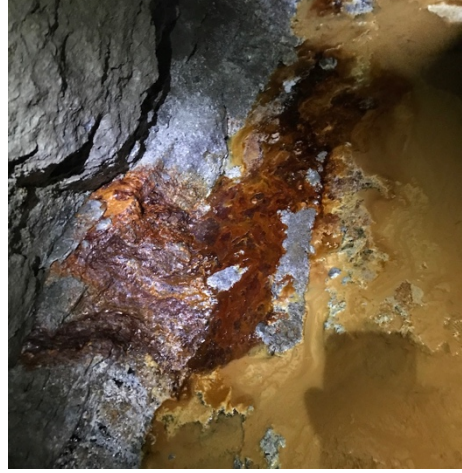
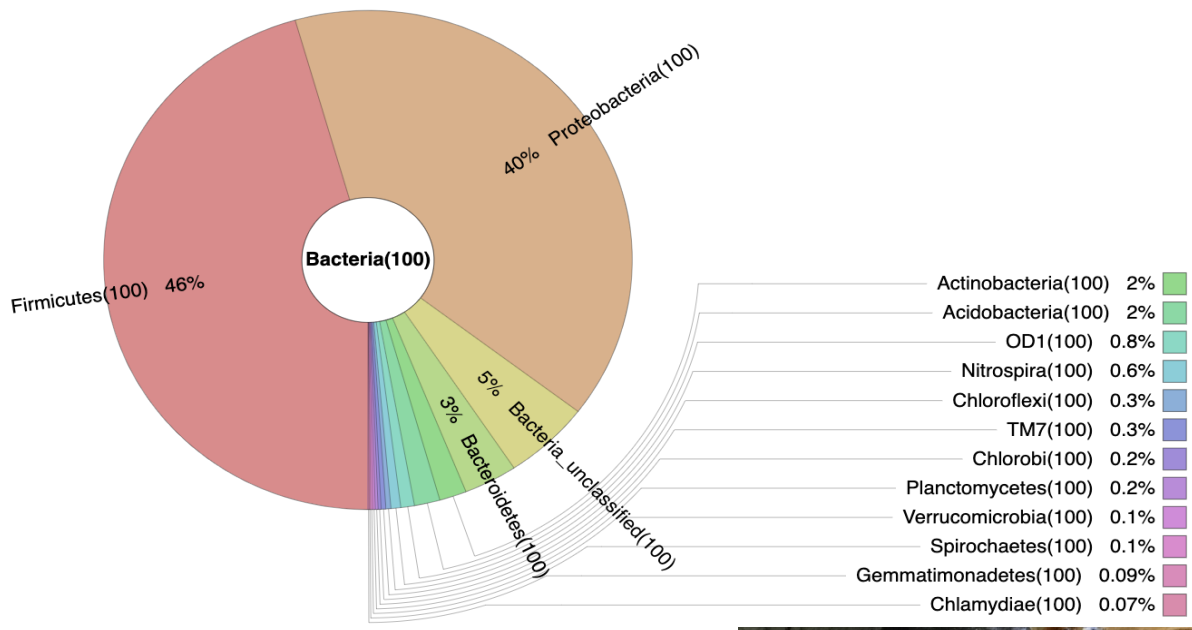
<i>Alpha-</i>	11	3	5	18
<i>Beta-</i>	17	25	16	14
<i>Gamma-</i>	5	10	17	3
<i>Delta-</i>	3	1	1	3
Unclassified	3	1	4	4



Upper Melics Creek (sample-11)

**Figure 4.3A.** Krona Diagrams showing OTUs of the upper Melics Creek outdoor microbial community (sample-11). A total of 66,207 reads are plotted. (top) Phylogenetic makeup of the community where % refers to the overall bacterial population abundance. (bottom) Breakdown of the classes of the Proteobacteria where % refers to the proportion of Proteobacteria present. Image taken at sample location (a small creek on the right).





Red goo at 315 m into the gallery (sample-10)

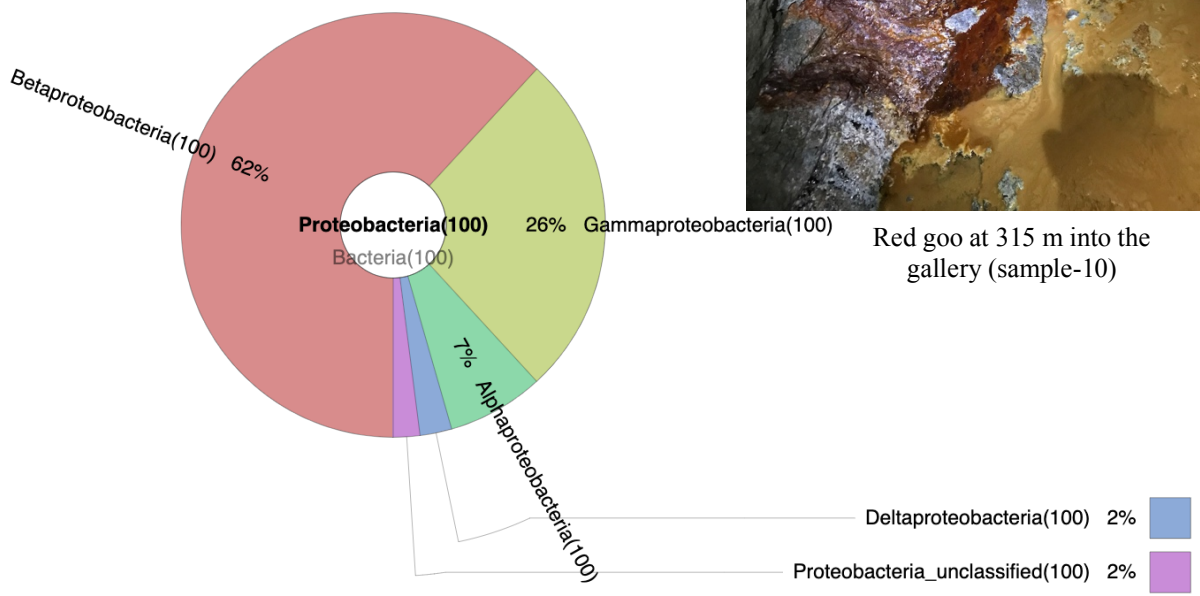


**Figure 4.3B.** Krona Diagrams showing OTUs of the microbial community at the sample-10 location inside of the 1330 Gallery (310 m from the entrance). A total of 79,555 reads are plotted Phylogenetic makeup of the community where % refers to the overall bacterial population abundance. (bottom) Breakdown of the classes of the Proteobacteria where % refers to the proportion of Proteobacteria present. Image of where the red goo sample was taken.

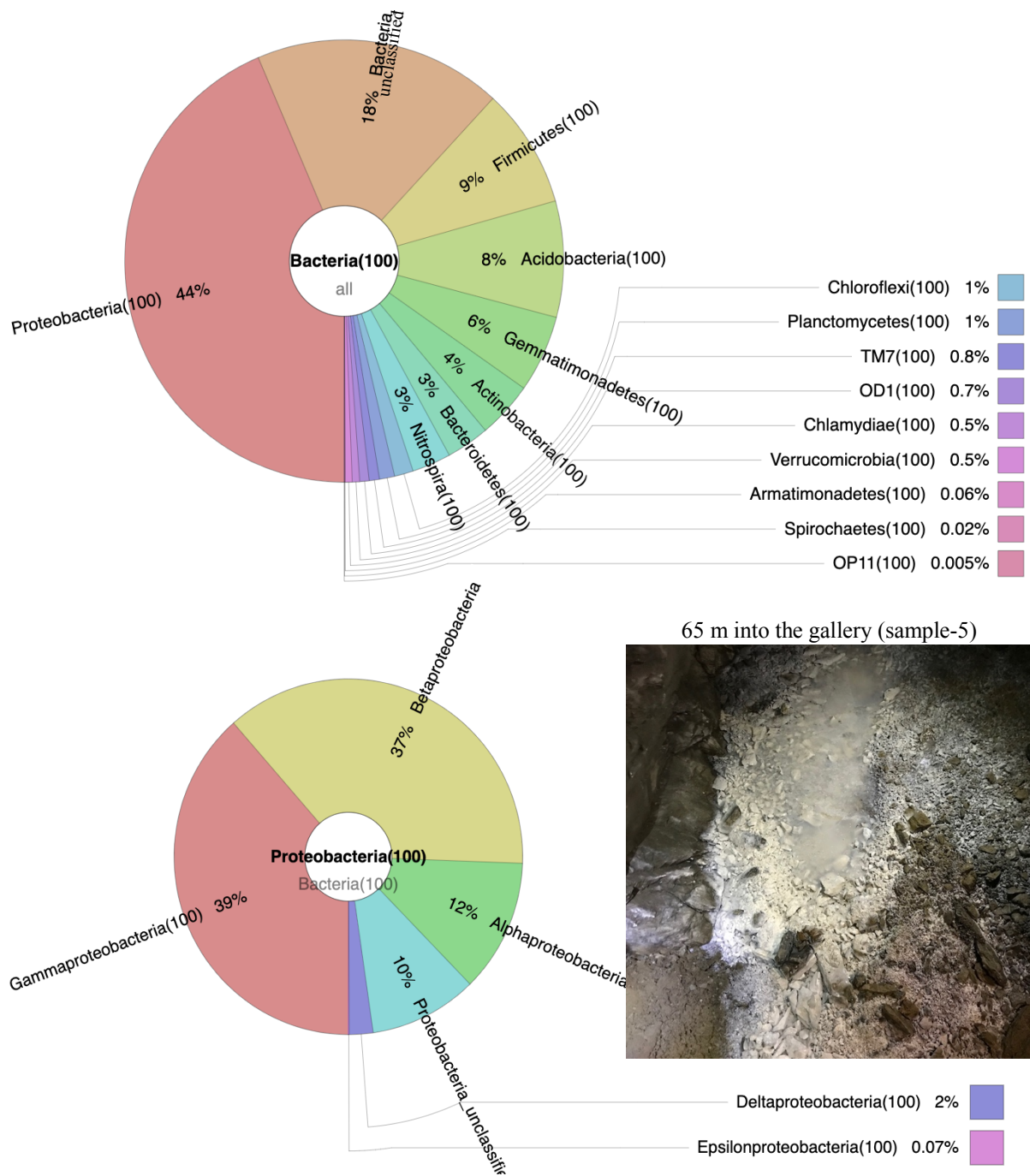


**Figure 4.3C.** Krona Diagrams showing OTUs of the microbial community at the sample-5 location inside of the 1330 Gallery (65 m from the entrance). Phylogenetic makeup of the community where % refers to the overall bacterial population abundance. (bottom) Breakdown of the classes of the Proteobacteria where % refers to the proportion of Proteobacteria present. The image is from where the sample was taken.

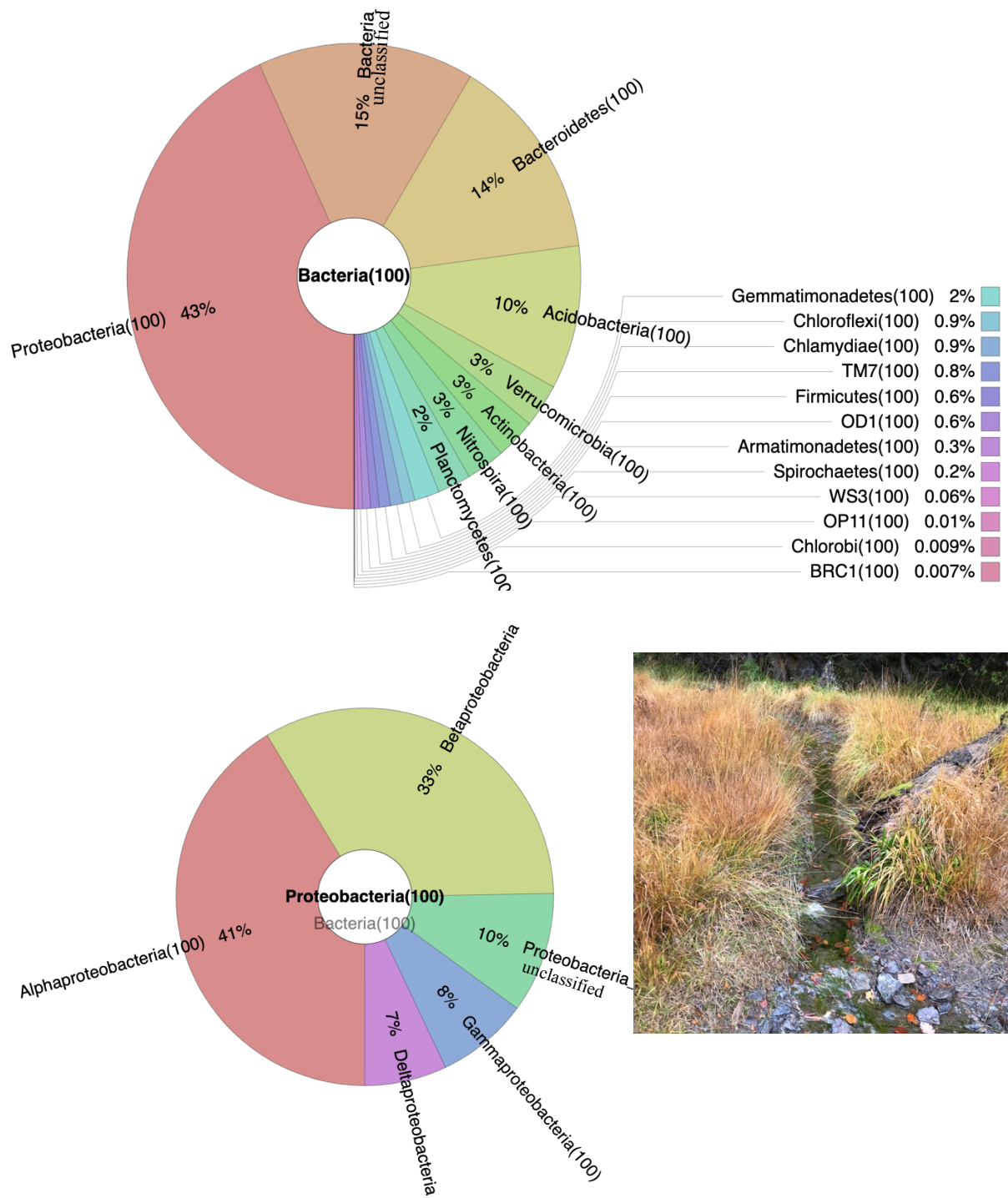


**Figure 4.3D.** Krona Diagrams showing OTUs of the outdoor microbial community at confluence of Melics Creek and the mine effluent (sample-3). Phylogenetic makeup of the community where % refers to the overall bacterial population abundance. (bottom) Breakdown of the classes of the Proteobacteria where % refers to the proportion of Proteobacteria present. The image is from where the sample was taken.

The microbial population in Melics Creek above the mine is considered to be the only location reflecting an environment that has not been heavily affected by mining activities (Figure 4.3A). In this analysis, 78,960 DNA sequences classified into 7,828 OTUs, and the inverse Simpson index is equal to 498.4 (Table 4.1). The bacterial population here is dominated by Proteobacteria (39% of total), which is dominated by *Betaproteobacteria* (17% of total).

Continuing downstream and into the mine, at 310 m from the entrance of the gallery, the sample-10 location shows a unique bacterial community with respect to the other three (Figure 4.3B). There are 79,551 sequences that are classified into 899 OTUs, resulting in an inverse Simpson index of 9.98 (Table 4.1). This site was composed of a red goo that was seeping from the wall and persisted on the floor. The microbial community here is dominated by the phylum Firmicutes (46% of total) rather than Proteobacteria (40% of total). *Betaproteobacteria* (25% of total) dominates the Proteobacteria population.

Approximately 245 m downstream from the sample-10 location inside the gallery, the sample-5 location consists of a community dominated by Proteobacteria (44% of total) and a significant Firmicutes population (9% of total, Figure 4.3C). There are 94,343 sequences classified into 1,492 OTUs resulting in an inverse Simpson index of 47.71 (Table 4.1). *Gammaproteobacteria* (17% of total) dominate the Proteobacteria population here.

Below the 1330 Gallery at the confluence of the mine effluent and Melics Creek, the sample-3 outdoor community is dominated by Proteobacteria (43% of total, Figure 4.3D). There are 76,335 sequences classified into 7,029 OTUs resulting in an inverse Simpson index value of 272.6 (Table 4.1). *Alphaproteobacteria* (18% of total) dominate the Proteobacteria at this location.

The sample-10 community is unique in comparison to the other three. There are relatively fewer unclassified genes, less diversity, and is the only community not dominated by Proteobacteria, but rather Firmicutes. Across all four sampling locations, Proteobacteria abundances are remarkably consistent ( $42 \pm 2\%$ ).

Several taxonomic differences between communities between indoor and outdoor communities can be identified. For instance, the outdoor communities are more diverse than the indoor communities (i.e. larger value for the inverse Simpson index, Table 4.1).

Additionally, indoor communities exhibit less Bacteroidetes, Verrucomicrobia, Planctomycetes, and Acidobacteria, and more Firmicutes than the outdoor communities. Meanwhile, Nitrospira and Chloroflexi are more evenly distributed between indoor and outdoor communities (Table 4.1).

The classes associated with the Proteobacteria can also be separated into indoor and outdoor categories according to their relative abundances. For instance, *Alpha-* and *Deltaproteobacteria* are more abundant in outdoor communities, while *Gammaproteobacteria* are more abundant in indoor communities. Generally, *Betaproteobacteria* are the most abundant across all communities (Table 4.1).

## 4.5. Discussion

### 4.5.1 Comparison to Literature

SEM images of biomineralized hydrozincite samples from the Naracauli River site (Figure 4.4, De Giudici *et al.* (2009)) do not show morphological similarities to the samples at the Victoria Mine (Figure 2.17). This observation suggests that the Victoria Mine precipitates are not a product of biomineralization. Further, the oligotrophic conditions in the gallery (DOC =  $0.8 \pm 0.3$  ppm, Table S3) are not conducive to fast metabolism, suggesting that if any biomineralization is occurring, it would be slow in comparisons to abiotic mineral precipitation simulated by the geochemical model (see chapter 3). The cyanobacteria species *Scytonema* reported by Podda *et al.* (2000) to be responsible for the bioprecipitation of hydrozincite were not found inside (as expected because there is no sunlight) or outside of the Victoria Mine. In fact, no cyanobacteria were found. This further suggests that hydrozincite at the Victoria Mine is a product of abiotic processes.

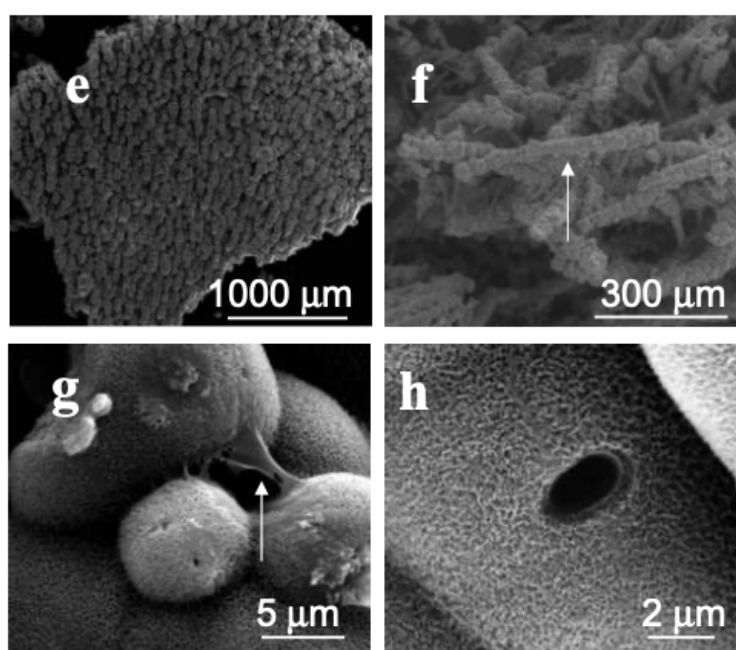


**Figure 4.4.** SEM images of natural hydrozincite biominerals from the Naracauli River site. Figure modified from De Giudici *et al.* (2009).

#### **4.5.2 Extent of Microbial Activity**

The results from the bioreactor experiments show that the outdoor community has no response to carbon stimulation. In contrast, the indoor community may have been negatively affected by the carbon amendment, such that the bacteria exposed to the carbon- and nutrient-rich conditions did not proceed with normal metabolism as defined by the control. Instead, the yeast extract appeared to inhibit normal metabolism. In the control reactor, bicarbonate, Zn, and Ni decreased over the 22-day period, suggesting that hydrozincite was precipitating. However, the relative molar consumption of Zn and bicarbonate was not proportional to that of hydrozincite. In general, any microbial activity occurring in these reactions was slow.

Modeling of abiotic hydrozincite precipitation suggests fast rates. For instance, Zn decreases approximately 0.4 mM in about 8 hours as water flows through the gallery (Figure 3.4). In contrast, the non-stimulated indoor community reactor exhibits a ~1 mM decrease in Zn over 22 days. This is a comparison between a through-flowing system and a batch reaction and therefore highly qualitative. Considering this, these results suggest that if microbial metabolism were responsible for decreasing the Zn concentration in the batch reactor experiments, it would be negligible in comparison to the abiotic rate.

#### **4.5.3 Diversity and Microbial Strategy**

Metagenomic analysis demonstrates that community diversity is higher outside of the mine than inside. Further, in the experiments, the indoor community metabolism may have been negatively affected by a carbon amendment, while the outdoor community was not. One explanation for these observations can be given by bacterial adaptation based on environmental variability.

In microbial ecology, a well-established concept is the notion that bacterial populations can be categorized as *r*- or *K*-strategists. The *r* term refers to the maximum net growth rate of a population, and the *K* term refers to the population density that can be supported in a given environment (i.e. carrying capacity) (Andrews and Harris, 1968). The *r*-strategists typically live in unstable and unpredictable environments. They have the ability to reproduce rapidly and adapt quickly. These organisms aim to flood their habitat with offspring when possible to increase the likelihood of survival when conditions change. In the context of a community, variable conditions lead to more opportunities for more different populations to succeed, thus

increasing diversity. Essentially, a community composed of *r*-strategist is an adaptable community.

The *K*-strategists tend to occupy more stable environments (e.g. caves). These organisms are typically more efficient and reproduce less than *r*-strategists. *K*-strategists are not as well-equipped to take advantage of, or protect themselves from, a change in conditions (e.g. temperature change, carbon stimulation). These organisms are well-adapted, but not adaptable. Stable conditions do not provide as many opportunities for organisms to compete, grow, and adapt as unstable conditions. Therefore, it is more likely to find a less diverse community in a stable environment, where *K*-strategists dominate.

The inverse Simpson indices (Equation 4.1) calculated for the communities illustrate the concept of environmental stability versus diversity. The gallery communities show significantly less diversity than the outdoor communities (Table 4.1). This agrees with the ecological theory of *r*- and *K*-strategists.

Applying this theory to the bioreactor experiments, the indoor communities would be expected to take advantage of and/or protect themselves from an environmental shift, while the indoor communities would not be expected to adapt as well. This is, in some ways, what was observed in the experiments. The indoor population is inhibited by the carbon-stimulation, while the outdoor population is unaffected. Thus, reaffirming that biomineralization of the hydrozincite is negligible in the mine, neither will it potentially occur in a hypothetical DOC-rich scenario to enhance precipitation.



## 4.6 Conclusions

Biominalization of hydrozincite is reported to exhibit significant control on heavy metal mobility in other abandoned mining sites (De Giudici *et al.* (2008); De Giudici *et al.* (2017), Podda *et al.* (2000), and Wanty *et al.*, 2013). However, at the Victoria Mine, evidence shows that the microbiological effects on both metal attenuation and aqueous geochemistry are of minor importance. Bioreactors inoculated with natural indoor and outdoor populations exhibit slow (if any) microbial activity, regardless of carbon stimulation. Comparison of SEM suggests no morphological similarities between biomineralized hydrozincite and the hydrozincite found in the Victoria Mine. Further, metagenomic analysis confirms that the cyanobacteria associated with biomineralization are not present.

Proteobacteria is the dominant phylum at the Victoria Mine and a relatively abundant Firmicutes population is found inside of the gallery. Inside the mine, where conditions are stable, community diversity is low when compared to that of the outdoor communities where conditions are less stable. Additionally, indoor communities in the bioreactors are hindered by carbon stimulation, while outdoor communities are unaffected. These behaviors are consistent with the ecological theory of *r*- and *K*- strategists.

In conclusion, the Victoria Mine exhibits patterns of microbial growth and community structure consistent with that of normal oligotrophic conditions. Thus, it can be reasonably assumed that metal mobility (i.e. hydrozincite precipitation) is controlled by abiotic process.



## CHAPTER 5 – GENERAL DISCUSSION AND CONCLUSIONS

An in-depth study of the biogeochemical processes affecting secondary mineral precipitation and metal mobility at the Victoria Mine in the Aran Valley, Catalonia, Spain has been performed. It includes a multi-year spatiotemporal characterization of the system, quantification of the critical geochemical processes that occur using the CrunchFlow reactive transport code, and an examination of the effects of microbial-mediated reactions.

Characterization of the solids found in the mine show that hydrozincite, smithsonite and calcite are precipitating inside the gallery. Hydrozincite is by far the most abundant solid. The hypothesis here is that hydrozincite formation is causing the observed loss of dissolved Zn, Ni, and Cd in the water as it moves through the gallery. This is supported by (1) the acid digestions, which demonstrate that hydrozincite incorporates significant amounts of Zn, Cd and Ni along with several other elements (e.g. S, Ca, K, Mg and Fe; Table 2.3) and (2) geochemical modeling. Additionally, previous research shows that hydrozincite is an effective metal sink mineral in geochemical conditions similar to that of the Victoria Mine (Podda *et al.*, 2000).

Further examination of the solids shows elemental zonation in hydrozincite, in particular Zn, occurs intermittently (in layers) as the mineral forms (Figures 2.18(A-D)). In one example, the nodule morphology, smithsonite and calcite form in repeating layers. This suggests that conditions in and above the mine change such that the water composition causes intermittent formation of (1) smithsonite and calcite and (2) the Zn-rich (pure) and Zn-poor (Ca-rich) hydrozincite. The elemental zoning in hydrozincite, detected by electron microprobe analysis in the botryoidal and floating skin morphologies (Figures 2.18(C-D)) is hypothesized to be product of variable oversaturation of the mineral. In short, when conditions lead to high oversaturation of the mineral, impurities can be more regularly incorporated into the solid. In essence, when atoms are attaching rapidly to the crystal growth sites (i.e. high precipitation rates), impurities are more likely to be "buried" under the subsequent additions to the crystal resulting in a less pure phase.

Comparison of the solid-to-liquid ratios of Cd and Ni (e.g.  $Cd_{(s)}/Cd_{(l)}$ ) between samples from the Victoria Mine and the Naracauli River (i.e. Podda *et al.*, 2000) highlights two consequential metal-incorporating effects. First, the effectiveness of trace metal polishing diminishes with increasing metal concentration across the range considered here (Cd: 105 – 3,280 ppb, Ni: 170 – 377 ppb), such that the solid-to-liquid ratio decreases with increasing dissolved metal concentration. Second, hydrozincite more readily uptakes Ni over Cd, which is likely caused by distinct mechanisms of incorporation. Ni is more likely incorporated into the crystal lattice because its charge and atomic radii are similar, whereas Cd is known to form amorphous surface precipitates (Lattanzi *et al.*, 2010).

Since formation of hydrozincite is the primary metal polishing mechanism, quantifying an equilibrium constant for the mineral is critical as it serves to parameterize the geochemical reactive transport model designed to simulate its formation. Therefore, the value of  $K_{eq}$  of a hydrozincite sample from the mine was determined by experiments to better inform the model described in Chapter 3. The value found in these experiments ( $\log[K_{eq}] = 30.01$  at  $7^{\circ}C$ ) was not highly sensitive to temperature and agrees with the value determined by Schindler *et al.* (1969) ( $\log[K_{eq}] = 30.14$  at  $25^{\circ}C$ ), who used a pure endmember sample. Applying the experimentally determined  $K_{eq}$  to calculate SI values for hydrozincite in the mine returned unexpectedly high SI values (SI = 5-12; Figure 2.21). The amorphous material, demonstrated by broad XRD peaks along with significant impurities in the analyzed solids, led to the hypothesis that there exists a variability in the solubility of hydrozincite beyond the pure endmember value. This is congruent with theory of mineral precursors (i.e. Ostwald's step rule (Van Santen, 1984)) in that less soluble amorphous precursors with (i.e. higher  $K_{eq}$  values) could form before hydrozincite. Given this, it is critical that such behavior (i.e. variability in  $K_{eq}$ ) be accounted for and constrained to improve modeling predictions. In section 2.4.1, two new  $K_{eq}$  values, assumed to describe the range in solubility and account for any precursor effects are calculated. This is done by assuming that the water, at two relevant locations, was in equilibrium (i.e.  $SI = 0 = \log[IAP/K_{eq(new)}]$ ) with hydrozincite where the mineral was found in the mine. The two new  $K_{eq}$  values correspond to a range of possible hydrozincite solubility values ( $30.01 < \log[K_{eq}] < 37.68$ ) and is thus applied to the model. This practice allows the model to make predictions that confidently represent the true behavior of the mineral.

Modeling of the Victoria Mine is done to (1) to quantify the geochemical processes occurring at the site and reproduce measured solute concentrations, (2) quantify the variability associated with metal mobility depending on realistic changes in the geochemical conditions and a realistic range of parameter values, and (3) explain the heterogeneity observed in the solid samples taken from the mine. Notably, it is assumed that metal mobility and hydrozincite precipitation are directly correlated. Therefore, changes to dissolved Zn concentrations directly correlate to changes in Cd and Ni concentrations.

The whole system model is constructed in two stages that are coupled by the conservation of concentrations. The first stage consists of two parallel 1D host rock models that vary only in sphalerite and pyrite mineral reactivity. The second stage is a 2D gallery model that mixes the resulting host rock waters before they flow down the 1330 Gallery where sampling took place. The initial goal is to generate a reference case in both parts of the model, where measured concentrations with distance are reproduced and the formation of hydrozincite, smithsonite, and calcite are simulated. Using the reference case as starting point, sensitivities of the model parameters that had not been well constrained are tested. In doing so, a range of results are produced as a way to capture the possible behavior of the system. Those tested parameters include the range of  $K_{eq}$  values associated with hydrozincite, flow velocity, dispersivity, and a homogenous host rock case. The homogenous host rock case serves to reinforce the initial assumption that the host rock above the mine is composed of different rock and mineral layers (i.e. calcite, sphalerite and pyrite).

The two 1D host rock models reproduce the solute concentrations observed at two locations discovered as water sources for the 1330 Gallery (Figure 3.3). The 2D gallery model reproduces both the measured solute concentrations (Figure 3.4) and the precipitation of hydrozincite, smithsonite, and calcite (Figure 3.5). The case for a homogeneous host rock demonstrates that the initial assumption of rock layers (Figure 3.1) is likely correct, as measured concentrations could not be reproduced in the homogenous case (Figures 3.11 and 3.12). Seven results from the different cases show that hydrozincite solubility (i.e. the  $K_{eq}$  value) is the parameter exhibiting the most dominant control on metal mobility (Table 3.6 and Figure 3.9). This is a significant finding, as a large body of geochemical modeling literature often assigns one  $K_{eq}$  value for a given mineral (i.e. pure endmember). In the case of hydrozincite such a practice could result in inaccurate predictions. This practice can improve predictions for other systems where hydrozincite is the primary metal polishing mechanism.

The simulated range of flow velocities (Figures 3.6 – 3.8) proportionate to the variability of discharge measured outside of the mine (section 2.3.2) gives unexpected results in terms of metal mobility. The fast and slow cases result in almost equal, yet a slightly higher metal flux out of the system when compared to the reference case (Table 3.6). This implies that several competing geochemical processes cause a non-linear relationship between volumetric discharge and metal mass flux out of the system. However, only three reasonable flow velocities were tested here. Further testing may demonstrate how flow velocity and volumetric discharge affects metal mobility.

The theoretical solids reproduced by the model are a result of the relative precipitation rates of hydrozincite, smithsonite and calcite. In the reference case, the model reproduces a theoretical solid that is almost completely hydrozincite with small amounts of calcite and smithsonite, similar to the samples collected in the mine (Figure 3.5). It is important to note that hydrozincite precipitation occurs under the local equilibrium assumption because kinetic parameters are unknown. One important finding is that changing flow rates results in changes to the mineral proportions in the resulting solid. For example, the slow flow case results in almost no smithsonite precipitation, while the fast flow case results in a solid that would have slightly more smithsonite than calcite (Figure 3.8). This helps to explain the mineral layering of smithsonite and calcite observed in the nodule morphology sample. Further, the changes in the hydrozincite precipitation rates provide an explanation of the observed Zn zonations in the botryoidal and floating skin morphologies consistent with the theory of impurity incorporation when waters are highly oversaturated with respect to the mineral. Generally, the modeling successfully captures the range of behavior observed at the mine, as well as the range of behavior expected to occur given significant perturbations to the system.

The model succeeds in theoretically reproducing the heterogeneity observed in the solid samples, suggesting that microbiological controls on mineral formation do not play a significant role at the Victoria Mine, unlike that of the Naracauli River case (De Giudici *et al.*, 2009; Podda *et al.*, 2000). Additionally, DOC concentrations were low in the mine ( $0.8 \pm 0.3$  ppm; Table S3) and therefore any microbial activity would likely be slow in comparison to the abiotic processes occurring. The metagenomic analysis of bacterial 16s rRNA from locations inside and outside of the mine reveals: (1) Proteobacteria dominate the local communities and (2) more taxonomic diversity occurs in communities living outside of the mine rather than inside. When the indoor and outdoor communities were placed in bioreactors and stimulated

with yeast extract, a labile organic carbon and nutrient source, the outdoor communities were unaffected and the indoor communities were inhibited from normal functioning. These results, both sequencing and experimental, align with the theory of *r*- and *K*-strategists in ecology. Indoor (less diverse) communities are composed of organisms more adapted to their current (stable) environment and more sensitive to changes in their conditions. This is the behavior of a community of *K*-strategists. Conversely, outdoor (more diverse) communities are more adaptable to new conditions (e.g. carbon stimulation), which reflects a community of *r*-strategists.

In conclusion, this work provides a detailed explanation for the natural metal attenuation of dissolved metals observed at the Victoria Mine and confirms that microbial metabolism is not significantly affecting secondary mineral formation. Analysis and characterization of the solids and liquids help constrain a CrunchFlow geochemical RTM. The model simulates the system's response to a realistic range of parameter values and geochemical perturbations. Thus, it successfully captures the behavior of metal mobility and, ultimately, the associated environmental impact. Fortunately, the Victoria Mine poses little threat to the environment, and is predicted to continue behaving in such a manner via secondary precipitation of hydrozincite. Such findings can and should be applied to other abandoned and active mining sites exhibiting similar characteristics. This work can help resolve potential remediation issues, and serve to improve our ability to predict harmful metal mobility in the future.





## SUPPLEMENTARY INFORMATION

**Table S1.** *In-situ* measurements and ion concentration results from three sampling campaigns. Values given in ppm and ppb.

Campaign Date	Sample Position	Temp. (°C)	pH	Cond. (µS/cm)	Alkalinity (ppm HCO <sub>3</sub> <sup>-</sup> )	Major Elements (ppm)							Minor Elements (ppb)						
						Na	K	Mg	S	Ca	Si	Zn	Cd	Sr	Al	Li	Ni	Fe	
June 7-9 2021	1	10.7	7.9	277	91	2.1	1.9	2.4	15.6	46.3	3.9	0.2	1	111	13	3	2	12	
	2	8.5	7.6	309	85	1.4	1.5	2.0	24.1	49.9	3.7	5.5	14	103	20	3	22	20	
	3	6.9	7.5	986	104	5.8	2.7	17.1	149.0	175.0	4.3	9.6	23	550	135	34	42	13	
	4	6.3	7.6	1,146	110	6.4	2.7	19.9	168.5	195.6	4.6	9.9	22	632	26	40	45	23	
	5	5.9	8.0	845	85	4.8	2.5	14.9	127.0	149.2	3.1	3.1	14	370	9	33	32	37	
	6	6	8.7	950	98	5.0	2.6	16.7	139.3	162.7	4.0	9.5	19	408	22	35	49	15	
	7	6	7.9	1,049	134	4.9	3.3	16.0	136.1	160.6	4.1	10.5	18	407	18	35	53	43	
	8	6.2	8.0	1,219	122	6.8	3.0	25.2	200.8	221.4	3.6	9.3	17	597	0	42	48	16	
	9	6.6	7.4	2,580	168	10.6	5.4	85.4	550.0	473.7	7.6	138.3	102	970	0	130	363	59	
	10	7.1	8.0	1,156	128	6.7	3.0	22.4	183.1	211.9	3.5	6.0	11	582	8	38	35	101	
	11	11.55	7.9	318	171	1.2	1.2	0.8	9.2	61.8	3.3	0.0	0	126	28	0	1	8	
<b>II (σ)</b>		0.25	0.1	8	24	0.2	0.1	0.2	5.2	1.9	0.3	0.0	0	3	3	0	1	3	
Drip Water 2021	5	NA	NA	NA	NA	5.2	4.6	6.8	66.4	76.6	3.2	0.0	0	294	35	12	11	25	
	6	7	8.3	468	85	3.5	1.8	7.6	91.0	133.6	4.3	0.0	0	225	17	19	22	12	
	8	6.5	7.6	763	98	3.5	2.8	10.6	103.1	110.4	6.2	37.5	47	233	3	28	111	9	
	9	6.6	7.5	2,580	168	10.0	4.6	85.5	559.0	462.4	5.2	154.8	105	985	0	132	377	299	
	1	14.1	7.6	272	98	2.3	1.4	2.8	16.8	45.4	4.7	0.3	1	106	7	2	0	5	
July 14-16 2020	2	10.7	7.1	315	104	1.6	1.1	2.7	21.8	51.2	4.5	6.1	16	91	5	4	22	3	
	3	8.7	7.0	997	110	5.4	2.7	18.9	148.1	172.0	4.5	15.1	34	425	13	32	53	4	
	4	7.0	7.1	1,271	104	7.2	3.2	26.1	202.3	226.6	4.7	19.5	43	661	3	45	66	3	
	5	6.7	7.0	936	85	5.1	2.8	18.5	139.1	160.5	4.6	10.5	26	331	0	33	55	2	
	6	6.6	7.0	1,009	85	5.4	2.7	20.3	152.1	171.2	5.1	19.1	30	353	3	36	70	4	
	7	6.1	7.1	1,015	116	5.2	2.9	20.7	154.5	171.8	5.1	21.0	31	355	1	35	69	5	
	8	7.0	7.9	1,279	110	7.7	3.1	28.9	213.3	239.5	5.1	15.1	21	638	0	47	70	0	
	10	7.0	7.9	1,236	134	7.0	3.2	25.7	193.6	229.1	3.8	7.0	13	634	4	39	36	30	
	11	11.6	8.1	328	189	1.1	0.5	1.2	6.4	70.4	4.0	0.0	0	137	3	0	0	15	
	<b>II (σ)</b>		0.5	0.1	8	6	0.1	0.2	0.1	3.2	1.1	0.4	0.0	0	9	1	0	0	3
	Oct. 20-23 2019	1	10.1	7.4	NA	110	2.6	1.8	3.7	27.3	60.2	4.1	0.2	1	141	5	3	3	9
3		6.1	7.0	NA	NA	6.7	2.9	19.9	158.8	196.6	4.5	9.6	22	615	2	37	42	3	
5		5.6	7.2	NA	NA	5.5	2.9	17.7	141.1	170.2	3.4	4.4	20	407	2	33	40	6	
8		6.3	7.1	NA	NA	7.5	3.4	28.4	221.0	251.0	3.8	15.8	28	638	4	52	66	6	
10		NA	NA	NA	NA	7.8	4.0	29.0	226.8	261.2	3.7	19.5	27	666	25	52	68	140	
11		7.4	7.4	NA	183	1.1	0.8	1.1	6.4	61.5	3.6	0.0	0	118	5	0	2	11	
<b>II (σ)</b>		0.1	0.1	NA	18.3	0.2	0.2	0.1	2.5	0.5	0.5	0.0	0.1	0.0	1.4	0.1	1.5	0.6	
<b>Detection Limit</b>		NA	NA	1.0	6.1	0.50	0.50	0.05	0.50	0.05	0.20	0.02	0.1	0.2	2.0	0.1	0.2	20.0	
<b>Analytical Error (±)</b>		0.01	0.05	0.5	6.1	6%	6%	6%	6%	6%	6%	6%	6%	6%	6%	6%	6%	6%	

**Table S2.** *In-situ* measurements and ion concentration results from three sampling campaigns. Values given in mM and  $\mu\text{M}$ .

Campaign Date	Sample Position	Temp. (°C)	pH	Cond. ( $\mu\text{S}/\text{cm}$ )	Alkalinity (mM $\text{HCO}_3^-$ )	Major Elements (mM)						Minor Elements ( $\mu\text{M}$ )						
						Na	K	Mg	S	Ca	Si	Zn	Cd	Sr	Al	Li	Ni	Fe
June 7-9 2021	1	10.7	7.9	277	1.5	0.09	0.05	0.10	0.49	1.16	0.14	0.00	0.01	1.27	0.49	0.38	0.04	0.22
	2	8.5	7.6	309	1.4	0.06	0.04	0.08	0.75	1.25	0.13	0.08	0.13	1.18	0.75	0.49	0.38	0.35
	3	6.9	7.5	986	1.7	0.25	0.07	0.70	4.65	4.37	0.15	0.15	0.20	6.28	5.02	4.91	0.72	0.24
	4	6.3	7.6	1,146	1.8	0.28	0.07	0.82	5.26	4.88	0.16	0.15	0.20	7.22	0.96	5.73	0.77	0.41
	5	5.9	8.0	845	1.4	0.21	0.06	0.61	3.96	3.72	0.11	0.05	0.12	4.22	0.34	4.74	0.55	0.66
	6	6	8.7	950	1.6	0.22	0.07	0.69	4.34	4.06	0.14	0.15	0.17	4.66	0.82	5.07	0.84	0.27
	7	6	7.9	1,049	2.2	0.21	0.08	0.66	4.24	4.01	0.14	0.16	0.16	4.64	0.66	5.01	0.90	0.77
	8	6.2	8.0	1,219	2.0	0.29	0.08	1.04	6.26	5.52	0.13	0.14	0.15	6.81	0.00	6.04	0.81	0.28
	9	6.6	7.4	2,580	2.7	0.46	0.14	3.51	17.16	11.82	0.27	2.12	0.90	11.07	0.00	18.75	6.19	1.05
	10	7.1	8.0	1,156	2.1	0.29	0.08	0.92	5.71	5.29	0.12	0.09	0.10	6.64	0.29	5.49	0.60	1.80
	11	11.55	7.9	318	2.8	0.05	0.03	0.03	0.29	1.54	0.12	0.00	0.00	1.44	1.06	0.01	0.01	0.14
	<i>II (<math>\sigma</math>)</i>	<i>0.25</i>	<i>0.1</i>	<i>8</i>	<i>0.4</i>	<i>0.01</i>	<i>0.00</i>	<i>0.01</i>	<i>0.16</i>	<i>0.05</i>	<i>0.01</i>	<i>0.00</i>	<i>0.00</i>	<i>0.03</i>	<i>0.11</i>	<i>0.01</i>	<i>0.01</i>	<i>0.06</i>
Drip Water 2021	5	NA	NA	NA	NA	0.23	0.12	0.28	2.07	1.91	0.11	0.00	0.00	3.35	1.31	1.70	0.20	0.45
	6	7	8.3	468	1.4	0.15	0.05	0.31	2.84	3.33	0.15	0.00	0.00	2.57	0.64	2.74	0.37	0.21
	8	6.5	7.6	763	1.6	0.15	0.07	0.44	3.22	2.76	0.22	0.57	0.42	2.66	0.10	4.06	1.89	0.17
	9	6.6	7.5	2,580	2.7	0.44	0.12	3.52	17.44	11.54	0.18	2.37	0.93	11.24	0.00	18.96	6.43	5.36
July 14-16 2020	1	14.1	7.6	272	1.6	0.10	0.03	0.11	0.52	1.13	0.17	0.00	0.01	1.21	0.26	0.36	0.00	0.08
	2	10.7	7.1	315	1.7	0.07	0.03	0.11	0.68	1.28	0.16	0.09	0.14	1.04	0.19	0.57	0.38	0.06
	3	8.7	7.0	997	1.8	0.23	0.07	0.78	4.62	4.29	0.16	0.23	0.31	4.85	0.50	4.65	0.91	0.07
	4	7.0	7.1	1,271	1.7	0.31	0.08	1.07	6.31	5.65	0.17	0.30	0.38	7.54	0.13	6.44	1.12	0.06
	5	6.7	7.0	936	1.4	0.22	0.07	0.76	4.34	4.00	0.16	0.16	0.23	3.78	0.02	4.77	0.93	0.04
	6	6.6	7.0	1,009	1.4	0.24	0.07	0.83	4.74	4.27	0.18	0.29	0.27	4.03	0.11	5.15	1.19	0.08
	7	6.1	7.1	1,015	1.9	0.23	0.07	0.85	4.82	4.29	0.18	0.32	0.27	4.06	0.05	5.04	1.17	0.09
	8	7.0	7.9	1,279	1.8	0.34	0.08	1.19	6.65	5.98	0.18	0.23	0.19	7.28	0.00	6.72	1.20	0.00
	10	7.0	7.9	1,236	2.2	0.30	0.08	1.06	6.04	5.72	0.14	0.11	0.11	7.23	0.14	5.65	0.61	0.54
	11	11.6	8.1	328	3.1	0.05	0.01	0.05	0.20	1.76	0.14	0.00	0.00	1.56	0.13	0.03	0.00	0.28
		<i>II (<math>\sigma</math>)</i>	<i>0.5</i>	<i>0.1</i>	<i>8</i>	<i>0.1</i>	<i>0.00</i>	<i>0.00</i>	<i>0.00</i>	<i>0.10</i>	<i>0.03</i>	<i>0.02</i>	<i>0.00</i>	<i>0.00</i>	<i>0.10</i>	<i>0.03</i>	<i>0.01</i>	<i>0.00</i>
Oct. 20-23 2019	1	10.1	7.4	NA	1.8	0.11	0.05	0.15	0.85	1.50	0.15	0.00	0.01	1.61	0.20	0.39	0.05	0.15
	3	6.1	7.0	NA	NA	0.29	0.07	0.82	4.95	4.91	0.16	0.15	0.20	7.02	0.07	5.27	0.72	0.05
	5	5.6	7.2	NA	NA	0.24	0.07	0.73	4.40	4.25	0.12	0.07	0.18	4.64	0.08	4.74	0.68	0.12
	8	6.3	7.1	NA	NA	0.33	0.09	1.17	6.89	6.26	0.13	0.24	0.25	7.29	0.16	7.46	1.12	0.11
	10	NA	NA	NA	NA	0.34	0.10	1.19	7.07	6.52	0.13	0.30	0.24	7.60	0.93	7.53	1.16	2.51
	11	7.4	7.4	NA	3.0	0.05	0.02	0.04	0.20	1.53	0.13	0.00	0.00	1.35	0.20	0.03	0.04	0.19
	<i>II (<math>\sigma</math>)</i>	<i>0.1</i>	<i>0.1</i>	<i>NA</i>	<i>0.3</i>	<i>0.01</i>	<i>0.01</i>	<i>0.00</i>	<i>0.08</i>	<i>0.01</i>	<i>0.02</i>	<i>0.00</i>	<i>0.00</i>	<i>0.00</i>	<i>0.05</i>	<i>0.02</i>	<i>0.03</i>	<i>0.01</i>
Detection Limit Analytical Error ( $\pm$ )		NA	NA	1	0.1	0.022	0.013	0.002	0.016	0.001	0.007	0.000	0.001	0.002	0.074	0.014	0.003	0.358
		0.01	0.05	0.5	0.1	6%	6%	6%	6%	6%	6%	6%	6%	6%	6%	6%	6%	6%

**Table S3.** Dissolved organic carbon (DOC) concentrations from 2020 sampling campaign. Samples were filtered through a 0.22  $\mu\text{m}$  membrane. Analytical error is 0.05 ppm.

Sample	DOC (ppm)
1	1.3
2	1.6
3	0.8
4	0.5
5	0.6
6	0.6
7	0.6
8	0.5
10	0.6
11	1.0
<b>11 (<math>\sigma</math>)</b>	<b>0.0</b>

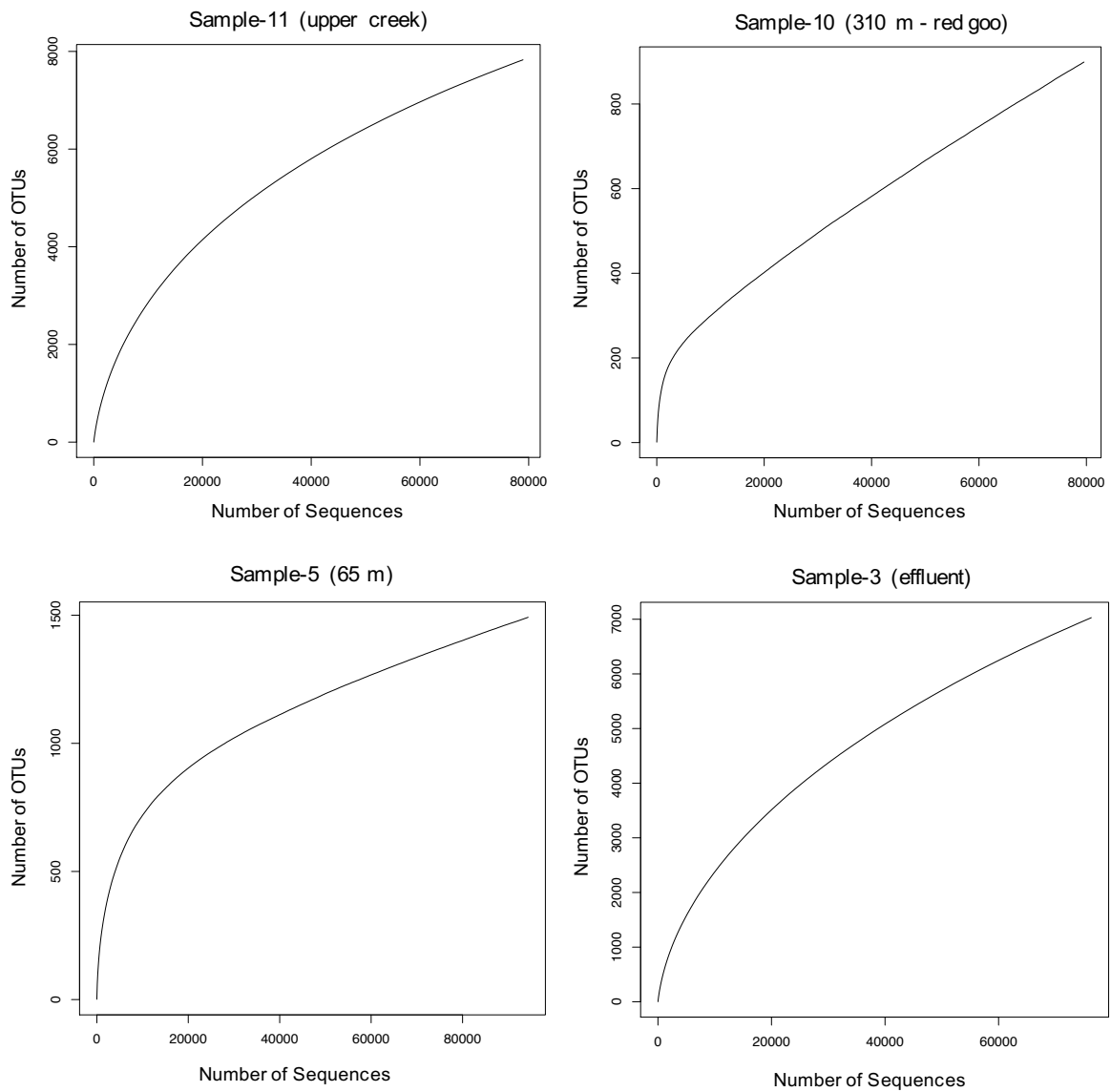


**Figure S1.** Rarefaction curves for each sample calculated using the Galaxy Ecology platform (Afgan *et al.*, 2018)

**Table S4.** Electron microprobe point analysis results given in ppm solid. CO<sub>2</sub> is calculated.

Sample	Analysis #	ZnO	CaO	SrO	CdO	NiO	MgO	FeO	MnO	CO <sub>2</sub>	Total (%)
Nodule	1	8,885	549,200	2,750	0	0	0	331	209	437,300	99.9
	2	643,400	16,200	0	4,356	1,753	0	1,506	90	364,300	103.2
	3	645,500	17,600	0	0	1,574	0	430	0	364,100	102.9
	4	38,300	516,900	1,966	646	0	344	588	97	428,200	98.7
	5	708,200	9,957	44	335	2,551	0	0	388	392,700	111.4
	6	31,000	522,500	2,773	0	24	0	177	126	428,200	98.5
	7	670,300	17,500	44	0	1,312	0	0	172	377,200	106.7
	8	11,805	545,600	1,828	357	0	0	46	0	435,500	99.5
	9	13,900	535,700	2,387	0	66	0	229	0	429,100	98.1
	10	15,400	536,000	2,068	790	0	36	0	0	430,200	98.4
	11	260,500	344,100	1,277	0	723	0	51	0	412,000	101.9
	12	19,600	524,900	1,795	395	0	144	220	0	423,800	97.1
	13	213,400	377,700	1,346	0	697	0	0	214	413,000	100.6
	14	21,200	508,400	2,283	413	0	5	0	34	411,600	94.4
Smooth	66	13,900	535,700	2,387	0	66	0	229	0	429,100	98.0
Layered	67	15,400	536,000	2,068	790	0	36	0	0	430,200	101.8
	68	260,500	344,100	1,277	0	723	0	51	0	412,000	105.4
	69	19,600	524,900	1,795	395	0	144	220	0	423,800	102.4
	70	213,400	377,700	1,346	0	697	0	0	214	413,000	106.2
	71	21,200	508,400	2,283	413	0	5	0	34	411,600	100.4
Floating Skin	15	282,000	1,391	186	0	183	0	0	0	153,800	43.8
	16	282,900	1,773	0	230	364	0	0	80	154,800	44.0
	17	331,100	2,396	352	0	143	0	0	0	181,200	51.5
	18	229,200	1,427	0	813	255	0	0	4	125,500	35.7
	19	325,000	2,133	348	313	152	0	0	55	177,800	50.6
	20	286,700	1,694	304	0	230	898	0	0	157,700	44.8
	21	373,600	2,455	77	583	327	0	60	28	204,500	58.2
	22	345,100	2,253	296	0	282	113	183	0	188,900	53.7
	23	288,200	1,582	0	416	157	0	0	0	157,400	44.8
	24	369,700	1,455	33	0	343	0	0	0	201,300	57.3
	25	275,800	1,179	645	270	198	0	139	19	150,700	42.9
	26	220,700	1,213	0	437	78	0	0	0	120,500	34.3
	27	239,200	1,625	644	770	314	0	0	0	131,400	37.4
	28	616,300	334	0	0	486	0	0	0	333,900	95.1
	29	292,300	1,750	0	934	190	0	7	81	159,900	45.5
	30	370,600	2,071	269	664	254	0	213	0	202,700	57.7
	31	303,800	1,787	151	395	207	0	0	0	166,000	47.2
	32	242,900	2,227	0	0	83	202	60	86	133,500	37.9
	33	144,900	1,511	786	602	0	0	0	49	80,100	22.8
	34	84,600	126	145	145	121	0	0	15	46,100	13.1
	35	224,500	688	0	0	131	0	0	0	122,000	34.7
	36	368,800	0	243	0	252	0	0	0	199,700	56.9
	37	202,400	1,705	158	104	168	0	0	52	111,000	31.6
	38	401,000	0	363	0	111	0	0	38	217,100	61.9
	39	634,000	1,013	0	0	613	0	0	0	344,100	98.0
	40	240,300	1,168	0	0	63	0	0	0	130,900	37.2
	41	295,300	1,811	0	931	97	0	10	46	161,600	46.0
	42	346,300	2,492	71	249	259	0	0	0	189,500	53.9
	43	380,800	2,430	0	0	280	0	0	62	208,100	59.2
	44	268,800	2,017	0	1,282	82	0	0	5	147,500	42.0
	45	226,200	1,360	0	0	178	72	0	0	123,600	35.1
	46	495,800	1,181	283	0	487	0	0	0	269,500	76.7
47	415,100	3,179	0	1,404	421	190	0	0	227,900	64.8	
48	423,600	3,096	0	0	147	0	0	265	231,800	65.9	
49	310,900	2,370	124	206	320	0	0	0	170,300	48.4	
50	411,700	1,973	427	0	260	0	0	0	224,600	63.9	
51	336,200	3,822	419	371	64	138	52	87	185,400	52.7	
52	252,200	510	0	2,370	129	0	911	41	138,300	39.4	
Botryoidal	53	678,700	5,144	845	165	760	0	0	0	372,000	105.8
	54	398,900	3,532	50	1,318	217	0	24	110	219,200	62.3
	55	553,800	3,975	0	0	356	0	0	18	302,900	86.1
	56	384,000	3,127	0	494	387	304	0	34	210,900	59.9
	57	524,800	5,044	589	103	932	601	0	96	289,400	82.2
	58	395,300	2,338	284	165	256	0	0	109	216,000	61.4
	59	467,800	3,869	0	0	646	0	0	62	256,500	72.9
	60	405,800	3,324	250	493	209	0	71	0	222,500	63.3
	61	504,000	3,244	0	123	354	0	214	87	275,600	78.4
	62	367,900	2,783	0	0	274	23	0	0	201,400	57.2
	63	622,900	4,372	0	0	1,219	0	0	87	341,100	97.0
	64	418,200	2,336	0	431	257	623	0	118	229,100	65.1
	65	526,100	3,917	0	0	720	0	0	0	288,100	81.9

Hyperlinks and URLs to Krona diagrams:

- [Sample-11](#)
  - file:///Users/max/Documents/Aran%20Valley/DNA/First%20Analysis/Krona/Sample11\_UpperMelics.html
- [Sample-10](#)
  - file:///Users/max/Documents/Aran%20Valley/DNA/First%20Analysis/Krona/Sample10\_RedGoo.html
- [Sample-5](#)
  - file:///Users/max/Documents/Aran%20Valley/DNA/First%20Analysis/Krona/Sample5\_65meters.html
- [Sample-3](#)
  - file:///Users/max/Documents/Aran%20Valley/DNA/First%20Analysis/Krona/Sample3\_Effluent.html



## REFERENCES

- Acinas, S. G., Marcelino, L. A., Klepac-Ceraj, V., & Polz, M. F. (2004). Divergence and redundancy of 16S rRNA sequences in genomes with multiple *rrn* operons. *Journal of bacteriology*, *186*(9), 2629-2635.
- Afgan, E., Baker, D., Batut, B., Van Den Beek, M., Bouvier, D., Čech, M., & Blankenberg, D. (2018). The Galaxy platform for accessible, reproducible and collaborative biomedical analyses: 2018 update. *Nucleic acids research*, *46*(W1), W537-W544.
- Agnew, U. M., & Slesinger, T. L. (2020). Zinc toxicity. *StatPearls Publishing*.  
<https://www.ncbi.nlm.nih.gov/books/NBK554548/>
- Albon, N., & Dunning, W. J. (1962). Growth of sucrose crystals: determination of edge energy from the effect of added impurity on rate of step advance. *Acta Crystallographica*, *15*(5), 474-476.
- Álvarez-Pérez, A., Campá-Viñeta, J. A., & Montoriol-Pous, J. (1977). Mineralogénesis de los yacimientos del área de Bossost (Vall d'Aran, Lérida). *Acta geológica hispánica*, *12*(4), 123-126.
- Andrews, J. H., & Harris, R. F. (1986). r-and K-selection and microbial ecology. *Advances in microbial ecology*, 99-147.
- Arbel, Y., Greenbaum, N., Lange, J., & Inbar, M. (2010). Infiltration processes and flow rates in developed karst vadose zone using tracers in cave drips. *Earth Surface Processes and Landforms*, *35*(14), 1682-1693.
- Bethke, C. M., Sanford, R. A., Kirk, M. F., Jin, Q., & Flynn, T. M. (2011). The thermodynamic ladder in geomicrobiology. *American Journal of Science*, *311*(3), 183-210.
- Braissant, O., Cailleau, G., Dupraz, C., & Verrecchia, E. P. (2003). Bacterially induced mineralization of calcium carbonate in terrestrial environments: the role of exopolysaccharides and amino acids. *Journal of Sedimentary Research*, *73*(3), 485-490.
- Brenner, D. J., Krieg, N. R., Staley, J. T., & Garrity, G. (2005). *Bergey's manual of systematic bacteriology*, Vol 2: The Proteobacteria. NY: Springer.
- Bruneel, O., Duran, R., Casiot, C., Elbaz-Poulichet, F., & Personné, J. C. (2006). Diversity of microorganisms in Fe-As-rich acid mine drainage waters of Carnoules, France. *Applied and Environmental Microbiology*, *72*(1), 551-556.
- Cardellach, E., & Álvarez-Pérez, A. (1979). Interpretación genética de las mineralizaciones de Pb-Zn del Ordovícico superior de La Vall d'Aran (Lérida). *Acta Geologica Hispanica*, *14*(1), 117-120.
- Cardellach, E., Canals, A., & Pujals, I. (1996). La composición isotópica del azufre y del plomo en las mineralizaciones de Zn-Pb del Valle de Arán (Pirineo Central) y su significado metalogenético. *Estudios geológicos*, *52*(5-6), 189-195.
- Davey, R. J. (1975). Adsorption of impurities at growth steps. *Journal of Crystal Growth*, *29*(2), 212-214.
- De Giudici, G., Podda, F., Sanna, R., Musu, E., Tombolini, R., Cannas, C., & Casu, M. (2009). Structural properties of biologically controlled hydrozincite: An HRTEM and NMR spectroscopic study. *American Mineralogist*, *94*(11-12), 1698-1706.
- De Giudici, G., Pusceddu, C., Medas, D., Meneghini, C., Gianoncelli, A., Rimondi, V., & Kimball, B. A. (2017). The role of natural biogeochemical barriers in limiting metal loading to a stream affected by mine drainage. *Applied Geochemistry*, *76*, 124-135.
- Descostes, M., Vitorge, P., & Beaucaire, C. (2004). Pyrite dissolution in acidic media. *Geochimica et Cosmochimica Acta*, *68*(22), 4559-4569.

- Druhan, J. L., Lawrence, C. R., Covey, A. K., Giannetta, M. G., & Oster, J. L. (2021). A reactive transport approach to modeling cave seepage water chemistry I: Carbon isotope transformations. *Geochimica et Cosmochimica Acta*, 311, 374-400.
- Fairchild, I. J., Baker, A. (2012). *Speleothem science: from process to past environments* (Vol. 3). John Wiley & Sons.
- Fairchild, I.J., Frisia, S., Borsato, A. & Tooth, A.F. (2006). Speleothems. In: *Geochemical Sediments and Landscapes* (ed. Nash, D.J. and McLaren, S.J.), Blackwells, Oxford (*in press*)
- Fang, C., & Achal, V. (2019). Biostimulation of calcite precipitation process by bacterial community in improving cement stabilized rammed earth as sustainable material. *Applied microbiology and biotechnology*, 103(18), 7719-7727.
- Frank, J. A., Reich, C. I., Sharma, S., Weisbaum, J. S., Wilson, B. A., & Olsen, G. J. (2008). Critical evaluation of two primers commonly used for amplification of bacterial 16S rRNA genes. *Applied and environmental microbiology*, 74(8), 2461-2470.
- García-Sansegundo, J. (1996). Hercynian structure of the Axial Zone of the Pyrenees: the Aran Valley cross-section (Spain-France). *Journal of Structural Geology*, 18(11), 1315-1325.
- Ghose, S. (1964). The crystal structure of hydrozincite,  $Zn_5(OH)_6(CO_3)_2$ . *Acta Crystallographica*, 17(8), 1051-1057.
- Groth, I., Saiz-Jimenez, C. (1999). Actinomycetes in hypogean environments. *Geomicrobiology Journal*, 16(1), 1-8.
- Hales, M. C., & Frost, R. L. (2008). Thermal analysis of smithsonite and hydrozincite. *Journal of Thermal Analysis and Calorimetry*, 91(3), 855-860.
- Inaba, T., Kobayashi, E., Suwazono, Y., Uetani, M., Oishi, M., Nakagawa, H., & Nogawa, K. (2005). Estimation of cumulative cadmium intake causing Itai-itai disease. *Toxicology letters*, 159(2), 192-201.
- Janda, J. M., & Abbott, S. L. (2007). 16S rRNA gene sequencing for bacterial identification in the diagnostic laboratory: pluses, perils, and pitfalls. *Journal of clinical microbiology*, 45(9), 2761-2764.
- Lane, D. J., Pace, B., Olsen, G. J., Stahl, D. A., Sogin, M. L., & Pace, N. R. (1985). Rapid determination of 16S ribosomal RNA sequences for phylogenetic analyses. *Proceedings of the National Academy of Sciences*, 82(20), 6955-6959.
- Lasaga, A. C. (2014). *Kinetic theory in the earth sciences*. Princeton university press.
- Lattanzi, P., Maurizio, C., Meneghini, C., de Giudici, G., & Podda, F. (2010). Uptake of Cd in hydrozincite,  $Zn_5(CO_3)_2(OH)_6$ : evidence from X-ray absorption spectroscopy and anomalous X-ray diffraction. *European Journal of Mineralogy*, 22(4), 557-564.
- Leita, L., De Nobili, M., Muhlbachova, G., Mondini, C., Marchiol, L., & Zerbi, G. (1995). Bioavailability and effects of heavy metals on soil microbial biomass survival during laboratory incubation. *Biology and Fertility of Soils*, 19(2), 103-108.
- Lian, B., Hu, Q., Chen, J., Ji, J., & Teng, H. H. (2006). Carbonate biomineralization induced by soil bacterium *Bacillus megaterium*. *Geochimica et cosmochimica acta*, 70(22), 5522-5535.
- Livingstone, A., & Champness, P. E. (1993). Brianyoungite, a new mineral related to hydrozincite, from the north of England orefield. *Mineralogical Magazine*, 57(389), 665-670.
- López, E. C., Álvarez-Pérez, A., & Montoriol-Pous, J. (1977). Contribución al conocimiento de la arsenopirita de Liat (Vall d'Aran, Lleida). *Acta Geologica Hispanica*, 12(4), 117-119.



- Madsen, E. L. (2011). Microorganisms and their roles in fundamental biogeochemical cycles. *Current opinion in biotechnology*, 22(3), 456-464.
- Maher, K., Steefel, C. I., DePaolo, D. J., & Viani, B. E. (2006). The mineral dissolution rate conundrum: Insights from reactive transport modeling of U isotopes and pore fluid chemistry in marine sediments. *Geochimica et Cosmochimica Acta*, 70(2), 337-363.
- Marguí, E., Queralt, I., Carvalho, M. L., & Hidalgo, M. (2007). Assessment of metal availability to vegetation (*Betula pendula*) in Pb-Zn ore concentrate residues with different features. *Environmental Pollution*, 145(1), 179-184.
- Marguí, E., Salvadó, V., Queralt, I., & Hidalgo, M. (2004). Comparison of three-stage sequential extraction and toxicity characteristic leaching tests to evaluate metal mobility in mining wastes. *Analytica Chimica Acta*, 524(1-2), 151-159.
- Marques, A. F., Queralt, I., Carvalho, M. L., & Bordalo, M. (2003). Total reflection X-ray fluorescence and energy-dispersive X-ray fluorescence analysis of runoff water and vegetation from abandoned mining of Pb-Zn ores. *Spectrochimica Acta Part B: Atomic Spectroscopy*, 58(12), 2191-2198.
- Merz, J., & Doppmann, G. (2006). Measuring Mountain Stream Discharge Using the Salt Dilution Method. *UoB PARDYP/ICIMOD and Hydrology Group (Editor)*, Kathmandu.
- Oster, J. L., Covey, A. K., Lawrence, C. R., Giannetta, M. G., & Druhan, J. L. (2021). A reactive transport approach to modeling cave seepage water chemistry II: Elemental signatures. *Geochimica et Cosmochimica Acta*, 311, 353-373.
- Palandri, J. L., & Kharaka, Y. K. (2004). *A compilation of rate parameters of water-mineral interaction kinetics for application to geochemical modeling*. United States Geological Survey Menlo Park, CA.
- Qin, B., Gao, G., Zhu, G., Zhang, Y., Song, Y., Tang, X., ... & Deng, J. (2013). Lake eutrophication and its ecosystem response. *Chinese Science Bulletin*, 58(9), 961-970.
- Queralt, I. (2006) The use of low-cost EDXRF instrumentation in Earth Sciences and Environmental geochemistry. SARX-2006 X Latin American Conference of Analysis by X-ray Techniques, Arica (Chile). Plenary Lecture, Abstracts Book
- Hiltemann, S. Batut, B., Clements, D. (2019). 16S Microbial Analysis with mothur (extended) (Galaxy Training Materials). <https://training.galaxyproject.org/trainingmaterial/topics/metagenomics/tutorials/mothur-miseq-sop/tutorial.html>
- Santamaria, J., Ros, E., & Gavalda, J. (2008). *La minería de la Val d'Aran*.
- Bernhoft, R. A. (2013). Cadmium toxicity and treatment. *The Scientific World Journal*.
- Schwartz, M. O. (2000). Cadmium in zinc deposits: economic geology of a polluting element. *International Geology Review*, 42(5), 445-469.
- Schwertmann, U. (1991). Solubility and dissolution of iron oxides. *Plant and soil*, 130(1), 1-25.
- Sears, G. W. (1958). Effect of poisons on crystal growth. *The Journal of Chemical Physics*, 29(5), 1045-1048.
- Schindler, P., Reinert, M., & Gamsjäger, H. (1969). Zur thermodynamik der metallcarbonate 3. Mitteilung [1]. Löslichkeitskonstanten und freie bildungsenthalpien von ZnCO<sub>3</sub> und Zn<sub>5</sub>(OH)<sub>6</sub>(CO<sub>3</sub>)<sub>2</sub> bei 25°. *Helvetica Chimica Acta*, 52(8), 2327-2332.
- Smith, M. B., Rocha, A. M., Smillie, C. S., Olesen, S. W., Paradis, C., Wu, L., & Hazen, T. C. (2015). Natural bacterial communities serve as quantitative geochemical biosensors. *MBio*, 6(3), 326-15.
- Steefel, C. I., Appelo, C. A. J., Arora, B., Jacques, D., Kalbacher, T., Kolditz, O., ... & Yeh, G. T. (2015). Reactive transport codes for subsurface environmental simulation. *Computational Geosciences*, 19(3), 445-478.

- Steefel, C. I., & Lasaga, A. C. (1992). Putting transport into water-rock interaction models. *Geology*, 20(8), 680-684
- Steefel, C. I., & Lasaga, A. C. (1994). A coupled model for transport of multiple chemical species and kinetic precipitation/dissolution reactions with application to reactive flow in single phase hydrothermal systems. *American Journal of science*, 294(5), 529-592.
- Vágvölgyi, V., Hales, M., Martens, W., Kristóf, J., Horváth, E., & Frost, R. L. (2008). Dynamic and controlled rate thermal analysis of hydrozincite and smithsonite. *Journal of thermal analysis and calorimetry*, 92(3), 911-916.
- Vallina, B., Rodriguez-Blanco, J. D., Brown, A. P., Blanco, J. A., & Benning, L. G. (2015). The role of amorphous precursors in the crystallization of La and Nd carbonates. *Nanoscale*, 7(28), 12166-12179.
- Van de Peer, Y., Chapelle, S., & De Wachter, R. (1996). A quantitative map of nucleotide substitution rates in bacterial rRNA. *Nucleic acids research*, 24(17), 3381-3391.
- Van Santen, R. A. (1984). The Ostwald step rule. *The Journal of Physical Chemistry*, 88(24), 5768-5769.
- Wanty, R. B., Podda, F., De Giudici, G., Cidu, R., & Lattanzi, P. (2013). Zinc isotope and transition-element dynamics accompanying hydrozincite biomineralization in the Rio Naracauli, Sardinia, Italy. *Chemical Geology*, 337, 1-10.
- Whitman, W. B., Coleman, D. C., & Wiebe, W. J. (1998). Prokaryotes: the unseen majority. *Proceedings of the National Academy of Sciences*, 95(12), 6578-6583.
- Wilkin, R. T. (2008). Contaminant attenuation processes at mine sites. *Mine Water and the Environment*, 27(4), 251.
- Woese, C. R. (1987). Bacterial evolution. *Microbiological reviews*, 51(2), 221-271.
- Xu, J., Fan, C., & Teng, H. H. (2012). Calcite dissolution kinetics in view of Gibbs free energy, dislocation density, and pCO<sub>2</sub>. *Chemical Geology*, 322, 11-18.
- Zuddas, P., & Podda, F. (2005). Variations in physico-chemical properties of water associated with bio-precipitation of hydrozincite [Zn<sub>5</sub>(CO<sub>3</sub>)<sub>2</sub>(OH)<sub>6</sub>] in the waters of Rio Naracauli, Sardinia (Italy). *Applied Geochemistry*, 20(3), 507-517.





\*(back cover) A group of miners from the Victoria Mine. Photo taken in ~1910. Ceded by Manolito de Çò de Paula. Arres de Jos.\*



**Supervisors:**

**Dr. Jordi Cama**

**Dr. Josep M. Soler**



**UNIVERSITAT DE  
BARCELONA**

